KU LEUVEN

ARENBERG DOCTORAL SCHOOL
Faculty of Engineering Science

Neonatal EEG Signal Processing

Vladimir MATIĆ

Dissertation presented in partial fulfillment of the requirements for the degree of Doctor in Engineering

March 2015

Neonatal EEG Signal Processing

Vladimir MATIĆ

Examination committee:
Prof. dr. A. Bultheel, chair
Prof. dr. ir. S. Van Huffel, supervisor
Prof. dr. ir. M. De Vos, co-supervisor
(University of Oxford)
Prof. dr. G. Naulaers
Prof. dr. ir. R. Puers
Prof. dr. ir. M. Moonen
dr. S. Vanhatalo
(Helsinki University)
dr. JP. Cherian
(Erasmus Medical Center Rotterdam)

Dissertation presented in partial fulfillment of the requirements for the degree of Doctor in Engineering

March 2015

© 2013 KU Leuven – Faculty of Engineering Science
Uitgegeven in eigen beheer, Vladimir MATIĆ, Kasteelpark Arenberg 10 box 2446, B-3001 Heverlee (Belgium)

Alle rechten voorbehouden. Niets uit deze uitgave mag worden vermenigvuldigd en/of openbaar gemaakt worden door middel van druk, fotokopie, microfilm, elektronisch of op welke andere wijze ook zonder voorafgaande schriftelijke toestemming van de uitgever.

All rights reserved. No part of the publication may be reproduced in any form by print, photoprint, microfilm, electronic or any other means without written permission from the publisher.

ISBN XXX-XX-XXXX-XXX-X
D/XXXX/XXXX/XX

Acknowledgements

Good? Bad? Who knows?

– Ajahn Brahm.

We say that life is a journey. So it is a PhD as well. In both, what is important are our attitudes. Do we take them for granted or not? Hence, we can care or be negligent towards our lives or our works. Usually, we are somewhere in between. However, this is the thesis about caring. It is a tiny part of a much higher goal. A goal whose purpose is to care. To care about babies. Those babies that need our help most. They are born under unfortunate circumstances as critically ill. Therefore, this PhD journey is not a single journey. It is a journey of all people who are dedicated to assist them. They fight for their lives! Care for them. Cure them. Help them. Here, we call them NeoGuardians. And here they are!

1. My supervisor, Prof. Dr. Sabine Van Huffel. Sabine, I am deeply thankful to you for all the guidance, help and encouragement that you have provided to me in the previous 5 years. You inspired me through your dedication, persistence and a life-living mission: that engineers with their tools assist clinical doctors. Thank you for all the vast knowledge that you shared, tough love when more work and organization from my side was lacking, social events that you hosted in your home and kind, supportive words in the moments of personal doubts. I am certain that you care for your students with your whole heart. Sabine, thank you!

2. My co-supervisor, Prof. Dr. Maarten De Vos. Maarten you were my daily supervisor and I want to thank you for all the great talks and activities that we shared. You were always there to encourage and to inspire me as a true leader! To move things one step forward. You were not only a mentor, but also a great friend. Someone with whom I was able to share both happy and doubtful moments and of course, the pintje of the infamous Belgium beer. I

learned a lot from you, how to think, how to be better organized and how to be more efficient. Maarten, thank you!

3. Prof. Dr. Gunnar Naulaers. Gunnar I see you as a truly unifying person. I recall that in 2011, "NeoGuard meeting" was hold with 3 persons only. With your leadership and action, today, more than 30-40 persons are actively involved in our joint research. The number is still increasing. Thank you for learning me about the clinical world, sharing your worldwide known expertise, instructing me what to do and giving precious advices how to approach collaborators. How to manage and unite everyone's interest (win-win situation, so to say :-)). Gunnar, thank you!

4. Dr. Perumpillichira Joseph Cherian . Joseph, I've spent numerous full-day visits with you in Rotterdam. I admire you for the real, sincere love for your work. Patience and pure enjoyment to help others. I really learned what it means to enjoy ones work and share your knowledge unconditionally with others. You were a great teacher about EEG, brain, collaborator and a great friend. You knew me better than I knew myself at occasions. When I needed a coffee or a walk to wake up (train to Rotterdam departs at 6 AM :-)), a criticism to perform better and magnificent (Hindu wisdom) support when the things were going tough. Joseph, thank you!

5. Dr. Sampsa Vanhatalo. Sampsa, I wish that I have met you much earlier! Your brilliance, amazing work, innovative ideas are something that influence scientists worldwide. You are the real master. From making the neonatal caps, high-quality signals, insightful conclusions and brilliant publications. Even debating about signal processing and engineering is challenging with you :-) I really cherished the moments of our collaboration started in Helsinki and my collaboration with you was very inspiring and profound. It seems that you are not working, but pursuing a dream. Sampsa, thank you!

As a list of NeoGuardians is never ending, I'll have to be a bit more concise. Leuven: Katrien, Jan, Anneleen, thank you for our joint work, EEG interpretations, and sharing with me direct experiences of caring about neonates in the NICUs. I really enjoyed it and was always visiting the NICU with great joy to meet you. Rotterdam: Paul, Renate, Leen, Gerhard, Jeroen, thank you for all the great work that we did together, inspiring meetings and fruitful conversations. Dear collaborators, Prof. Dr. Robert Puers, Hans, Prof. Dr. Wilfried Philips, Ivana, Danilo, Dirk it was a pleasure seeing how mathematical algorithms you craft into the real hardware device and a real 3D images!

Next, my great thanks go to my colleagues and buddies from the BIOMED group. Both 'older' and 'younger' ones. I want to thank to: Ivan, Yipeng, Amir-Dude (and Neda), Ninah-aligator, Joachim. Bogdan, Katrien, Wouter,

Bori, Rob. Diana, Nicolas, Anca, Maria, Kris, Barath, Adrian ... Milica, Devy, Steven, Lieven... Alexander, Carolina, Tim... Vanya, Laure, Griet, Kirsten, Ben, Jan...Alexander, Wouter. I had an amazing social events with you, conferences that we attended, birthdays, lunches and brainstorming meetings.

Special thanks go to my native friends living in Leuven (random order :-)): Ivan (travel buddy), Ivana, Bogi, Mire delija, Anja, Dusko, Milica, Milan Kumic and Sneza, Topke Kralj and Marija, Jelena Zeka, Ljilja, Natasa, Ana. Pavle, Acko, Ilija, LicWu, Andjelo, Dusan, Aca. Dries, Hasse. Danilo (coach), Milica. Uros and Milica Kresovic. Cvetkovic's family and their hospitality! Altogether, I cherish the great times at barbeques, travels, amazing parties, going-outs, sports and drinks at Oude Maarkt! My friends from Serbia: Kum Milos, Daca, Kumce Joca, Kum Zoki, Milica, Zile, Nemanja, Rale, Milica, Vojin, Zlateski, Ana C., Pirko, Ana P., Milena and many many others... :-) As the number of persons who profoundly affected and enriched my life is never ending, this is a special thanks to all of you !!! :-)

And finally, my biggest thanks go to my loving family! Veliko hvala bratu Miskecu. Voli te brat! Hvala celoj tetkinoj porodici Sulic i stricevoj porodici Matic. Takodje, svoj mojoj rodbini iz Bijeljine i Zrenjanina! Mama MirooOOoo, hvala na svemu! Na kraju sam postao doktor, ne medicine, ali nadam se da je i ova titula zadovoljavajuca. Samo jedna je majka. Cale, jedno veliko hvala! Kad porastem bicu stena i faca kao i ti. Bojana, ovoga puta necu zaboraviti da te potpisem kao na razglednici kada sam imao 7 godina :-) Puno te voli tvoj brat i hvala ti na svemu! Veliko je bogatstvo imati sestru. Vladimire, zete moj, hvala na podrsci! Nikola, nadam se da ovo vec umes da procitas: "Vlajce je postao doktor i puno te voli :-)". I nasem najmladjem i najmilijem clanu Nemanji posvecujem ovu tezu! Nemanja puno te voli tvoj ujak Vlajce!

At the end, I want to thank you ticMa! :-) You are both difficult to cope with and amazing person to have fun at the same time !

Uzdravlje !!! Cheers !!! Proost !!!

Abstract

The Neonatal Intensive Care Unit (NICU) is the very busy medical unit where preterm and critically ill full-term newborn babies are admitted. Worldwide, there are 15 million preterm deliveries (n=3642; Flanders, in 2008) from which one million neonates do not survive annually. In addition, another million of neonatal deaths are caused by hypoxia (n=449 (from mild to extremely severe hypoxia); Flanders, in 2008). Commonly there is a narrow window of opportunity that enables clinicians to intervene with neuroprotective therapies and medications. To promptly diagnose the level of brain injuries, continuous multi-channel electroencephalography (cEEG) can be used in NICUs as the optimal bed-side monitoring utility. However, a high level of expertise is required for the interpretation of the complex EEG patterns, and most NICUs, even the very large ones, are lacking this invaluable and expensive support. For instance, after the initial recruitment for hypothermia treatment, further cEEG monitoring generates approximately 100 hours of EEG data. Therefore, even when the expert's support is available, visual interpretation of cEEG is very laborious, subjective and continuous expert support is required for several days/nights. Additionally, due to the high costs of this support, not every neonate that requires cEEG examination will receive this monitoring. Therefore, neonatologists often use a simplified alternative: amplitude integrated EEG (aEEG), which provides insight into brain functioning using compressed 2-channels EEG. Compared to cEEG, this utility cannot detect milder brain injuries neither the majority of relevant clinical patterns. In addition, the compressed aEEG form proves to be very vulnerable to artefacts, thereby resulting in potential erroneous interpretations. As a result, the latest clinical recommendations advise the use of multi-channel EEG, and express the need for automated software to support the interpretation of cEEG monitoring of critically ill babies.

Within this thesis the automated algorithms for the EEG-based assessment of the brain functioning have been developed. Their goal is to assess the severity of the hypoxic brain injuries in the asphyxiated infants. This estimate will

assist clinicians to promptly diagnose and to guide further treatment decisions. Three main contributions are developed. First, an algorithm that detects dynamic interburst intervals has been extended with a post processing step that removes dubious and uncertain detections. In this way, a trustworthy algorithm has been developed. Second, we explored quantification of long-range temporal behavior of the neonatal EEG. We explored (Multifractal) Detrended Fluctuation Analysis and, further on, we proposed four metrics that show potential to differentiate the EEG background grades. Third, an automated method for the background EEG classification has been developed. As the first step, it maps shorter, segmented, EEG segments' features into segments' feature space, thereby creating a 3D distribution. Next, this 3D structure is represented as a data tensor that is used for further dimensionality reduction and robust classification.

The algorithms and their performances have been verified by expert EEG readers, demonstrating its potential. In addition, the efficient visualization developed within our project NeoGuard will enable fast insight into the algorithms' output and, hopefully, very soon be implemented in the NICUs.

Nomenclature

Symbols

$a, b, \ldots$	scalars
$\mathbf{a}, \mathbf{b}, \ldots$	vectors
$\mathbf{A}, \mathbf{B}, \ldots$	matrices
$\mathcal{A}, \mathcal{B}, \ldots$	tensors
a_{ijk}, $(\mathcal{A})_{ijk}$	element of three-way tensor $\mathcal{A}$ at position (i, j, k)

Basic operations

$\sum$	sum
$\|\mathbf{A}\|$	Frobenius norm of a matrix $\mathbf{A}$
$\mathbf{A}^T$	transpose of a matrix $\mathbf{A}$
$\mathbf{A}^{-1}$	inverse of a matrix $\mathbf{A}$
$\operatorname{rank}(\cdot)$	rank
$\langle \cdot, \cdot \rangle$	inner/scalar product
$\circ$	outer product
$\otimes$	Kronecker product
$\odot$	Khatri-Rao product
$\mathcal{A} \times_n \mathbf{U}$	mode-n product of a tensor $\mathcal{A}$ and a matrix $\mathbf{U}$
$\mathbf{A}_{(n)}$	mode-n unfolding or matricisation of a tensor $\mathcal{A}$

Metrics

Hz	Hertz
mV	millivolt
μV	microvolt
s	seconds
h	hour

Abbreviations

aEEG	Amplitude-integrated Electroencephalogram
ANOVA	Analysis of Variance
BSS	Blind Source Separation
CCA	Canonical Correlation Analysis
CFM	Cerebral Function Monitor
CNS	Central Nervous System
DFA	Detrended Fluctuation Analysis
DFT	Discrete Fourier Transform
dIBI	dynamic Interburst Interval
DWT	Discrete Wavelet Transform
ECG	ElectroCardioGram
EEG	ElectroEncephaloGram
EMG	ElectroMyoGram
EOG	ElectroOculoGram
FIR	Finite Impulse Response
fMRI	Functional Magnetic Resonance Imaging
HIE	Hypoxic Ischaemic Encephalopathy
HO-SVD	Higher-Order Singular Value Decomposition
HODA	Higher-Order Discriminant Analysis
HRV	Heart Rate Variability
IBI	Interburst Interval
ICA	Independent Component Analysis
JADE	Joint Approximate Diagonalization of Eigenmatrices
LDA	Linear Discriminant Analysis
LRTC	Long-Range Temporal Correlation
LS-SVM	Least Squares Support Vector Machine
MRI	Magnetic Resonance Imaging
MF-DFA	Multifractal Detrended Fluctuation Analysis
NICU	Neonatal Intensive Care Unit
PCA	Principal Component Analysis
SOBI	Second Order Blind Identification
SVD	Singular Value Decomposition
SVM	Support Vector Machine

Contents

Acknowledgements i

Abstract v

Nomenclature vii

Contents ix

List of Figures xv

List of Tables xxix

1 Introduction 1

1.1 Critically ill Neonates 1

1.2 Problem Statement 3

1.3 Collaboration 4

1.4 Contribution of the thesis 6

2 Human brain and EEG monitoring 9

2.1 The human brain 9

2.1.1 Anatomy of the brain 9

2.1.2 Neural activity 10

2.2 The Electroencephalography 12
2.2.1 Scalp EEG 12
2.2.2 EEG characteristics 15
2.2.3 Practical applications of EEG 17
2.3 The neonatal brain 17
2.3.1 Perinatal brain injury due to hypoxia-ischemia 17
2.3.2 EEG monitoring of the neonates 18
2.3.3 Amplitude integrated EEG - aEEG 20
2.4 Artifacts in the neonatal EEG 22
2.4.1 EEG in the healthy term neonate 24
2.4.2 EEG patterns associated with neonatal brain damage . . 25
2.4.3 Visual scoring of the EEG background 27
2.5 Conclusion 32

3 Essential mathematical techniques 33

3.1 Data Representation 33
3.2 Neonatal EEG data representation - 1D Signal decomposition . . 34
3.2.1 Time-frequency signal decompositions 34
3.2.2 Discrete Wavelet Transform 36
3.2.3 Fractal Analysis 38
3.3 Fundamentals of multilinear algebra 40
3.4 Matrix and Tensor Decomposition Models 42
3.4.1 Singular Value Decomposition - SVD 42
3.4.2 Principal Component Analysis - PCA 43
3.4.3 Independent Component Analysis - ICA 44
3.5 Tensor decompositions 46
3.5.1 TUCKER decomposition model 46

3.5.2 Higher Order Discriminant Analysis approach for multi-way features . . . 48
3.6 Machine Learning Foundations . . . 51
3.6.1 Linear Discriminant Analysis . . . 51
3.6.2 Support vector machines . . . 53
3.7 Conclusion . . . 55

4 Automated detection of dynamic interburst intervals 57

4.1 Introduction . . . 58
4.2 Methods and Materials . . . 60
4.2.1 Dataset . . . 60
4.2.2 Exploratory definition of dynamic interburst interval . . . 61
4.2.3 Automated detection of dIBIs . . . 63
4.2.4 Classification of EEG segments into the low amplitude class 64
4.2.5 Detection of dIBI candidates . . . 66
4.2.6 Improving reliability of monitoring background EEG dynamics . . . 67
4.2.7 Framework for the reliability parameterization of dIBI . . 75
4.3 Results . . . 82
4.3.1 Dataset DA . . . 82
4.3.2 Dataset DB . . . 82
4.3.3 Validation of the complete algorithm - Dataset DC 83
4.3.4 Benchmarking: dIBI duration and amplitude vs. expert visual background EEG scoring . . . 85
4.4 Discussion . . . 87
4.4.1 Added Clinical Value of dIBI parameter . . . 91
4.5 Conclusion . . . 93

5 Heart Rate Variability in asphyxiated neonates 95

5.1 Introduction 95
5.2 Materials and Methods 96
5.2.1 Dataset 96
5.2.2 Heart Rate Variability parameters 97
5.3 Discussion 99
5.4 Conclusion 100

6 Long-range temporal behavior as a quantitative marker of abnormality 101

6.1 Introduction 102
6.2 Methods and Materials 103
6.2.1 Datasets 103
6.2.2 Feasibility of DFA in the neonatal EEG 104
6.2.3 Feasibility of MF-DFA in the neonatal EEG 106
6.2.4 Benchmarking with EEG grades 107
6.3 Results 107
6.3.1 DFA 107
6.3.2 Multifractal DFA (MF-DFA) 110
6.4 Discussion 119
6.5 Conclusion 122

7 Holistic approach for automated background EEG assessment 123

7.1 Introduction 124
7.2 Methods 125
7.2.1 Dataset 125
7.2.2 Multi-dimensional structure for capturing EEG dynamics 126
7.2.3 Design of segments' features 127
7.2.4 Creating a tensor distribution structure 131

7.2.5 Tensor decomposition techniques: dimensionality reduction step . . . 133
7.2.6 Classification . . . 138
7.3 Results . . . 141
7.3.1 Automated assessment of background EEG of 1h long epochs . . . 141
7.3.2 Benchmarking . . . 143
7.4 Discussion . . . 143
7.5 Conclusion . . . 149

8 Conclusion and Future work 151
8.1 Overview of the developed algorithms . . . 151
8.2 Future Work . . . 154
8.2.1 Monitoring the speed of the HIE recovery . . . 154
8.2.2 Novel data-driven findings . . . 155
8.2.3 Improvements in dIBI parameter detections . . . 156
8.2.4 Clinical validation of the developed algorithms . . . 158
8.3 Using automated approach to recruit infants for the hypothermia treatment . . . 158
8.4 Benefits of multichannel EEG recordings . . . 159
8.5 Future development of the algorithms' accuracy . . . 159
8.6 Bringing decision-support systems into the NICUs . . . 160

Appendices 163

Bibliography 163

Curriculum 177

Publication list 179

List of Figures

1.1 A distribution (%) of direct causes of 4 million neonatal deaths for the year 2000. Most of the incidents are reported in the undeveloped countries (adapted from [73]) 2

1.2 (Left) Critically-ill neonate in the NICU. Every electrode is manually attached and EEG monitoring is performed. (Right) A healthy neonate being monitored with the use of neonatal EEG caps. 2

1.3 The official logo of the NeoGuard consortium, which has been designed by Ivana Despotovic. 5

1.4 Four main thesis's contributions and the mathematical theory being used. The neighboring circles in the scheme were used for the benchmarking purposes. 8

2.1 A Human brain anatomy consists of three parts: cerebrum, cerebellum and brain stem. In addition, four different lobes are distinguished. 10

2.2 The cortical gray matter consists of cell bodies and dendrites and can be found at the outmost surface of the brain (the cortex) and in some deeper structures. On the other hand, the inner part of the brain consists of the axons of the nerve cells and is called white matter. 11

2.3 A scheme of the basic parts of the neuron's structure. From [131] 12

2.4 Propagation of the action potential along an axon is illustrated. From [131]. 13

2.5 Illustration of two electrodes placed on the human scalp in order to measure brain electrical activity. 14

2.6 Hans Berger, German scientist who was the first to record human EEG activity in 1924. 14

2.7 The first EEG signal recorded in humans. 10Hz signal was used as a reference to observe the morphology of the EEG signal. . . . 14

2.8 International 10-20 system for the standardized electrode placement. From [131]. 15

2.9 Examples of different rhythms of brain activity. 16

2.10 Phases of the brain development. From [34] 19

2.11 Neonatal EEG montages. A: Restricted 10–20 system using nine electrodes; B: Full 10–20 system of electrode placement using 17 electrodes. From [103]. 20

2.12 Original neonatal EEG signal recorded for a duration of 600s (10 min). 22

2.13 Transformed EEG signal, after filtering and rectifying. Next, the minimum and maximum segments' points are marked by asterisks. 23

2.14 Final aEEG data points show in a compressed way 10 min of EEG with only 40 data points. 24

2.15 An example of the neonatal EEG signal that is corrupted with the ECG artifact. 25

2.16 Awake EEG at term age. Theta and delta activity is shown with normal voltage (20–70 μ V). The band width between 5 and 20 μ V is normal, and the fluctuations suggest sleep–wake cycling. From [103]. 26

2.17 Normal quiet sleep of the term infant. Tracé alternant with lower voltage during 2–5 seconds, and higher voltage in the next 3 seconds. 27

2.18 Different neonatal EEG patterns are illustrated. Green rectangle implies the lower voltage states, which are associated with the brain injuries in term neonates. However, in preterm neonates, some patterns represent normal phases of EEG maturation (e.g. burst-suppression and tracé discontinue). Blue rectangle illustrates low amplitude in discontinuous (interburst) periods. Adapted from [123]. 28

2.19 Trace discontinu in a neonate with moderately severe HIE. Background activity is of low voltage (<20 μ V). The discontinuous periods, with a mean voltage of 10 μ V, are interrupted by bursts of EEG activity of 2–3 seconds duration. aEEG trend covering 30 minutes shows a band width of 2–7 μ V. Sleep–wake cycling is absent. 29

2.20 Burst suppression (BS) pattern in severe birth asphyxia. Severely suppressed background activity (<5 μ V) with intermittent bursts of 10–20 μ V. As opposed to tracé discontinu [2.19], no EEG activity is discernible during the discontinuous periods. aEEG trend of 30 minutes shows BS and absent variability. Mean band width of the suppressed periods is <2 μ V 29

2.21 Ideal examples of neonatal background EEG patterns From [68] 30

2.22 An 8-grade scoring system for the background EEG abnormalities. One grade is assigned to neonates, thus allowing easy categorization of neonates according to the EEG grades. From [103]. 31

3.1 Heisenberg time-frequency boxes of two wavelets, $\psi_{u,s}$ and ψ_{u_0,s_0} . When the scale s decreases, the time support is reduced but the frequency spread increases and covers an interval that is shifted toward high frequencies. Adapted from [79]. 37

3.2 The time-frequency boxes of a wavelet basis define a tiling of the time-frequency plane. 38

3.3 (A) Columns, (B) rows and (C) tubes in a third-order tensor. . . 41

3.4 (A) Horizontal, (B) vertical and (C) frontal slices of a 3D tensor. 41

3.5 Illustration of the PCA using the sum of the outer product vectors (upper) and the multiplication of the two matrices $\mathbf{M}$ and $\mathbf{S}$ (bottom). 44

3.6 An illustration how ICA can be applied to reconstruct different sources from the scalp EEG recordings. The ICA determines the sources s which are generated deep inside the scull. 45

3.7 An illustration of the ICA algorithm (SOBI) being applied onto the neonatal EEG signal from the Figure 2.15 generated 12 independent components. We can clearly identify that the independent component number 11 corresponds to the ECG activity. 47

3.8 Illustration for a 3D TUCKER decomposition. The objective is to find the optimal (factor) matrices $\mathbf{U}^{(n)}$ and the core tensor $\mathcal{G}$, which is commonly of a much smaller dimension as compared to $\mathcal{X}$. 48

3.9 Illustration of feature extraction from a set of 3-way data tensors $X^{(k)}$, k=1,2,..,K. The objective is to estimate common factor matrices (basis) $\mathbf{U}^{(n)}$, n=1,2,3 and the core tensors $\mathcal{G}^{(k)}$. 50

3.10 Illustration of the two (A) and three (B) classes classification problem. 52

4.1 Classical burst suppression pattern detected in the early stage of the EEG recording. 61

4.2 Detected tracé discontinue patterns with higher interburst amplitudes that evolved over 24h from patterns shown in Figure 4.1. 62

4.3 In the upper trace the EEG signal is shown. Two concatenated sliding windows (red and blue, 256 samples or 1s long each) are moved along the EEG signal incrementally for one sample. For every sample point amplitude and frequency content inside the windows are compared. This results into the signal, Total Difference (TD), shown in the lower trace, which is used for the segmentation. Local maxima of this signal determine the changes in EEG signal and are used to locate segments' boundaries. . . . 63

4.4 In the upper trace, signal Total Difference (TD) is smoothed with a moving average filter (of order 64 that corresponds to 0.25s) to enhance the segmentation of suppressed epochs. In addition, the TD signal is thresholded with a value 1, thereby favoring the creation of prolonged low amplitude segments. In addition, we limited the duration of segments to a minimal value of 0.75s. In the lower trace, segment boundaries are marked for the EEG signal. 65

4.5 The EEG signal is segmented and low amplitude class (L) segments are coloured in blue. Red 'areas' illustrate parameter 'area amp 10'. This parameter represents the total area of the signal that exceeds the threshold values at $\pm 10\mu$V. In addition, the segment, which is not coloured in blue, has 'area amp 10' higher than 50, and it is not a low amplitude segment (L). 66

4.6 First, the EEG signal is adaptively segmented. Next, segments are classified into the low amplitude class (blue). Automatically detected dIBI candidates with the algorithm A are marked with black rectangles. The first detected dIBI cannot be regarded as a definite dIBI because of its ambiguous morphology. On the other hand, the second detected dIBI would be visually marked as definite by the majority of EEG readers. 68

4.7 Low amplitude temporal profile (LTP) signal is created for the EEG signal in Figure 4.6. In this example, LTP signal is thresholded at the value 11 (=20 channels/2 +1). The time interval when this signal exceeds the threshold determines the duration of dIBI. Intervals above the threshold and shorter than 3 seconds are not considered as dIBI detections. 69

4.8 Detection of dIBI candidate. As previously described, EEG signal is first segmented (A1) and segments are classified into the low amplitude class (A2). The Low amplitude Temporal Profile (LTP) signal is calculated and used to detect dIBIs (A3). 70

4.9 Ambiguous EEG pattern occurring close in time as the patterns in Figure 4.2. Note that it is better to exclude this detection as it does not express clearly distinguishable burst-suppression-burst complex. 71

4.10 Examples of false positive detections that are produced by the epileptic seizure activity. 72

4.11 Artifact interrupts the suppressed interval, thereby falsely shortening dIBI duration and amplitude assessment. Instead of one longer, two shorter dIBI candidates are detected. 73

4.12 Bursts with very low amplitudes ('peak to peak' $< 20\mu$V) are missed by the detection algorithm, producing falsely prolonged dIBI detection. 74

4.13 Two transitioning points are illustrated for milder EEG discontinuity (dIBI<10s; left) and for severe EEG discontinuity (dIBI>10s; right). Note that for shorter dIBI amplitude of the suppressed part shows more variability and the transitioning point is more challenging to be validated. On the other hand, longer dIBI (classical burst-suppression) shows non-responsive amplitude, thereby making recognition of definite dIBIs much easier. 75

4.14 Amplitude distribution of definite dIBIs is depicted for each dIBI group. Groups are defined according to dIBI duration: Group I: 3s≤dIBI<5s; Group II: 5s≤dIBI<10s; Group III: 10s≤dIBI<20s; Group IV: 20≤dIBI (<40s). For these dIBI duration groups, we performed a one-way ANOVA and found a significant difference in the mean amplitude distribution applying Bonferroni correction (F-statistic=337.8, p<0.001). 76

4.15 Flow chart of the algorithm for automated detection of definite dynamic interburst intervals. The detected dIBI candidate is parameterized and obtained values are used as classifiers' input feature vectors. To optimally account for diverse duration-related dIBI morphological differences, four different LS-SVM classifiers are independently optimized. They make a decision whether a dIBI candidate is definite dIBI and whether it should be used for EEG quantification. On the other hand, uncertain detections, will be excluded from further EEG analysis as misclassified dIBIs. 77

4.16 A detected dIBI candidate is marked with large black rectangle, whereas low amplitude segments (L) are marked with smaller ones. The reliability parameter transitioning examines the dIBI segmentation accuracy and the certainty of the complete complex burst-suppression-burst. For each channel, 3s of the burst part (red) and 3s of the suppressed part (blue) are compared. Here, only two such examples are illustrated with red/blue rectangles. In addition, an illustration of the parameter longest is depicted in green. It calculates the longest possible duration of the consecutive segments with low amplitude (L) within dIBI. In channel C4-O2, this value is maximal (=1), whereas for the channel Fp2-T4 this value is 0.5 (50% of the duration of dIBI candidate). Parameter longest is useful to exclude ambiguous EEG discontinuity and other uncertain detections. 79

4.17 Illustration of how the parameter flatness is calculated within the suppressed dIBI part (4s long) for a single channel. Two horizontal red lines are adaptively adjusted until they meet two criteria. First, they need to enclose 95% of the signal samples. Second, the calculated distance between them has to be minimal. In this example the calculated distance is 14μV. 80

4.18 Transitioning parameter is illustrated for detected EEG discontinuity. The first 3s of the signal represents a burst period, whereas the last 3s corresponds to the suppressed segment (upper plot: purple-original EEG signal, black - approximated EEG signal). In two lower figures, wavelet coefficients (levels from 2 to 4 are displayed as they carry the largest portion of signal power) are depicted in black for zero values and in white and yellow for larger absolute coefficient values (middle plot). After sparse approximation, large wavelet coefficients would be retained mainly within the abrupt burst activity (bottom plot). Therefore, in this example, the parameter transitioning (value close to 1) would imply that vast majority of abrupt activity is localized within the left (burst) part of the signal, whereas the right part (suppression) does not contain any significant component of EEG activity with higher frequency. Note that high energy coefficients (colored in white) capture the 'high activity burst' behavior as compared to the suppressed periods where such activity is lacking. Therefore, the calculation of transitioning parameter efficiently characterizes the presence of distinguishable burst/suppression alternations. 81

4.19 ROC curves presenting the performance of classifier for group I (3s ≤ dIBI < 5s). 83

4.20 (ROC curves presenting the performance of classifier for group II (5s ≤ dIBI < 10s). 84

4.21 ROC curves presenting the performance of classifier for group III (10s ≤ dIBI < 20s) 84

4.22 ROC curves presenting the performance of classifier for group IV (20s ≤ dIBI). 85

4.23 For every duration-related dIBI group, the first bar (A) represents the distribution (ratio) of definite dIBIs (blue) and misclassified ones (red) as visually marked by an experienced clinical neurophysiologist (PJC). After the refinement step, the classifier selects a subset of dIBIs. Consequently, the size of the second bar (B_1) is represented by proportionally shrinking the size of the bar (A). Here, dIBIs that are retained in the reliable subset (B_1) and previously marked as definite are shown in blue. The red bar segments corresponds to misclassified detections (false positives). 86

4.24 The results of automated definite dIBI detections in dataset DC as compared to the visual scoring. First, the algorithm A detected dIBI candidates (both definite and misclassified) and this is presented in the 2nd column. The number of visually scored definite dIBIs is presented in the 3rd column. After the refinement step, the algorithm B retains definite dIBIs which are compared with the visual scoring. The true positive rate (%) is presented in the 4th column, whereas the false positive rate (%) is presented in the 5th column. The results are presented for four dIBI duration groups and the total number of detections is given. 87

4.25 Output of the algorithm is compared with the background EEG abnormalities visually graded by an experienced clinical neurophysiologist. Median duration and amplitude of definite dIBIs detected within 1h of cEEG are plotted as a single data point (4 data points per neonate). Background EEG abnormality of the corresponding 1h epoch is scored by the clinical neurophysiologist as mild (blue), moderate (red) or severe (black). 88

4.26 Interdependence of dIBI duration and amplitude. Data points represent 2079 definite dIBIs (<40s). There was a strong correlation between the two parameters for dIBIs (<20s): 1807 data points, Spearman ρ=-0.51, p<0.001. In contrast, correlation between the two parameters for dIBI duration from 20s to 40s was less significant: 272 data points, Spearman ρ=-0.14, p=0.02. 92

4.27 Interburst amplitude distribution is shown for dIBIs and BS-IBI (shaded boxes) lasting from 3-5s. The following groups are created: 1 - dIBI amplitude for good outcome group, 2 - dIBI amplitude for poor outcome group, 3 - BS-IBI amplitude for good outcome group and 4 - BS-IBI amplitude for poor outcome group. dIBI amplitude better discriminates the two outcome groups. . . 93

4.28 Interburst amplitude distribution is shown for dIBIs and BS-IBI (shaded boxes) lasting from 5-10s. The following groups are created: 1 - dIBI amplitude for good outcome group, 2 - dIBI amplitude for poor outcome group, 3 - BS-IBI amplitude for good outcome group and 4 - BS-IBI amplitude for poor outcome group. dIBI amplitude better discriminates the two outcome groups. . . 94

5.1 Subset of HRV parameters that achieved the best discrimination between groups with good and poor outcome. All parameters are depicted using normalized values. 98

6.1 (A) An example of normal neonatal EEG signal with continuous background pattern. (B) The signal is band-pass filtered between 3-8 Hz (blue), and the instantaneous amplitude envelope (red) is calculated using Hilbert transform. (C) The DFA fluctuation function is presented along the y axis, whereas the size of the windows analysed in the DFA method are displayed in the x axis. The red line presents an example of linear fluctuation function that is here fitted for the time scale 10-60 seconds to obtain its slope, the DFA scaling exponent α. (D) DFA fluctuation functions are plotted for 15 min EEG epochs from different background EEG abnormalities (Mild-blue, Moderate-red, Severe-black). (E) Comparison of scaling exponent α between different background EEG grades shows a significant difference between grades 2 and 3. (F) An example of the DFA fluctuation function (moderate EEG grade) where clear existence of the crossover points are illustrated. 109

6.2 Application of MF-DFA paradigm on two different neonatal EEG signals, continuous (A1) and burst-suppression (A2), respectively. In Fig. (B1)-(B2), the q-order fluctuation function, Fq, is shown for two processes. (C1)-(C2). q-order Hurst exponent, Hq, is obtained as the linear fitting coefficient of the Fq fluctuation lines from Figs. (B1) and (B2). (D1)-(D2). Multifractal spectra are displayed for continuous and burst-suppression neonatal EEG periods. 112

6.3 (A)-(C) MF-DFA spectra lines are randomly selected and displayed for various background EEG degrees of abnormality: A-mild (blue), B-moderate (red) and C-severe (black). (D). Average of all 1088 multifractal spectra lines is displayed for three background EEG classes. (E)-(H). results of Kruskal-Wallis mean value group comparisons are displayed for mean hq ($p<0.01$), width hq ($p<0.001$), mean Dq ($p<0.01$) and height Dq (not significant). 113

6.4 (A1-A3) Three examples of burst-suppression, tracé discontinue and continuous EEG periods are shown as aEEG trends and EEG epoch in an infant who is showing recovery from initial severe hypoxic insult. (B) Three multifractal spectra lines are shown for the corresponding three states quantifying 15 min of burst-suppression (black-recorded at 6h postpartum), tracé discontinue (red-recorded at 12h post partum) and continuous EEG period (blue-recorded at 18h postnatal age). (C1)-(C4) from 15 min segments mean IBI, mean hq, width hq and mean Dq values are represented as one data point (24 in total; 2h x 4 (15 min epochs in 1h) x 3 epochs). 116

6.5 Correlation between IBI and MF-DFA metrics computed from the whole MD-DFA spectra. The four left side columns present significance levels and the four right side columns show the corresponding Spearman correlation coefficients. Significant correlations ($p < 0.01$) are highlighted with green, and their corresponding ρ values are highlighted in orange. The correlations in each patient were computed from 32 epochs. 117

6.6 Correlation between IBI and MF-DFA metrics computed from the right side of the MD-DFA spectra. The four left side columns present significance levels and the four right side columns show the corresponding Spearman correlation coefficients. Significant correlations ($p < 0.01$) are highlighted with green, and their corresponding ρ values are highlighted in orange. The correlations in each patient were computed from 32 epochs. Comparison to Figure 6.5 shows that the sign of correlation is more consistent when measuring the right side of spectra only. 118

6.7 Five neonates in which mean IBI values are highly correlated with the MF-DFA metrics (calculated from the right part of the multifractal spectra). Figures (A1)-(A4) respectively, represent the correlation between mean hq, width hq, mean Dq and height Dq values with the mean IBIs. This approach for calculation of MF-DFA based metrics avoids insensitivity to the asymmetry which affects the originally proposed parameters calculated for the complete spectra (see [136]). 120

7.1 Three blocks represent the parameterization of the cEEG data stream. **A**. First, EEG signal is adaptively segmented. **B**. Segment's features are calculated for each segment and depending on the quantized features' index values (m_1, m_2, m_3) they are mapped into the discretized segments' feature space. **C**. 3D distribution is parameterized using the tensor representation to effectively capture the structure of the distribution. That is, tensor elements represent prevalence of segments with a particular discretized feature distribution. 127

7.2 An EEG epoch is adaptively segmented and the segments are classified into three peak-to-peak amplitude classes: Low<20 μ V (blue), 20 μ V ≤ Medium < 40 μ V (green) and High ≥ 40 μV (red). 129

7.3 Three temporal profile signals (LTP, MTP and HTP) count the occurrences of the amplitude classes across EEG channels. . . . 130

7.4 Global grade of the spatial EEG amplitude, m_2 value, is derived using the signals (LTP, MTP and HTP). 131

7.5 Epoch of EEG signal is adaptively segmented. The segments are colored according to their amplitude values into blue (Low), green (Medium) and red (High). Five segments are marked to illustrate the quantification of various interplays with the adjacent segments: A(2, 4, 1) B (7, 5, 9), C(2, 6, 4) D (4 ,2 ,6) , E (2 ,4, 1). 132

7.6 Feature index values m_2 representing global amplitude are displayed. 133

7.7 Mapping of the EEG segments from Figure 7.5 into the distribution structure. The view is displayed along the axis m_1 and m_2, whereas the color bar represents the number of EEG segments in a particular frequency bin. 134

7.8 Mapping of the EEG segments from Figure 7.5 into the distribution structure. The view is displayed along the axis m_1 and m_3, whereas the color bar represents the number of EEG segments in a particular frequency bin. 135

7.9 2D distribution of mild background EEG abnormalities displayed along modes m_1 and m_2, whereas the color bar represents the number of EEG segments in a particular frequency bin. 136

7.10 2D distribution of mild background EEG abnormalities displayed along modes m_1 and m_3, whereas the color bar represents the number of EEG segments in a particular frequency bin. 137

7.11 2D distribution of moderate background EEG abnormalities displayed along modes m_1 and m_2, whereas the color bar represents the number of EEG segments in a particular frequency bin. 138

7.12 2D distribution of moderate background EEG abnormalities displayed along modes m_1 and m_3, whereas the color bar represents the number of EEG segments in a particular frequency bin. 139

7.13 2D distribution of severe background EEG abnormalities displayed along modes m_1 and m_2, whereas the color bar represents the number of EEG segments in a particular frequency bin. 140

7.14 2D distribution of severe background EEG abnormalities displayed along modes m_1 and m_3, whereas the color bar represents the number of EEG segments in a particular frequency bin. 141

7.15 Illustration of a tensor decomposition using a Tucker-3 model. The objective is to estimate factor matrices $\mathbf{U}^{(n)}$ and a core tensor $\mathcal{G}$. In general, the constraints are imposed on factor matrices $\mathbf{U}^{(n)}$ such as orthogonality, non-negativity and/or statistical mutual independence. If the orthogonality is imposed, the decomposition can be seen as an extension of the singular value decomposition (SVD) into a higher dimension. 142

7.16 Flow chart illustrating a classification procedure based on the Tucker decomposition of the concatenated tensor $\mathcal{X}$ consisting of all sampling training data $\mathcal{X}^{(k)}$. Reduced features are obtained by projecting the testing data tensor $\dot{\mathcal{X}}$ onto the feature subspace spanned by factors (bases) $\mathbf{U}^{(n)}$ (Projection filter). The most discriminative elements are selected from the core tensors, using the Fischer selection score and used for the final classification. Output of the Least-Squares Support Vector Machine (LS-SVM) classifiers provides the assessed background EEG grade. 142

7.17 Confusion matrix represents agreement of automated classification method and the expert EEG reader. 1h cEEG epochs were classified into mild, moderate or severe background EEG class. All classified epochs represent non-preselected, real case EEG recordings. The overall classification accuracy of 89% (=(73+44+126)/272) has been achieved. 143

7.18 Comparison of background EEG grades scored on 1h of cEEG by an experienced clinical neurophysiologist (red) and automated assessment of those grades (blue). These grades show correlation with the median interburst interval (IBI) values. Background EEG activity not containing IBIs are not displayed here (40 out of 80 mild (to normal) background EEG grades). 144

8.1 Median dIBI durations are plotted for processed four 1h EEG distinctive post partum hours of monitoring: (1) 21-22h, (2) 27-28h, (3) 33-34h and (4) 39-40h. In this example, there is an improvement of the infant's condition. Consequently, this neonate had a normal follow-up at 6 months examination. 152

8.2 Median dIBI amplitudes are plotted for processed four 1h EEG distinctive post partum hours of monitoring: (1) 21-22h, (2) 27-28h, (3) 33-34h and (4) 39-40h. This is the same infant as in the Figure 8.1. 153

8.3 Qualitative comparison of the algorithms developed in this thesis. The strength is presented with +++, whereas the weaknesses are presented with +. 154

8.4 The figure illustrates how distribution of 2 simultaneously measured segments' features will behave when the EEG recovers from severe to moderate background EEG. Interpretation is that the recovered EEG will consist of more shorter segments with higher amplitudes and more variability. In addition, low amplitude (lower delta-2 power values), non-responsive segments creating prolonged segments (3-5s long) will be disappearing. . . 156

8.5 Modeling of the duration of detected dIBIs as the log-normal distribution. 157

8.6 The 1st layer of the GUI is shown for the routine clinical use in the NICUs. Developed by IPI Group - University of Ghent and NeoGuard consortium. 161

8.7 Detected parameters will be displayed on the 3D brain model for the expert clinical use. Developed by IPI Group - University of Ghent and NeoGuard consortium 161

List of Tables

1.1 An extensive international survey of 210 NICUs: Use of aEEG/EEG and the presence of brain experts in the EU and US [15]. 3

2.1 Table that summarizes scoring grades for the visual background EEG classification as proposed in [90]. 28

7.1 Index feature m_1 obtains values according to the corresponding amplitudes ranges. 128

7.2 A segment is classified into one of the three amplitude classes: Low (L), Medium (M) or High (H). Within the single EEG channel, adjacent segments that express the same amplitude class are merged and duration of this interval is calculated. The interval duration determines the values for m_3 index parameter according to the table. All consecutive segments which are merged in this way would have the same m_3 index values regardless of their position in this segments' stream. 129

Chapter 1

Introduction

1.1 Critically ill Neonates

Functional brain development during the neonatal period is a critical time in the individual's life span: medical conditions that compromise brain function (such as perinatal asphyxia) have a high risk for neurodevelopmental problems, including cognitive deficits, motor disability and behavioral problems [43]. Consequences are lifelong burdens for the individuals and their families, and a major socio-economic impact for the health care system and the society. Hence, any alleviation of perinatal adversities holds promise of improved quality of life for the individual, and a major benefit for the society. The Neonatal Intensive Care Unit (NICU) is the very busy medical unit where preterm and critically-ill term newborn babies are admitted. The former represent a larger population of patients and worldwide, there are 15 million preterm deliveries that lead to one million neonatal deaths annually (Figure 1.1). At the local level, in Flanders, around 70, 000 births are registered annually with 7% of the babies born prematurely. The group of patients with perinatal asphyxia has fortunately decreased in the developed countries and happens in 1-6 per 1,000 deliveries. In 2008, 449 neonates with perinatal asphyxia were admitted in the NICUs in Flanders [19]. In large regional NICU centers (e.g. UZ Gasthuisberg Leuven, EMC Rotterdam), the number of annually admitted neonates with asphyxia is from 10-20. The consequences of asphyxia are commonly very severe and may lead to a very poor outcome.

In spite of the rapid improvement of diagnostic methods, there is still an important, widely recognized, need for new ways of high quality monitoring

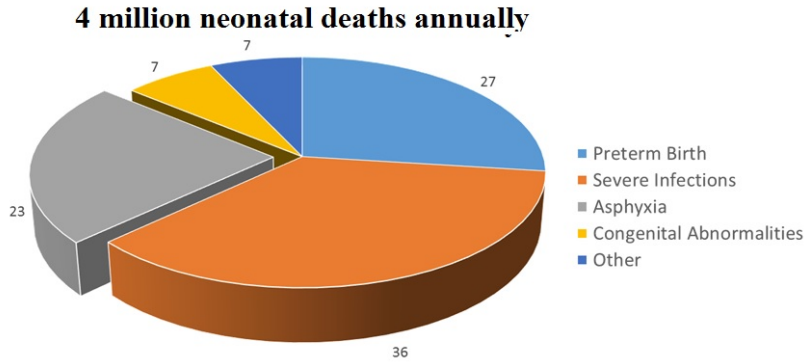

Figure 1.1: A distribution (%) of direct causes of 4 million neonatal deaths for the year 2000. Most of the incidents are reported in the undeveloped countries (adapted from [73])

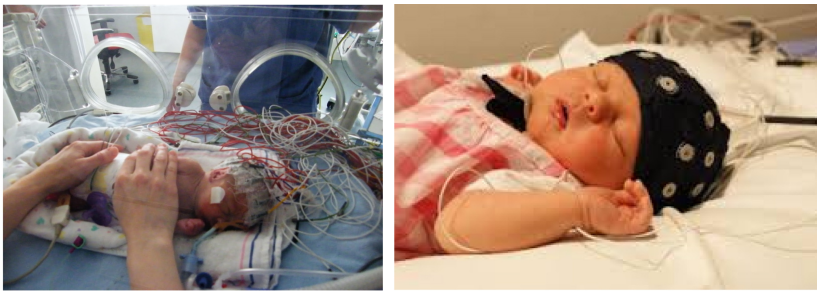

Figure 1.2: (Left) Critically-ill neonate in the NICU. Every electrode is manually attached and EEG monitoring is performed. (Right) A healthy neonate being monitored with the use of neonatal EEG caps.

of the brain function in the early life. Among all known brain recording methods (electroencephalography (EEG), functional MRI (fMRI), near infrared spectroscopy (NIRS), and magnetoencephalography (MEG)), EEG is a non-invasive technique that is easily applicable in a clinical context and can reliably detect infant brain activity with a direct relevance to acute neurological illness and future neurocognitive outcomes (Figure 1.2). However, clinical analysis of neonatal EEG has been fully based on a graphological approach: visual assessment of individual waveforms and patterns of ongoing EEG activity. The limitations of this have been obvious for a few decades already, and several mathematical signal analysis paradigms have been introduced. The only currently used signal analysis method in clinical practice is the time-compressed

amplitude visualization known as “amplitude integrated EEG” trend (aEEG; a.k.a. CFM-commercial software solution). aEEG is easy to use and the visual pattern recognition can be used by neonatologists and nurses to interpret the background pattern and convulsions [53]. In contrast, EEG modality will provide much more clinically relevant information. For instance, aEEG (only 2-channel signal) cannot detect (milder) brain injuries that are not seen in the central brain area (C3-C4 is the common electrode positioning used for aEEG; C-central).

In NICUs, while treating critically ill neonates, neonatologists may rely on the expert EEG decision support from the Clinical Neurophysiology Department. On the other hand, in some NICUs, a neonatologist may be experienced in aEEG/EEG interpretation, though this experience is either not available or is present in a lesser extent. Therefore, a clinical neurophysiologist, for instance, may provide support by reviewing the EEG signal remotely and consult neonatologists in the NICU. Apart from being scarce and expensive, this support is not available 24/7 (during nights and weekends), although in many cases the decisions has to be brought promptly and continuous expert support may be needed for several days. In addition, the visual interpretation of EEG is very laborious, time consuming and subjective. According to the very extensive international survey, the use of aEEG/EEG monitoring as well as the presence of brain experts are shown in Table 1.1.

Table 1.1: An extensive international survey of 210 NICUs: Use of aEEG/EEG and the presence of brain experts in the EU and US [15].

EEG device	No brain expert	With brain expert
No EEG	10%	-
aEEG	16%	4%
full EEG	20%	50%

Consequently, the latest clinical recommendation standards advise the use of multi-channel EEG, and express the need for automated software solutions to support the interpretation of EEG-based diagnostics in critically-ill babies [16].

1.2 Problem Statement

The main goal of this PhD thesis is the development of a decision support system for diagnosis of abnormal background EEG patterns in term infants with encephalopathy. The main task is to incorporate the clinical expertise into the algorithms, which can be reliably used by the neonatologist in the NICUs. Along

with the translation of the experts' diagnostics into mathematical algorithms, the focus was put to the objective automated EEG analysis (data-driven), which may lead to the novel insights and clinical biomarkers. The verification of the algorithms was done visually by the EEG expert readers as well as by comparisons with other clinical parameters such as findings on the MRI and/or the assessment of the neurodevelopmental scores. Hence, the goal of the thesis was to address the main challenges in the NICUs via software solutions: 1) manual (subjective) interpretation of the EEG signals, 2) the around the clock availability of the EEG experts and 3) the time-demanding laborious EEG interpretation. With respect to this, the algorithms need to have a high level of robustness and to process long-streams of the EEG data (e.g. hours or days) in real-time. The output of the algorithms needs to visualize in a concise way the insight into the neonatal brain functioning (degree of injury) both for expert and non-expert EEG users.

1.3 Collaboration

My PhD research was conducted within the Biomedical data processing research group, STADIUS, Department on Electrical Engineering (ESAT), KU Leuven, under the supervision of Prof. Sabine Van Huffel. My work has also been closely co-supervised by Prof. Maarten De Vos, while working previously at the University of Oldenburg and now at the University of Oxford. I was a member of EEG subgroup and BioTensor group, mainly collaborating with Ninah Koolen, Amir Hossein Ansari, Yipeng Liu, Devy Widjaja and Borbala Hunyadi.

My PhD thesis has been developed within the *NeoGuard* consortium group (*https://neoguard.net*) (Figure 1.3). In particular, neonatologists and EEG experts were providing support starting with the high quality EEG data registrations, data interpretation as well as the co-development and the verification of the algorithms.

- University Hospital Gasthuisberg, Department of Neonatology, Leuven (Prof. Dr. Gunnar Naulaers MD, Dr. Katrien Jansen MD, Anneleen Dereymaeker MD, Jan Vervisch MD) were responsible for the guidance and co-ordination of the NeoGuard project, EEG algorithm specification and co-development, EEG data interpretations and insightful suggestions how to create a user-friendly visualized output (Chapter 4).
- Erasmus MC, University Medical Center Rotterdam, Department of Neonatology, Rotterdam, the Netherlands (Dr. Paul Govaert MD, Leen



Figure 1.3: The official logo of the NeoGuard consortium, which has been designed by Ivana Despotovic.

De Wispelaere MD, Dr. Jeroen Dudink MD, Dr. Renate Swarte MD) In the Rotterdam NICU, the majority of the EEG data has been recorded, which were subsequently analyzed in this thesis (Chapter 4).

- Erasmus MC, University Medical Center Rotterdam, Department of Clinical Neurophysiology, Rotterdam, the Netherlands (Dr. Joseph P. Cherian MD, Dr. Gerhard Visser MD) This department is responsible for the interpretation and scoring of the recorded neonatal EEG signals. They provided the guidance and ideas what EEG patterns are relevant and how EEG signal should be quantified. During the work of thesis, numerous meetings were held to validate the ideas and discuss the challenging EEG cases (Chapters 4 and 7).

- Department of Children's Clinical Neurophysiology, Helsinki University Central Hospital, Finland (Dr. Sampsa Vanhatalo) This collaboration resulted in the development of the objective method for the assessment of the background EEG abnormality. The work has been initiated in Helsinki, Finland under the guidance and supervision of the Dr. Sampsa Vanhatalo MD (Chapter 6).

- KU Leuven, Department of Electrical Engineering, MICAS (Prof. Dr. ir. Robert Puers; Hans De Clercq Phd). The expertise of the research group are the development of the state of the art solutions in microelectronics and development of sensors. This group has developed the hardware EEG device monitoring platform within the NeoGuard project.

- University of Ghent, The Faculty of Engineering, Department of Telecommunications and Information Processing (TELIN), Image Processing and Interpretation Research Group (IPI) (Prof. Dr. ir., Wilfried Philips; Prof. Dr. Ewout Vansteenkiste; Ivana Despotovic, PhD; Danilo Babin, Phd; Dirk Van Haerenborgh). This group has developed the Graphical User Interface for the NeoGuard monitoring device. During joint meetings we discussed the communication protocol between the GUI and the developed algorithms.

1.4 Contribution of the thesis

The goal of the thesis is to develop robust automated solutions that can be used for the assessment of abnormality in brain functioning in asphyxiated newborns. The contribution includes the development of new bio-marker metrics as well as pragmatic methods for the bedside use in the NICUs.

1. Automated dIBI detector: a novel algorithm for the detection of the dynamic interburst intervals (dIBIs) has been developed. In addition, a refinement step which improves the good detection ratio has been incorporated. The novelty of this approach is that burst-suppression-burst complexes are analyzed in mild-to-moderately asphyxiated neonates and interburst amplitude is introduced as an additional measure for the EEG quantification. Chapter 4.

2. HRV assessment: Heart Rate Variability study explores the use of ECG-derived parameters for the quantification of HIE. A set of HRV parameters has been tested to reveal insights if the HIE is correlated with the decrease in the HRV. Three parameters are identified as potentially useful to complement EEG-derived parameters. Chapter 5.

3. MF-DFA based assessment of the neonatal EEG background: This method has been derived from the analysis of the long-range temporal correlations in a neonatal EEG signal. It merits an objective EEG parameterization, completely unbiased from the human EEG expert exploiting the concepts of the Multifractal Detrended Fluctuation Analysis (MF-DFA). Chapter 6.

4. Holistic tensor-based approach: This method is developed to quantify background EEG abnormality within 1h of duration. It suggests both temporal and spatial EEG quantification and obtains high classification accuracy when compared with the expert EEG reader. The novelty may

be seen in the EEG data structuring and effective data reduction by the use of multi-linear (tensor-based) decomposition methods. Chapter 7.

Additional contributions not included in this thesis are:

1. Compression and sparse approximation of the neonatal EEG studied within the compressive sensing framework.
2. Distinguishing tremor artifacts from the neonatal epileptic seizures.
3. Implementation of the aEEG software together with the Master students.
4. Software development for the neonatal EEG analysis.
5. Effective Data Structures for processed EEG signals, necessary for the communication with the GUI platform
6. Website development and maintenance *https://neoguard.net*

Four major thesis contributions are organized in separate chapters as illustrated in Figure 1.4.

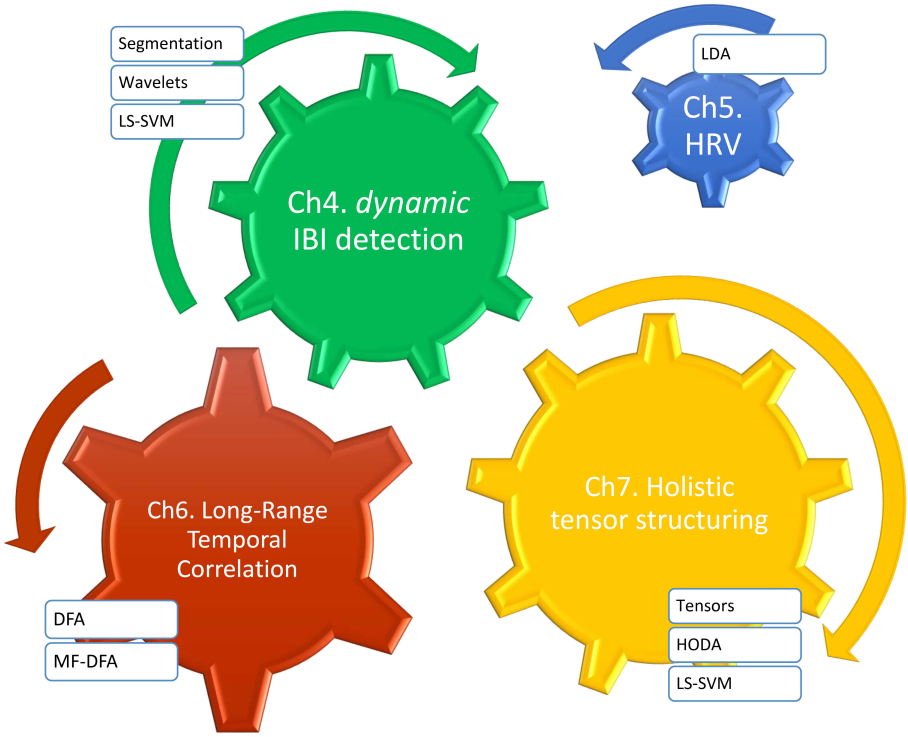

Figure 1.4: Four main thesis's contributions and the mathematical theory being used. The neighboring circles in the scheme were used for the benchmarking purposes.

Chapter 2

Human brain and EEG monitoring

We start with a basic overview of the human brain anatomy and EEG signal acquisition. Next, we focus on the neonatal brain, causes of perinatal asphyxia and EEG monitoring techniques in the NICUs. An essential explanation of the EEG patterns, which are seen both in the healthy and in the neonates affected by perinatal asphyxia are provided. Adverse effects of the most common EEG artifacts are illustrated and explained.

2.1 The human brain

2.1.1 Anatomy of the brain

Brain represents the most complex human organ and it is constituted of more than 100 billion neurons. It may be divided from the anatomical point of view into three parts: the cerebrum, cerebellum and brain stem (Figure 2.1). The cerebrum consists from highly convoluted surface layers called cerebral cortex. This part of the brain distinguishes humans from other mammals. The cortex represents the layer that is folded and in this way the surface area is increased. The cortex is constituted of four lobes, which are called: frontal, parietal, occipital and temporal lobe (Figure 2.1). They include the areas for motor control, conscious awareness, language, emotions, complex analysis and behavior. Although the human brain represents only 2% of the body weight, it

receives 15% of the cardiac output, 20% of total body oxygen consumption and 25% of total body glucose consumption. In Figure 2.2, a horizontal slice of the brain is shown. One can easily distinguish different colors corresponding to the white and to the gray matter areas (cells).

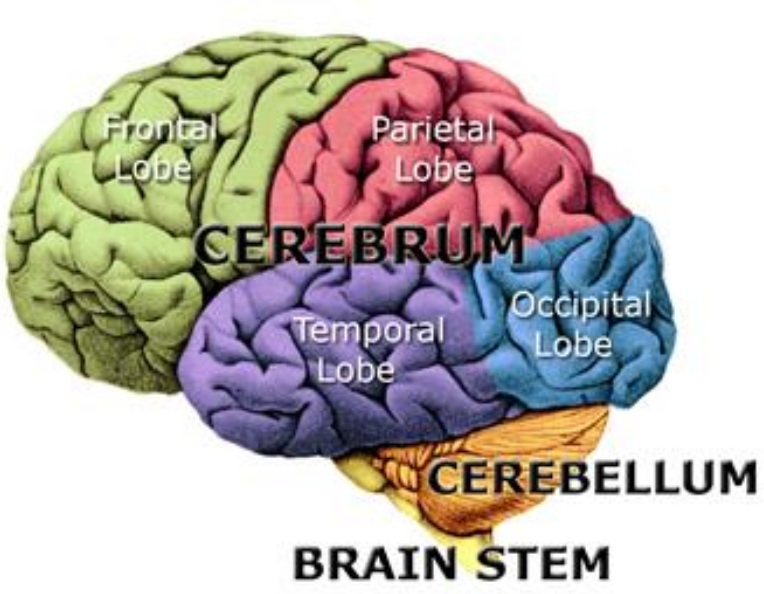

Figure 2.1: A Human brain anatomy consists of three parts: cerebrum, cerebellum and brain stem. In addition, four different lobes are distinguished.

2.1.2 Neural activity

The human central nervous system (CNS) consists of nerve cells (neurons) and glia cells. The former ones are excitable, transmit the information and constitute the functional units of CNS. The latter ones, glia cells (*glia* – Greek for *glue*), provide structural support to the neurons and maintain the surrounding area of the neurons. Further, every neuron consist of axons, dendrites and cell bodies (soma) as illustrated in Figure 2.3. Nerve cells respond to stimuli and transmit information over long distances. An axon is a long cylinder, along which the electrical impulses are transmitted and it is responsible for delivering proteins to the neural cells. Dendrites are connected to either axons or dendrites of other cells. A common neuron in a human brain is connected to approximately 10,000 other neurons, mostly through dendritic connections. The junctions of axons

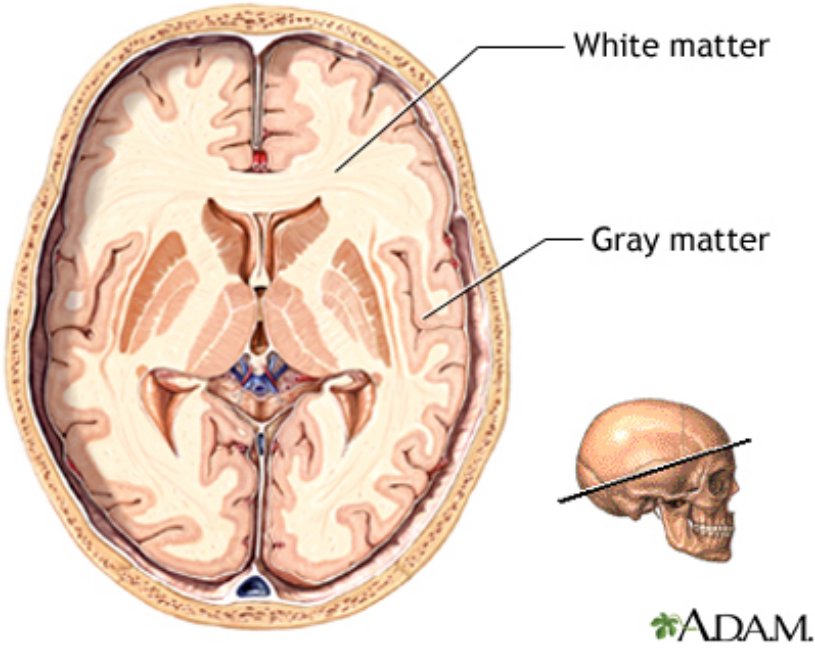

Figure 2.2: The cortical gray matter consists of cell bodies and dendrites and can be found at the outmost surface of the brain (the cortex) and in some deeper structures. On the other hand, the inner part of the brain consists of the axons of the nerve cells and is called white matter.

and dendrites establish pathways for the synaptic currents which represent the electrical activities in the CNS.

A neuron transmits the information, which is called an action potential (AP). It represents a small pulse of electrical activity that enables communication between neurons. APs are generated by an exchange of ions across the neuron membrane. Hence, an AP is a rapid change in the membrane potential that is transmitted along the axon. It is usually initiated in the cell body and normally travels in one direction. Under the membrane of the neuron cell, there is a resting potential of –70 mV. The membrane potential depolarizes (becomes more positive), thereby producing a spike in the function of membrane's potential over time. Following the maximum of the spike, the membrane repolarizes (becomes more negative). Next, the potential becomes more negative than the resting potential and then returns to normal. The action potentials of most neurons last between 5 and 10 milliseconds. They are generated by gradients of positive ions of sodium, Na^+, potassium, K^+, calcium, Ca^{++}, and the negative

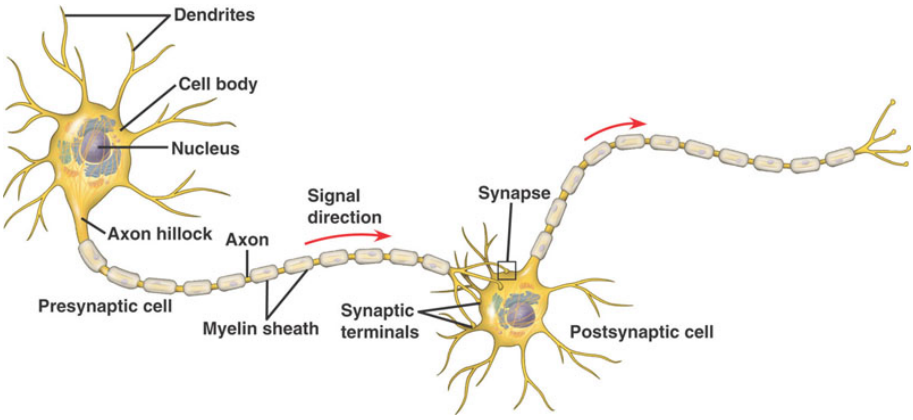

Figure 2.3: A scheme of the basic parts of the neuron's structure. From [131]

ion of chlorine, Cl^-, through the neuron membranes. The direction of their flow is governed by the membrane potential.

Therefore, an EEG signal is a consequence of the currents that flow during synaptic excitations of the dendrites of many pyramidal neurons in the cerebral cortex. When brain cells (neurons) are activated, the synaptic currents are produced within the dendrites. This current generates a primary magnetic field and a secondary electrical field over the scalp. The secondary electrical field is measurable by EEG devices. Differences of electrical potentials on the scalp can be detected due to the synchronous activity of numerous pyramidal cells that create sufficiently large potentials (Figure 2.4).

2.2 The Electroencephalography

2.2.1 Scalp EEG

Neurons in the brain generate currents that are measurable on the human scalp. Despite the large attenuation of the signal by spinal fluid, skull and scalp, the potential can still be recorded. These potentials range from 2-150 μV. Hence, EEG represents a difference of potentials measured between electrodes as a function of time. This is illustrated in Figure 2.5.

The first EEG measurement has been obtained by the German scientist Hans Berger in 1924 [11]. (Figures 2.6 and 2.7). Next, for several decades analog EEG devices have been used. Today digital EEG devices are used in everyday

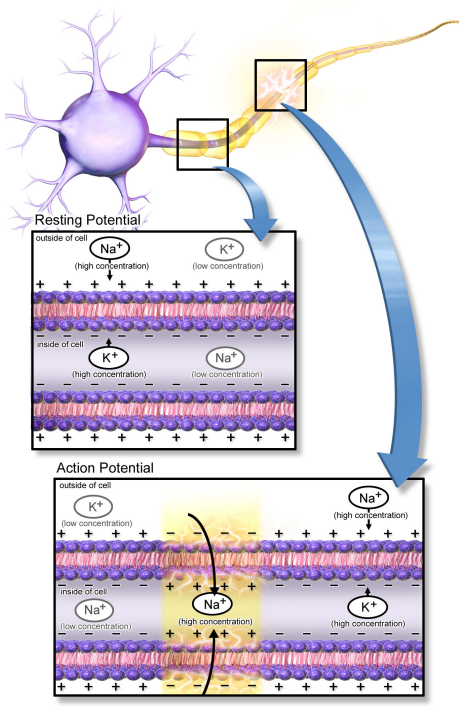

Figure 2.4: Propagation of the action potential along an axon is illustrated. From [131].

clinical and research practice. This enables the application of digital signal processing concepts for an improved EEG study and analysis.

EEG recordings are performed in a standardized way. Specifically, the electrode positioning commonly follows, the so-called, 10-20 international system. The name is derived from the approach in which the head marking is split into slices of 10% and 20% (as illustrated in the Figure 2.8). Landmark points represent the nasion and inion. The distance between these points over the scalp are divided into 10% and 20% segments. Thus, positions for 21 electrodes are defined. The nomenclature of the electrodes is derived from the underlying brain lobes: F-Frontal, C-central, P-parietal, O-Occipital and Fp – Frontal polar). Odd numbers are assigned to the electrodes positioned on the left hemisphere, whereas the even numbers are assigned to the electrodes positioned on the right hemisphere.

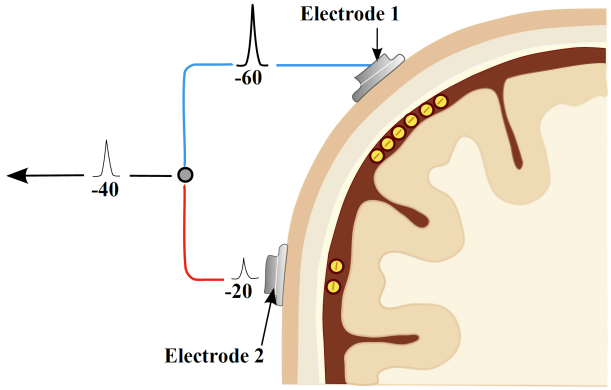

Figure 2.5: Illustration of two electrodes placed on the human scalp in order to measure brain electrical activity.



Figure 2.6: Hans Berger, German scientist who was the first to record human EEG activity in 1924.



Figure 2.7: The first EEG signal recorded in humans. 10Hz signal was used as a reference to observe the morphology of the EEG signal.

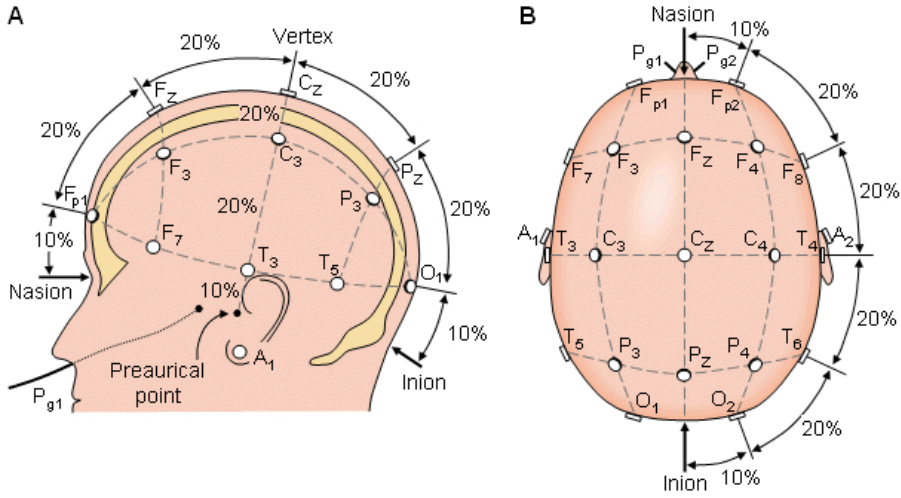

Figure 2.8: International 10-20 system for the standardized electrode placement. From [131].

2.2.2 EEG characteristics

In clinical practice, the EEG signal is still routinely inspected visually. This is done by an inspection of EEG waveforms, called graphoelements. The time resolution of the EEG is very high and patterns lasting at the order of hundreds of milliseconds can be identified. In general, visual scale is set to 10s and all channels are inspected simultaneously together with the recorded polygraphy signals. The amplitude of the signals is in the range from 2µV till several hundreds of microvolts, whereas the frequency range is from 0.1Hz up to 100Hz. Most commercial EEG machines use the sampling frequency of 256 Hz for the standard clinical practice. The high-pass filter is commonly set to 0.3-1Hz, whereas the low pass filter is set to 30-70Hz depending on the application of interest. In the area of neonatal EEG research, it has been shown that very slow oscillations carry significant information as well. In particular, the infraslow oscillations (0.01Hz – 0.5Hz) represent important hallmarks of the neonatal EEG activities ([126], [125]).

Furthermore, while inspecting the grapholelments, EEG readers commonly assess the following time-domain properties: duration, voltage, waveform (morphology), repetition and interhemispheric coherence (symmetry/synchrony). Moreover, to accurately interpret EEG patterns and report the findings, EEG activity is characterized within different frequency bands. The following frequency bands

are defined for EEG analysis (Figure 2.9):

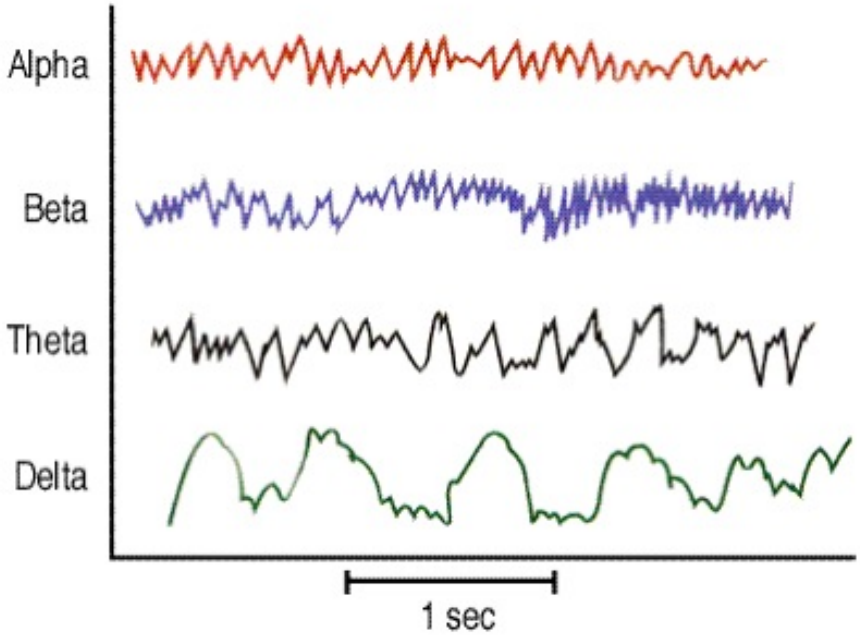

Figure 2.9: Examples of different rhythms of brain activity.

$$\text{Delta: } 0.5 \leq f < 4Hz;$$

$$\text{Theta: } 4 \leq f < 8Hz;$$

$$\text{Alpha: } 8 \leq f < 13Hz;$$

$$\text{Beta: } 13 \leq f < 30Hz;$$

The proportion (or absence) of certain frequency content is correlated with the behavioral states of the patients (or experimental subjects) and it is used for diagnostic purposes. For instance, the presence of alpha EEG patterns can be observed during sleep stages in adults.

To bring diagnostic decisions, clinicians and researchers concise their EEG expertise into descriptive guiding rules and tables for scoring. Hence, the visual EEG analysis may be regarded as subjective and in many cases the inter-rater disagreement may be substantial. For instance, for the assessment of

the background EEG abnormalities in neonates with asphyxia over 17 different visual scoring systems have been proposed [129]. All this leads to a great confusion among medical practitioners. The algorithmic approaches, such as the one developed in this thesis, may assist and improve the standardization, since they exploit data-driven findings. Hence, they may be considered as more objective.

2.2.3 Practical applications of EEG

EEG is widely used both in clinical practice and within research context. EEG offers high temporal resolutions and hardware devices are relatively low priced. The main research and clinical EEG application areas include: epilepsy, coma, brain death, encephalitis, attention deficit hyperactivity disorder (ADHD), trauma, depth of anesthesia, brain computer interface (BCI), cognitive science and other neuroscience research areas.

EEG is recognized to have a poor spatial resolution, as the scalp electrode positioning is rather sparse. Nevertheless, due to high temporal resolution EEG remains an important modality in brain research. It is usually combined with other brain monitoring modalities, such as, functional magnetic resonance imaging (fMRI), magentoencepalography (MEG) and near-infrared spectroscopy (NIRS).

2.3 The neonatal brain

2.3.1 Perinatal brain injury due to hypoxia-ischemia

A major cause of neonatal brain damage is asphyxia or hypoxic-ischemic encephalopathy (HIE). Hypoxia refers to an insufficient oxygen supply to the brain cells, whereas ischemia represents a lack of blood supply to the brain cells. Therefore, the underlying cause of HIE in infants is a combination of insufficient delivery of both blood and oxygen to the neonatal brain. Numerous problems during pregnancy, labor, delivery, and post-delivery can cause HIE.

Without the oxygen and energy, the brain cells are unable to maintain their equilibrium. Subsequently, the events like seizures, intracellular calcium ($Ca2^{+}$) accumulation, free radicals formation disrupt cell structure yielding permanent cell damage [25]. This is called apoptosis (programmed cell death), which is a protective strategy of the human body in which damaged cells are destroyed in a controlled regulated way. Apoptosis lasts for several hours and the damage to

the brain is permanent. The window time between the initial lack of oxygen supply and the cell death represents the window of intervention where the neuroprotective strategies may be effective.

Asphyxia - adapted from [103]

Perinatal hypoxic ischemic encephalopathy (HIE) is a major cause of morbidity and mortality world-wide ([51], [64] and [106]). Common sequelae in survivors include cerebral palsy, epilepsy, sensory and cognitive problems. Even in the developed countries, the exact factors triggering perinatal asphyxia as well as the time of onset of brain injury are often difficult to determine, and it remains a major clinical problem ([51], [26] and [103]). Monitoring of brain function using the electroencephalogram (EEG), is well-suited to give insight into brain function and its dynamic changes in neonatal HIE and helps to guide treatment as well as prognostication ([83]). The degree of hypoxic brain injury is mainly determined by the severity and duration of the insult [50] as well as the gestational age (GA) of the infant. As such, the goal of the EEG monitoring is to try to determine this initial impact in order to guide treatment and establish future neurodevelopmental prognosis.

Neuroprotection. In cerebral tissue that is capable of recovery after a hypoxic insult, the secondary injury develops over a time period of a few hours [103]. This provides a potential 'therapeutic time window' during which neuroprotective strategies are expected to work. The best studied and most promising neuroprotective strategy is therapeutic hypothermia. Decreasing the temperature by 2 to 3 degrees Celsius markedly affects (protects against) hypoxic brain injury [85]. In experiments done on animals, hypothermia is consistently associated with dose-related, long-lasting neuroprotection [49]. Both selective head cooling [46] as well as whole body hypothermia ([110], [4]) safely decreased the combined outcome of death or disability at 12-24 months in infants with HIE. The combination of pharmacological agents with hypothermia may show a synergistic effect in neuroprotection [24]. Therefore, it is beneficial to use EEG to detect harmful changes in brain function at an early stage (e.g. 6 hours after the initial insult), when the process is still potentially reversible.

2.3.2 EEG monitoring of the neonates

The illustration of how the brain of the fetus develops during pregnancy is shown in the Figure 2.10. Hence, the newborn has developed brain whose activity can be studied. It is surprising that the initial exploration of a neonatal EEG in 1933 claimed that EEG activity cannot be identified within the first 35 days of life [10]. Five years later, however, Smith showed that EEG in a full-term neonate consists of mixed activities from 4-7Hz and 12-14Hz as well as slow

waves (2-3 Hz) [112]. First prospective studies of neonatal EEG were done by French scientists during 1953-1955, where the neonatal EEG nomenclature has been established (e.g. tracé alternant, activité moyenne) and first publications on the prognostic value of the neonatal EEG and sleep studies were published ([37]; see also overview in [3]).

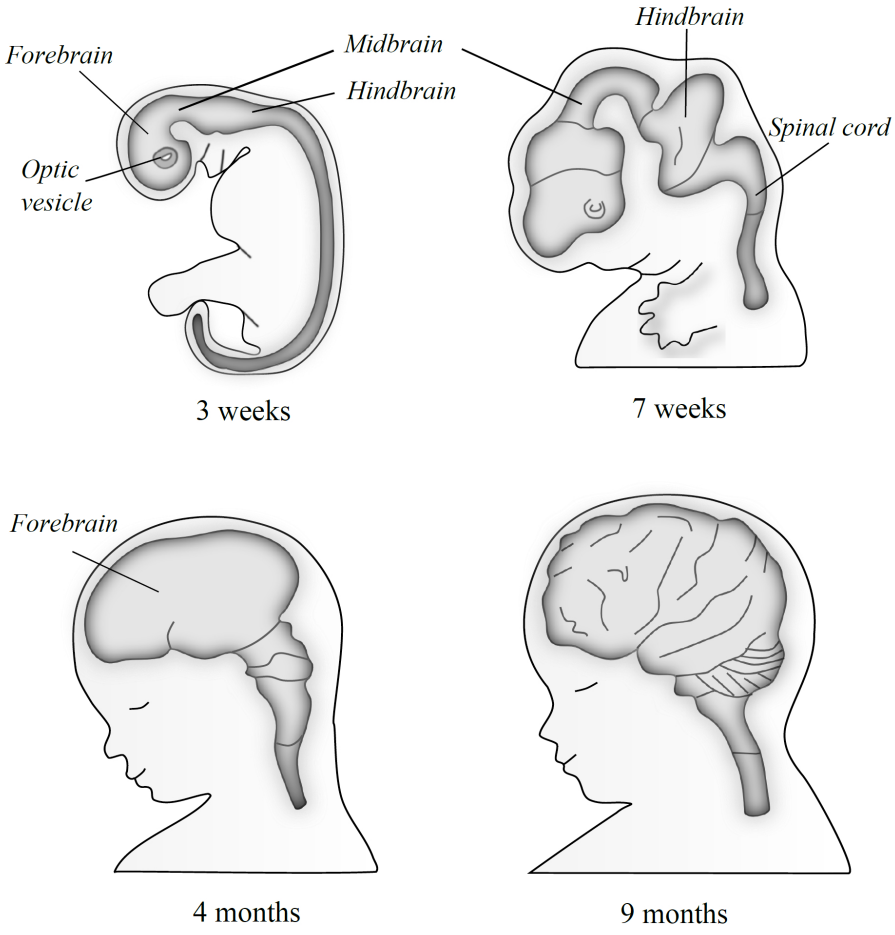

Figure 2.10: Phases of the brain development. From [34]

Neonatal EEG recording is widely recognized to be of great importance for the neurological evaluation of the newborn [3]. To perform the neonatal EEG recording, the procedures should not hinder the infant's behavior and standard care in the incubators. For full-EEG recordings, the requirement is to include

at least eight EEG electrodes (Fp2, C4, T4, O2, Fp1, C3, T3, O1), whose positions are equidistant on the scalp according to the 10-20 system adapted for neonates (Figure 2.11). In the EEG analysis, both visual and automated, bipolar montage derivation are used as illustrated in Figure 2.16. In recent years, neonatal EEG caps have been developed and their use is adopted in some NICUs in order to enable faster set-up and easier EEG monitoring [117]. Commonly, during EEG monitoring, other vital signals are measured as well (polygraphy), that include eye movements, electrocardiogram (ECG), respiration and muscle activity. As a standard practice in the NICUs, the video recording is also included. All these signals are assistive in the neonatal EEG interpretation for the truthful identification of EEG artifacts, paroxysmal phenomena like seizures and differentiation of sleep stages.

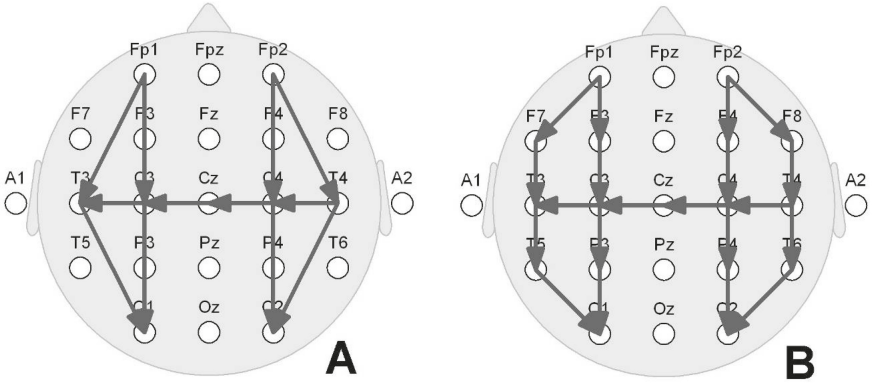

Figure 2.11: Neonatal EEG montages. A: Restricted 10–20 system using nine electrodes; B: Full 10–20 system of electrode placement using 17 electrodes. From [103].

While interpreting neonatal EEG, several aspects need to be accounted for: age of neonate, clinical information (e.g. Apgar score, occurrences of seizures), use of medications and state of the patient (e.g. sleep, awake).

2.3.3 Amplitude integrated EEG - aEEG

Everyday clinical practice in the busy NICU environment depends on several logistic factors. Presence of the required expertise to interpret EEG is commonly scarce as well as the expertise to record the high quality EEG signals. Usually, this is present only in large regional NICUs. Therefore, many neonatologists

opt to use aEEG signal. An attractive feature of aEEG is that it readily enables insight into the EEG trend over several hours (or days), which is important for the study of prognostic parameters such as an evolution (improvement/deterioration) of EEG background as well as presence of sleep-wake cycles. Nevertheless, the limitation of aEEG are seen in the poor spatial coverage (only 2 central channels; or central and parietal areas (4-channels)). In this way, milder brain asymmetry and asynchrony (as seen in the EEG) will be missed, although they are important diagnostic factors. In addition, many patterns, shorter in duration (e.g. <60s) will be seen in aEEG as less than 4 data points (see Figure 2.14). Hence, it is obvious that short duration epileptic seizures, rolandic sharp waves and other paroxysmal activities may be easily missed if only aEEG is used. Moreover, aEEG is highly susceptible to numerous artifacts. In particular, persistent continuous artifacts such as, ECG, muscle or respiratory will obscure the findings and may lead to misinterpretation of the EEG patterns. On the other hand, full-EEG recordings allow identification of majority of relevant patterns as well as artifacts due to high temporal resolution.

aEEG implementation. In the NICUs, aEEG signal has been popularized in the 1990s. Initially, the implementation of aEEG was analog, and then, the signal, drawn on the paper, was covering 6cm per 1h of the EEG recording. Today, the digital counterpart is used, following the same principle. It provides digital output at one sample per 15s. aEEG implementation consists of the following EEG processing steps:

- Asymmetric filtering
- Rectifying (absolute value calculation)
- Envelope detection
- Segmentation
- Creation of aEEG data point (minimum and maximum points within the segment)
- Time compression
- Amplitude compression into linear-logarithmic scale (linear for $<10\ \mu$ V and logarithmic for $>10\ \mu$ V)

Illustration of these steps, where raw EEG is transformed into aEEG is shown in Figures 2.12 2.13 and 2.14. This algorithm implementation has been developed during a students' project as part of the course H03I7A "Design in Medical Technology" with the support of Jan Vervisch (UZ Leuven, Gasthuisberg) and personnel from OSG company (Belgium).

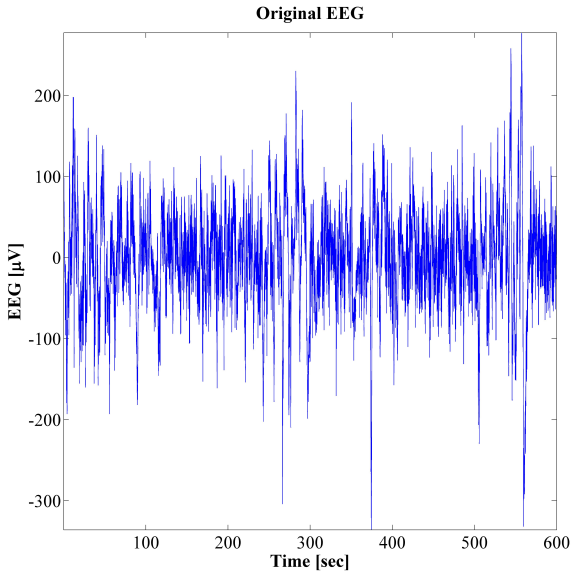

Figure 2.12: Original neonatal EEG signal recorded for a duration of 600s (10 min).

2.4 Artifacts in the neonatal EEG

Main work in this thesis is automated detection of EEG discontinuity and low voltage intervals (hallmarks of the background EEG abnormality). Hence, the presence of artifacts, which are superimposed on the EEG patterns, significantly affects the automated algorithms' performance and represents the major challenge and an open problem. Depending on the duration, we classify EEG artifacts into:

1) transient

- movement artifacts
- electrode/wire artifacts
- eye blink aritfacts
- nystagmus

2) continuously persistent

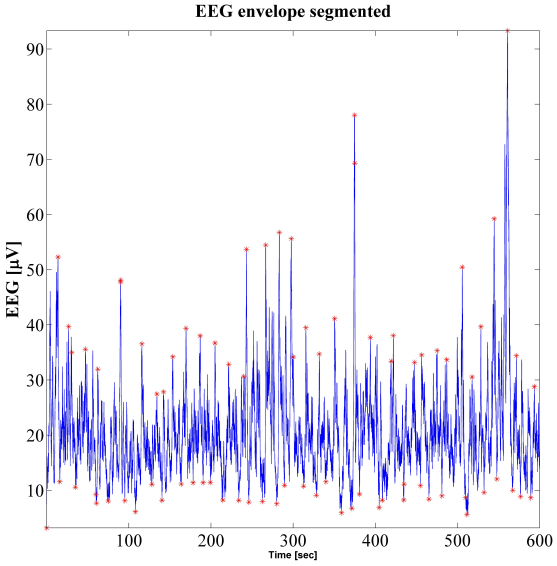

Figure 2.13: Transformed EEG signal, after filtering and rectifying. Next, the minimum and maximum segments' points are marked by asterisks.

- ECG
- respiratory
- muscle
- heating pump artifact
- mechanical ventilation
- power line artifacts at 50Hz and 100 Hz

Transient artifacts mainly hinder the detection of interburst intervals as they are difficult to be distinguished from bursts. Even for an expert human EEG rater, it is sometimes challenging to distinguish burst activity (that can be also seen in polygraphy channels) from artifact , even with the use of polygraphy signals. On the other hand, the continuously persistent artifacts bias the estimate of the amplitude values within the interburst interval (e.g. ECG, muscle artifacts) that we proposed in this thesis (see further Chapter 4; dynamic IBI). In addition, the persistent artifacts markedly influence the estimate of background EEG scores using the methods proposed in Chapters 6 and 7). In addition, the presence of

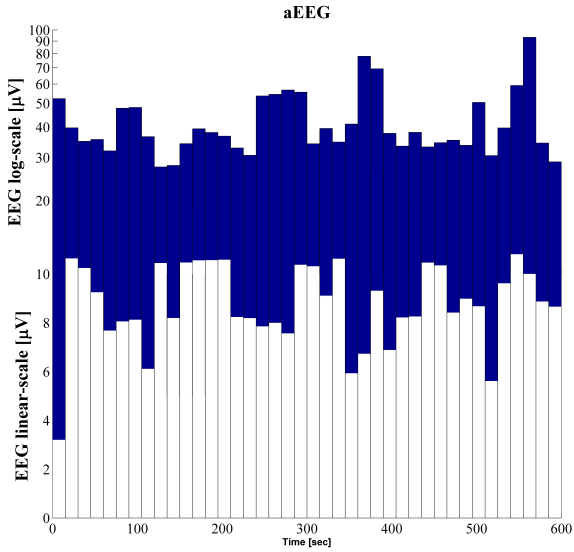

Figure 2.14: Final aEEG data points show in a compressed way 10 min of EEG with only 40 data points.

epileptic seizures, which are common among asphyxiated neonates, can also be regarded as hindering confounder and treated as the artifact-like EEG activity. An example of the ECG artifact is presented in figure 2.15.

2.4.1 EEG in the healthy term neonate

The EEG in the healthy term neonate is differentiated according to the sleep stages. In contrast to adult humans, one sleep cycle in neonates lasts approximately 1h. Major classification of background EEG activity is differentiation of continuous and discontinuous EEG periods [123].

Awake EEG. It consists of continuous frequency activity (activité moyenne) encompassing theta and delta activity of 70–100 μ V (Figure 2.16). Theta activity in short durations of 1–3 seconds and 50 μ V amplitude may be seen over the central region. From [103].

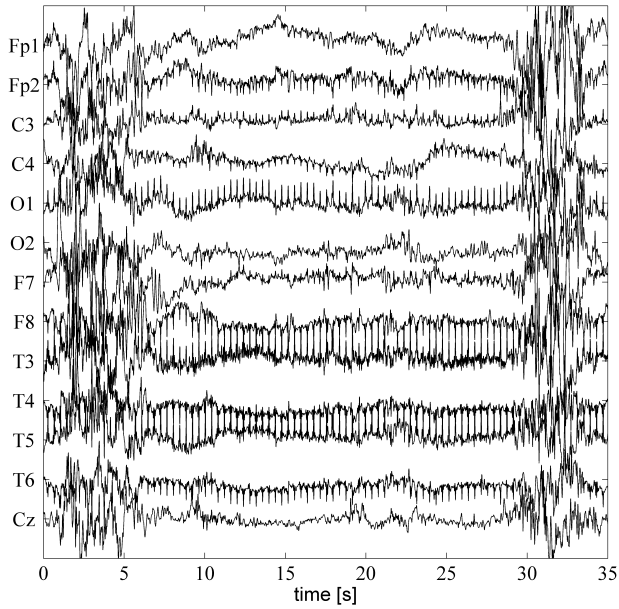

Figure 2.15: An example of the neonatal EEG signal that is corrupted with the ECG artifact.

Sleep periods often start with active sleep (AS) and it constitutes about 50% of the overall sleep time. The EEG in AS shows continuous activity in all frequency bands with an amplitude of 50–70 μ V. It is similar in morphology to the awake EEG. Next, two types of quiet sleep (QS) are identified: tracé alternant (TA), an alternating pattern of 'bursts' and relatively quiet periods (Figure 2.17) and slow QS. TA shows activity higher than 25 μ V (usually 40–50 μ V) during the quiet periods. The 'burst' periods show theta and delta activity of up to 200 μ V. From [103].

2.4.2 EEG patterns associated with neonatal brain damage

Major characteristic of abnormal EEG patterns is reflected in low EEG voltage levels. The first sign of disrupted normal EEG activity is the loss of sleep-wake cycle. The easiest way for its recognition is by the use of aEEG signal (Figure 2.16 upper trace). With respect to the degree of acute EEG background abnormality we differentiate the appearance of discontinuous and continuous

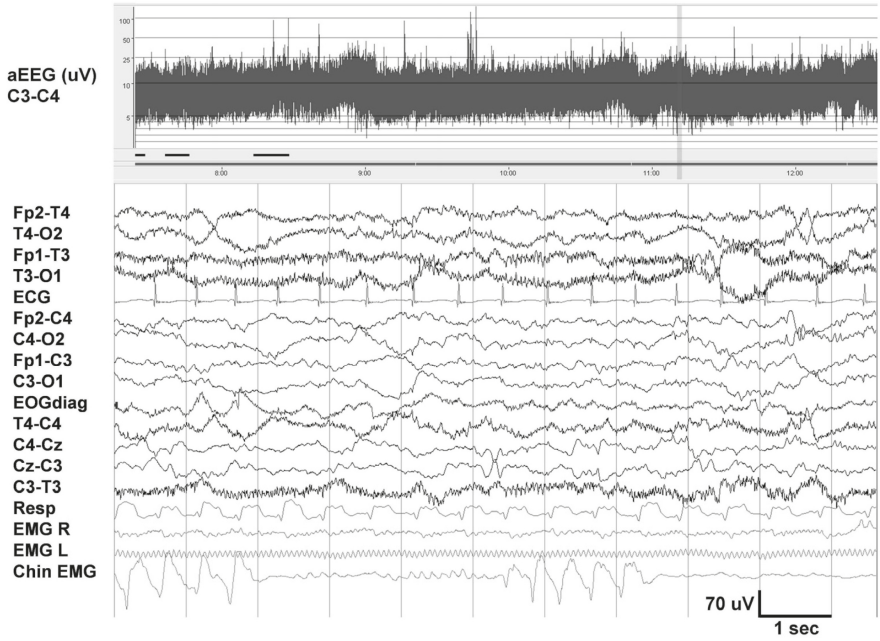

Figure 2.16: Awake EEG at term age. Theta and delta activity is shown with normal voltage (20–70 μ V). The band width between 5 and 20 μ V is normal, and the fluctuations suggest sleep–wake cycling. From [103].

low amplitude EEG periods (Figure 2.18). Discontinuous EEG periods are recognized as higher voltage 'bursts' of electrical activity interrupted by lower voltage 'interbursts' [123]. The interburst interval (IBI) in neonates is defined very broadly as a pattern with peak-to-peak amplitude <25-50 μ V. Within this definition, three IBI patterns are identified in term neonates: (1) tracé alternant (TA-IBI>25 μ V) – an EEG pattern present within the quiet sleep stage in healthy newborns (2) tracé discontinue (TD-IBI<25 μ V) – a pattern in neonates with mild and moderate HIE and (3) burst-suppression (BS-IBI<5-10 μ V) – a pattern in neonates with severe HIE (see [123] and Figures 2.18 and 2.20).

In addition, continuous EEG periods with persistently low voltage represent unfavorable prognostic factors as well.

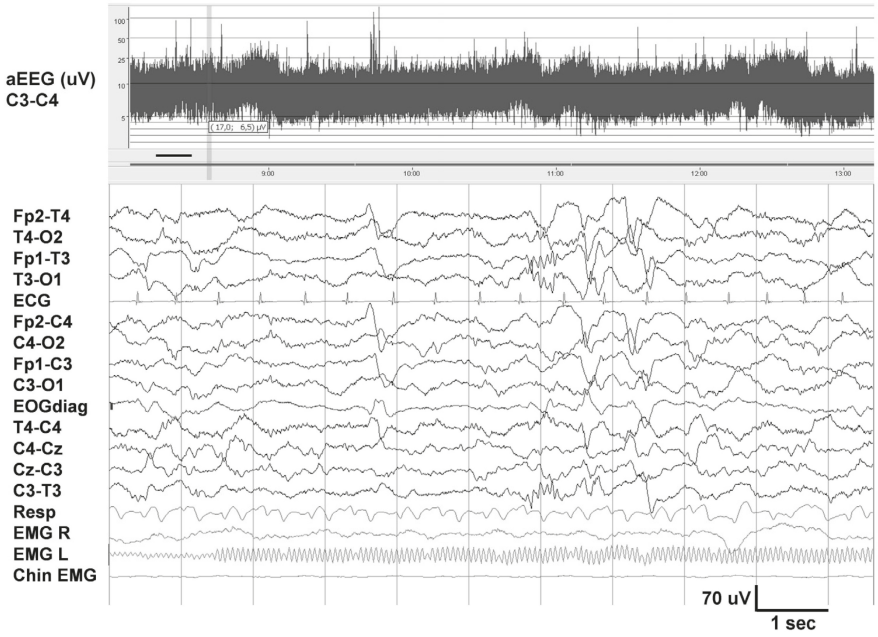

Figure 2.17: Normal quiet sleep of the term infant. Tracé alternant with lower voltage during 2–5 seconds, and higher voltage in the next 3 seconds.

2.4.3 Visual scoring of the EEG background

In clinical practice it is important to have easy to use, descriptive system for a visual EEG interpretation. During the last few decades, numerous visual scoring systems have been developed following the similar concepts. Researchers would prospectively study the large cohort of neonates and they would determine which EEG patterns are associated with good and which with poor neurodevelopmental outcome. One of the most distinctive hallmark that many researchers adopted within their scoring systems are duration of interburstintervals. One of the mostly used scoring system was suggested by Murray et al. [90], which is summarized in the Table 2.1 and Figure 2.21.

It is important to note that the EEG grades need to be carefully interpreted at distinctive time points after the initial brain injury. Namely, it is known that HIE injury evolves over time (improvement/deterioration occurs) and commonly the EEG background pattern is scored over distinctive time points to quantify the speed of the recovery. For instance, the EEG may be scored at 6h, 12h, 24h, 36h, 48h, 72h and 96h after birth. Classification algorithms developed in this

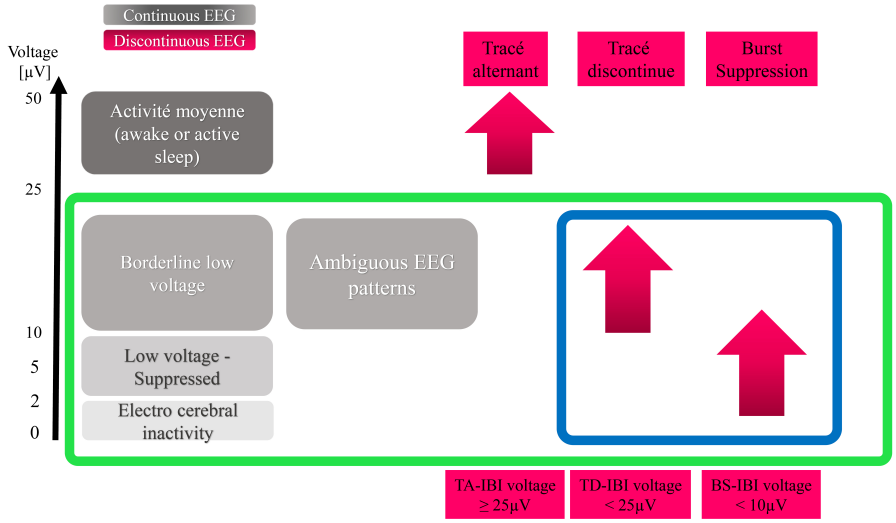

Figure 2.18: Different neonatal EEG patterns are illustrated. Green rectangle implies the lower voltage states, which are associated with the brain injuries in term neonates. However, in preterm neonates, some patterns represent normal phases of EEG maturation (e.g. burst-suppression and tracé discontinue). Blue rectangle illustrates low amplitude in discontinuous (interburst) periods. Adapted from [123].

Grade	**Descriptive rule**
0	Normal EEG findings: continuous backgrounds pattern with normal physiologic features such as anterior slow waves
1	Normal/mild abnormalities: continuous background pattern with slightly abnormal activity (mild voltage depression, poorly SWC, mild asymmetry)
2	Discontinuous activity with IBI <10s, no clear SWC or clear asymmetry/asynchrony
3	Major abnormalities: discontinuous activity with IBI of 10-60 s, severe attenuation of background patterns, no SWC
4	Inactive EEG findings: background activity of < 10μV or severe discontinuity with IBI of > 60s

Table 2.1: Table that summarizes scoring grades for the visual background EEG classification as proposed in [90].

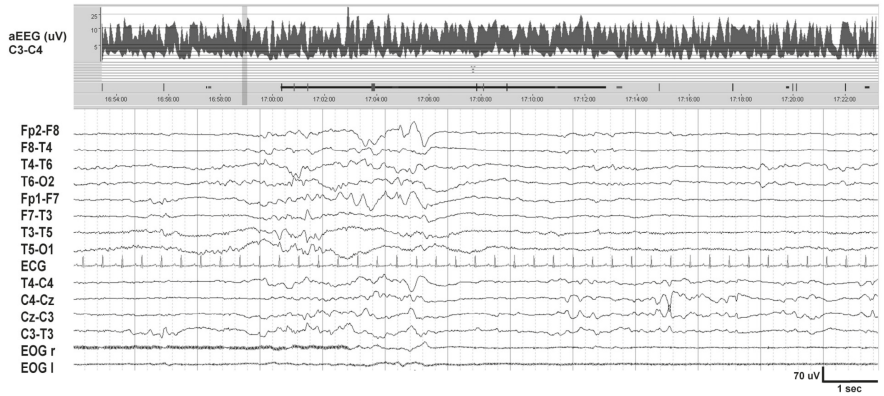

Figure 2.19: Trace discontinu in a neonate with moderately severe HIE. Background activity is of low voltage (<20 μ V). The discontinuous periods, with a mean voltage of 10 μ V, are interrupted by bursts of EEG activity of 2–3 seconds duration. aEEG trend covering 30 minutes shows a band width of 2–7 μ V. Sleep–wake cycling is absent.

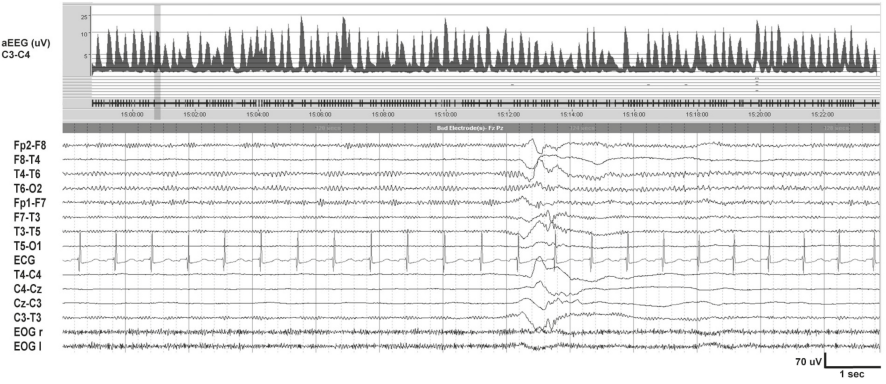

Figure 2.20: Burst suppression (BS) pattern in severe birth asphyxia. Severely suppressed background activity (<5 μ V) with intermittent bursts of 10–20 μ V. As opposed to tracé discontinu [2.19], no EEG activity is discernible during the discontinuous periods. aEEG trend of 30 minutes shows BS and absent variability. Mean band width of the suppressed periods is <2 μ V

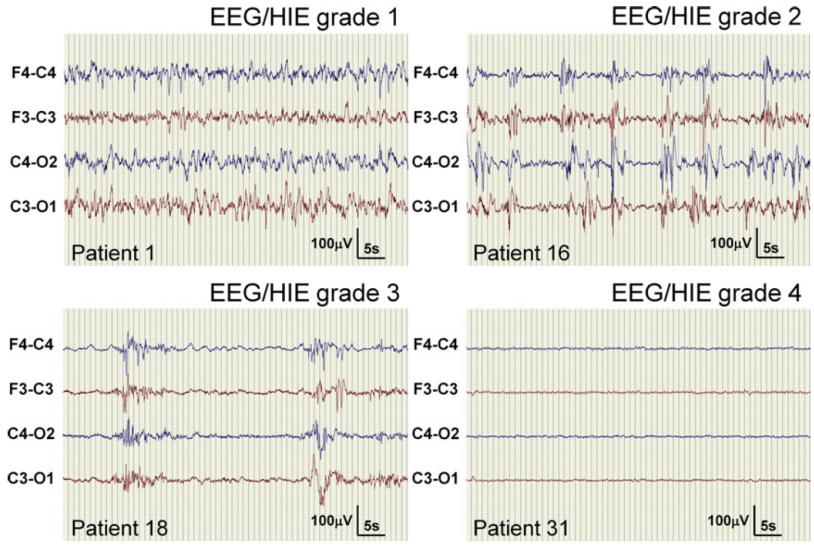

Figure 2.21: Ideal examples of neonatal background EEG patterns From [68]

thesis are designed to partly automatically replicate this grading system or to use the scored grades as a benchmarking metric. For instance, automatically detected duration and amplitude of dynamic IBIs show high correlation with the scored background EEG grades. In addition, other scoring systems take into account the evolution of the background EEG activity over 24h. Hence, a refined grading system assigns only one out of eight background EEG grades for the whole EEG recording (neonate). In this way, the neonates with various degree of HIE may be grouped and separately analyzed according to their unique EEG grade. This method is summarized in Figure 2.22. In Chapter 4, the emphasis was placed on the correct differentiation of neonates between grades 1, 2 and 3 (scored according to 8-grade system in Figure 2.22), as they represent the most challenging cases.

Consideration in interpretation. It is important to note that visual and automated background EEG abnormalities should be reported with caution. Many extracerebral conditions, such as poor electrode impedance, inaccurate placement or scalp edema may result in lower voltage activity or interhemisperic voltage asymmetry [123]. In addition, it is also known that medication affects the background EEG, which may lead to low voltage EEG and increase in discontinuity. Duration of the medication effects depends on the dose and administrated medication. For instance, phenobarbital will produce

1. EEG background scoring based on evolution of discontinuity & SWC over 24 h

Grade	*DurIBI*	*AmpIBI*	*SWC*	*Improve*	*Reac*	*Variab*	*Other findings*
0	NA	≥25-50	++	NA	+	+	Normal for CA
1	≤5	10-25	+/-	↑SWC	+	+	↑ ShW, <6 sec runs of theta/delta
2	<10	<10	-	↓IBI	+	+	*
3	10-20	<10	-	to grade 2	+	+	-
4	>20	<10	-	to grade 2	+/-	+/-	-
5	10-20	<10	-	No	+/-	+/-	-
6	>20	<10	-	to grade 5	-	-	-
7	10-20	<10	-	Worsen	-	-	↑ IBI >20 sec
8[†]	>20	<10	-	No/worsen	-	-	

SWC: sleep-wake cycles. ***h***: hours, ***CA***: conceptional age. ***NA***: not applicable. ***IBI***: inter-burst interval. ***DurIBI***: length of IBI in seconds. ***AmpIBI***: mean amplitude of IBI in μV. ***Improve***: improvement in 24 h. ***React***: reactivity. ***Variab***: variability. ***ShW***: sharp waves. * Excessive inter-hemispheric asynchrony and amplitude asymmetry were also classified as at least grade **2**. [†] includes also persistent low voltage (<10 μV) and isoelectric EEG background.
↑ increased. ↓ decreased.

Figure 2.22: An 8-grade scoring system for the background EEG abnormalities. One grade is assigned to neonates, thus allowing easy categorization of neonates according to the EEG grades. From [103].

discontinuous EEG periods which may recover after 2 hours, whereas lidocaine effect will recover only after 24h. In the recent years, the hypothermia treatment (cooling of the neonates) affects the EEG background as well. During the hypothermia, standard parameters such as, time of return of the sleep-wake cycles (normalization as seen in the EEG; good prognostic factor), need to be redefined. Therefore, before making final EEG diagnosis, factors that need to be considered are EEG signal quality, medication administration and hypothermia treatment. Hence, developed automated methods are *insensitive* to those factors.

2.5 Conclusion

In the NICUs, there is a high necessity for an accurate and prompt diagnosis of newborns' brain functioning. As the first step, obtaining a high quality EEG registration is challenging, though very important as aEEG monitoring alone may be seen as a sub-optimal modality. To effectively treat asphyxiated infants, an expert EEG diagnostic is continuously needed for several days. In most NICUs, this support is commonly scarce or not available. Therefore, the development of automated decision-support systems is highly needed to assist medical doctors to treat newborns. On the other hand, the EEG signal will always be degraded by artifacts and this represents a challenge for the development of automated algorithms for EEG processing. Last but not least, the accuracy and reliability of the developed automated solutions need to be extremely high, which is a challenge that has been solving in this thesis.

Chapter 3

Essential mathematical techniques

In general, mining of the EEG data is done in two steps: (1) extraction of relevant features and (2) classification and development of the algorithms for supportive automated diagnostics. Hence, this chapter covers basic linear and multi-linear algebra methods for the data decomposition as well as techniques for the efficient data representation and feature extraction. Next, we explain the essentials for the quantification of long-range temporal correlations within time series. Finally, we provide a brief overview of the basic machine learning methods used for pattern classification.

3.1 Data Representation

As the first prerequisite step, an efficient data processing requires well-organized and structured data. The way in which signals are structured allows different processing techniques to be applied. In particular, this is important for input data with large dimensions, especially for brain recordings performed over several days. For instance, 50-100 hours of EEG recordings per neonate are analyzed in the thesis. Even 1h of the EEG, recorded with 12 bipolar montage channels, accumulates a lot of data. This results into 11, 059, 200 data samples (12 (channels) x 3600 (s) x 256 (Hz - sampling rate)). Hence, an efficient (if possible sparse) representation of the EEG data will assist in better processing and quantification of the EEG patterns. This will enhance capturing of the

essential and hidden structures within the large-scale high-dimensional datasets.

Single channel EEG data is analyzed as a signal consisting of discrete-time data points. Hence, each EEG signal channel is represented as a vector. Moreover, as EEG is inherently a multi-channel signal, matrix representation, which is a 2D data structure will be used as well. For instance, the most famous example of 2D data structures are images. Furthermore, we can also map (transform) the EEG signal in diverse ways and then it can be represented as a 3D (3-way) or higher order tensor (data structure). Other examples of 3D data are videos, where a set of images (frames) are aligned along the time axis (e.g. determined by the frame sampling rate). In contrast to grey images, colored images are also tensors as commonly 3 colors are used to represent image pixel values (so called RGB (red, green and blue) images).

3.2 Neonatal EEG data representation - 1D Signal decomposition

3.2.1 Time-frequency signal decompositions

Natural representation of the signals is in the time domain. All signals carry relevant information and quite often this information is, however, not obvious when the signal is analyzed in time domain. For the purposes of signal analysis, compression and pattern recognition, signals (or images) are often transformed into another domain where their processing is more suitable. Sometimes, it is not easy to determine which domain would offer maximal benefits for processing and certain trade-offs are necessary when choosing the optimal domain for the processing.

Let us consider an example from Figure 2.7. We see that in the first experiments with EEG, the scientist used a 10Hz sine signal as the reference. They were able to visually determine whether the EEG activity is faster or slower than the reference one. This can be seen as the prior attempt to measure the frequency content of the EEG signal. With the advent of digital revolution, EEG signals are digitized and today for their analysis frequency spectra are commonly calculated. Although continuous time signal transformations merit a lot of attention, in this prompt overview we will describe transformations of discrete time signals. We will start with the mathematical formulation of the Discrete Time Fourier Transform:

$$\mathbf{X}(k) = \sum_{n=0}^{N-1} x(n) e^{-i2\pi kn/N}, k = 0, 1, ..., N$$

In simple words, a Discrete Time Fourier transform explains the frequency content of the signal that we are analyzing. In case that the signal sampling frequency is 256 Hz (Fs), we will be able to study the frequency content up to the 128 Hz (sampling frequency divided by 2). The discrete signal of length N, can be then decomposed into N/2 frequency components with the resolution of N/256. Hence, the lowest frequency component from [0-N/Fs] will tell us to what extent this frequency component is present in the signal. Next, we may imagine that for the signal with duration of N=512, the lowest frequency resolution would be from [0-512/256] or from [0-2] Hz. In case that the brain shows two activities at 0.5Hz and 1.5 Hz, we will not be able to separate them with the use of such a short time windows (N=512s or 2s). Then, an intuitive solution is to analyze EEG signal within longer time periods (e.g 30s), where better frequency resolution would be obtained. However, if we continue increasing the time window, we will not be able to analyze transient EEG activity of higher frequency. For instance, beta activities of approximately 10Hz may be transient in time and with the use of longer windows to study spectra, we will not be able to determine when this activities happened. This is the fundamental property of the signal processing theory known as the Heisenberg Uncertainty principle. It tells us that the multiplication of the time resolution and frequency resolution is constant. In other words, if we want to precisely determine the frequency content we will need to analyze longer EEG epochs, thereby loosing the necessary time localization information. On the other hand, if we want to say accurately when certain event occurred (characterized by its frequency), we will not be able to estimate the exact frequency accurately.

One trade-off for the improved time-frequency resolution is the Short-Time Fourier Transform. The idea is similar to the Discrete Time Fourier Transform, with the improved time resolution at the expense of the frequency resolution. Commonly, this is illustrated in the so-called time-frequency plane, that offers appealing insight into the signal behavior. Other variations of the Fourier Transform are cosine transforms and extensions into the so called, local cosine packet transforms. For more details we refer to the [40].

The cosine-based transforms were used throughout the work on the thesis to characterize neonatal EEG signal in the sparse way. This means, that the signal can be approximated with only few frequencies leading to effective parametrization (feature extraction) and compression of the EEG signal.

However, neonatal EEG morphology is more complex consisting of not only smooth oscillations (for which cosine-based transformations are suitable), but

also from high activity bursts and seizure patterns (spikes). Therefore, to better characterize such time-varying patterns within the EEG, the Discrete Wavelet Transform was used as well.

3.2.2 Discrete Wavelet Transform

Main idea of the Wavelet decomposition subsides on the fact that we can analyze high frequencies within the shorter time windows and low frequencies within the longer time windows. In contrast to Fourier-related transforms that decompose signals into (complex) cosine waves, within the wavelets theory aperiodic waveforms (wavelets) will be used. The construction of the wavelets is rather technical and further in-depth insights can be found in [40].

The Discrete Wavelet Transform decomposes the signal into two parts: low and high frequency components. This is done by splitting the spectra into (approximately) two halves. Mathematically, we can formulate this in the following way obtaining the approximation and the detail coefficients:

$$\mathrm{a}_j[n] = \langle f, \phi_{j,n} \rangle$$
$$\mathrm{d}_j[n] = \langle f, \psi_{j,n} \rangle$$

The approximation coefficients are related to the slow components. The detail coefficients correspond to the high frequency activity and they are well localized in time. The j variable corresponds to the level of the decomposition, whereas n represents time variable. The ϕ and ψ functions are the scaling and the wavelet functions which are used for the signal decomposition. They are used for the wavelet transform formulation from the perspective of harmonic analysis.

With the previous set of equations we have described wavelet transform using the 1 level of decomposition. Commonly, we continue the decomposition process iteratively by further decomposing the approximation part of the signal, whereas the calculated details coefficients are kept. Note that the number of the coefficients $a_j[n]$ and $d_j[n]$ is the same as of the original signal, meaning that the coefficients are downsampled by the factor of 2 as compared to the original signal.

In addition, at the next decomposition level, this implies that the scaling and the wavelet functions would be 'stretched' in time domain. This allows better

localization of the lower frequency components of the signal as longer time periods are used for the calculations.

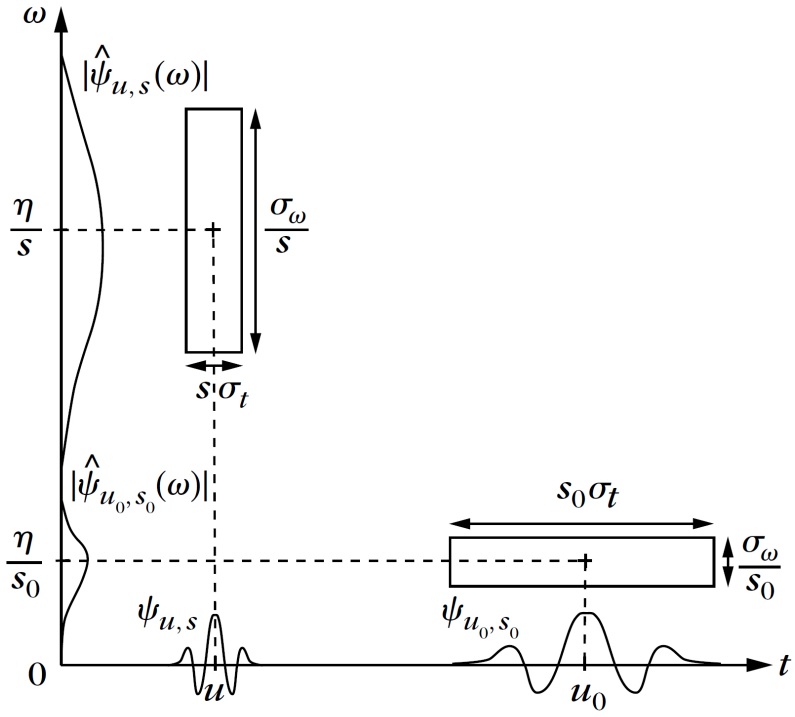

Figure 3.1: Heisenberg time-frequency boxes of two wavelets, $\psi_{u,s}$ and ψ_{u_0,s_0} . When the scale s decreases, the time support is reduced but the frequency spread increases and covers an interval that is shifted toward high frequencies. Adapted from [79].

It is interesting to illustrate the wavelet decomposition within the time-frequency plane. It can be seen that the wavelet functions are finite in duration (as compared to cosine-based basis) and offer a good trade-off between the time-frequency localization.

In addition, the wavelet decomposition can also be described using the digital signal processing approach. Within this concept the so called conjugate mirror filters are constructed as the low pass and high pass dual filters. For better insight, a detailed description is provided in [40].

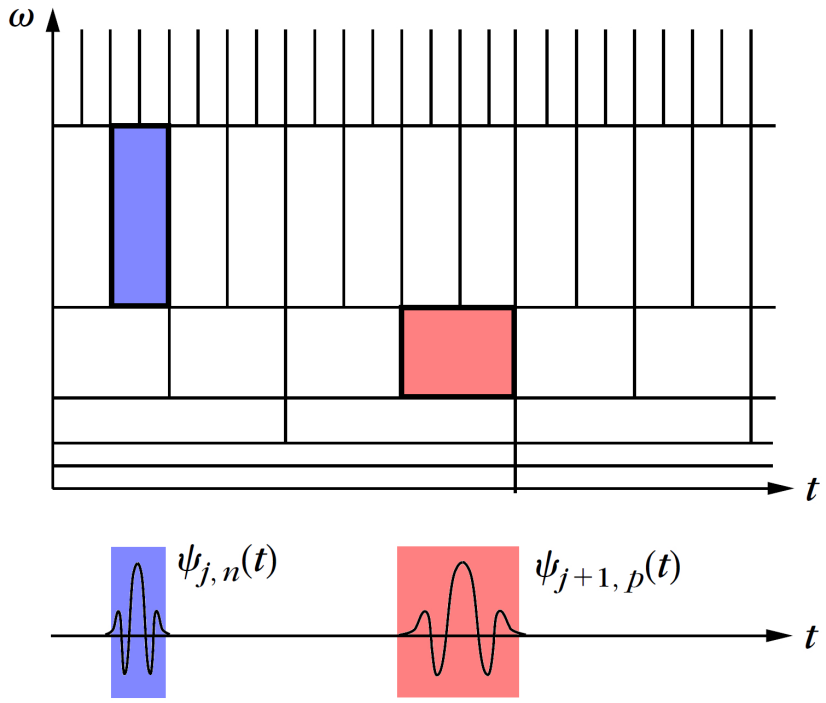

Figure 3.2: The time-frequency boxes of a wavelet basis define a tiling of the time-frequency plane.

3.2.3 Fractal Analysis

Previously described mathematical concepts are mainly applied for EEG data structuring, and they quantify time correlation between shorter temporal scales. For instance, EEG dynamics occurring with the interval longer than 60s is not directly considered during EEG quantification. In this paragraph we give an outline of time series analysis procedure that explores long-range temporal correlations within EEG signal. In other words, EEG is treated as a recorded brain process, properties of which are quantified over a longer duration of time (e.g. over 15 min). Indeed, recent work in basic neuroscience has provided ample evidence that brain behavior exhibit, so called, scale-free properties ([8]), [107], [42], [59]). Scale-free dynamics in a complex system can give rise to self-similarity over temporal scales, i.e. long-range temporal correlations (LRTC), which may be assessed from the EEG using detrended fluctuation

analysis (DFA; [101]; [52]). Recent development of signal analysis methods has extended DFA to multifractal DFA (MF-DFA), which characterizes time series with multiple co-existent dynamic processes that may give rise to temporally local fluctuations including both extreme small and large magnitudes. Several studies have reported MF-DFA to offer additional insight in experimental and clinical neuroscience contexts ([62], [136]). The neonatal EEG is, indeed, an example of a signal with extreme, apparently erratic fluctuations in signal amplitudes, making it potentially suitable for the MF-DFA paradigm as well.

Detrended Fluctuation Analysis (DFA), was introduced by Peng et al. to quantify long-range temporal correlation with weaker stationarity assumptions. However, not all time series can be characterized as monofractal processes and described with a single DFA scaling exponent. In such cases, the crossover time points are observable at different scales, the time series have different working regimes. Hence, instead of a single DFA exponent, the time series is characterized as an interwoven series of different fractal exponents – multifractal. The outline of both algorithms and their differences are given as described in ([62]; [52]):

Step 1: compute the cumulative sum of the time series to create the signal profile Y:

$$Y(i) = \sum_{k=1}^{i} x_k - \langle x \rangle, i = 1, 2, .., N \tag{3.1}$$

where $\langle x \rangle$ is mean of the time series.

Step 2: Define a set of $Ns = int(N/s)$ window sizes of length s, which are equally spaced on a logarithmic scale between the lower bound of four samples and the length of the signal.

Step 3: Calculate the local trend y of each of the segments Ns using a least-squares fit of the series. Next, determine the variance of the detrended segment as a function of window size s and the segment number :

$$F^2(s, v) = \frac{1}{s} \sum_{i=1}^{s} \{Y[(v-1)s + i)] - y_v(i)\}^2, v = 1, 2, .., N_s \tag{3.2}$$

Step 4: Average over all segments to obtain the qth order fluctuation function:

$$F_q(s) = \left\{ \frac{1}{N_s} \sum_{v=1}^{N_s} \left[F^2(s, v) \right]^{q/2} \right\}^{1/q} \tag{3.3}$$

For a single value q=2, the monofractal DFA algorithm is obtained. The fluctuation function F is plotted along the logarithmic axes. The DFA scaling exponent, α, is the slope of the linear approximation in the range of time-scales of interest and can be estimated using linear regression. An example of a DFA and MF-DFA fluctuation plots are illustrated in Chapter 6 (Figures 6.1 and 6.2).

Alternatively, for multifractal DFA, the value of q is commonly selected from -5 till 5, with an equidistant unit step of 0.5 (or 0.2). In this way, a set of q-order based fluctuation functions can be obtained. The differences between monofractal and multifractal time series may be encountered if the time series express local large and small fluctuations. Within the MF-DFA paradigm, the large variations will be dominant for positive q values, whereas the small fluctuations will be characterized with negative q values. In contrast, monofractal DFA will be mainly insensitive to local fluctuations. The quantification of long-range temporal correlations is used in Chapter 6 as a novel approach to quantify neonatal EEG and EEG discontinuity.

3.3 Fundamentals of multilinear algebra

We will start with the basic notations and essential mathematical definitions that are applied throughout the thesis ([105], [104] [23]). We define vectors (1-way tensors) as lowercase bold letters (e.g. $\mathbf{a}$). The matrices will be denoted with bold capital letters, e.g. $\mathbf{A} = [\mathbf{a}_1, \mathbf{a}_2]$. Thus, vectors can be seen as 1-way tensors ($\mathbf{a} \in^{I\times 1}$), whereas matrices correspond to 2-way tensors ($\mathbf{A} \in^{I\times J}$). Furthermore, tensors will be denoted with calligraphic letters: $\mathcal{A}, \mathcal{X}, \mathcal{G} \in^{I_1\times I_2\times I_3}$.

An entry of a vector $\mathbf{a}$, a matrix $\mathbf{A}$, or a tensor $\mathcal{A}$ is denoted by a_i, $a_{i,j}$ or $a_{i,j,k}$, depending on the number of modes (dimensions). At times, it is practical to represent matrices as a set of columns or rows. On the other hand, tensors offer much more possibility for the basic decompositions. Some examples we will illustrate using 3D tensors. Tensors can be represented as a set of vectors (also called fibers) as shown in the Figure 3.3. In addition, tensors are commonly decomposed as slices (matrices): frontal, lateral or horizontal (Figure 3.4).

Definition 1. The mode-n product of a tensor $\mathcal{A} \in^{I_1\times I_2\times\cdots\times I_N}$ with a matrix $\mathbf{U} \in^{J\times I_n}$ is denoted as $\mathcal{A} \times_n \mathbf{U}$ and is of size $I_1 \times \cdots \times I_{n-1} \times J \times I_{n+1} \times \cdots \times I_N$. The entries of the mode-n product are defined as:

$$(\mathcal{A} \cdot_n \mathbf{U})_{i_1\cdots i_{n-1} j i_{n+1}\cdots i_N} = \sum_{i_n=1}^{I_n} a_{i_1 i_2\cdots i_n\cdots i_N} u_{j i_n}.$$

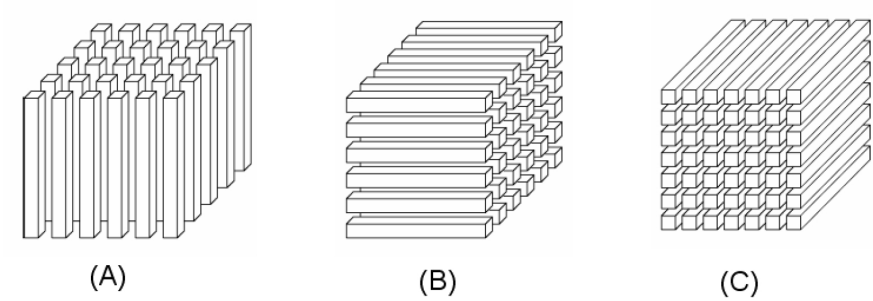

Figure 3.3: (A) Columns, (B) rows and (C) tubes in a third-order tensor.

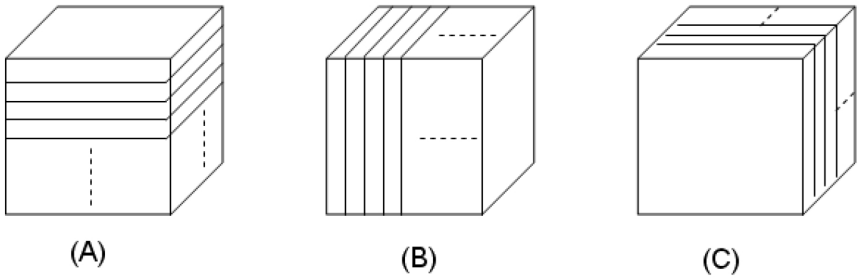

Figure 3.4: (A) Horizontal, (B) vertical and (C) frontal slices of a 3D tensor.

Definition 2. The outer product $\mathcal{A} \circ \mathcal{B}$ of a tensor $\mathcal{A} \in^{I_1 \times \cdots \times I_M}$ and a tensor $\mathcal{B} \in^{J_1 \times \cdots \times J_N}$ is the tensor defined by:

$$(\mathcal{A} \circ \mathcal{B})_{i_1 \cdots i_M j_1 \cdots j_N} = a_{i_1 \cdots i_M} b_{j_1 \cdots j_M}, \tag{3.4}$$

for all different values of the indices.

Definition 3. The mode–n matricisation or unfolding $\mathbf{A}_{(n)}$ of an Nth-order tensor $\mathcal{A} \in^{I_1 \times I_2 \cdots I_N}$ maps the tensor element with indices $(i_1, \cdots, i_N)$ to a matrix element (i_n, j) such that

$$j = 1 + \sum_{k=1, k \neq n}^{N} (i_k - 1) J_k \text{ with } J_k = \begin{cases} 1 & \text{for } k = 1 \text{ or } (k = 2 \text{ and } n = 1) \\ \prod_{m=1, m \neq n}^{k-1} I_m & \text{otherwise.} \end{cases} \tag{3.5}$$

For a third order tensor, the unfolding takes the form:

$$(\mathbf{A}_{(1)})_{i_1,(i_2-1)I_3+i_3} = (\mathcal{A})_{i_1 i_2 i_3},$$

$$(\mathbf{A}_{(2)})_{i_2,(i_3-1)I_1+i_1} = (\mathcal{A})_{i_1 i_2 i_3},$$

$$(\mathbf{A}_{(3)})_{i_3,(i_1-1)I_2+i_2} = (\mathcal{A})_{i_1 i_2 i_3},$$

for all values of the indices.

We also introduce the multiplication of the tensor of the order N, with the matrices along the all possible modes as:

$\mathcal{G} \times \{\mathbf{A}\} = \mathcal{G} \times_1 \mathbf{A}^{(1)} \ldots \times_N \mathbf{A}^{(N)}$

In addition, the multiplication of a tensor with all modes except along the mode n is written as:

$\mathcal{G} \times_{-n} \{\mathbf{A}\} = \mathcal{G} \times_1 \mathbf{A}^{(1)} \times_2 \mathbf{A}^{(2)} \ldots \times_{n-1} \mathbf{A}^{(n-1)} \times_{n+1} \mathbf{A}^{(n+1)} \ldots \times_N \mathbf{A}^{(N)}$

3.4 Matrix and Tensor Decomposition Models

3.4.1 Singular Value Decomposition - SVD

One of the fundamental results of the linear algebra is a Singular Value Decomposition (SVD) method. It is a very powerful and widely applied mathematical transformation (e.g. used within the Google's search algorithm PageRank [93]). Before proceeding further, let us define the matrix rank.

Matrix rank. The row (column) rank of the matrix is defined as the maximum number of linearly independent rows (or columns). The row rank is equal to the column rank and this is denoted as the matrix *rank*, *rank*($\mathbf{A}$). In case that a rank of the matrix (e.g. $\mathbf{A}_{n\times m}$) is 1, implies that the matrix can be constructed as the outer product of two vectors. In this case, the rows (columns) are linearly dependent and they are different only by the scaling factor (e.g. *exact up to the scaling factor*).

SVD represent matrix decomposition as proposed:

$$\mathbf{A} = \mathbf{U}\Sigma\mathbf{V}^*, \tag{3.6}$$

where $\mathbf{U}$ and $\mathbf{V}$ are unitary matrices, $\mathbf{V}^*$ is the conjugate transpose of $\mathbf{V}$, and $\mathbf{\Sigma}$ is a diagonal matrix. The diagonal elements of $\mathbf{\Sigma}$, denoted as σ_i, are positive by convention, appear in decreasing order and are called the singular values of $\mathbf{A}$. Alternatively, $\mathbf{A}$ can be written as the weighted sum of their outer products:

$$\mathbf{A} = \sum_i \sigma_i U_i \circ V_i, \tag{3.7}$$

The number of non-zero singular values is the rank of the matrix. Truncating the summation at the first r elements gives the best rank-r approximation of $\mathbf{A}$ in the least-squares sense. In case that the relatively small σ_i values appear in the decomposition, they are commonly discarded and the matrix is effectively approximated. Commonly, the noise components are discarded in this way within some applications. Hence, the SVD model allows reduction in the model and computational complexity.

3.4.2 Principal Component Analysis - PCA

Principal Component Analysis (PCA) is defined as a mathematical orthogonal linear transformation that transforms the data into a new coordinate system by maximizing the variance of the input data. We can illustrate PCA application within the EEG context. For instance, n channels (e.g. =12) that constitute the EEG signal can be represented as a (matrix) $\mathbf{X}$ (12 x 256 * 60). Depending on the sampling frequency (e.g. 256Hz) we may stack an epoch of 60s long EEG into $\mathbf{X}$. The idea is that EEG channels will be correlated (due to proximity of the electrodes) and we may transform X into another coordinate system $\mathbf{S}$. We say that we applied PCA onto $\mathbf{X}$, thereby generating a matrix $\mathbf{S}$ with m vectors (m<n) in such a way that the redundancy induced by correlations is removed. The new coordinate system is obtained by finding a rotated orthogonal coordinate system such that new coordinates become uncorrelated. In other words, the EEG samples can be seen as points in the 12-dimensional space (defined with the 12 EEG channels), that describes the brain activity. What PCA tells us is that usually, we can observe this activity in the much lower subspace (e.g. 3-7 dimensions which is determined by the EEG complexity - brain activity). At the same time, the variances of the projections of $\mathbf{X}$ on the new coordinate axes are maximized so that the first axis corresponds to the maximal data variance, the second axis corresponds to the maximal variance in the direction orthogonal to the first axis, and so on.

Mathematically, PCA of the matrix X, can be defined [47] as:

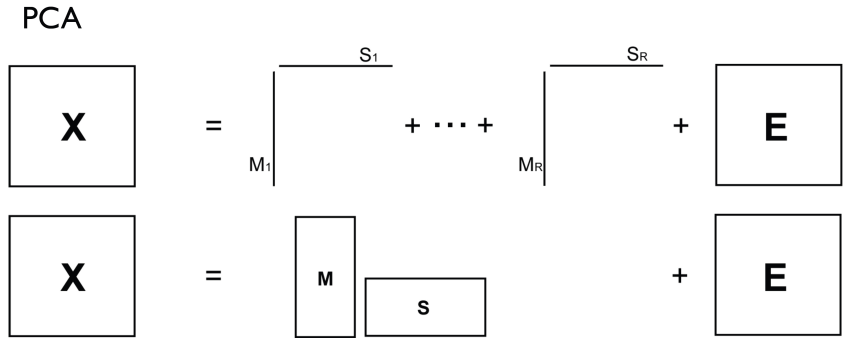

Figure 3.5: Illustration of the PCA using the sum of the outer product vectors (upper) and the multiplication of the two matrices **M** and **S** (bottom).

$\mathbf{X} = \mathbf{MS^T}$, for which, $\|\mathbf{X} - \mathbf{MS^T}\|^2$ is minimal. We also illustrate PCA as shown in the Figure 3.5.

3.4.3 Independent Component Analysis - ICA

The subsequent mathematical technique, closely related to PCA, is the Independent Component Analysis (ICA). ICA is a tool for solving the broader class of the problem also known as Blind Source Separation (BSS) methods [57]. In its basic form the linear ICA model is as follows:

$$\mathbf{X} = \mathbf{M} \cdot \mathbf{S}$$

The famous example for the ICA illustration is the, so called, *cocktail party* problem. We may imagine that there are several people (=n) in the room and at least that much microphones ($m \geq n$). First of all, we do not know *a priori* the number of people in the room and thier exact positions in the room. Microphones, scattered across the room, receive different speech sounds depending on the peoples' positioning (modeled by the mixing matrix **M**). The underlying ICA assumption is that the amplitude of the different sound signals recorded at the microphones are statistically independent. These signals, that are recorded at each microphone, we will call mixtures (**X**). Hence, the ICA methods succeed to determine the speech of the speakers, that is, the original sources (**S**), although the matrix (**M**) is unknown.

Similar concept is heavily exploited in the neuroscience in general as well as within the EEG processing. We assume that the brain activities (as well as the non-cerebral origin artifacts) are independent sources - $\mathbf{S}$, originating deep under the scalp. The EEG electrodes, placed on the surface of the head, are analogous to the microphones' recordings in the cocktail-party problem. We may recall that the EEG activity is generated by the electromagnetic fields, which are propagating through the head with very high speed [57]. Because of this, the basic *instantaneous* ICA model is usually applied as we can assume that the mixtures are generated at the scalp electrodes instantaneously.

The difficult question is how an equation with 3 variables and only one known ($\mathbf{X}$) can be solved ($\mathbf{M}$ and $\mathbf{S}$ are not known)? Within the ICA concept, the assumption of statistical independence of the components is exploited for the design of the criteria function. An optimization of the criteria function (e.g. with convex optimization methods) will lead to the desired solutions of $\mathbf{M}$ and $\mathbf{S}$. Starting point for the criteria function formulations are links of statistical independence and the non-gaussianity of the independent sources. Furthermore, the maximization of the non-gaussianity can be formulated via measures of kurtosis, negative entropy (negentropy), maximum likelihood estimation or maximum information to name a few. An illustration of the ICA application on the EEG signal processing is shown in Figure 3.6.

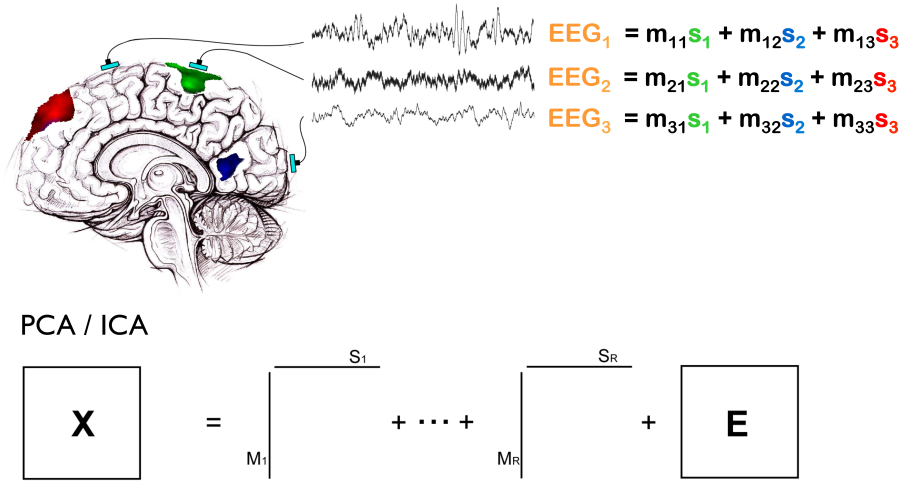

Figure 3.6: An illustration how ICA can be applied to reconstruct different sources from the scalp EEG recordings. The ICA determines the sources s which are generated deep inside the scull.

In the 1990s, different ICA criteria functions and convex optimization methods were developed, thereby leading to a large number of ICA algorithms. One should be aware that depending on the morphology of the source signals, different performance will be obtained. For instance, certain algorithms are developed to accurately model source signals, which are auto-correlated or exhibit quasi-periodicity (e.g. Second Order Blind Identification - SOBI [9], BSS-CCA [28]). In contrast, other algorithms are better suited for the signals that exhibit super-Gaussian distributions (e.g. JADE [20], RobustICA [134]). These algorithms are mainly applied in our research groups for the cancellation of certain non-cerebral artifacts and are used for the EEG filtering in this thesis ([82], [31]). An example of ICA (algorithm SOBI) applied onto an EEG segment is shown in Figure 3.7. We can see that one of the components clearly corresponds to the ECG signal.

3.5 Tensor decompositions

The previously explained decomposition methods were developed for 2D data structures, that is, matrices. Here, we provide a fundamental overview of the decomposition methods for the 3D or higher-order tensors. We will proceed sequentially and provide overview of the TUCKER decomposition model, higher-order SVD and the Higher Order Discriminant Analysis (HODA), which has been used in this thesis for the classification of the long-streams of the EEG data.

3.5.1 TUCKER decomposition model

For 3D and higher order tensors, TUCKER decomposition is the essential model for the data extraction and reduction of model complexity [105]. Illustration of the TUCKER model is shown in Figure 3.8.

$$\mathcal{X} = \mathcal{G} \times_1 \mathbf{U}^{(1)} \times_2 \mathbf{U}^{(2)} \times_3 \mathbf{U}^{(3)} + \mathrm{E}$$

In general, a TUCKER-3 decomposition model is not unique. Therefore, it is common to impose additional constraints on the hidden factors and the core

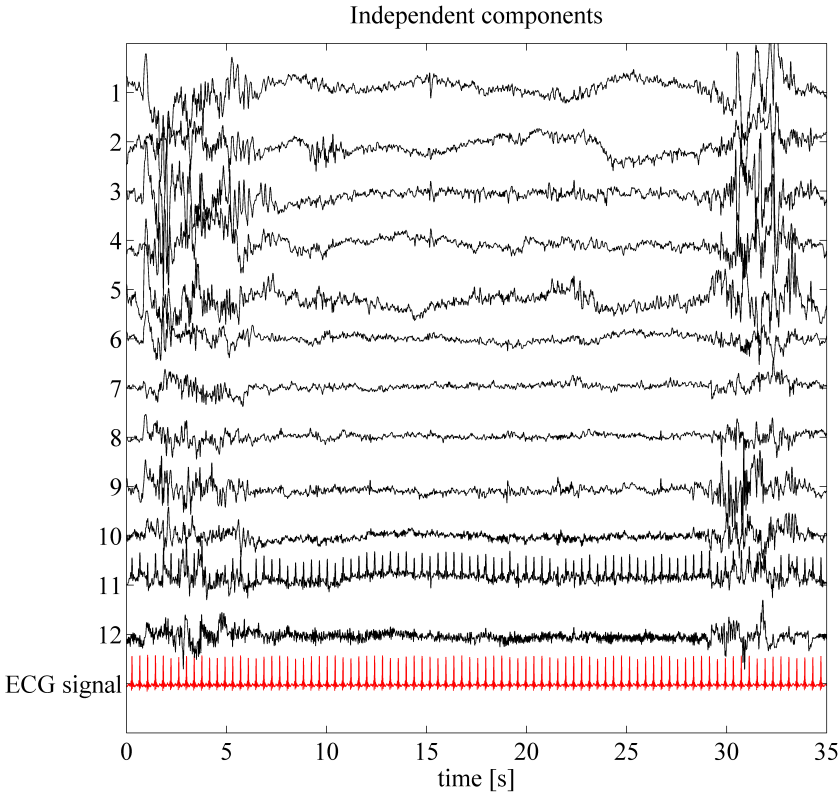

Figure 3.7: An illustration of the ICA algorithm (SOBI) being applied onto the neonatal EEG signal from the Figure 2.15 generated 12 independent components. We can clearly identify that the independent component number 11 corresponds to the ECG activity.

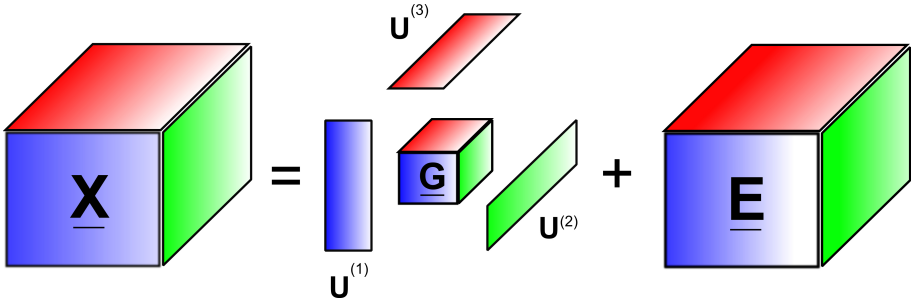

Figure 3.8: Illustration for a 3D TUCKER decomposition. The objective is to find the optimal (factor) matrices $\mathbf{U}^{(n)}$ and the core tensor $\mathcal{G}$, which is commonly of a much smaller dimension as compared to $\mathcal{X}$.

tensor of the TUCKER decomposition (e.g. [63] , [89]). In case that we impose orthogonality constraints on the factor matrices ($\mathbf{U}^{(1)}$,$\mathbf{U}^{(2)}$, $\mathbf{U}^{(3)}$) we obtain a model known as HO-SVD (Higher Order Singular Value Decomposition). It is also known as the HOOI (Higher Order Orthogonal Iterations) introduced by De Lathauwer et al. ([29] , [30]). It is important to note the similarity with the SVD, where matrix Σ generalizes to the core tensor $\mathcal{G}$. The values of the core tensor $\mathcal{G}$ convey information about the underlying interplay and effects between factor matrices. In a similar way, the large values of the σ_i within the SVD concept were more important, thereby modeling the data information content. Hence, within the SVD as well as within the HO-SVD, both reduction and efficient representation of the model are assumed. However, the decomposed values (e.g. σ_i within SVD) and the corresponding core tensors do not necessarily capture discriminative information that can be used for further classification purposes. One of the solutions is to decompose the data such that the factor matrices are orthogonal, while imposing discriminative criteria that can be useful for the classification as well. In this thesis, we applied constraints to create a core tensor with discriminative properties that is useful for the multi-class classification tasks known as Higher Order Discriminant Analysis - HODA [105].

3.5.2 Higher Order Discriminant Analysis approach for multi-way features

Consider an available set of multidimensional tensors $\mathcal{X}^{(k)}$, (k=1,2,..,K), representing a training data belonging to C classes. Each training sample $\mathcal{X}^{(k)}$ is given a label ck indicating the category (class) to which it belongs.

In our problem label *ck* represents the class (degree) of background EEG abnormality as scored visually by an expert EEG reader, whereas 1h long EEG recording is structured as 3D tensor. To perform a dimensionality reduction and to extract significant features, we apply simultaneous approximate tensor decompositions (Figure 3.9):

$$\mathcal{X}^{(k)} = \mathcal{G}^{(k)} \times_1 \mathbf{U}^{(1)} \times_2 \mathbf{U}^{(2)} \times_2 \mathbf{U}^{(3)} + \mathrm{E}^{(k)} \ ,$$
$$k = 1, 2, \ldots, K$$

where the compressed core tensors $\mathcal{G}^{(k)}$ are of lower dimension than the original data tensors $\mathcal{X}^{(k)}$. Here, we assume that the factors (basis matrices) $\mathbf{U}^{(n)}$ are the same for all training data tensors (k=1,2,..,K).

The simultaneous approximate tensor decomposition problem is equivalent to performing a Tucker-N decomposition of a tensor obtained by concatenating all N-way data tensors into a tensor of order N+1 [105]. In other words, to compute the factor matrices $\mathbf{U}^{(n)}$ and the core tensors $\mathcal{G}^{(k)}$, we concatenate all training tensors into one 4th order training data tensor $\mathcal{X} = cat(\mathcal{X}^{(1)}, \mathcal{X}^{(2)}, \ldots, \mathcal{X}^{(K)}, N+1)$, with N+1=4. Next, we perform the Tucker-3 decomposition:

$$\mathcal{X} = \mathcal{G} \times_1 \mathbf{U}^{(1)} \times_2 \mathbf{U}^{(2)} \times_3 \mathbf{U}^{(3)} + \mathrm{E}$$

The sample tensors $\mathcal{G}^{(k)}$ can be extracted back from the concatenated tensors by fixing the 4th index at a value k, i.e. $\mathcal{X}(:,:,:,k) = \mathcal{X}^{(k)}$ and the individual features (corresponding to different classes) are extracted from the core tensor $\mathcal{G}$ as $\mathcal{G}^{(k)} = \mathcal{G}(:,:,:,k)$, with $J_4 = k$. In other words, the features of a specific training data $\mathcal{X}^{(k)}$ are represented by the k-th row of the mode-4 matricized version of the core tensor $\mathcal{G}$. Furthermore, the problem needs to estimate the basis matrices $\mathbf{U}^{(n)}$ for the concatenated tensor of all training data $\mathcal{X}^{(k)}$ incorporating the known labels (class membership) as an *a priori* information. This represents an algorithm, higher order discriminant analysis (HODA) [105].

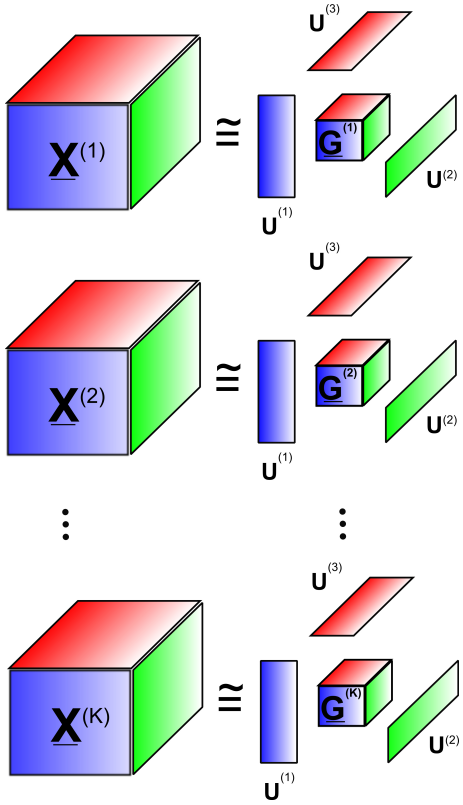

Figure 3.9: Illustration of feature extraction from a set of 3-way data tensors $X^{(k)}$, k=1,2,..,K. The objective is to estimate common factor matrices (basis) $\mathbf{U}^{(n)}$, n=1,2,3 and the core tensors $\mathcal{G}^{(k)}$.

In general, the HODA algorithm finds the orthogonal basis $\mathbf{U}^{(n)}$ based on the maximization of the Fisher ratio between the core tensors $\mathcal{G}^{(k)}$:

$$\phi = \underset{\mathbf{U}^{(1)},\ldots,\mathbf{U}^{(n)}}{\arg\max} \frac{\sum_{c=1}^{C} K_c \left\| \overline{G}^{(c)} - \overline{\overline{G}} \right\|_F^2}{\sum_{k=1}^{K} \left\| G^{(k)} - G^{(c_k)} \right\|^2}$$

Here, $\overline{\mathcal{G}}^{(c)}$ is the mean tensor of the cth class consisting of K_c training samples, c_k denotes the class to which the k-th training sample $\mathcal{X}^k$ belongs and is $\overline{\overline{\mathcal{G}}}$ the mean tensor of all training samples.

Here, the class labels are incorporated into the algorithm to better capture and model the differences of input data tensors ($\mathcal{X}$) between data classes. The applied algorithm, higher order discriminant analysis (HODA), represents the generalization of the 1D linear discriminant analysis to the multi-linear one ([23], [104]). The core tensor $\mathcal{G}$ consists of elements that capture the differences between the different classes and can be used for classification.

3.6 Machine Learning Foundations

The previous mathematical concepts were focused on the methods to parametrize the EEG signal and/or to extract features from certain EEG patterns. Next, they were used for further pattern recognition. In this thesis, two EEG-derived data patterns were important to be classified:

1. *dynamic* interburst interval patterns were classified into definite or misclassified automated detections, thereby representing the refinement step.
2. 1h of neonatal EEG recording was classified into one out of the three classes as judged by an expert EEG reader.

In both cases, for the final data representations vectors were used, so we will illustrate fundamental machine learning concepts for the classification of feature vectors. First, we explain Linear Discriminant Analysis (LDA) as it is essential for the complete understanding of the HODA algorithm. Second, we provide an overview of the Support Vector Machine classifiers (SVM). We also explain an adaptation of this algorithm, Least Squares Support Vector Machines (LS-SVM), that was used for the vector classification in this thesis.

The examples of two class and three class classification problems are illustrated in Figure 3.10. The goal of the classification is to determine the boundaries between classes of the given labeled dataset (supervised learning). The boundary is characterized by the decision function, which is calculated using the labeled datasets. Hence, the classifiers learn from the data to classify new data points into the corresponding classes.

3.6.1 Linear Discriminant Analysis

Linear discriminant analysis (LDA) assigns each vector $\mathbf{x}_i$ a class value which has the highest posterior probability, as expressed by Bayes's theorem [41]. The

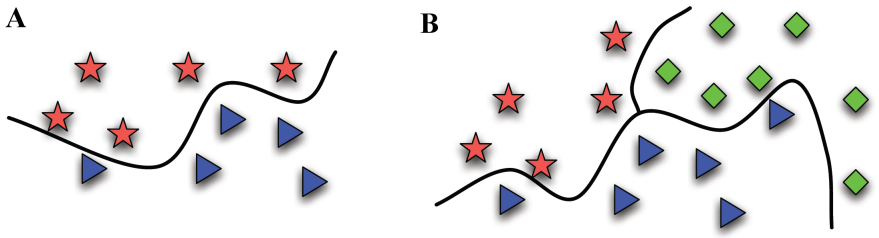

Figure 3.10: Illustration of the two (A) and three (B) classes classification problem.

underlying assumption is that data are sampled from a multivariate normal distribution with class means μ_1 and μ_2 and that the class covariance matrices $\mathbf{S}_1 = \mathbf{S}_2 = \mathbf{S}$ are equal. The decision LDA function is defined in the following way [72]:

$$f(\mathbf{x}) = D(\mathbf{x}) = [x - \frac{1}{2}(\mu_1 + \mu_2)]^T S^{-1}(\mu_1 - \mu_2), \tag{3.8}$$

It can also be written in the following form as well [109]:

$$\begin{aligned} D(\mathbf{x}) &= \mathbf{w}^T x + b \\ \mathbf{w} &= (\mu_1 - \mu_2)S^{-1} \\ b &= -\frac{1}{2}(\mu_1 + \mu_2)\mathbf{w}^T \end{aligned} \tag{3.9}$$

Then $\mathbf{w}$ and b are the normal vector and the bias describing the hyperplane which separates the classes. Fisher's discriminant analysis (FDA) [39] derives $\mathbf{w}$ by maximising the Rayleigh coefficient, i.e. the ratio of between-class variance to within-class variance:

$$J(\mathbf{w}) = \frac{\mathbf{w}^T \mathbf{S}_B \mathbf{w}}{\mathbf{w}^T \mathbf{S}_W \mathbf{w}} \tag{3.10}$$

where $\mathbf{S}_W = \sum_{i=1}^{2} \mathbf{S}_i$ with $\mathbf{S}_i = \sum_{\mathbf{x} \in C_i} (\mathbf{x} - \mu_i)(\mathbf{x} - \mu_i)^T$ is the within-class and $\mathbf{S}_B = \frac{1}{2} \sum_{i=1}^{2} (\mu - \mu_i)(\mu - \mu_i)^T$ with $\mu = \frac{1}{2} \sum_{i=1}^{2} \mu_i$ is the between-class variance.

Note, that this formulation defines the feature vector classification problem. The extension of this formula to higher dimensions (feature higher-order tensor) is presented in section 3.5.2.

3.6.2 Support vector machines

The most important property of the classifier is the generation of the, so-called decision function. For the LDA classification it has a linear formulation (e.g. hyperplane). For many classification problems, the non-linear classification decision functions show better classification results (accuracy and generalization property). Examples of non-linear functions are illustrated in Figure 3.10. One class of the classifiers that create non-linear decision functions are support vector classifiers. Initially, feature vectors are used to characterize the data samples and the classification is obtained according to the *similarity* of the feature vectors. The similarity is often characterized using the distance measures between two feature vectors (class instances) and inner vector product is used for its calculation. However, the fundamental idea, embedded within support machine classifiers is that the input data are first mapped into the high dimensional feature space (that can be even infinite dimensional). Interestingly, in the new feature space, the so-called Kernel trick is used for the mapping, calculation of distances (similarity) and for further classification.

Mathematically, the support vector machine is defined by

$$y(x) = \text{sign}(\mathbf{w}^T \varphi(\mathbf{x}) + b), \tag{3.11}$$

where $\mathbf{w}$ is a weighting vector and φ is a possibly non-linear feature mapping. The objective in the SVM formulation is to construct a separating hyperplane in the feature space with maximal margin. This can be translated to the following optimization problem:

$$\min_{\mathbf{w},e_i,b} \left(\frac{1}{2}\mathbf{w}^T\mathbf{w} + C\sum_{i=1}^{N} e_i\right), \tag{3.12}$$

subject to

$$y_i[\mathbf{w}^T\varphi(\mathbf{x}) + b] \geq 1 - e_i,\ e_i \geq 0,\ i = 1, ..., N$$

where C is a regularization constant. By constructing the Lagrangian and taking the conditions for optimality, one obtains the dual problem, which is the following quadratic programming problem:

$$\max_{\alpha}(\sum_{i=1}^{N}\alpha_i - \frac{1}{2}\sum_{i=1}^{N}\sum_{j=1}^{N}\alpha_i\alpha_j y_i y_j K(\mathbf{x}_i,\mathbf{x}_j)), \tag{3.13}$$

subject to

$$\sum_{i=1}^{N}\alpha_i y_i = 0 \text{ and } 0 \le \alpha_i \le C \text{ for } i = 1,...,N,$$

where $\mathbf{x}_i \in {}^{d}$ and $K(\mathbf{x},\mathbf{x}_i)$ is a symmetric and positive definite kernel function satisfying the Mercer theorem, which is expressed as

$$K(\mathbf{x},\mathbf{x}_i) = \varphi(\mathbf{x})^T\varphi(\mathbf{x}_i) \tag{3.14}$$

Equation (3.14) is often called the kernel trick. It facilitates the use of high dimensional feature spaces without actually making explicit computations in this space. For detailed theoretical background behind the kernel trick we refer to [119].

The x_i input vectors corresponding to non-zero α_i values are called support vectors. The classifier in the dual space takes the form:

$$y(x) = \text{sign}[\sum_{i}\alpha_i y_i K(\mathbf{x},\mathbf{x}_i) + b] \tag{3.15}$$

Throughout this thesis we applied the least-squares support-vector machine introduced by [118]. In this formulation equality constraints are used instead of inequality constraints in (3.12):

$$\min_{\mathbf{w},e_i,b}(\frac{1}{2}\mathbf{w}^T\mathbf{w} + \gamma\sum_{i=1}^{N}e_i^2), \tag{3.16}$$

subject to

$$\hat{y}_i[\mathbf{w}^T\varphi(\mathbf{x}) + b] = 1 - e_i,$$

Taking the optimality conditions and eliminating $\mathbf{w}$ and $e = [e_1, ..., e_N]^T$ simplifies the computation to solving a set of linear equations instead of a quadratic programming problem:

$$\left[\begin{array}{c|c} 0 & y^T \\ \hline y & \Omega + \gamma^{-1} I \end{array}\right] \left[\begin{array}{c} b \\ \hline \alpha \end{array}\right] = \left[\begin{array}{c} 0 \\ \hline 1_N \end{array}\right] \tag{3.17}$$

with $y = [y_1, ..., y_N]^T$, $1_N = [1, ..., 1]^T$, $\alpha = [\alpha_1, ..., \alpha_N]^T$, $\Omega_{kl} = y_k y_l K(\mathbf{x}_k, \mathbf{x}_l)$.

3.7 Conclusion

In this Chapter, we have provided a brief overview of the basic mathematical methods. The essentials of the mathematical tools to be applied depend on the way how the input data are structured. With respect to this, we may analyze neonatal EEG data as the vectors, matrices or higher-order tensors. We provided an essential overview of the time-frequency signal representations as well as the representation methods for the quantification of the long-range temporal signal behavior. Moreover, we gave overview of the basic matrix and tensor decomposition methods that are used to reduce the dimension of the signals. Finally, we provide an overview of the machine learning methods that are applied throughout the thesis.

Chapter 4

Automated detection of dynamic interburst intervals

Main hallmark encountered in the EEGs of asphyxiated term infants is the occurrence of EEG discontinuity, that is, interburst intervals. At present, clinicians visually assess the duration of these patterns and establish diagnosis. In this chapter we present the algorithm for the automated detection of interburst intervals. The main emphasis of this approach is to detect not only burst-suppression-burst patterns in severe asphyxia, but also in mildly asphyxiated neonates. Therefore, we introduce the term dynamic interburst interval (dIBI). In addition, this parameter quantifies duration and amplitude of EEG discontinuity in neonatal EEG and adequately characterizes milder background EEG abnormalities.

The initial algorithm performs well on the relatively clean EEG periods and well defined burst-suppression EEG periods. However, once we tested the algorithm on long EEG recordings for more than 48h per neonate, a significant number of misclassified and dubious detections were encountered. Therefore, as the next step, we optimized machine learning classifiers (LS-SVMs) to differentiate between definite dIBI detections and misclassified ones. Furthermore, we show that in the patient group with HIE and milder EEG discontinuities, dIBI improves characterization of the neonates with good clinical outcome as compared to classification based on the traditionally used interburst interval.

4.1 Introduction

In clinical care of asphyxiated neonates, it is necessary to accurately assess the degree of HIE severity. In many NICUs, this is done by interpreting EEG signals as well as their dynamic changes. This procedure enables accurate prognostication in two extreme categories of neonatal HIE. More specifically, the mildest forms of HIE, characterized by normal or mildly disturbed EEG background with preserved sleep-wake cycles are associated with a good clinical outcome. In contrast, severe HIE, characterized by persistent non-responsive burst-suppression pattern (e.g. IBIs>10-20s) and the absence of sleep-wake cycle (at 48-hours post partum) is associated with a poor clinical outcome ([38], [21], [90]). On the other hand, compared to these two extreme groups, clinical and EEG assessment of mild and moderate neonatal HIE is challenging.

The interburst interval in neonates is defined very broadly as a pattern with peak-to-peak amplitude <25-50 μV. Within this definition, three IBI patterns are identified in term neonates: (1) tracé alternant (TA-IBI>25 μV) - an EEG pattern present within the quiet sleep stage in healthy newborns (2) tracé discontinue (TD-IBI<25 μV) - a pattern in neonates with mild and moderate HIE and (3) burst-suppression (BS-IBI<5-10 μV) - a pattern in neonates with severe HIE [123]. In the literature, the IBI pattern is usually associated with the classical BS-IBI, defined as a pattern without variability within the suppressed interval. Therefore, a simple amplitude definition threshold is commonly applied: interburst amplitude <5-10 μV ([78], [38]). On the other hand, mild and moderate EEG discontinuities (e.g. tracé discontinue - TD-IBI) cannot be characterized with such a restrictive definition [38] and their automated detection is thus more challenging.

Recently, several studies have proposed automated methods to assess EEG background in neonates with HIE. In [68], a combination of quantified EEG (qEEG) features such as EEG discontinuity, amplitude and frequency content were found useful to assess the severity of HIE in full-term neonates. However, this approach was not successful to differentiate normal EEG background from mild-to-moderate EEG abnormalities. In addition, other studies have presented algorithms for the detection of BS-IBIs in full-term and premature neonates ([76], [95], [60], [86], [67]). These algorithms are developed for the characterization of term neonates with severe HIE (IBIs>10s) and premature neonates (EEG consists of simplified burst-suppression patterns). These methods use nonlinear transformation of the EEG signal, which is followed by thresholding operator. For instance, nonlinear energy operator (NLEO), line length and envelope of the signal are applied on the raw EEG, which are subsequently thresholded. The values above the threshold correspond to bursts, whereas lower values determine the suppressed periods.

However, the quantification of mild and moderate background EEG abnormalities faces three major problems that are not addressed with the previously described automated approaches. First, complex EEG background patterns are often encountered, which consists of varying degrees of EEG amplitude attenuation. Usually, discontinuous EEG periods are intermixed and alternate with continuous EEG periods. As a result, such EEGs cannot be categorized into a simple dichotomy of either burst or suppression patterns as done in neonates with severe HIE or premature neonates. Second, neonatal HIE is not static and EEG background activity evolves over time. At present, there is no automated method which has been developed to quantify the evolution (improvement/deterioration) of the EEG background over longer periods of time (24-48h). For instance, recovery of severely abnormal EEG background is characterized by a progressive shortening of BS-IBIs and increase in amplitude of the suppressed periods (decrease in burst amplitude) ([130], [56]). That is, in newborns recovering from HIE, EEGs gradually become more continuous, whereas IBIs evolve from burst-suppression patterns to tracé discontinue and further to tracé alternant patterns. Due to the evolution of encephalopathy, an automated method designed to detect only severe EEG discontinuity (IBI>10-20s) will no longer function accurately. Third, it is known that EEG signal is very vulnerable to vast amount of artifacts and large inter-rater variability. Hence, it is important to verify whether the output of the thresholding algorithm is an accurate quantification of *real* burst-suppression-burst complex or a false detection produced by intermittent artifacts.

This chapter will focus on detection of definite EEG discontinuities, viz. classical burst-suppression as well as a range of tracé discontinue patterns that express higher interburst amplitudes. We will show that the traditional definition of EEG discontinuity is sub-optimal as there is an intrinsic dependency of duration and amplitude of the suppressed EEG patterns. This insight will allow us to monitor the evolution of brain injury and to better model EEG discontinuity, thereby analysing IBIs with respect to their duration. For this purpose, we will call the patterns analysed in this study 'dynamic interburst intervals (dIBIs)', thereby taking into consideration both the amplitude and the duration of the EEG discontinuity that can evolve over the course of EEG monitoring. Moreover, by detecting definite dIBIs and discarding dubious detections, we develop a system that can be regarded as trustworthy and consistent with a diagnostic interpretation of EEG experts. In addition, we show that using the new algorithm to detect dIBIs, we significantly improve the characterization of neonates with milder encephalopathy and good outcome as compared to a traditionally used classical BS-IBI parameter.

4.2 Methods and Materials

4.2.1 Dataset

The 53 neonates included in this study were part of a larger cohort of 119 full-term newborns who underwent continuous polygraphic video EEG monitoring (cEEG) as part of a prospective study that evaluated the utility of cEEG monitoring in term neonates with perinatal asphyxia (from March 2003 till August 2007). All EEG data were recorded at the Sophia Children's Hospital, Erasmus University Medical Center, Rotterdam, in the Netherlands. The study had the approval of the Erasmus MC Medical Ethical Review Board. Informed consent was obtained from the parents/guardians prior to the onset of the registration. The inclusion criteria for EEG monitoring were clinical features of encephalopathy and having at least one of the following features of birth asphyxia: a) arterial pH of umbilical cord blood $\leq$ 7.1, and b) Apgar score $\leq$ 5 at 5 minutes. Babies with congenital cardiac abnormalities and multiple congenital anomalies were excluded [22] as well as infants with constantly isoelectric background EEG. The EEG sampling frequency was 256 Hz. The recordings were started 2-48 (median 19) hours post partum, using a set of 17 EEG electrodes, whereas in some patients a reduced set of 13 electrodes was used. All EEG signals were filtered using high-pass and low-pass FIR filters at 0.7Hz and 20Hz respectively.

The full dataset was split into 3 non-overlapping groups.

Dataset DA consists of 157 hours of cEEG segments from seven neonates with mild and moderate background EEG abnormalities. This dataset was used to optimize the algorithm's parameters for the detection of suppressed intervals (dIBI candidates).

Dataset DB consists of cEEG data from 38 neonates. It was used to improve modeling of milder EEG discontinuities and to optimize the refinement post-processing step. cEEGs of 1h duration were selected exactly one hour after the beginning of the recording. We did not exclude EEG segments due to the presence of artifacts or epileptic seizures (n=18). The expressed EEG background patterns in this group included mild, moderate and severe abnormalities.

Dataset DC consists of eight neonates with predominantly mild and moderate EEG background abnormalities and was used for the validation of the overall system. We used this selection of data for the validation because it is most challenging to accurately detect mild and moderate EEG discontinuities (3s<dIBI<10-15s). From each neonate, 30 minutes of EEG was randomly

selected for the analysis.

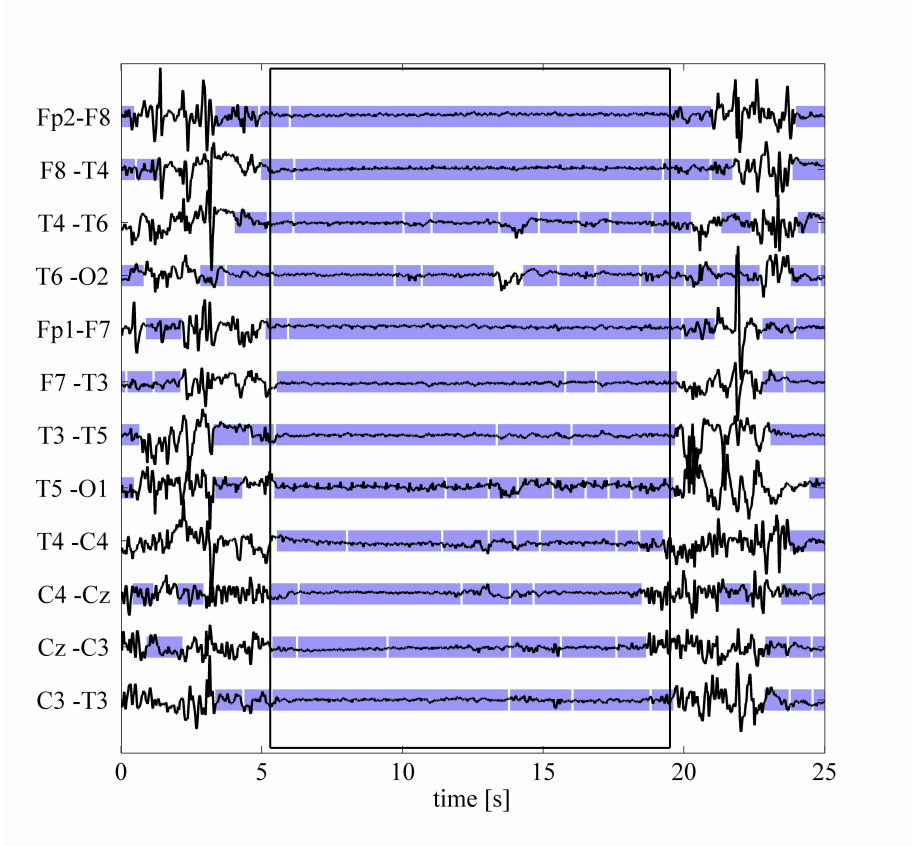

Figure 4.1: Classical burst suppression pattern detected in the early stage of the EEG recording.

4.2.2 Exploratory definition of dynamic interburst interval

In this study, our goal is to develop a system for long-term HIE monitoring. Typically, background activity in HIE is characterized by both classical BS-IBI patterns (Figure 4.1) as well as TD-IBIs ($<25\mu$V; Figure 4.2). Hence, an ideal quantification would detect both related patterns into a single parameter. The first burst-suppression-burst complex is commonly encountered during the initial phase of asphyxia (severe background EEG abnormalities). The second one commonly emerges from classical IBIs after 12-48 hours of monitoring in

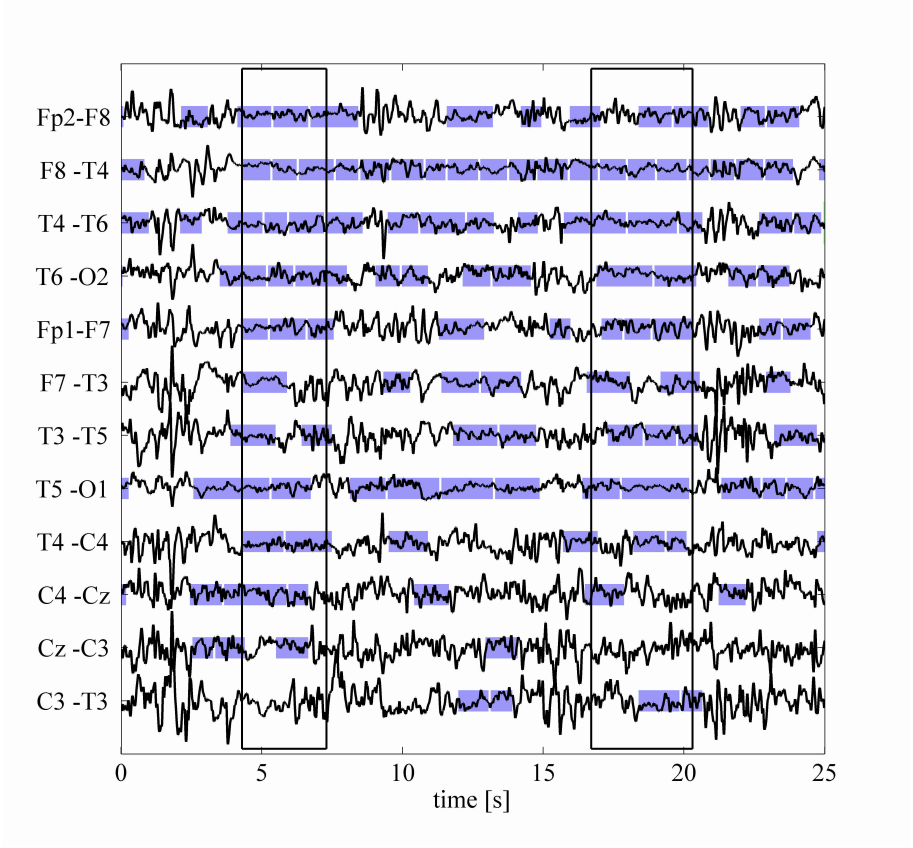

Figure 4.2: Detected tracé discontinue patterns with higher interburst amplitudes that evolved over 24h from patterns shown in Figure 4.1.

patients showing recovery (mild and moderate background EEG abnormalities). The newly defined parameter, dynamic interburst interval, captures changes from BS to TD states in the case of recovery and opposite changes in the case of deterioration of infant's condition. The novelty in this study is that we will use measures of not only duration (as traditionally done), but also a measure of dIBI amplitude to characterize EEG background. Therefore, the assessment of amplitude need to be calculated within definite dIBI detections which are not affected by artifacts in order to to provide a trustworthy measure.

4.2.3 Automated detection of dIBIs

The main goal of the segmentation step is to distinguish and separate locally suppressed EEG periods from burst periods. First, the EEG signal is segmented using an adaptive segmentation algorithm that has been applied for sleep analysis in newborns ([70], [97]). The algorithm segments the EEG using two fixed-length concatenated sliding windows (256 samples or 1s long) (Figure 4.3).

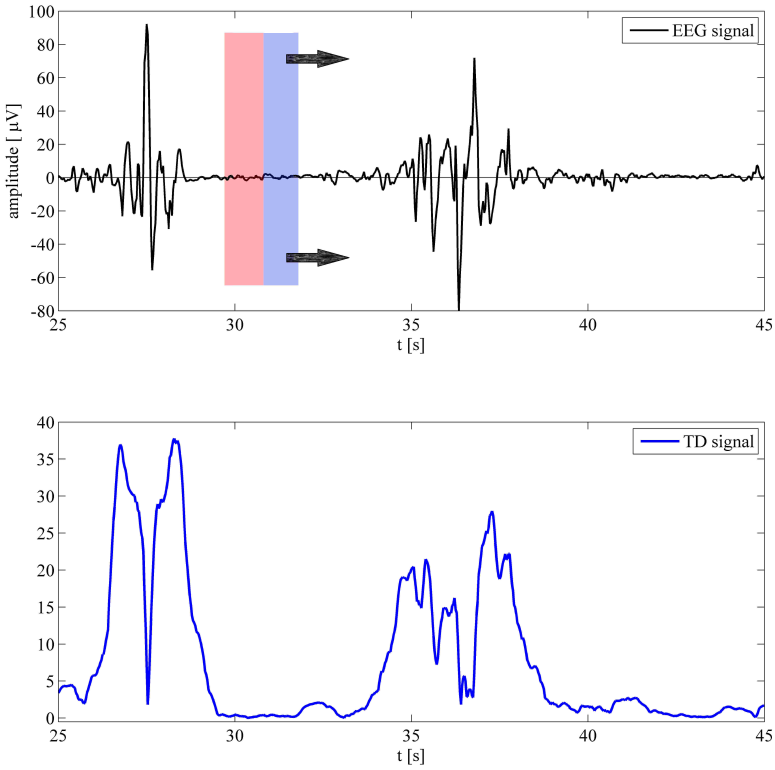

Figure 4.3: In the upper trace the EEG signal is shown. Two concatenated sliding windows (red and blue, 256 samples or 1s long each) are moved along the EEG signal incrementally for one sample. For every sample point amplitude and frequency content inside the windows are compared. This results into the signal, Total Difference (TD), shown in the lower trace, which is used for the segmentation. Local maxima of this signal determine the changes in EEG signal and are used to locate segments' boundaries.

The windows are moved along the EEG signal and values related to amplitude (Aw) and frequency content (Fw) are calculated within each window ([70], [97]):

$$Aw = \frac{1}{Nw} \sum_{i=1}^{Nw} |x_i|$$

$$Fw = \frac{1}{Nw} \sum_{i=2}^{Nw} |x_i - x_{i-1}|$$

Here, Nw represents the number of EEG samples within the sliding windows (Nw=256 samples). Accordingly, A_{wdiff} and F_{wdiff} are defined as the absolute differences of Aw and Fw between the two concatenated windows. Accordingly, a signal, called Total Difference (TD), is calculated, and thresholded with a value 1:

$$TD = |A_{w1} - A_{w2}| + |F_{w1} - F_{w2}| = A_{wdiff} + F_{wdiff}$$

$$TD = \begin{cases} TD-1, if TD-1>0 \\ 0, otherwise \end{cases}$$

Next, we smoothed the TD signal using a moving-average filter (of order 64 that corresponds to 0.25s). In this way, local maxima of TD signal that do not reflect valid change in EEG stationarity are excluded. Next, local maxima are detected in the TD signal resulting in segment boundaries (Figure 4.4). Finally, whenever local maxima are less than 0.75s apart, only the largest one is retained. This step ensures that the lengths of the EEG segments are sufficiently long and, therefore, more suitable for the further detection of globally suppressed periods.

4.2.4 Classification of EEG segments into the low amplitude class

After the segmentation step, EEG segments are classified into the low amplitude class (L) if the segment's amplitude is $<10\mu$V. In addition, in case that the segment's amplitude exceeds the threshold of $\pm 10\mu$V, we calculate the 'area under' the signal and above the threshold ($\pm 10\mu$V). This is illustrated in Figure 4.5, where the corresponding area fragments are coloured in red. We define a new parameter, that we call 'area amp 10'. If the following relation is satisfied,

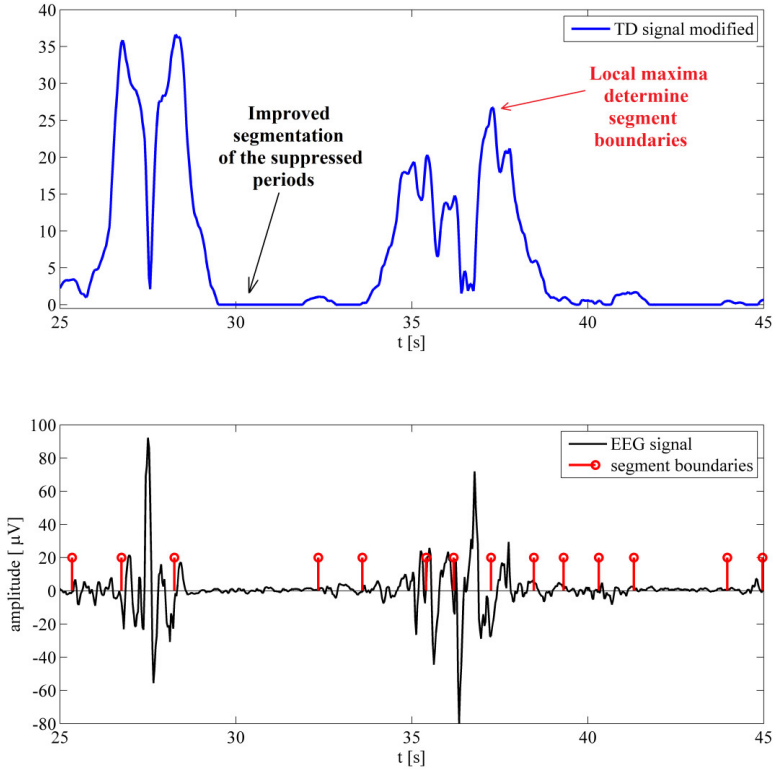

Figure 4.4: In the upper trace, signal Total Difference (TD) is smoothed with a moving average filter (of order 64 that corresponds to 0.25s) to enhance the segmentation of suppressed epochs. In addition, the TD signal is thresholded with a value 1, thereby favoring the creation of prolonged low amplitude segments. In addition, we limited the duration of segments to a minimal value of 0.75s. In the lower trace, segment boundaries are marked for the EEG signal.

'area amp 10'<50, the segment will be regarded as a low amplitude class (L) segment and in Figure 4.5 all low amplitude segments (L) are coloured in blue. Parameter, 'area amp 10' enhances more robust classification in case of very sharp, transient artifacts frequently encountered in the EEG.

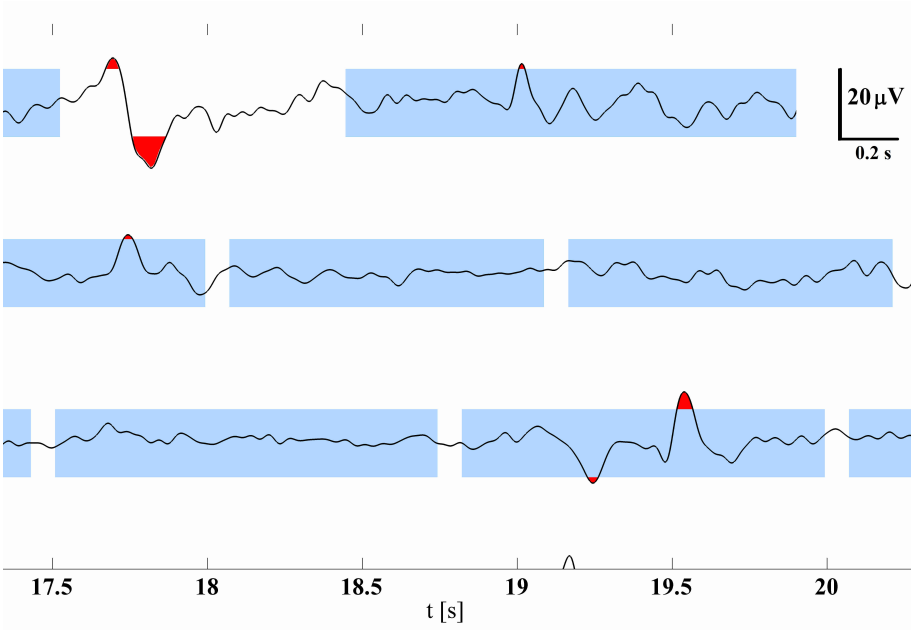

Figure 4.5: The EEG signal is segmented and low amplitude class (L) segments are coloured in blue. Red 'areas' illustrate parameter 'area amp 10'. This parameter represents the total area of the signal that exceeds the threshold values at $\pm 10\mu$V. In addition, the segment, which is not coloured in blue, has 'area amp 10' higher than 50, and it is not a low amplitude segment (L).

4.2.5 Detection of dIBI candidates

Up to now, EEG channels were processed separately. In this last step, we merge the information present in different EEG channels as follows. After the segmentation/classification step, we monitor the spatial distribution of low amplitude segments (L) across EEG channels. To achieve this, at a particular time point, we sum the number of EEG channels that express low amplitude segments (L). This results into a new signal, called Low amplitude Temporal Profile (LTP), which expresses values from zero up to a total number of EEG channels. For example, in Figure 4.6, during the last 4 seconds, low amplitude

segments are present in all 20 EEG channels (LTP=20 in Figure 4.7). Finally, we define a dIBI candidate whenever the LTP signal values exceed half of the total number of EEG channels for more than 3 seconds. These calculations represent the algorithm, which is designed to processes EEG signal with both 20 and 12 montage EEG channels used in this study. The execution of the algorithm is illustrated in Figure 4.6. First, the EEG signal is segmented and low amplitude segments (L) are coloured in blue. In Figure 4.7, the LTP signal is thresholded at the value 11. Consequently, in Figure 4.6, two dIBIs are detected and marked with black rectangles.

Finally, all segments of the algorithm are combined and illustrated in Figure 4.8.

4.2.6 Improving reliability of monitoring background EEG dynamics

Our automated approach is developed to first detect attenuated periods of burst-suppression-burst complexes (which we refer to as dIBI candidates). Subsequently, we suggest several engineering features for each dIBI candidate that allow us to discriminate between definite dIBIs and artifacts/seizures (misclassified - see Figures 4.10 and 4.11). This post-processing of dIBI candidates is crucial for reliable background quantification. For instance, it may happen, that EEG is both highly variable and attenuated and that visual interpretation of IBI duration is quite challenging. In such cases (see Figure 4.9), we say that the EEG is ambiguous. Note that in such examples it is better to exclude such patterns as they do not express clearly distinguishable burst-suppression-burst complex. Without the refinement step, falsely prolonged detections may appear and jeopardize the automated diagnostic grading of the severity of encephalopathy (Figure 4.9). This is commonly encountered in cases when the EEG is evolving from tracé discontinue patterns to normal (continuous) background EEG and a system can falsely classify a recovering neonate as being very sick. In order to decide whether a dIBI candidate should be included into further statistics or not, we will train machine learning classifiers for this task.

The algorithm uses machine-learning techniques to distinguish definite and misclassified dIBI detections. For every detected dIBI candidate, a set of parameters is calculated that allow to quantify dIBI detection certainty. Thirteen parameters are implemented as a heuristic translation of visual analysis done by the experienced clinical neurophysiologist (PJC) while assessing whether dIBI candidates are definite dIBIs or dubious (misclassified) dIBIs. These parameters quantify in a mathematical way the level of dIBI amplitude, the number of EEG channels that show suppression, the largest duration of suppression along

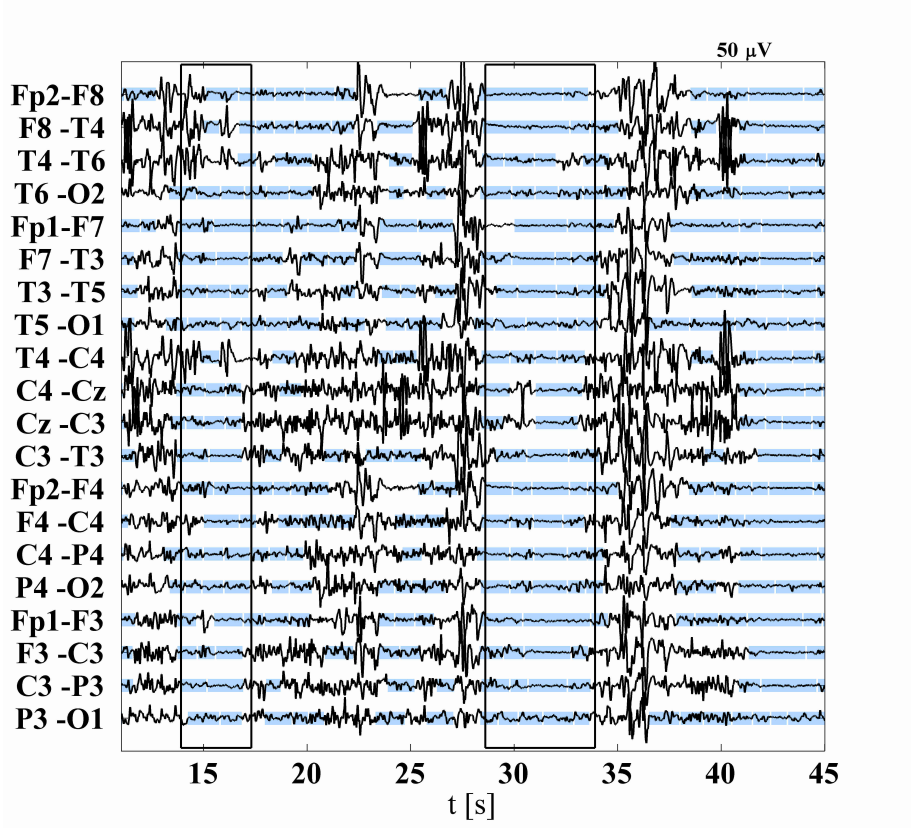

Figure 4.6: First, the EEG signal is adaptively segmented. Next, segments are classified into the low amplitude class (blue). Automatically detected dIBI candidates with the algorithm A are marked with black rectangles. The first detected dIBI cannot be regarded as a definite dIBI because of its ambiguous morphology. On the other hand, the second detected dIBI would be visually marked as definite by the majority of EEG readers.

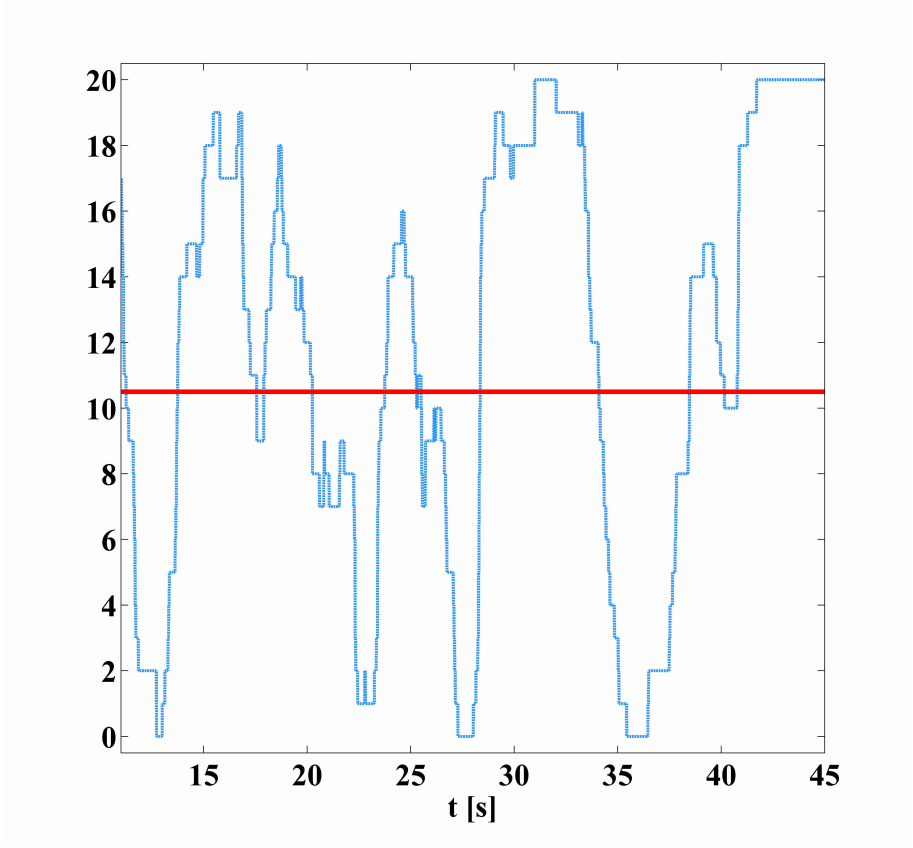

Figure 4.7: Low amplitude temporal profile (LTP) signal is created for the EEG signal in Figure 4.6. In this example, LTP signal is thresholded at the value 11 (=20 channels/2 +1). The time interval when this signal exceeds the threshold determines the duration of dIBI. Intervals above the threshold and shorter than 3 seconds are not considered as dIBI detections.

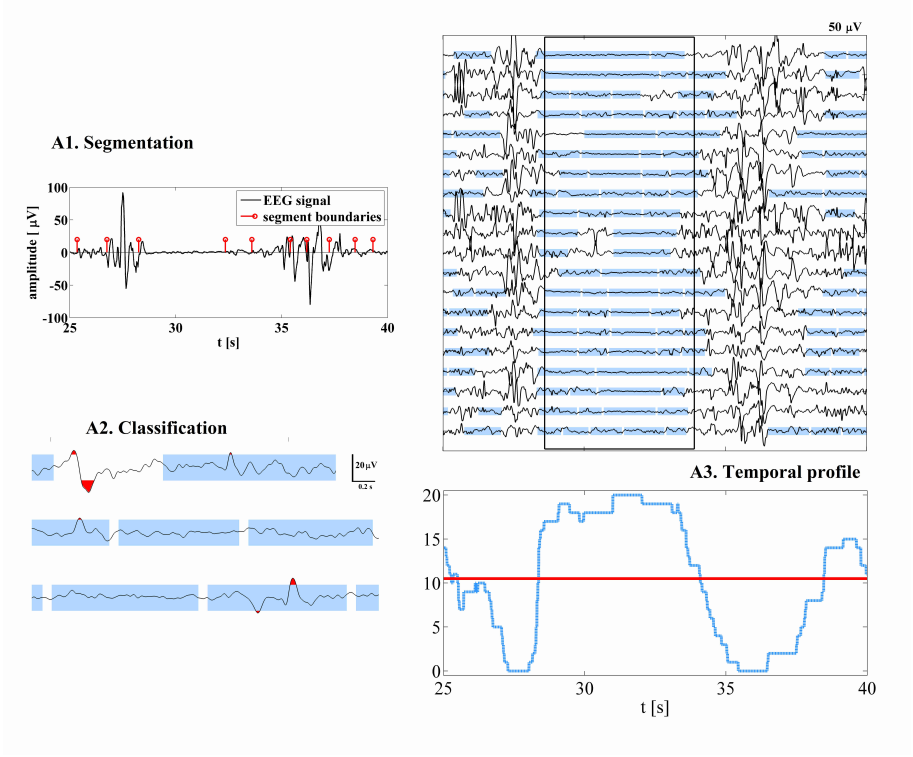

Figure 4.8: Detection of dIBI candidate. As previously described, EEG signal is first segmented (A1) and segments are classified into the low amplitude class (A2). The Low amplitude Temporal Profile (LTP) signal is calculated and used to detect dIBIs (A3).

single channel and the presence (existence) of borderline bursts for a detected suppressed period.

In Figure 4.13 for two dIBI detections (upper traces) we illustrate how one of the features, the presence of borderline bursts, is examined. For this purpose, we used Discrete Wavelet Transform, which is suitable for the detection of transitioning point (4.13 lower traces). Wavelet coefficients at the decomposition level 2-4 (4-32 Hz mainly) are expected to have higher absolute values for bursts periods as compared to suppressed periods (flat EEG or very smooth oscillations). Next, we compare 3s of the burst part versus the 3s of the suppressed interval. Majority of large values of absolute wavelet coefficients contained within the burst part would imply the accurate transitioning point. For instance, this will be the case for the definite dIBIs in the Figures 4.1 and 4.2, but less likely for

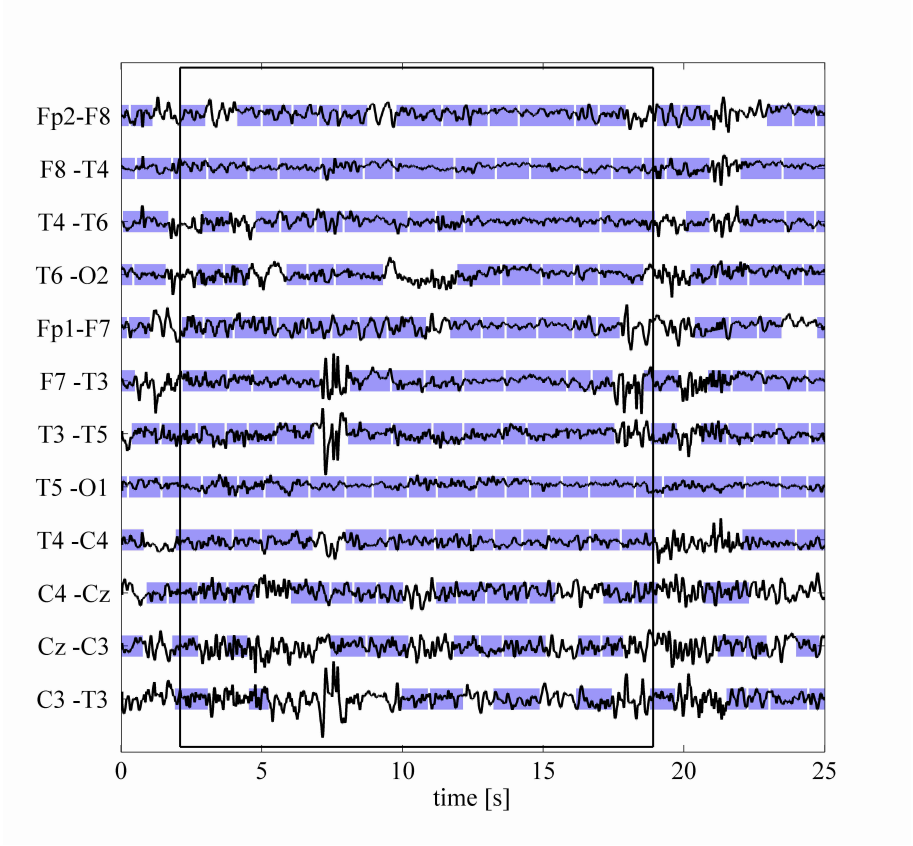

Figure 4.9: Ambiguous EEG pattern occurring close in time as the patterns in Figure 4.2. Note that it is better to exclude this detection as it does not express clearly distinguishable burst-suppression-burst complex.

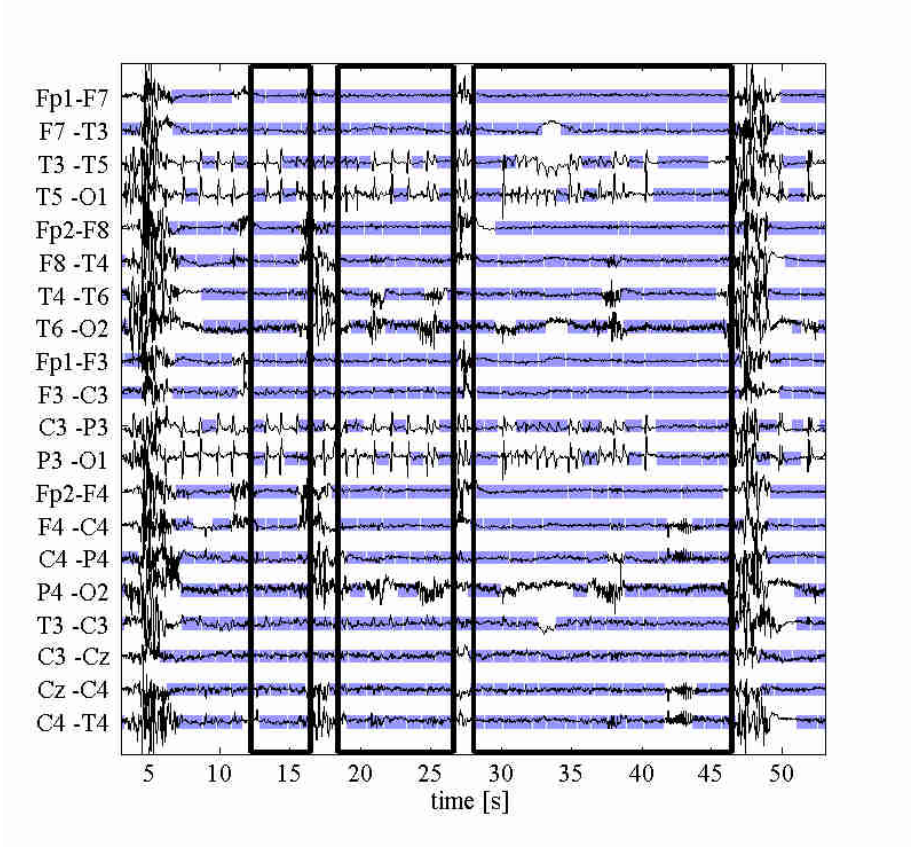

Figure 4.10: Examples of false positive detections that are produced by the epileptic seizure activity.

the dubiously detected transitions in the example Figures 4.9, 4.10, 4.11 and 4.12.

Furthermore, due to encountered differences in dIBI morphology with respect to its duration, we suggest categorizing all definite dIBIs into four duration-related groups as:

We can see that shorter definite dIBIs have higher amplitude, whereas longer ones show more suppressed amplitude (Figure 4.14). This amplitude-duration interdependence enables enhanced modelling of EEG discontinuity.

Next, the parameters that quantify dIBI candidates are used as input feature vectors into Least Squares Support Vector Machine (LS-SVM) classifiers [118].

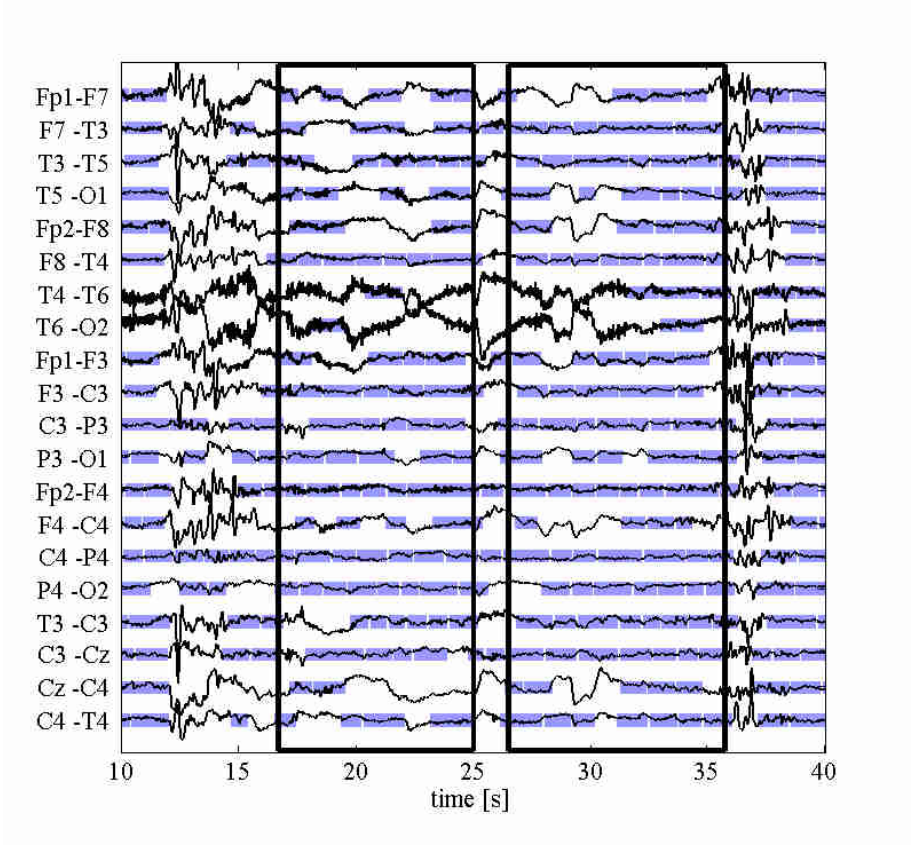

Figure 4.11: Artifact interrupts the suppressed interval, thereby falsely shortening dIBI duration and amplitude assessment. Instead of one longer, two shorter dIBI candidates are detected.

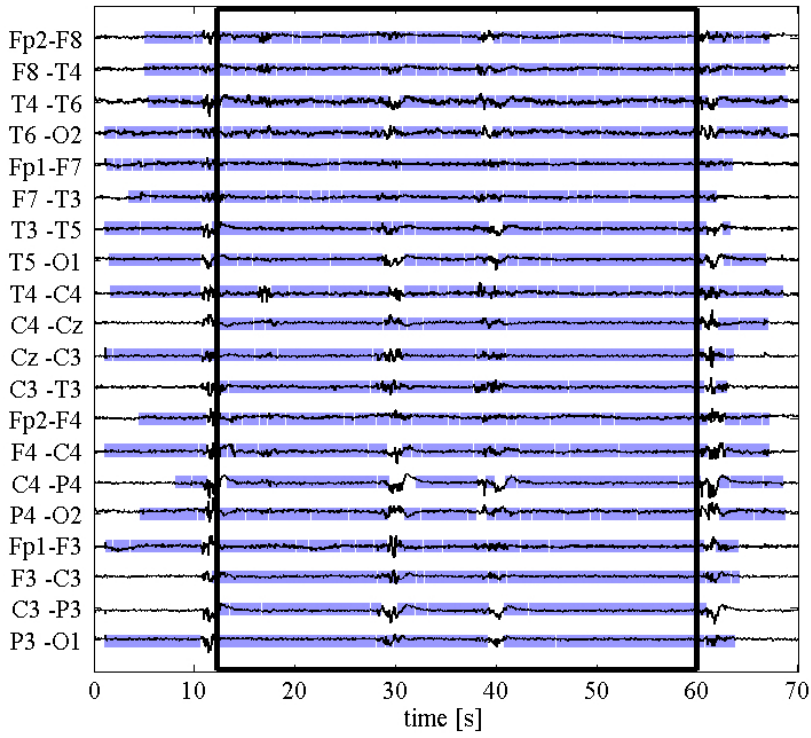

Figure 4.12: Bursts with very low amplitudes ('peak to peak' $< 20\mu$V) are missed by the detection algorithm, producing falsely prolonged dIBI detection.

Initially, we optimized only one LS-SVM classifier. However, shorter dIBIs with higher interburst amplitudes were more challenging for classification than longer dIBIs (data not shown). Therefore, four LS-SVM classifiers are used to enhance the classification accuracy and to adjust the algorithm to the dynamic changes/evolution of EEG discontinuity (TD-IBIs are shorter with higher amplitude compared to BS-IBIs). The state flow of the complete algorithm is illustrated in Figure 4.15.

The objective of the classifiers is to estimate whether the newly detected dIBI is definite - '1' or misclassified - '0'. To optimize classifiers, four mutually exclusive training datasets were created depending on dIBI duration by randomly selecting 80% of dIBIs. The remaining 20% of dIBIs from each group were used to test the corresponding LS-SVM classifiers. The LS-SVMlab $v1.8$ toolbox

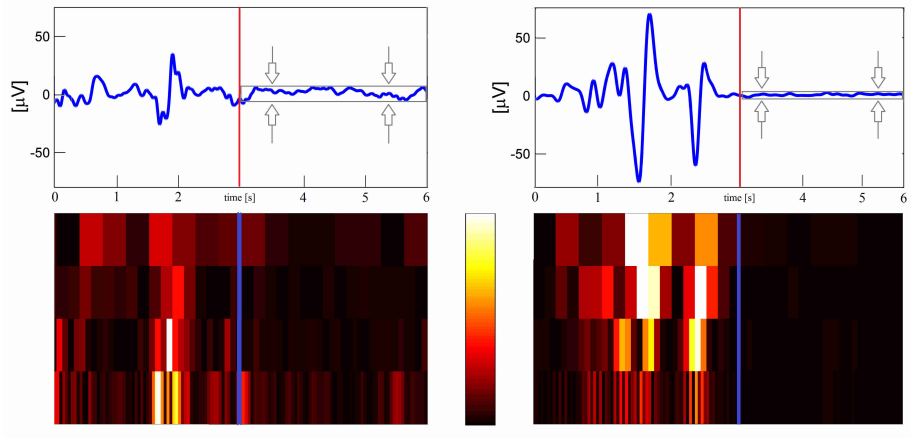

Figure 4.13: Two transitioning points are illustrated for milder EEG discontinuity (dIBI<10s; left) and for severe EEG discontinuity (dIBI>10s; right). Note that for shorter dIBI amplitude of the suppressed part shows more variability and the transitioning point is more challenging to be validated. On the other hand, longer dIBI (classical burst-suppression) shows non-responsive amplitude, thereby making recognition of definite dIBIs much easier.

$$dIBI = \begin{cases} \text{group I}, & 3\text{s} \le dIBI < 5\text{s} \\ \text{group II}, & 5\text{s} \le dIBI < 10s \\ \text{group III}, & 10\text{s} \le dIBI < 20s \\ \text{group IV}, & 20\text{s} \le dIBI\,(< 60) \end{cases}$$

implementation was used in this study [100]. In all cases, a Gaussian kernel was applied. Tuning of the parameters was conducted in two steps. First, coupled simulated annealing is performed [133] and afterwards, a second optimization procedure (simplex) was applied to perform a fine-tuning step. The five-fold cross-validation misclassification error was used as an optimization criterion.

4.2.7 Framework for the reliability parameterization of dIBI

To distinguish definite dIBI detections according to the detection certainty, we parameterize the 'burst-suppression-burst' complex. These parameters are developed to characterize classification process done by a clinical neurophysiologist to confirm definite dIBIs. Some of the parameters are optimized to confirm definite dIBIs, whereas others are adjusted to exclude

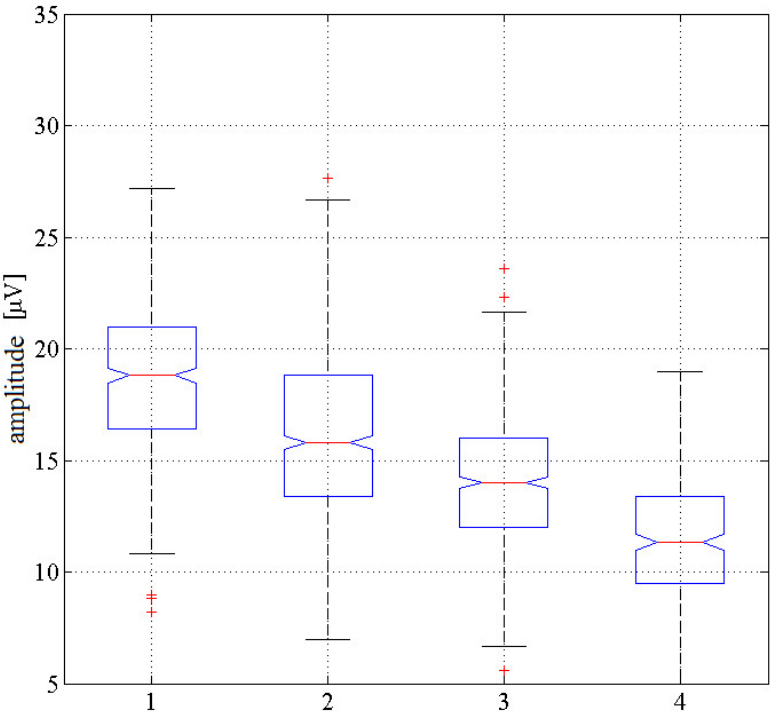

Figure 4.14: Amplitude distribution of definite dIBIs is depicted for each dIBI group. Groups are defined according to dIBI duration: Group I: 3s≤dIBI<5s; Group II: 5s≤dIBI<10s; Group III: 10s≤dIBI<20s; Group IV: 20≤dIBI (<40s). For these dIBI duration groups, we performed a one-way ANOVA and found a significant difference in the mean amplitude distribution applying Bonferroni correction (F-statistic=337.8, $p<0.001$).

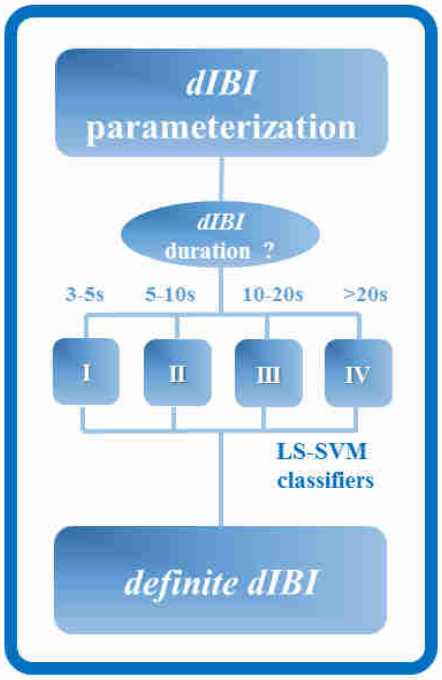

Figure 4.15: Flow chart of the algorithm for automated detection of definite dynamic interburst intervals. The detected dIBI candidate is parameterized and obtained values are used as classifiers' input feature vectors. To optimally account for diverse duration-related dIBI morphological differences, four different LS-SVM classifiers are independently optimized. They make a decision whether a dIBI candidate is definite dIBI and whether it should be used for EEG quantification. On the other hand, uncertain detections, will be excluded from further EEG analysis as misclassified dIBIs.

misclassified dIBI detections. We provide a detailed description of the reliability parameters and illustrate how they are calculated within the burst-suppression-burst complex in Figure 4.16.

The following parameters are used to parameterize every detected dIBI candidate:

1. Suppression (1 parameter): is defined as a single median value of the rectified EEG signal within the suppressed dIBI period across all EEG channels.

2. Flatness (4 parameters): is calculated for each EEG channel independently within the suppressed dIBI period. We adjusted two horizontal border lines, so that they enclose 95% of all EEG samples within the dIBI. The minimum possible distance between these two horizontal lines represents the parameter flatness (Figure 4.17). Next, the flatness is calculated for each EEG channel and the obtained values are sorted into ascending order. Subsequently, these values are split into four equal groups. For each group, a median value is calculated, resulting into four parameters that estimate the suppression level of the dIBI.

3. Longest (4 parameters): within the dIBI, for each EEG channel, we calculate the longest interval of the low amplitude segment (L) classes that are not interrupted by a higher amplitude activity (Figure 4.16). If several consecutive low amplitude segments are present next to each other we will merge them into a single one. This parameter ranges from 0% (no low amplitude segments) to 100% (only low amplitude segments). It is an important descriptor for decisions whether the dIBI suppressed period is interrupted, especially in cases when higher amplitude EEG activity is distributed randomly across suppressed period. Similarly to the parameter flatness, we sort all values calculated for each channel in ascending order and calculate 4 parameters as median value of the corresponding quartile groups.

4. Number of channels (1 parameter): For the presumed duration of the dIBI (suppressed part), we calculate the mean value of the Low amplitude Temporal Profile (LTP) signal. Next, this value (number of EEG channels expressing LTP signal) is divided with the total number of (bipolar montage) EEG channels. As dIBI was thresholded at a value of one more than half the number of total EEG channels, this parameter will be in the range from 55% to 100% (0.55 - 1).

5. Transitioning (2 parameters): This parameter examines the presence of bursts and how distinguishable burst/suppression segments are. Six

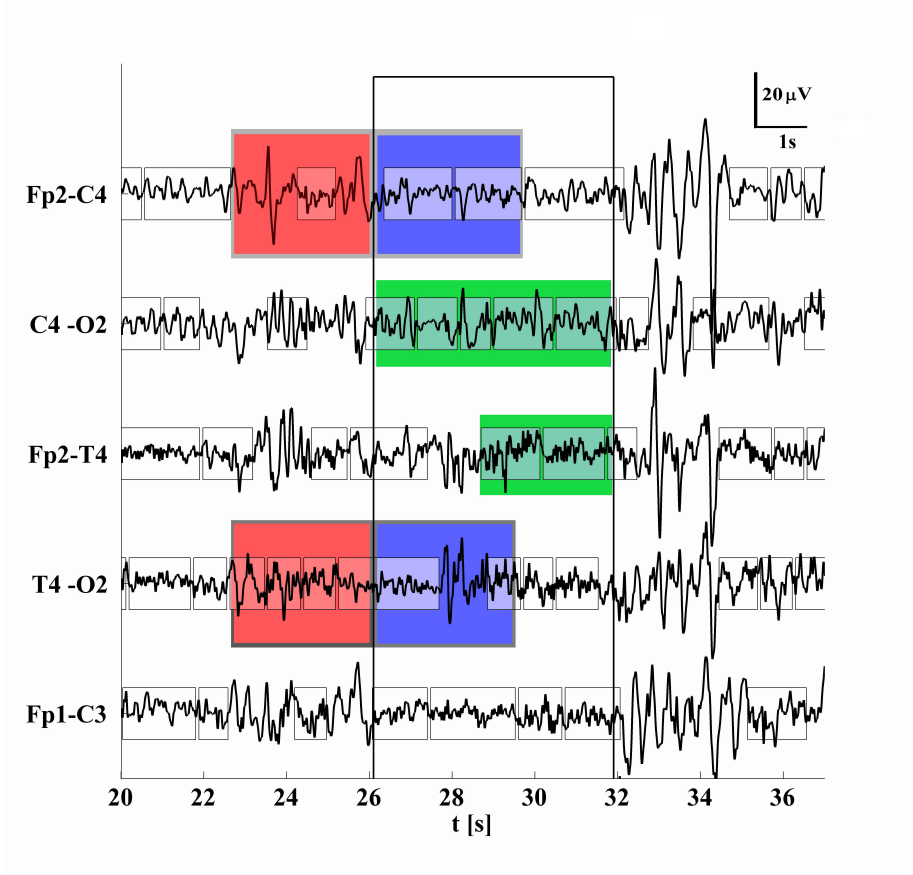

Figure 4.16: A detected dIBI candidate is marked with large black rectangle, whereas low amplitude segments (L) are marked with smaller ones. The reliability parameter transitioning examines the dIBI segmentation accuracy and the certainty of the complete complex burst-suppression-burst. For each channel, 3s of the burst part (red) and 3s of the suppressed part (blue) are compared. Here, only two such examples are illustrated with red/blue rectangles. In addition, an illustration of the parameter longest is depicted in green. It calculates the longest possible duration of the consecutive segments with low amplitude (L) within dIBI. In channel C4-O2, this value is maximal (=1), whereas for the channel Fp2-T4 this value is 0.5 (50% of the duration of dIBI candidate). Parameter longest is useful to exclude ambiguous EEG discontinuity and other uncertain detections.

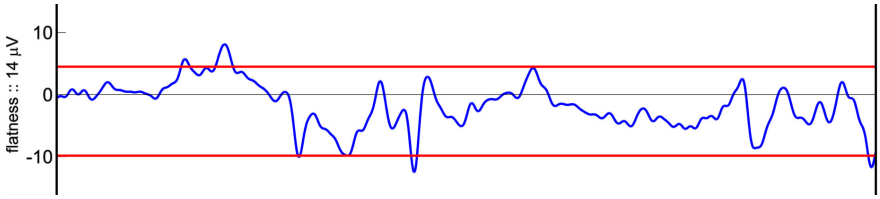

Figure 4.17: Illustration of how the parameter flatness is calculated within the suppressed dIBI part (4s long) for a single channel. Two horizontal red lines are adaptively adjusted until they meet two criteria. First, they need to enclose 95% of the signal samples. Second, the calculated distance between them has to be minimal. In this example the calculated distance is 14μV.

seconds of the EEG signal are selected with a center exactly at the detected burst/suppression transition point. In Figure 4.16, burst parts (red) and suppressed parts (blue) are marked. Next, this signal is decomposed using the Discrete Wavelet Transform (DWT) [40]. We applied Daubechies 4 mother wavelet and 5 levels of decompositions. In this way, the burst part (3s) is characterized with wavelet coefficients that express higher absolute values, whereas the suppressed part (3s) is characterized with wavelet coefficients close to zero (Figure 4.18, middle plot). To further enhance the differences between burst and suppression segments, we sort absolute values of wavelet coefficients into ascending order. Then, iteratively, starting from the smallest values, we set small wavelet coefficient values to zero. We repeat this process while keeping more than 90% of the original signal power within the remaining wavelet coefficients (Figure 4.18, bottom plot). In this way, the approximated signal (in Figure 4.18, upper plot - marked in black) preserves the active burst period, whereas the majority of wavelet coefficients within the suppressed period are set to zero. The percentage of power retained by wavelet coefficients within the burst part compared to the total power of all wavelet coefficients, after the sparse approximation, determines the transitioning parameter. Furthermore, this parameter is averaged across all EEG channels. Thus, if the burst/suppression transition represents a clear cut-off, the value of transitioning parameter is expected to be approximately 90-100%. However, if this value is around 50-65% it is doubtful whether a distinguishable burst/suppression alternation exists. Furthermore, as both transitions, at the beginning and at the end of the dIBI, are important, we calculate for every dIBI 2 transitioning parameters.

6. NLEO local maxima: In some cases, bursts can occur synchronously with relatively low amplitude (<10μV) and can be missed by the processing

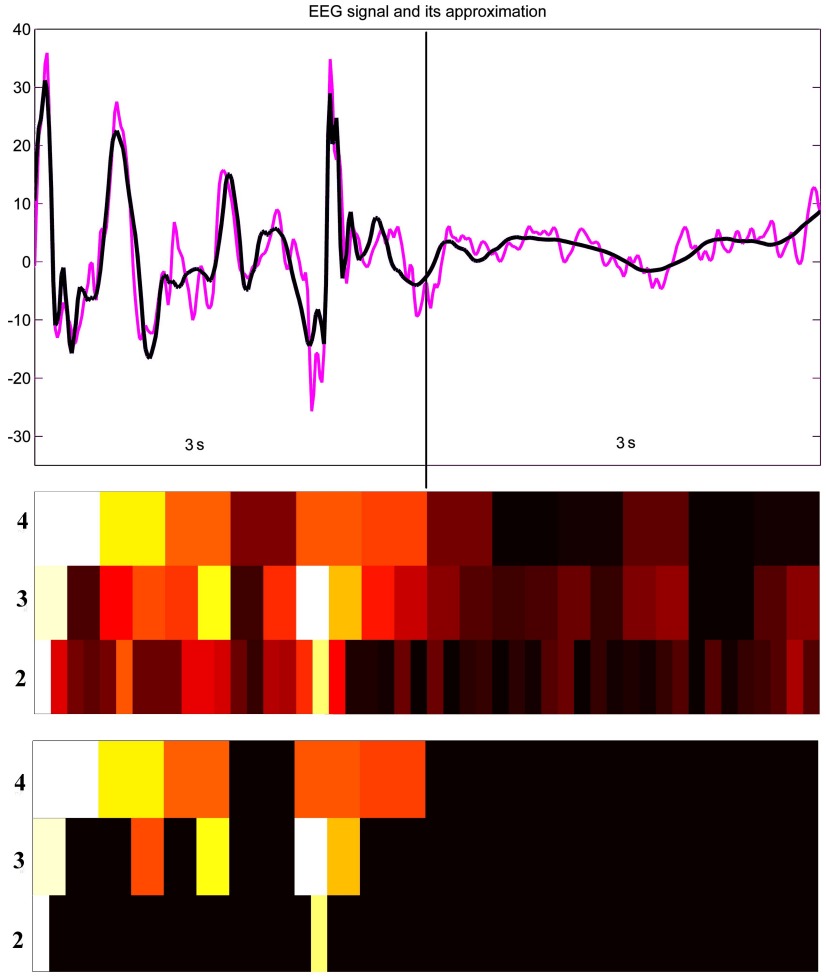

Figure 4.18: Transitioning parameter is illustrated for detected EEG discontinuity. The first 3s of the signal represents a burst period, whereas the last 3s corresponds to the suppressed segment (upper plot: purple-original EEG signal, black - approximated EEG signal). In two lower figures, wavelet coefficients (levels from 2 to 4 are displayed as they carry the largest portion of signal power) are depicted in black for zero values and in white and yellow for larger absolute coefficient values (middle plot). After sparse approximation, large wavelet coefficients would be retained mainly within the abrupt burst activity (bottom plot). Therefore, in this example, the parameter transitioning (value close to 1) would imply that vast majority of abrupt activity is localized within the left (burst) part of the signal, whereas the right part (suppression) does not contain any significant component of EEG activity with higher frequency. Note that high energy coefficients (colored in white) capture the 'high activity burst' behavior as compared to the suppressed periods where such activity is lacking. Therefore, the calculation of transitioning parameter efficiently characterizes the presence of distinguishable burst/suppression alternations.

algorithm. Another scenario is that a burst is present on less than 50% of EEG channels. This can produce a false merging of two shorter dIBIs into a longer one. To examine the presence of potentially missed bursts, we apply a Nonlinear Energy Operator (NLEO) as a very effective method for detection of bursts and dynamic EEG activity (Palmu et al., 2010). NLEO is calculated using the following formula:

$$\psi(x[n]) = x^2[n] - x[n-1] \cdot x[n+1]$$

We calculate an average NLEO across all EEG channels and use maximal value of this signal as the final parameter.

4.3 Results

4.3.1 Dataset DA

The initial detection algorithm, including adaptive segmentation, amplitude based classification and dIBI detection, was optimized using a training dataset DA. In total, 157h of cEEG from seven neonates was processed and analyzed. The 18802 detected dIBIs were visually checked for precise burst/suppression transitioning in each channel and for accurate detection of dIBI duration. This meticulous evaluation of EEG discontinuity patterns enabled us to optimally set and fix the parameters of the algorithm for the detection of dIBI candidates. We do not present statistics for this dataset as it was used for the tuning of the algorithm. Nevertheless, although we improved our initial version of the algorithm ([80]; average rate of misclassified dIBIs was 30-50%) the false positive detection rate was still substantial.

4.3.2 Dataset DB

A test dataset DB is processed with the algorithm to further study definite, correctly detected dIBIs. Using the initial algorithm, 4408 dIBI candidates were detected within 38h of cEEG. After visual checking of these detections, 2273 dIBIs were marked as definite dIBIs, whereas 2135 dIBIs were excluded from further analysis as misclassified (false positive and dubious cases).

Subsequently, LS-SVM classifiers were trained to optimally match the visual classification done by the clinical neurophysiologist. The total number of dIBIs per duration group was: 1239 (3s≤dIBI<5s), 1382 (5s≤dIBI<10s), 881 (10s≤dIBI<20s) and 906 (dIBI≥20s). The performance of the classifiers is

illustrated using Receiver Operating Characteristic (ROC) curves (Figures 4.19, 4.20, 4.21 and 4.22). High Area Under the ROC Curve values (AUC) are achieved for all four classifiers: 0.91, 0.94, 0.94 and 0.97, implying that high discrimination between definite and misclassified dIBIs have been achieved. The highest AUC was achieved for the class with longest dIBIs (BS-IBI), which implies that these dIBIs have a more definite (simpler) morphology.

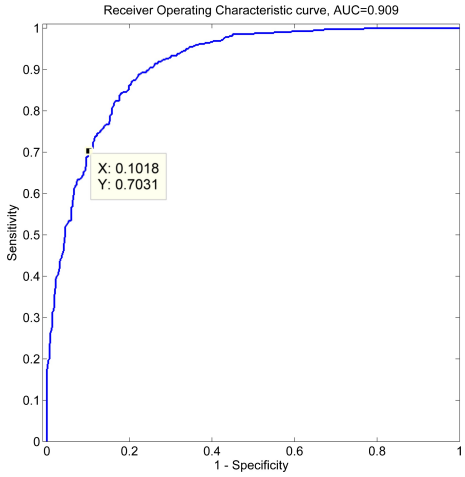

Figure 4.19: ROC curves presenting the performance of classifier for group I ($3s \leq dIBI < 5s$).

Next, it is important to show how four classifiers would work in the clinical practice. The working points of the ROC curves are selected using the 'rate of misclassification' error criteria (see Figures 4.19, 4.20, 4.21 and 4.22). We show the percentage of true positive and false positive detections after the refinement step (Figure 4.23). We can see that large number of definite dIBI detections will be kept after the refinement step, which is essential for further statistical analysis (e.g. median dIBI; histogram). Furthermore, the false positive detection rate has decreased per dIBI duration group from (61%, 44%, 36% and 55%) to (28%, 17%, 14% and 16%) respectively.

4.3.3 Validation of the complete algorithm - Dataset DC

To illustrate how powerful the complete algorithm is, the validation results are shown on an independent validation dataset DC. First, an experienced clinical pediatric neurologist (KJ) visually marked dIBIs, allowing higher dIBI amplitude as compared to BS-IBIs and excluding all difficult to classify detections. Next,

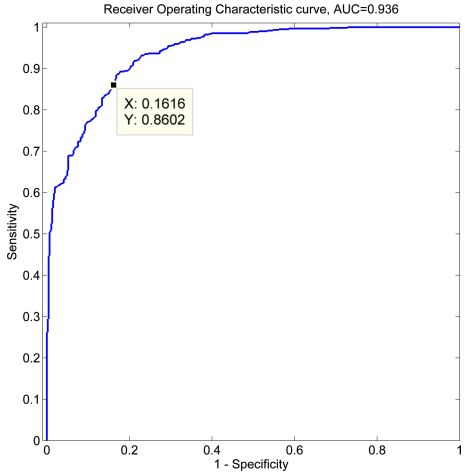

Figure 4.20: (ROC curves presenting the performance of classifier for group II (5s ≤ dIBI < 10s).

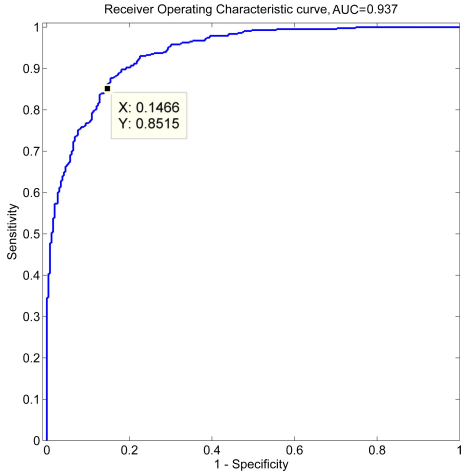

Figure 4.21: ROC curves presenting the performance of classifier for group III (10s ≤ dIBI < 20s)

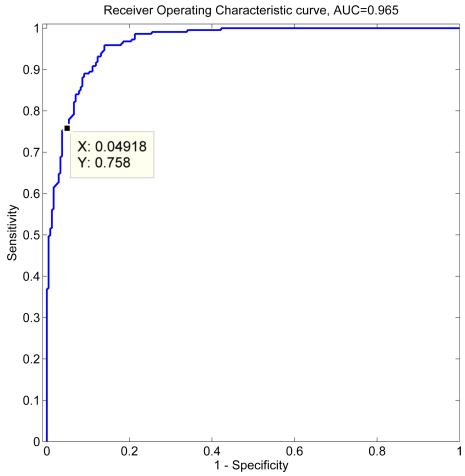

Figure 4.22: ROC curves presenting the performance of classifier for group IV (20s ≤ dIBI).

the EEGs were processed with the automated algorithm and the results were compared. Figure 4.24 illustrates that after detection of dIBI candidates without post-processing step, good results have been obtained, but the number of misclassifications was rather high as compared to the EEG expert. After the post-processing step, and the analysis of definite dIBIs, the true positive rate achieved very high values: 98%, 97%, 88% and 95%. In addition, the false positive rate remained very low, thereby demonstrating high reliability of the algorithm.

4.3.4 Benchmarking: dIBI duration and amplitude vs. expert visual background EEG scoring

The main objective of our automated system is to apply it as an assistive decision-support system to assess the severity of EEG background discontinuity. Here, we show the results of fully automated processing of cEEG epochs within dataset DB (38 neonates). From each neonate, we equidistantly selected four 1h cEEG segments across the whole EEG recording. An experienced clinical neurophysiologist (PJC) visually assessed background EEG of these neonates. Background EEG abnormalities within 1h duration were classified into mild, moderate and severe classes. The applied grading system was adapted from the one proposed by Murray et al. [90] resulting in: a) mild/normal - approximately dIBIs<5s; poorly organized sleep wake cycle b) moderate - approximately 5s≤

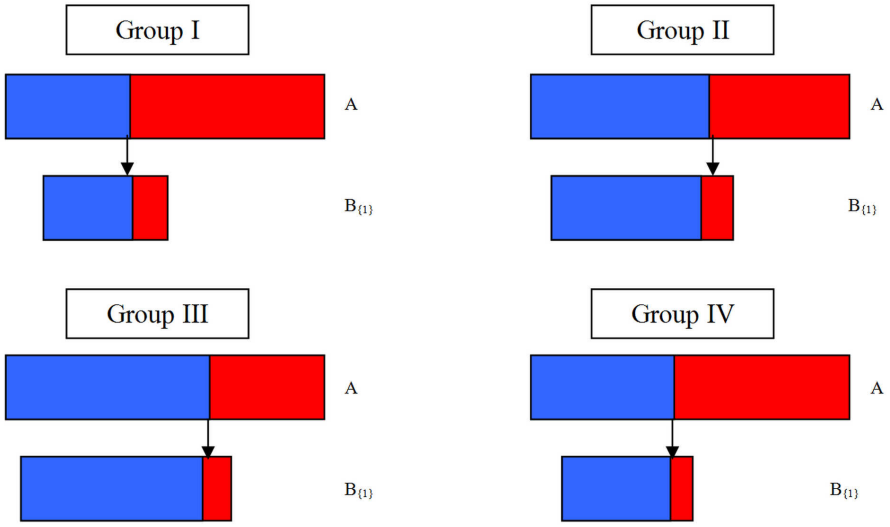

Figure 4.23: For every duration-related dIBI group, the first bar (A) represents the distribution (ratio) of definite dIBIs (blue) and misclassified ones (red) as visually marked by an experienced clinical neurophysiologist (PJC). After the refinement step, the classifier selects a subset of dIBIs. Consequently, the size of the second bar (B_1) is represented by proportionally shrinking the size of the bar (A). Here, dIBIs that are retained in the reliable subset (B_1) and previously marked as definite are shown in blue. The red bar segments corresponds to misclassified detections (false positives).

dIBIs<10s c) severe abnormality - dIBIs>10-20s, characterized by prolonged and marked suppressions. The EEG from some neonates cannot be described with only one class due to evolution of the background activity. For instance, the background EEG abnormalities of a neonate with recovering HIE may be graded as: severe (21-22h Post Partum-PP), severe (27-28h PP), moderate (33-34h PP) and mild (39-40h PP). At this stage, during the development phase of the algorithm, we have restricted ourselves to median dIBI duration and amplitude and do not aim to perform comprehensive automatic grading of the background EEG activity. For the latter, many other parameters need to be taken into account such as frequency content, morphology and variability of EEG bursts, sleep-wake cycles, EEG asymmetry, asynchrony and presence of sharp waves. Within each 1h EEG segment, median duration and median amplitude of dIBIs were automatically calculated to characterize the trend of the EEG background activity. This is shown in Figure 4.25 where each data point corresponds to a 1h cEEG segment (4 data points per neonate). Introducing dIBI amplitude as

dIBI duration group	Number of detected *dIBI candidates* by algorithm A in dataset DC	Number of *definite dIBIs* marked by the visual rater in dataset DC (gold standard)	True positive rate after the refinement step with algorithm B	False positive rate after the refinement step with algorithm B
I	280	189	125 / 128 (98 %)	3 / 91 (3 %)
II	330	254	202 / 209 (97 %)	7 / 76 (9 %)
III	169	126	90 / 102 (88 %)	12 / 43 (28 %)
IV	56	32	19 / 20 (95 %)	1 / 24 (4 %)
Total	835	601	436 / 459 (95 %)	23 / 234 (10 %)

Figure 4.24: The results of automated definite dIBI detections in dataset DC as compared to the visual scoring. First, the algorithm A detected dIBI candidates (both definite and misclassified) and this is presented in the 2nd column. The number of visually scored definite dIBIs is presented in the 3rd column. After the refinement step, the algorithm B retains definite dIBIs which are compared with the visual scoring. The true positive rate (%) is presented in the 4th column, whereas the false positive rate (%) is presented in the 5th column. The results are presented for four dIBI duration groups and the total number of detections is given.

a feature, we enhanced the separation between the classes compared to the use of only duration of dIBIs. In particular, this can be observed in the separation between mild and moderate classes. Therefore, incorporating a trustworthy measure of dIBI amplitude enabled high agreement with background EEG scores as done by an experienced clinical neurophysiologist.

4.4 Discussion

The goal of the current study was to develop a reliable automated method for reliable assessment of a broad range of background EEG discontinuities in full-term asphyxiated neonates. To the best of our knowledge, this is the first study that used an automated method to study EEGs over long monitoring hours and to accurately detect milder EEG discontinuities. These patterns are predominantly encountered in neonates diagnosed with mild and moderate HIE. This sub-group of HIE neonates still represents a great challenge for clinicians aiming to standardize a visual grading system for their systematic study and to predict their neurodevelopmental outcome [129]. In this context, we defined a new, visually interpretable parameter, dynamic interburst interval (dIBI), as an extension of the classical BS-IBI concept. In general, dIBI can be seen as a burst-suppression-burst pattern with evolving activity encountered during both the suppressed and burst periods. In addition, apart from temporal information, the novelty of dIBI is that it incorporates various interburst amplitude levels.

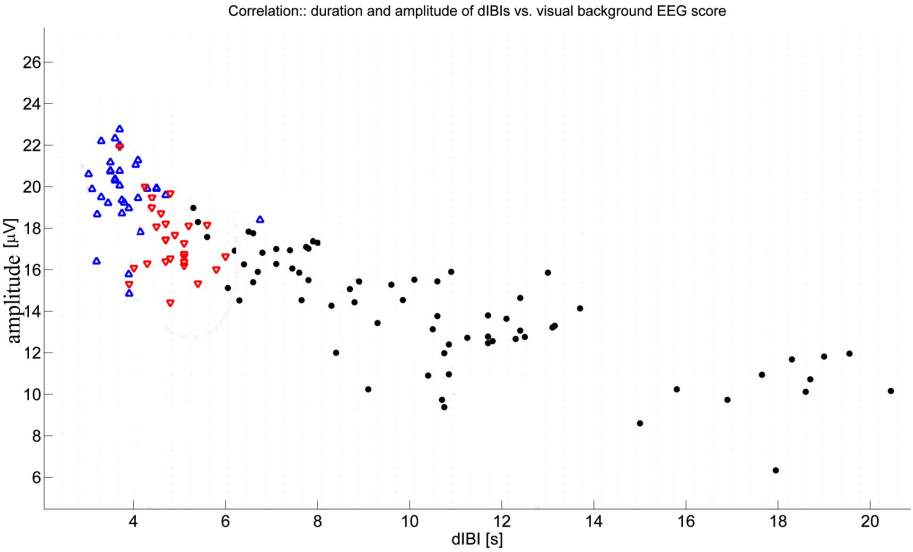

Figure 4.25: Output of the algorithm is compared with the background EEG abnormalities visually graded by an experienced clinical neurophysiologist. Median duration and amplitude of definite dIBIs detected within 1h of cEEG are plotted as a single data point (4 data points per neonate). Background EEG abnormality of the corresponding 1h epoch is scored by the clinical neurophysiologist as mild (blue), moderate (red) or severe (black).

The post-processing step, estimates diverse dIBI amplitude values, and accordingly, we optimized four LS-SVM classifiers. In this way, we improved the detection accuracy compared to the use of only one classifier. It is also noteworthy that not only the amplitude, but also the overall dIBI morphology is different depending on duration. For instance, for dIBIs<10s, the transition points of burst/suppression are milder and more gradual. In contrast, burst/suppression alternations for dIBIs>20s are much more pronounced and abrupt. Last but not least, the post-processing step enables analysis of all encountered background EEG states within neonates with HIE. Hence, manual data pre-selection by clinicians is not needed and the algorithm can be used for long-term continuous monitoring. In contrast, some of the published algorithms are developed to process and tackle only discontinuous burst-suppression EEG states ([76], [95], [67]). With our algorithm, 'discontinuous' tracé alternant pattern and continuous EEG patterns can be processed as well without affecting the algorithm's performance.

Few research groups have attempted to develop methods for automated grading

of background EEG abnormalities in full-term asphyxiated neonates. A notable contribution is the work of ([75], [76]) where a method for suppression/burst detection has been developed. As the first step, the method first detects 'burst-suppression' states and then quantifies the background EEG with an IBI detector. However, this method does not propose effective quantification of less severe discontinuities. Mild to moderate EEG discontinuities were not analyzed in their study, which is a significant limitation. Moreover, for the development of this method, the researchers included only a small number of neonates (six), expressing only prolonged BS-IBIs (>10s) [76]. In a follow-up validation study of this method [40] in 21 neonates, a highly dichotomous separation of neonates into 'good' and 'poor' outcome groups has been achieved using detected median IBI values. It is surprising that none of the neonates showed recovery and evolution of background EEG (although nine were clinically judged to have mild-moderate HIE and later had good clinical outcomes). On the other hand, our algorithm is able to ascertain a continuous and gradual transition of background EEG states as we have implemented detection of mild discontinuities as well.

Other automated detection methods have studied 'burst/suppression' patterns in premature EEG ([95], [60], [86], [67]). Compared to these, the dIBI parameter includes more complex burst-suppression-burst patterns, thereby encompassing a broader range of EEG discontinuities. In addition, the number of dIBI patterns that we analyzed is at least 10 times higher covering much more hours of EEG recordings. The aforementioned methods can be compared with our algorithm detection of dIBI candidates. They are all designed to 'threshold' either suppressed or burst EEG periods. However, these studies have not addressed and explored the adverse effects of artifacts/seizures that can falsely interrupt the suppressed periods and be erroneously detected as bursts. In addition, we aimed to identify a large set of correctly detected definite dIBIs that would be confirmed with high inter-rater agreement. As part of this strategy, uncertain and ambiguous EEG patterns would be excluded, reducing significantly the number of misclassified detections.

Due to recovery of brain injury and background EEG evolution in mild and moderate HIE, dIBIs significantly change in morphology and makes detection rather challenging. At the beginning of the recordings (<24h post partum), burst periods tend to be low in amplitude (e.g. pure theta activity <10-20μV [17]), with extremely attenuated suppressed segments. When the EEG background improves along with recovery from HIE, the amplitude of both suppressed and active burst periods would increase, whereas the duration of dIBIs would decrease. Hence, the encountered scenarios may include bursts registered at 12h post partum that are lower in amplitude than suppression segments at 48h post partum. This will result in an overlap between suppression/burst periods

at various time points that static burst/suppression detection algorithms will not be able to distinguish. For instance, quantified EEG parameters (mainly amplitude based) used for supervised learning (e.g. [76]) will be insensitive to detect such changes in EEG morphology. In contrast, dIBI candidates are detected with high sensitivity and the presence of borderline bursts is examined afterwards. Here, the algorithm compares how burst/suppression patterns are relatively distinguishable regardless of their amplitude values (see parameter 'transitioning'). Subsequently, as dIBIs become shorter with more active suppressions, a corresponding duration-related LS-SVM classifier would be applied to classify them as definite dIBIs. Approaches presented in ([76], [95], [60]) are not sensitive to the evolution of background EEG activity. On the other hand, our method is adaptable to dynamic changes in the background EEG, which is a distinct advantage.

In [68], authors proposed a method to quantify background EEG without direct assessment of EEG discontinuity. The authors showed that a combination of quantitative EEG (qEEG) features can be applied to assess background EEG abnormality as determined by experienced clinical neurophysiologists within 1h segments of EEG. The method is designed to replicate experts' grading of HIE severity, resulting in a single output value. Generally, this value represents a grade from 1 to 4 (mild, moderate, severe or isoelectric), which helps to partly replace visual EEG classification. However, this output, which uses a combination of many qEEG features, does not reveal new insights into the various characteristics of EEG discontinuity in neonatal HIE. In contrast, our automated output offers more insight than just four discrete values. Therefore, the speed of EEG improvement/deterioration can be evaluated more effectively using a dIBI amplitude-duration plot. For instance, a neonate who is recovering from severe HIE would be initially simply graded as 3 (severe) according to the approach described by Korotchikova et al. [68], whereas in dIBI amplitude-duration plot (Figure 4.25) we will be able to observe progressive dIBI duration shortening and amplitude increase. In other words, our method enables finer monitoring of speed of the HIE recovery, which is known to be a very important clinical parameter. Moreover, it is also difficult to estimate how the proposed systems [68] would tackle many hindrances like artifacts and seizures, which were manually excluded. According to the authors, the EEG datasets were preselected and represent ideal-like scenarios with consistent background EEG grades. Compared to this study, our dataset included major artifacts and electrographic seizures and used non-preselected EEG segments, representing real-life scenarios.

4.4.1 Added Clinical Value of dIBI parameter

By introducing the concept of dIBI amplitude measure we achieved better background EEG quantification compared to the classical BS-IBI. According to our analysis, BS-IBI was mainly suited for quantifying EEGs in neonates expressing severe background abnormalities and poor clinical outcome [22]. On the other hand, neonates recovering from HIE with improving background EEG lacked a suitable quantified parameter for their characterization. Here, we have shown that dIBI can accurately quantify milder background EEG discontinuities. Neonates persistently showing these milder EEG abnormalities had no thalamus-basal ganglia injuries on MRI and, subsequently, had good clinical outcomes [22]. In addition, our findings corroborate the results of previous studies that visually studied amplitude differences in discontinuous EEG patterns in full-term neonates with HIE. In [17] analysed EEG recordings within the first 24h of life and found that neonates with HIE and non-responsive EEG suppressed intervals ($<5\mu$V) died or developed severe sequelae. In contrast, infants expressing higher interburst amplitudes of 5-10μV survived without any sequelae. In another study [111], researchers analyzed suppressed EEG intervals in term neonates with HIE and their relationship with clinical outcome. In particular, they defined classical BS-IBI with the amplitude consistently $<5\mu$V (n=15 neonates) and 'modified BS-IBI' expressing higher interburst amplitude $>5\mu$V (n=8 neonates). The neonates expressing 'modified BS-IBI' showed more favourable outcome compared to the BS-IBI group. In another study [38], the authors analyzed discontinuous EEG intervals that could not be classified as classical BS-IBIs. This study included neonates with HIE during the first seven days post partum, and, therefore, their findings cannot be directly compared with ours. However, the expressed trends appear to be similar and higher interburst amplitudes implied a more favourable clinical outcome.

Amplitude of dIBI parameter

dIBI vs. classical BS-IBI.

To demonstrate the added value of the dIBI parameter, compared to the classical BS-IBI, we performed the following analysis. Neonates with HIE from the DB database were divided according to their 2-year follow-up neurological outcome data into good (n=18) and poor outcome groups (n=18). The follow-up results for two neonates were not available, so they were not included in this analysis. More details about this division are explained in the research study [22]. For these two groups, we compared interburst amplitudes of dIBI and of classical BS-IBI. Assuming that BS-IBI is defined with a static threshold, from definite dIBI detections we selected BS-IBIs if the interburst amplitude was less than 15μV. This is depicted in Figure 4.26, where data points beneath the horizontal

line would correspond to BS-IBIs.

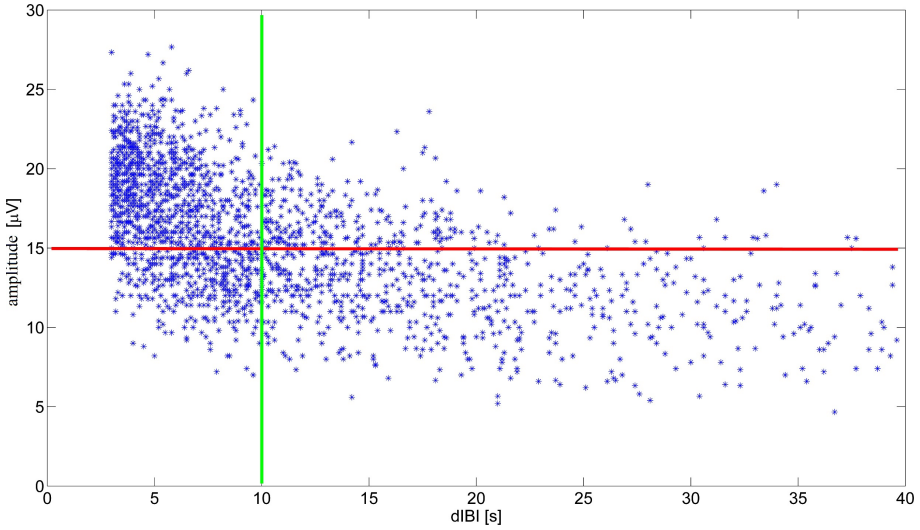

Figure 4.26: Interdependence of dIBI duration and amplitude. Data points represent 2079 definite dIBIs (<40s). There was a strong correlation between the two parameters for dIBIs (<20s): 1807 data points, Spearman ρ=-0.51, p<0.001. In contrast, correlation between the two parameters for dIBI duration from 20s to 40s was less significant: 272 data points, Spearman ρ=-0.14, p=0.02.

Here, we tested the hypothesis whether the enhanced amplitude variability incorporated within dIBI, can be used as an additional parameter to refine early prognostication of outcome. We compared interburst amplitudes for the intervals 3-5s and 5-10s as they represent difficult interval groups for the visual background EEG grading and the outcome assessment. The mean interburst amplitudes were assessed from dIBI (and BS-IBI) detections within 24h-36h post partum for each neonate. We assumed that for neonates with a good clinical outcome, amplitude recovery would most likely occur within this time interval [90]. Complete analysis was made automatically and the EEG segments were reviewed to ensure the accurate analysis.

The results of the clinical validation are presented in Figures 4.27 and 4.28. We plotted the amplitude ranges for the following groups: (1) dIBI - good outcome, (2) dIBI - poor outcome, (3) BS-IBI - good outcome and (4) BS-IBI - poor outcome. In addition, we performed a two-way ANOVA for the mean amplitude of dIBIs and BS-IBIs within the intervals 3-5s and 5-10s. The outcome group (good-poor) was defined as a fixed factor, whereas parameter (dIBI - BS-IBI) was a random factor. The differences in mean amplitude

values between groups (1)-(3) and (2)-(4) are statistically significant (Figures 4.27 and 4.28). These results show that the good outcome group expresses significantly higher mean amplitude values compared to the poor outcome group. In addition, the significant interaction between the two factors implies that dIBI amplitude better discriminates the two outcome groups. We also see that levels of dIBI amplitude for group (2), although values were not bounded from above, are in the similar range as levels of BS-IBI amplitude for group (4). This suggests that in neonates with poor outcome, dIBI amplitude did not recover and remained at the attenuated level as assessed with the BS-IBI. On the other hand, by incorporating higher interburst amplitudes into dIBI, mean amplitude values in group (1) increased compared to group (3) (Figures 4.27 and 4.28), demonstrating the clinical superiority of this parameter.

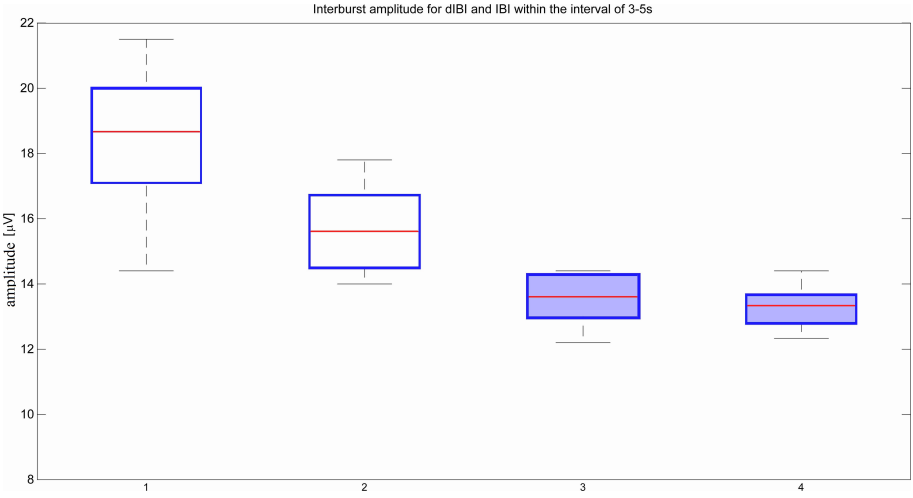

Figure 4.27: Interburst amplitude distribution is shown for dIBIs and BS-IBI (shaded boxes) lasting from 3-5s. The following groups are created: 1 - dIBI amplitude for good outcome group, 2 - dIBI amplitude for poor outcome group, 3 - BS-IBI amplitude for good outcome group and 4 - BS-IBI amplitude for poor outcome group. dIBI amplitude better discriminates the two outcome groups.

4.5 Conclusion

We have presented the method for the automated quantification of the abnormalities in brain functioning in asphyxiated infants. However, even though our definition of dIBI incorporates amplitude and duration and takes

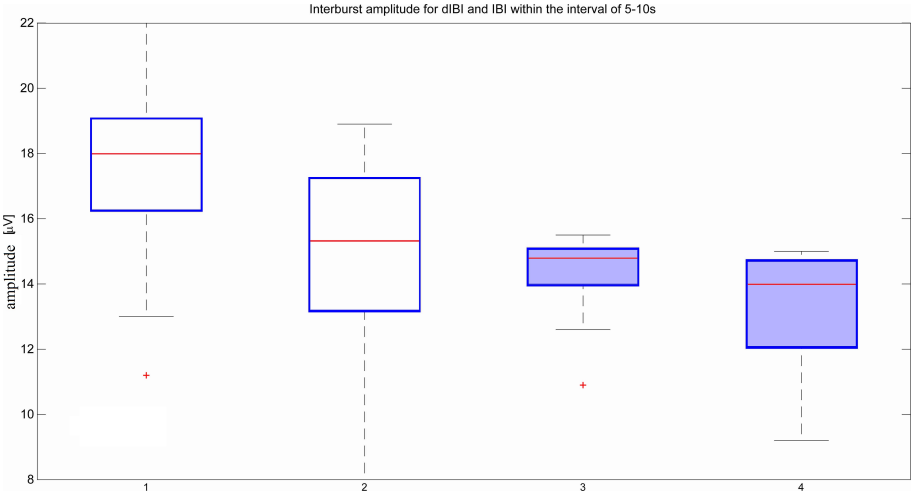

Figure 4.28: Interburst amplitude distribution is shown for dIBIs and BS-IBI (shaded boxes) lasting from 5-10s. The following groups are created: 1 - dIBI amplitude for good outcome group, 2 - dIBI amplitude for poor outcome group, 3 - BS-IBI amplitude for good outcome group and 4 - BS-IBI amplitude for poor outcome group. dIBI amplitude better discriminates the two outcome groups.

into account the various types of transitioning between bursts and dIBIs, it could be argued that an attempt to represent a complex and chaotic signal like EEG with a single parameter is fundamentally flawed. However, in encephalopathic neonates, we would expect a relative simplification of EEG patterns, resulting in discontinuity of the EEG and the appearance of definite dIBIs which would be detected by our automated system. Since our aim with automated dIBI detection is to develop a method to grade HIE and monitor its evolution in neonatal encephalopathy and not to encapsulate the entire range of complexities of the EEG signal from normal to abnormal, we feel that our approach is justified. Furthermore, the advantage of our refinement step is that it selects only highly certain dIBI detections, which would have very good inter-rater agreement. To further investigate the potential of the dIBI parameter for scoring background EEG abnormalities and its prognostic value, it is necessary to perform further multi-center validation studies with even larger datasets. This analysis could also lead to a widely acceptable EEG background grading system in HIE using data-driven rules and be an important aid in guiding treatment decisions.

Chapter 5

Heart Rate Variability in asphyxiated neonates

In this chapter we assessed the utility of heart rate variability (HRV) in newborns with acute HIE undergoing simultaneous continuous EEG (cEEG) and ECG monitoring. HIE was classified using clinical criteria as well as visual grading of cEEG. Newborns were divided into two groups depending on the severity of the hypoxic injury and outcome. Various HRV parameters were compared between these groups and significantly decreased HRV was found in neonates with severe HIE. As HRV is affected by many factors it is difficult to attribute this difference solely to HIE. However, this study suggests that further investigation of HRV as a monitoring tool for acute neonatal hypoxic injury is warranted. As compared with other chapters, this is the only chapter where the ECG signal is used. In addition, as the main focus is EEG processing a detailed overview of the HRV is not provided and may be found at [18].

5.1 Introduction

It is well known that background EEG activity is affected in HIE neonates [22]. In addition, heart rate variability (HRV) may be affected in HIE. This can be due to direct effect of asphyxia on the heart or due to impaired central (cerebral and brain stem) regulation of heart rate, or both, and may help in prediction of outcome. An earlier study investigated HRV in term asphyxiated newborns [2]. In that study HRV was examined 7 days post partum. Therefore,

although valuable for estimation of the outcome, that study does not show HRV properties at an early stage of the injury (first 3 days post partum) when treatment interventions are expected to be maximally effective. The aim of the present study is to examine the use of HRV obtained by continuous electrocardiogram (ECG) monitoring done simultaneously with continuous EEG registrations (cEEG) in patients with HIE as a diagnostic tool. We compare heart rate parameters between two groups of neonates, group I with mild HIE and group II with moderate to severe HIE, using long-term ECG recordings. Although many factors influence HRV parameters, our goal is to examine whether the differences in HRV parameters are sufficiently discriminative between these two groups of newborns. To test these differences, a linear discriminant analysis (LDA) classifier was used.

5.2 Materials and Methods

5.2.1 Dataset

All data were recorded at Sophia Childrens Hospital, Erasmus MC (Rotterdam, the Netherlands). We studied 19 newborns with HIE and without recorded epileptic seizures. They were preselected from a larger set of 119 newborns who underwent continuous EEG video monitoring. Sampling frequency of the simultaneously recorded ECG signal was 256 Hz. Continuous 2-h artifact-free ECG recordings were selected. In total, we analyzed 36 ECG segments recorded within 18-48 h after birth. The number of analyzed segments ranged from 1-4 per patient. The severity of encephalopathy was assessed using both clinical grading (Sarnat scores) and grades of background EEG activity [1]. The scoring of the background EEG was performed by an experienced clinical neurophysiologist (PJC). Newborns were divided into two groups: group I (n=10) with mild HIE and good outcome, and group II (n=9) with moderate to severe HIE and poor outcome. Outcome was classified into good outcome [normal or mild disability (minimal abnormalities at neurological examination or mild cerebral palsy; the Gross Motor Functional Classification System (GMFCS 1-2)] and poor outcome [death or Mental Developmental Index (MDI) < 70 or severe cerebral palsy (GMFCS 3-5)]. In these datasets we selected 2-h ECG recordings, as this was the longest artifact-free period we could find. This duration of ECG recordings was sufficient to accurately calculate and estimate long-term HRV parameters [18]. In total, we had 22 ECG segments from group I with a good outcome and 14 ECG segments from group II with a poor outcome.

5.2.2 Heart Rate Variability parameters

To calculate HRV parameters the first step is to detect R peaks within the QRS complex of the ECG signal. We improved the accuracy of the HRV parameters by upsampling the ECG signal to 1000 Hz and used it for further analysis. The Pan-Tompkins algorithm was applied for R peak detection. This way, we obtained a tachogram signal, also known as the RR interval. All 2-h ECG segments were visually inspected to ensure that there were no missed R peaks or false-positive R peak detections. In this way, we obtained an NN interval (normal to normal beat [18]).

Three groups of HRV parameters were calculated: time, geometry and frequency domain parameters. All these parameters are calculated as proposed in [18]. As the first time domain parameter, mean NN interval is calculated. Variable SDNN is based on the standard deviation of NN time series and reflects the total power of the HRV spectra. By increasing the duration of the ECG recordings the SDNN parameter increases as well. Therefore, it is important to compare this parameter using the ECG recordings of the same duration. The SDANN parameter reflects changes in NN time series using 5-min epochs. It represents the standard deviation of average NN intervals calculated over 5 min of recordings. Additionally, the SDNN index is calculated as a mean value of the 5-min standard deviations calculated over 2 h.

A commonly used time domain parameter is the RMSSD, the square root of the mean squared differences of successive NN intervals. pNN25 is the number of interval differences of successive NN intervals ≥ 25 ms divided by the total number of NN intervals and multiplied by 100. Finally, we calculated SDSD, the standard deviation of differences between adjacent NN intervals. Additionally, we calculated standard geometric parameters as proposed in [18]. Triangular index, related to the histogram of the NN intervals and parameters SD1 and SD2 of the Poincaré plots, were calculated.

To calculate frequency parameters, we interpolated NN intervals using 4 Hz sampling frequency. Thus we obtained an equidistantly sampled signal. We then calculated power spectral density using Welchs periodogram. Three frequency bands were defined (VLF, LF and HF) of which the spectral power was expressed in absolute values (in ms^2) and in normalized units (n.u.) which represent the relative value of each power component in proportion to the total power minus the VLF component. The frequency bands were adapted to the newborns heart rate: 0.01Hz-0.04Hz, 0.04Hz-0.2Hz, 0.2Hz-2Hz, as proposed in [36]. The goal of this study is to examine whether HRV parameters from 2-h ECG are discriminative enough, i.e. to verify whether the outcome group can be predicted accurately using only parameters derived from the ECG signal. For this purpose,

the leave-one-out method was applied in these experiments. We used ECG segments and corresponding HRV parameters from a single patient as an input to a LDA classifier. The classifier was trained using the HRV parameters obtained from the remaining patients. As the output, the classifier is expected to estimate the appropriate group of the patient: i.e. good or poor outcome. Input features into the LDA classifier represented a subset of all calculated HRV parameters. As we did not know a priori which features would be the most discriminative, we combined features into different subsets to increase the discriminative power. The number of features was relatively low and we were able to create subsets of various sizes and use an exhaustive combinatorial search to determine an optimal set of parameters.

In total, 24 HRV parameters were calculated as proposed in [18] and they were used as input features into the LDA classifier. The best set of parameters achieved an accuracy of 80% in discriminating the two groups of newborns. The most descriptive parameters were standard deviation of the heart rate signal (SDNNindex), low frequency power of the heart rate spectra (LF) and SD2 parameter of the Poincaré plot. Normalized values of these parameters are shown in Figure 5.1. More importantly, there was a reduced HRV in the patient group with more severe HIE.

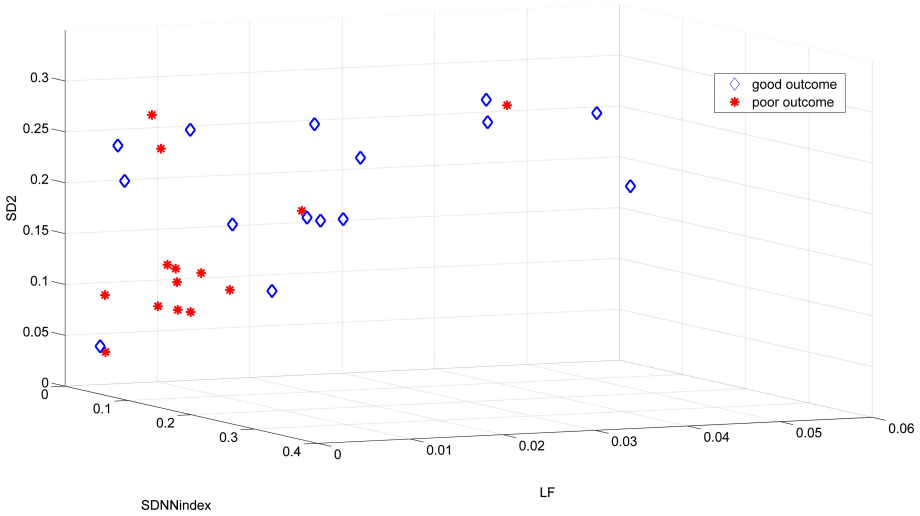

Figure 5.1: Subset of HRV parameters that achieved the best discrimination between groups with good and poor outcome. All parameters are depicted using normalized values.

5.3 Discussion

In patients with HIE it is important to estimate the degree of hypoxic injury at an early stage. The most informative tool is the cEEG and in this study we wanted to examine the use of continuously recorded ECG signal and HRV as a potential additional tool. Advantage of the ECG signal is its well-defined morphology and straightforward and easy calculation of HRV parameters. A difficulty can arise in interpretation of the HRV parameters.

In this study, we tried to make our database as homogenous as possible by excluding patients who were treated with antiepileptic drugs. Many patients were excluded from the present study because the monitoring started more than 48 h post partum, or because the ECG recordings were corrupted by artifacts. Additionally, there is an inherent difficulty in making a new, better controlled study. Start of the ECG and EEG recordings is influenced by many medical and logistic factors that are often difficult to control.

In addition to hypoxic injury, HRV is influenced by many factors such as autonomic nervous system dysfunction, changes in blood pressure, temperature, respiration, and administered medications. Hence, in the present study it is difficult to draw definite conclusions about HIE as the major determinant of the HRV findings.

Despite these limitations, our results show that there is a significant relationship between the severity of HIE as graded clinically and by cEEG and HRV. In [2], reduced HRV was also reported in term asphyxiated newborns 7 days after birth; in that study the Sarnat score was used to classify the patient groups. In our study, we used both the Sarnat score and the evolution of the background EEG to better classify encephalopathy. This is important because hypoxic injury usually evolves and brain function can recover or deteriorate over time. Additionally, we used the brain injury patterns seen on MRI scans done in the first week after birth and neurodevelopmental outcome in survivors at follow-up after 2 years. This made the classification of patients into two outcome groups more reliable. For future study, more insight into HRV in perinatal HIE can be obtained by comparing HRV parameters at specific time points, such as 12, 24, 48 and 72 h post partum. In that way maturational effects of the central nervous system as encountered in studies done after 1-2 weeks post partum can be avoided. Such investigations would be valuable to confirm the possibility to use HRV as a tool to monitor the evolution of HIE recovery, as well as to identify neonates requiring additional interventions or neuroprotection. In the case that correlations and dynamics do exist between HRV parameters and parameters derived from the cEEG (e.g. duration of inter-burst intervals) they can contribute to improve the assessment and monitoring of perinatal hypoxic

brain injury. Inclusion of a larger number of neonates with varying degrees of HIE, as well as studying HRV evolution over a longer period of time, would help to clarify the application of these parameters in the refinement of the assessment and prediction of outcome after perinatal hypoxic injury.

5.4 Conclusion

This thesis's Chapter is unique in the aspect that the ECG signal has been used for the characterization of the asphyxiated neonates. This was chosen for two reasons. First, ECG signal is commonly recorded as one of the polygraphy channels. Hence, HRV parameters are relatively straightforward to be calculated. In addition, more sophisticated algorithms do exist for the HRV parameter extraction than the Pan-Tompkins algorithm used here. Hence, they allow more robust estimates of the parameters. From the perspective of our goal, it is, therefore, beneficial to have additional differentiating features to be used as bio-markers for HIE severity characterization. Second, in many cases of neonatal diseases HRV proved to be a useful bio-marker for an early detection diagnosis. Examples are diagnosis of sepsis and apnea ([7], [102]). In those studies (e.g. apnea), diagnosis are established while differentiating different sleep stages (e.g. REM). Therefore, our exploratory study shows that future study are necessary to fully reveal the potential of the HRV parameters as additional bio-markers for HIE characterization.

Chapter 6

Long-range temporal behavior as a quantitative marker of abnormality

In this Chapter, we studied whether long range temporal correlations quantified by detrended fluctuation analysis (DFA) could be used in the neonatal EEG to distinguish different grades of abnormality in the background EEG activity. We applied DFA on 15 min long, non-overlapping EEG epochs (n=1088) filtered from 3-8Hz. Our formal feasibility study suggested that DFA exponent can be reliably assessed in only two thirds of the EEG epochs, and in only relatively short time scales (10-60sec), while it becomes ambiguous due to crossover phenomenon when wider time scale are considered. This prompted further exploration whether multifractal DFA (MF-DFA) could be applied in a more efficient way, and whether metrics from MF-DFA paradigm could yield useful benchmark with existing clinical EEG gradings.

Comparison of MF-DFA metrics showed a significant difference between three visually assessed background EEG grades. MF-DFA parameters were also significantly correlated to interburst intervals quantified with our previously developed automated detector. Finally, we piloted the intra-patient application of MF-DFA metrics and showed their evolution during patient recovery from asphyxia. Theoretically, our exploratory study showed that neonatal EEG can be characterized as a monofractal process in short time scales only, whereas multifractal modeling may offer more robust and representative characterization of neonatal EEG dynamics. Clinically, our findings show that the MF-DFA

metrics might offer a suitable parameter to quantify the grade of EEG background, or to monitor changes in brain state that take place during long-term brain monitoring.

6.1 Introduction

The current main challenge in the EEG interpretation is to objectively and quantitatively characterize the spontaneous, ongoing brain activity, often called 'background activity' in the EEG nomenclature. It has been shown that the EEG background is most informative when it comes to assessing acute state or predicting future outcome of the brain ([87], [130], [84]). Several background grading systems have been published over the years ([130], [90], [129], [22]), and they combine visually (i.e. subjectively) observed EEG properties to yield one, holistic EEG grade. Perhaps due to the high interindividual variability and ambiguity in visual assessments, the clinically used EEG grading is remarkably rough. For instance, ranges of interburst intervals (IBI) between mild and moderate EEG grades go in 5 second increments from <5s to 5-10s till >10s, respectively ([90], [22]).

It is intuitively obvious, that so rough EEG grading cannot adequately reflect the time-varying physiological state of the brain, although it allows a technically straightforward translation of the criteria into automated classifiers. Intriguingly, classifiers based on these same criteria are not able to fully emulate the visual grading ([90], [68], [114]), which indirectly calls for identification of novel EEG features with clinical relevance.

Recent work in basic neuroscience has provided ample evidence that many brain behaviors exhibit scale-free properties where dynamics of a given feature have no spatial or temporal scale ([8], [107], [42], [59]). This was also recently shown to be the case for the EEG activity of full-term neonates that recover from perinatal asphyxia ([59], [107]), one of the most common reasons for continuous EEG monitoring in the NICUs.

Scale-free dynamics in a complex system can give rise to self-similarity over temporal scales, i.e. long-range temporal correlations (LRTC), which may be assessed from the EEG using detrended fluctuation analysis (DFA; [101], [52]). Recent work has shown that LRTC in brain function is significantly affected by various clinical conditions ([74], [96], [113], [88]). Compared to the conventional, visually defined EEG features, LRTC reaches beyond the visually perceived time scales, while it also integrates multiple time scales (from seconds to minutes) into one mathematically and conceptually transparent estimate. Moreover, DFA as a paradigm is very strongly supported by theoretical, experimental and

clinical studies (for review, see [52]). Recent development of signal analysis methods has extended DFA to multifractal DFA (MF-DFA), which characterizes time series with multiple co-existent dynamic processes that may give rise to temporally local fluctuations including both extreme small and large magnitudes. Several studies have reported MF-DFA to offer additional insight in experimental and clinical neuroscience contexts ([62], [136]). The neonatal EEG is, indeed, an example of signal with extreme, apparently erratic fluctuations in signal amplitudes, making it potentially suitable for MF-DFA paradigm as well.

The present study was set out to examine the possibility that neonatal EEG exhibits LRTC, which can be used as a feature to assess brain condition in a clinically relevant context. This entails answering the following questions: First, is it possible to assess mathematically relevant DFA exponents from the neonatal EEG at clinically relevant time scales? Second, if DFA is suboptimal, can MF-DFA represent neonatal EEG in a meaningful way? Third, is it possible to use these measures to distinguish background grades of the neonatal EEG? The last question offers a benchmark to the existing analysis paradigms, while it is also directly relevant for development of novel features for automated background EEG classifiers.

6.2 Methods and Materials

Sequentially, we first examined the mathematical and physiological feasibility of the DFA approach in neonatal EEG analysis, and we studied the DFA fluctuation plots for differences in our clinical populations (different EEG grades). After observing mathematical limitation with the DFA paradigm, the work was continued to test MF-DFA paradigm, and finally to benchmark MF-DFA metrics with clinical and automated EEG grading.

6.2.1 Datasets

We used altogether 1088 15min epochs (total 272 hours) from 34 neonates that were recorded for clinical reasons at Sophia Children's Hospital, Erasmus MC (Rotterdam, the Netherlands). These neonates were part of a larger cohort of term asphyxiated neonates who were monitored from March 2003 till August 2007. Other results from this cohort have been published previously ([33], [22], [31], [81]). The clinical inclusion criteria for EEG monitoring were: gestational age of 37-43 weeks with clinical features of encephalopathy, and having at least one of the following features of birth asphyxia: a) arterial pH of umbilical cord blood $\leq$ 7.1, b) Apgar score $\leq$ 5 at 5 minutes, and c)

high clinical suspicion (like fetal distress, umbilical cord prolapse, difficult labour, or a history of convulsions). Exclusion criteria were: congenital cardiac abnormalities or other multiple anomalies, inborn errors of metabolism, and constantly isoelectric ($<5\mu$V) EEG activity. The study had the approval of the Erasmus MC Medical Ethical Review Board. Informed consent was obtained from the parents/guardians prior to the onset of the registration. The EEG recordings started 2-48 (median 19) hours post partum. The median (range) duration of EEG was 31 (20-96) hours. Seizures were recorded in 18 patients and were treated with anti-epileptic drugs, however this clinical information was not considered in the later analyses.

EEG sampling. The EEG was recorded with NicOne EEG recorder (Cardinal Healthcare, Madison, WI, USA) at sampling frequency of 256Hz and our current data analysis was performed using bipolar montage with 12 derivations. Four epochs of 2h continuous EEG recordings were selected per neonate with a minimal distance between them longer than 4h.

6.2.2 Feasibility of DFA in the neonatal EEG

Detrended Fluctuation Analysis (DFA), originally introduced by Peng et al. [101], is a widely applied method to quantify LRTC in various biological time series that exhibit self-similarity over multiple time scales. In the context of EEG analysis, DFA is typically computed by measuring amplitude dynamics of selected frequency bands (cf. [52]). In the first step, after band-specific amplitude extraction, the DFA procedure splits the signal into time windows (time scale - s), detrends the EEG segment, and computes the variance of amplitude fluctuations. In the second step, a DFA plot is generated by plotting the average signal variance per each window size on log-log coordinates (time scale – s, Fluctuation function – F in Figures 6.1 C and E). Finally, a linear fit of this fluctuation function gives the DFA output, the scaling exponent α (cf. [52]).

Use of DFA paradigm requires defining several parameters so that they comply with the a priori known characteristics of the given biological signal. These include definitions of 1) the frequency band which is used for the signal envelope extraction 2) the epoch lengths, *time scales*, that are used to calculate the fluctuation function as well as 3) the range of time windows over which the slope of the linear fit (exponent α) is calculated (see Figure 6.1). The first two can be defined a priori, whereas the last one needs to be reasoned physiologically, and finally set after inspecting the data.

Epoch length. We analysed data epochs of 300s, 600s, 900s and 3600s duration, but the final analysis was then carried out using 900s (15min) epochs. The

choice was to strike a practical compromise between obtaining enough data for a reliable DFA plot, yet having likely a consistent background state in the given window. Our clinical background grading was performed initially in 15min epochs, hence 900s was practical for benchmarking purposes.

Frequency band. Neonatal EEG, especially in the acute state after asphyxic injury as in our data series, is dominated by intermittent bursting activity that consists of oscillations at about 0.1-10Hz. The lowest frequencies may be unpredictably contaminated by movement and other artefacts, so they were filtered out using a FIR highpass filter at 3 Hz. We chose to use a lowpass FIR filter at 8 Hz to maximally limit our analysis to the previously described 3-8Hz band ([95], [122], [92]). However, we also examined other frequency bands (1-3Hz and 1-5Hz), and we got qualitatively comparable findings (data not shown).

Time scale (DFA window). Feasibility of the DFA method requires that the signal does exhibit genuine LRTC, which in an ideal case could be seen over all time scales up to the limits of the recording time. The shortest time scale is defined by the durations of amplitude fluctuations of interest, and multiple fluctuations need to be included in the shortest time scale to really assess its temporal correlations (cf. [52]). In the present context, the amplitude fluctuations in the early recovering neonatal EEG consist of intermittent bursting at multi-second scale. The selected frequency band (3-8 Hz) gives slowest fluctuations with a duration of around 1sec ([122]), which suggested to use the lowest reasonable time scale of 10s. The upper range can be physiologically limited by the spontaneous changes in the brain state over time, especially vigilance state cycling that occurs 1-3 times per hour in the neonatal brain [116]. However, the upper limit of feasible scales can also be reasoned mathematically, since estimation of the DFA exponent α is based on linear fitting in the DFA plot over the given time scale (see below; Figure 6.1 C).

Next, we continued quantitatively by analysing how well the linear fitting suits to different ranges of windows (5-60s, 10-60s, 10-100s and 10-300s) in the fluctuation functions. Two independent techniques were used: The first method was developed by Botcharova et al. [14] based on the maximum likelihood approach that compares a set of alternative models: linear, polynomial, root, exponential, logarithmic and spline functions. This paradigm identifies the best fit model when the involved number of parameters is minimal and the over-fitting is penalised. During the process of this study, we found that this method may be compromised because it so readily indicates models other than linear (e.g. polynomial: quadratic or cubic) which by themselves have no physiological meaning in the present context. Hence, a second method was adopted from prior studies (e.g. [74]), based on computing the standard linear regression fit, R^2, and using a predefined threshold of 0.97 to indicate acceptance of the

epochs for DFA study.

6.2.3 Feasibility of MF-DFA in the neonatal EEG

Various complex systems and physiological time series may show LRTC although they cannot be characterized with a single parameter (monofractal; for a review, see [58]). For instance, there may be clear monofractal dynamics at distinct, narrow time scales bounded by deflections in the log-log fluctuation plot (so called "crossover points"; [62]). Then, instead of a single linear approximation, the fluctuation function can be better described as a set of linear approximations, yielding different scaling exponents for different time scales. They are called multifractal time series, where the set of scaling exponents, or parameters, are called q-order (generalized) Hurst exponents [58]. For monofractal time series, the q-order Hurst exponents will have equal values, whereas in multifractal time series, the q-order Hurst exponents will be significantly diversified. A common reason for multifractality is that the signal may exhibit different LRTC for temporally local small and large fluctuations. In contrast, monofractal time series are mainly noise like (e.g. white noise; cf. [58]) and they do not show local periods of either extremely small or large fluctuations. Hence, the known non-stationarity of the fluctuations in the neonatal EEG does, indeed, suggest that MF-DFA may offer better handling of the temporal EEG dynamics (e.g. local suppression and burst periods). Mathematically, MF-DFA differs from the DFA only in the calculation of the q-order fluctuation functions, Fq (Figures 6.2 B1 and B2), which is followed with the extraction of the q-order Hurst exponents (Figures 6.2 C1 and C2). Next, MF-DFA can be plotted as a so called multifractal spectrum, which can be quantified with mathematically robust metrics. The multifractal spectrum is generated by converting q-order Hurst exponent into q-order singularity exponent (hq) and q-order singularity dimension (Dq). For more details we refer to [58]. The conventional MF-DFA metrics included mean hq, width hq, mean Dq and height Dq (see Figure 6.3 D for their graphical presentation). The width hq is calculated as the difference between maximal and minimal hq values, whereas height Dq is calculated as the difference between maximal and minimal Dq values (as suggested in [136]). Mean hq and mean Dq are calculated by averaging all data points across spectra and across 12 channels. The statistical results are presented in Figures 6.3 E-H. In addition, the difference between DFA and MF-DFA can be observed only within the relatively short time scales (e.g. less than 100s) and within MF-DFA concept the linear fitting from 1s till 128s was applied in this work.

6.2.4 Benchmarking with EEG grades

The ultimate goal in the present study was to establish the applicability of DFA or MF-DFA metrics in quantification of background EEG abnormalities. To this end, we had two benchmarking methods, visual and automated background classification. Both DFA exponent and four MF-DFA metrics were calculated for each 15 min EEG epochs that also had a known visual background EEG grade inherited jointly for all four 15min epochs within the given hour of EEG.

The visual background grading was performed by an experienced clinical neurophysiologist (PJC), blinded to the clinical details of the neonates. A three level EEG grading was adapted from Murray et al [90] as follows: a) normal/mild (IBIs<5s; poorly organized sleep-wake cycle; recovered, continuous background EEG), b) moderate (5s ≤ IBIs < 10s), and c) severe (10s ≤ IBIs < 60s; dominated by prolonged and marked suppressions).

The automated background grading was taken from the automatically computed inter-burst intervals (IBI). This was generated using the automated IBI detection method described in [80] and Chapter 4. Subsequently, we used mean IBI values and compared them with MF-DFA based parameters. All data points were extracted from 15min cEEG epochs, thereby providing for every neonate 32 data values (= 4 (epochs of 2h) x 2 (hours) x 4 (15 min segments in 1h cEEG).

Statistical analysis. Group comparisons were performed with the Kruskal-Wallis test. Significance level was set to 0.01, and Bonferroni correction was used in case of multiple comparisons. Correlations between MF-DFA metrics and IBI values were computed using Spearman correlation coefficient.

6.3 Results

6.3.1 DFA

Visual Observations

DFA fluctuation function plots (an example shown in Figure 6.1 C) were computed and examined first visually from hundreds of EEG segments. As a general observation, all plots showed a monotonically rising trend between DFA window and fluctuation amplitudes, however the ranges of window lengths with possible linear relationships were variable and limited. Our systematic qualitative comparison of window lengths ranging from 5-60s to 10-300s (data not shown) suggested that linear fit should preferably be attempted at time

scales of up to about 60s. Then, we also reasoned that the lowest feasible limit should be around 10s to avoid measuring trivial autocorrelations in the amplitude fluctuations (for further reasoning regarding the choice of minimum length, please see [52]). A direct comparison of hundreds of DFA fluctuation plots from EEG epochs with different EEG backgrounds showed that they all follow the same overall course, however, they also appear to differ in the segment corresponding to the shorter time windows (Figure 6.1 E).

Testing the feasibility of DFA

In above, we had defined the epoch length to 900s, which was a partly theoretical, partly practical choice. Theoretical reasoning was that we found DFA fluctuation plots become more stable with longer epochs. The practical reasoning was that the epoch length could be chosen as a multiple of our manual EEG grade classification that was set to 1h. Obviously, a 900s long, fixed epoch lengths cannot follow the dynamic changes known to take place in brain state of these babies (see also [12]), and other epoch lengths may be worth trying in future neonatal applications. The actual feasibility of conventional DFA was tested by examining whether linear fit can adequately characterize the fluctuation plot within the tested range of windows. First, our analysis of 1088 epochs using the 'maximum likelihood'-based technique suggested that only minority of them could be modelled with a linear fit. This finding was consistent even when we systematically varied frequency band (1-3Hz, 1-5Hz and 3-8Hz) or the range of fitting scale (5-60s, 10-60s, 10-100s and 10-300s). The best set of parameters was 3-8Hz frequency band and 10-60s window fitting size, and even then, only 200 out of 1088 15min cEEG epochs (18%) were successfully modelled as linear. We also examined how different EEG background grades are related to the linearity model, and found that continuous background EEG (grade 1) is most likely to fit linear model (data not shown). Second, we also studied the more commonly applied measure, the linear fit R^2 using the previously adopted threshold of R^2=0.97. We found that about two thirds (68%; 731 out of 1088) of EEG epochs passed this test.

Benchmarking with clinical EEG grades

For benchmarking with clinical EEG grades, we chose only those EEG epochs that had passed our linear fitting test (R^2>0.97), and we computed their DFA exponents (α). Group-wise comparison of α shows a wide variation within all EEG grades, while the mean α increases towards more severe EEG background. Notably, the normal/mild EEG grade (continuous EEG activity) was close to α=0.5, Figure 6.1 D, (an 'uncorrelated' process; cf. [52]), while the most severe

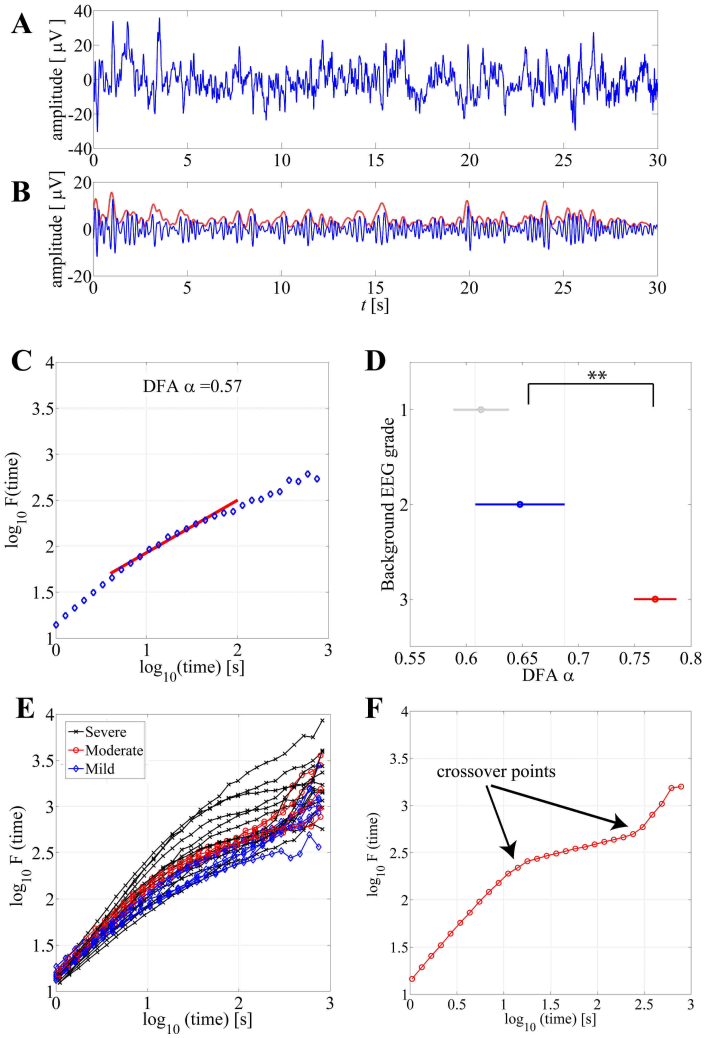

Figure 6.1: (A) An example of normal neonatal EEG signal with continuous background pattern. (B) The signal is band-pass filtered between 3-8 Hz (blue), and the instantaneous amplitude envelope (red) is calculated using Hilbert transform. (C) The DFA fluctuation function is presented along the y axis, whereas the size of the windows analysed in the DFA method are displayed in the x axis. The red line presents an example of linear fluctuation function that is here fitted for the time scale 10-60 seconds to obtain its slope, the DFA scaling exponent α. (D) DFA fluctuation functions are plotted for 15 min EEG epochs from different background EEG abnormalities (Mild-blue, Moderate-red, Severe-black). (E) Comparison of scaling exponent α between different background EEG grades shows a significant difference between grades 2 and 3. (F) An example of the DFA fluctuation function (moderate EEG grade) where clear existence of the crossover points are illustrated.

EEG background approached 1.0 (a process with a strong positive correlation). Statistical group comparison of α shows that group 3 is significantly different from the other two groups ($p<0.01$; Kruskal-Wallis test)).

Crossover points

Finally, we visually inspected a large number of DFA plots to observe possible systematic differences between EEG grades. Figure 6.1 E shows an example where it can be already seen that the plots have different overall forms: Those computed from the severe EEG grade epochs (black) are at the top, and the plots from the mild EEG grades (blue) are on the bottom of the group. It was also apparent, that the range of linear-appearing trends varied between EEG grades, and that they were often clearly multiphasic: short time scales with steep rise, middle window lengths with flatter rise, and again steep rise at the longest time scales. An example of an EEG epoch with very clear "crossover points", i.e. change of slope in the fluctuation function [52] is shown in Figure 6.1 F. Finding such crossover points, suggests presence of multiple overlaying fractal processes, and the signal may hence exhibit multifractal behaviour ([62], [58]). Describing such signal with one exponent, as in the conventional monofractal DFA, will overlook key dynamic properties, the results will be particularly sensitive to chance factors in the conventional DFA analysis.

In our dataset, the crossover point in the burst-suppression background (red and black DFA fluctuation functions in Figure 6.1 E) was usually encountered within 30-60s window time in the DFA fluctuation plot (1.5-2 in log10(time) s). On the other hand, continuous EEG background (blue DFA fluctuation functions) were successfully modeled as linear for longer window sizes (up to 100s or 2 in log10(time) s). In this case, the crossover points mainly appeared in the interval of 100-300s (2-2.5 in log10(time) s). In comparing different EEG grades, the different crossover points preclude use of single, monofractal DFA exponent, and supports exploration of MF-DFA metrics.

6.3.2 Multifractal DFA (MF-DFA)

We next studied the feasibility of MF-DFA in neonatal EEG by applying a previously published method ([62], [58]). The special clinical attraction in MF-DFA comes from its clear metrics that have been recently shown to aid discrimination of brain states [136] and pathologies [135]. It is also attractive in MF-DFA that it can be applied on all datasets, and it is not critical about absence of linear fit over the whole time range, as required in the conventional, monofractal DFA.

Feasibility of MF-DFA

The first step here was to show that neonatal EEG signal is characterized by multiple rather than single exponents. The presence of multifractal behaviour in at least some neonatal EEG data becomes apparent when comparing the temporal behaviour of two common neonatal EEG patterns in asphyxiated infants, the normal continuous EEG signal and the severely abnormal EEG with marked intermittency called burst-suppression (see Figures 6.2 A1-A2). For those signals, we calculated the q-order fluctuation functions Fq (Figure 6.2 B1-B2) with q values from -5 till 5, equidistantly sampled with a 0.5 unit-step. The q factor is able to detect mixed occurrence of large fluctuations with periods of negligible fluctuations, which in our case characterizes the burst-suppression background. In contrast, the continuous EEG consists of neither very large nor very small fluctuations (Figure 6.2 A1). Comparison of q-order fluctuation functions (Fq) taken from these two different EEG patterns shows their fundamental difference. In the normal, continuous EEG activity, the slopes of the fluctuation functions appear comparable to each other. Hence, they could also be reasonably described with only one DFA fluctuation function (Figure 6.2 B1; this is the fluctuation function corresponding to q=2), and hence be considered to represent a monofractal process. In sharp contrast to this, EEG periods with burst-suppression are much more variable, and different time epochs exhibit a notably wide spread of Fq (Figure 6.2 B2), suggestive of an underlying multifractal process (see also [58]). Taken together, these observations suggest that measuring LRTC in neonatal EEG datasets like ours should allow quantification of multifractal dynamics.

Subsequently, we calculated q-order Hurst exponents, Hq [58], which returns linear approximation of the Fq fluctuation functions (Figure 6.2 C1 and C2). This again discloses a clear difference between our example EEG activity patterns. In the continuous EEG, the relation between Hq and q factor shows a monotonic decrease (characteristic of a monofractal process; [58]), whereas the Hq plot of burst-suppression EEG (Figure 6.2 C2) shows a relatively sharp and nonlinear decline (characteristic of a multifractal process). These q-order Hurst exponent functions can be readily transformed into a multifractal spectrum (Figures 6.2 D1 and D2), which outlines the relation of local temporal changes of the Hq and the distribution of its probability density function (see [58]). Multifractal spectrum represents two measurable dimensions, the Dq (q-order singularity/fractal dimension) and the hq (q-order singularity exponent). In the visual assessment of multifractal spectra, differences can be noticed in a horizontal and vertical positioning (hq, Dq values), a width (width hq), as well as in the general shape of the multifractal spectra reflecting temporal variations of local Hurst exponents. The MF-DFA spectra were then computed for each (n=1088) of the 15 min long EEG epochs. Example of these spectra are plotted

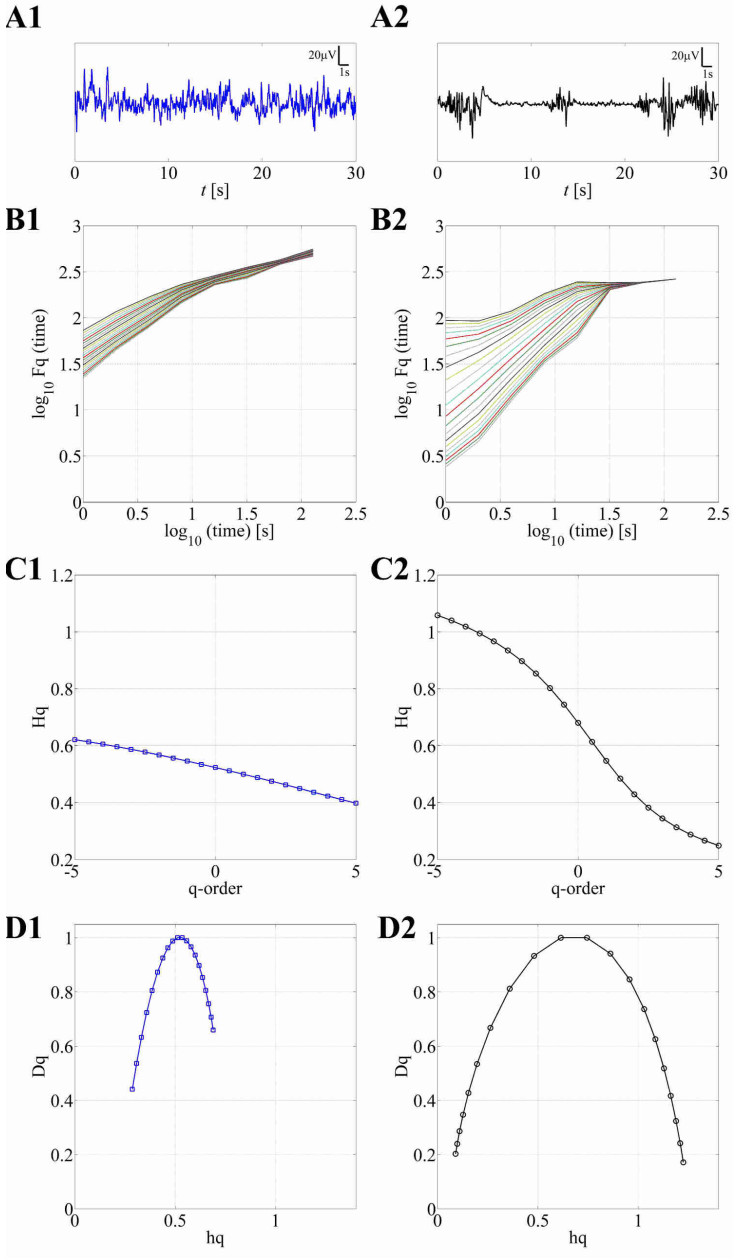

Figure 6.2: Application of MF-DFA paradigm on two different neonatal EEG signals, continuous (A1) and burst-suppression (A2), respectively. In Fig. (B1)-(B2), the q-order fluctuation function, Fq, is shown for two processes. (C1)-(C2). q-order Hurst exponent, Hq, is obtained as the linear fitting coefficient of the Fq fluctuation lines from Figs. (B1) and (B2). (D1)-(D2). Multifractal spectra are displayed for continuous and burst-suppression neonatal EEG periods.

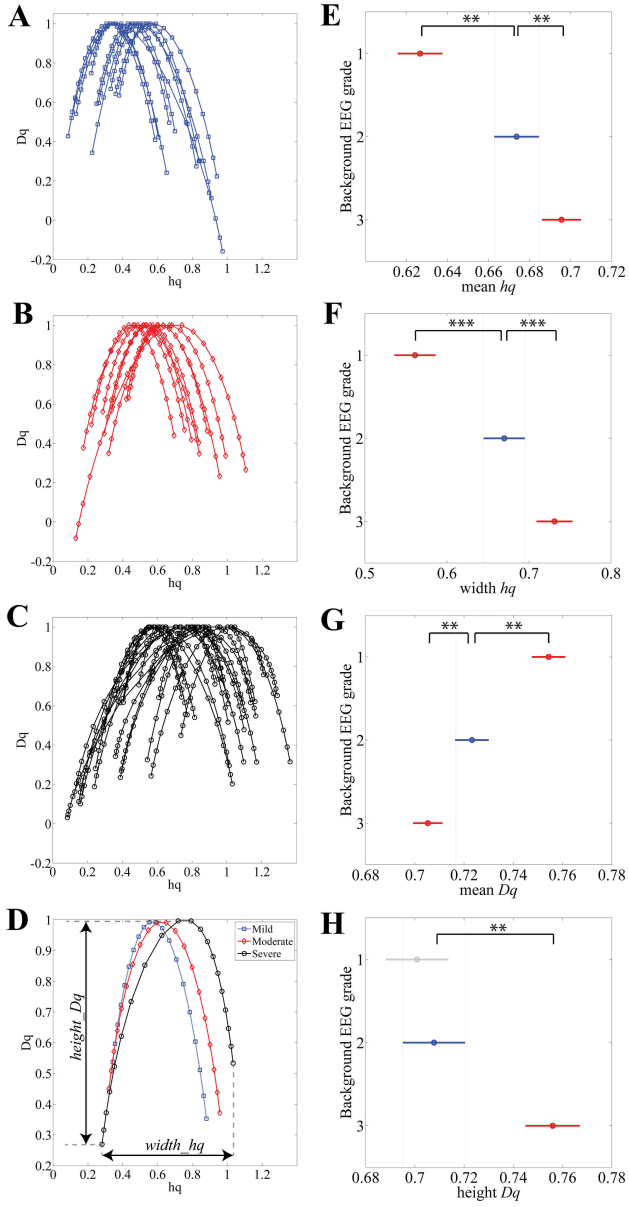

Figure 6.3: (A)-(C) MF-DFA spectra lines are randomly selected and displayed for various background EEG degrees of abnormality: A-mild (blue), B-moderate (red) and C-severe (black). (D). Average of all 1088 multifractal spectra lines is displayed for three background EEG classes. (E)-(H). results of Kruskal-Wallis mean value group comparisons are displayed for mean hq ($p<0.01$), width hq ($p<0.001$), mean Dq ($p<0.01$) and height Dq (not significant).

from each EEG background grade (Figures 6.3 A-C). Visual inspection of the spectra shows that worsening of EEG background (from mild to severe) is associated with a shift to the right (higher hq value). Grand averages of the spectra are shown in Figure 6.3 D (1088 epochs from 12 channels: total 13056 spectra). Other differences among EEGs were also observed visually within the tails of the spectra: the left tails, corresponding to positive q values, are longer in the EEG with local large fluctuations, i.e. the severe EEG grade with IBIs>10s (Figure 6.3 C). Moderate and milder EEG background traces do not have such pronounced structural differences and the corresponding tails are respectively shorter (Figures 6.3 A and B). On the other hand, the right tails, reflect the amplitude fluctuations within local periods of low activity (e.g. suppressed EEG periods).

Benchmarking with clinical EEG grades

Comparison of MF-DFA metrics between EEG grades showed highly significant differences between the three EEG grades. The mean height of spectra, mean hq, was significantly ($p<0.01$) increased with EEG severity (mild 0.63 ± 0.10; moderate 0.67 ± 0.09; severe 0.70 ± 0.09). The width of the spectra, width hq, was also significantly ($p<0.001$) increased with increasing severity of EEG background (mild 0.56 ± 0.13; moderate 0.67 ± 0.16; severe 0.73 ± 0.19). At the same time, the mean Dq decreased significantly ($p<0.01$) with increasing severity of EEG background (mild 0.75 ± 0.05; moderate 0.72 ± 0.05; severe 0.70 ± 0.06). Height of the MF-DFA spectra, height Dq, was significantly ($p<0.01$) different between moderate and severe EEG grades (moderate 0.70 ± 0.09; severe 0.76 ± 0.11). These findings together show convincingly that MF-DFA is superior to the conventional DFA in distinguishing between neonatal EEG grades. A further inspection of the shapes of MF-DFA spectra shows additional qualitative spectral features that are different between background grades. Namely, the mild/normal EEG grade does typically correspond to asymmetric spectra with a longer right side tail, whereas the spectra of severe EEG grade are more asymmetric with longer left side tail. This asymmetry is not measured by the currently used, established MF-DFA metrics. It may, however, readily explain the lesser differences between groups seen in mean Dq and height Dq, which are insensitive to asymmetry. To examine this further in a quantitative manner, we also computed the metrics from the right side tail only (see below).

Benchmarking and application into intraindividual context

While the group level findings above are by themselves strong, clinical applicability of any novel study paradigm requires performance at individual

level as well (see discussion in [1]). In order to preliminarily probe this issue, we studied those 34 neonates in our dataset that had four EEG epochs of 2h duration randomly selected at time points with at least 4 hours intervals. We then computed MF-DFA metrics from 15min segments within each 2h epochs (total 32 epochs in each infant). The long intervals between epochs yielded us datasets where EEG grade, or at least the mean IBI, was changing due to variation in the clinical state of the patient. As a benchmark to MF-DFA metrics, we calculated the mean IBI for each 15min epoch using our previously described automated detector [80]. Nine patients were excluded because their range of IBIs was too narrow to reasonably compute correlation coefficients with another parameter, i.e. IBI range was only within 3 to 6s interval. This left 25 babies for our analysis. Finally, non-parametric, ranking correlation (Spearman) was computed between mean IBI levels and MF-DFA spectra metrics in each patient.

Measures of the full MF-DFA spectra. Individual results are shown in Figure 6.5. We observed that in 10 out of 25 babies there was a significant ($p<0.01$) correlation, which finding is statistically very significant at the group level ($p<1e-10$; Binomial statistics). As shown in Figure 6.4, for an example infant (n=21), a visually apparent temporal relationship was observed between decreasing IBI trend and changes in at least three of the MF-DFA parameters (mean hq, width hq, and mean Dq).

Measures of the right side tail of MF-DFA spectra. However, closer inspection showed that the signs of correlation coefficients (ρ) were inconsistent even for infants with statistically significant correlations (Figure 6.5). To search for reasons we inspected further the shapes of MF-DFA spectra, and observed their asymmetry, especially in the severe EEG grades. For instance, visual comparison of individual MF-DFA spectra shown in Figure 6.4 B from different time epochs during recovery shows that the shape of spectra changes over time, most notably as a shift from longer left tail to longer right tail as well as the shift of the right tail to the left when going from severe to normal EEG background, respectively. Since the current MF-DFA metrics are insensitive to asymmetry of the multifractal spectra, it is possible that change in symmetry with EEG grades would confound the comparisons. Hence, we investigated the parameterization of the right tail of the MF-DFA spectra, and we found these metrics to exhibit much stronger relationship to the mean IBI values. In particular, for 13 out of 25 patients, we found that at least 3 metrics (namely width hq (ρ = -0.70±0.15), mean Dq (ρ = 0.68±0.13) and height Dq (ρ =-0.67±0.11), were significantly correlated with the mean IBI values, showing consistent range of correlation coefficient values (ρ) as detailed at subject level in Figure 6.6.

Finally, temporal evolution of MF-DFA metrics was also examined to see how it could perform at individual level as a putative neuromonitoring index.

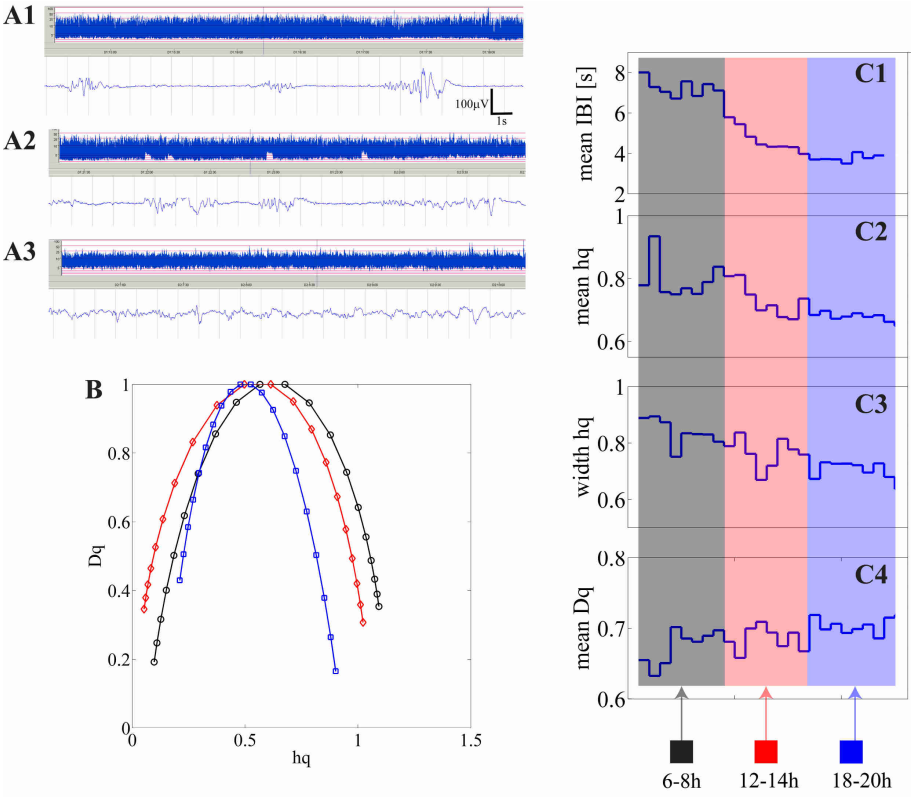

Figure 6.4: (A1-A3) Three examples of burst-suppression, tracé discontinue and continuous EEG periods are shown as aEEG trends and EEG epoch in an infant who is showing recovery from initial severe hypoxic insult. (B) Three multifractal spectra lines are shown for the corresponding three states quantifying 15 min of burst-suppression (black-recorded at 6h postpartum), tracé discontinue (red-recorded at 12h post partum) and continuous EEG period (blue-recorded at 18h postnatal age). (C1)-(C4) from 15 min segments mean IBI, mean hq, width hq and mean Dq values are represented as one data point (24 in total; 2h x 4 (15 min epochs in 1h) x 3 epochs).

***p*-value**: Spearman correlation p values of MF-DFA metrics with mean IBI values.					ρ: Spearman correlation coefficient values of MF-DFA metrics with mean IBI values.				
Patient number	mean hq	width hq	mean Dq	height Dq	Patient number	mean hq	width hq	mean Dq	height Dq
1	<0.01	0.24	0.15	0.63	**1**	0.52	0.21	-0.26	-0.09
2	0.67	0.19	0.39	0.90	**2**	0.08	0.24	-0.16	0.02
3	0.06	0.30	0.31	0.89	**3**	0.34	0.19	-0.18	0.03
6	0.02	0.43	0.69	0.61	**6**	0.40	-0.15	0.07	-0.09
7	<0.01	0.52	0.58	0.26	**7**	0.70	-0.12	0.10	-0.20
11	0.37	0.14	0.61	0.83	**11**	-0.16	0.27	-0.09	0.04
12	<0.01	0.30	0.39	<0.01	**12**	-0.47	0.19	-0.16	0.66
14	0.81	0.06	0.66	0.07	**14**	0.05	-0.33	0.08	-0.32
16	0.12	0.51	0.67	0.04	**16**	0.28	0.12	0.08	-0.36
17	0.10	0.80	0.61	0.01	**17**	-0.29	0.05	-0.09	0.44
18	<0.01	<0.01	<0.01	<0.01	**18**	0.61	-0.82	0.81	-0.65
19	<0.01	0.76	<0.01	0.20	**19**	-0.51	0.06	-0.51	0.23
20	0.06	0.27	0.18	0.01	**20**	-0.33	-0.20	0.24	-0.45
21	<0.01	<0.01	0.01	0.75	**21**	0.61	0.61	-0.48	0.06
22	0.62	0.31	0.12	0.37	**22**	0.09	-0.18	0.28	-0.16
23	0.65	0.06	0.08	0.05	**23**	0.08	0.33	-0.31	0.35
24	0.25	<0.01	<0.01	<0.01	**24**	0.21	0.68	-0.71	0.58
25	0.10	0.33	0.17	<0.01	**25**	0.30	0.18	0.25	-0.71
26	0.01	0.01	0.25	<0.01	**26**	-0.47	-0.46	0.21	0.50
27	<0.01	0.81	0.95	0.65	**27**	0.68	-0.04	0.01	-0.08
28	<0.01	0.48	0.24	<0.01	**28**	-0.57	0.13	-0.21	0.68
30	0.32	0.74	0.83	0.57	**30**	-0.18	-0.06	0.04	0.10
31	0.22	<0.01	0.09	0.05	**31**	0.22	-0.60	0.31	0.35
32	0.01	0.85	0.33	0.71	**32**	-0.44	0.03	-0.18	0.07
33	0.80	0.58	0.94	0.45	**33**	-0.05	0.10	-0.01	-0.14

Figure 6.5: Correlation between IBI and MF-DFA metrics computed from the whole MD-DFA spectra. The four left side columns present significance levels and the four right side columns show the corresponding Spearman correlation coefficients. Significant correlations ($p < 0.01$) are highlighted with green, and their corresponding ρ values are highlighted in orange. The correlations in each patient were computed from 32 epochs.

***p*-value**: Spearman correlation *p* values of MF-DFA metrics with mean IBI values.					***ρ***: Spearman correlation coefficient values of MF-DFA metrics with mean IBI values.				
Patient number	mean *hq*	width *hq*	mean *Dq*	height *Dq*	Patient number	mean *hq*	width *hq*	mean *Dq*	height *Dq*
1	<0.01	0.01	<0.01	<0.01	**1**	0.75	-0.46	0.57	-0.70
2	0.09	0.88	0.77	0.42	**2**	0.30	0.03	0.05	-0.15
3	0.02	0.89	0.78	0.72	**3**	0.41	-0.03	0.05	-0.06
6	0.03	0.42	0.72	0.54	**6**	0.39	-0.15	0.07	-0.11
7	<0.01	0.16	0.15	0.10	**7**	0.72	-0.26	0.26	-0.30
11	0.54	0.01	<0.01	<0.01	**11**	-0.11	-0.46	0.49	-0.52
12	0.95	<0.01	<0.01	<0.01	**12**	0.01	-0.82	0.85	-0.84
14	0.58	<0.01	<0.01	<0.01	**14**	0.10	-0.72	0.72	-0.75
16	0.18	0.14	0.02	<0.01	**16**	0.24	-0.27	0.42	-0.52
17	0.23	0.98	0.64	0.65	**17**	-0.22	-0.01	-0.09	0.08
18	<0.01	<0.01	<0.01	<0.01	**18**	-0.81	-0.83	0.78	-0.65
19	0.07	0.08	0.11	0.26	**19**	-0.34	-0.33	0.30	-0.21
20	0.20	0.09	0.02	<0.01	**20**	-0.23	-0.31	0.42	-0.49
21	<0.01	0.02	0.01	<0.01	**21**	0.65	-0.42	0.48	-0.60
22	0.93	0.38	0.35	0.24	**22**	-0.02	-0.16	0.17	-0.21
23	0.14	<0.01	<0.01	<0.01	**23**	0.27	-0.65	0.61	-0.61
24	<0.01	0.20	0.72	0.04	**24**	0.71	0.23	-0.07	-0.36
25	0.26	<0.01	<0.01	<0.01	**25**	0.21	-0.51	0.66	-0.84
26	<0.01	<0.01	<0.01	<0.01	**26**	-0.69	-0.79	0.76	-0.74
27	<0.01	<0.01	<0.01	<0.01	**27**	0.60	-0.54	0.55	-0.55
28	0.05	<0.01	<0.01	<0.01	**28**	-0.35	-0.84	0.81	-0.69
30	0.22	<0.01	<0.01	<0.01	**30**	-0.22	-0.63	0.63	-0.66
31	0.01	<0.01	<0.01	<0.01	**31**	-0.44	-0.87	0.86	-0.78
32	0.40	0.90	0.85	0.69	**32**	-0.16	-0.02	0.03	-0.07
33	0.84	0.71	0.67	0.37	**33**	0.04	-0.07	0.08	-0.16
					mean		**-0.70**	**+0.68**	**-0.67**
					std		**0.15**	**0.13**	**0.11**

Figure 6.6: Correlation between IBI and MF-DFA metrics computed from the right side of the MD-DFA spectra. The four left side columns present significance levels and the four right side columns show the corresponding Spearman correlation coefficients. Significant correlations ($p < 0.01$) are highlighted with green, and their corresponding ρ values are highlighted in orange. The correlations in each patient were computed from 32 epochs. Comparison to Figure 6.5 shows that the sign of correlation is more consistent when measuring the right side of spectra only.

Additionally, we illustrate how the MF-DFA parameters (extracted from the right tail of the spectra) are correlated with IBI values for five infants that showed higher Spearman correlation p-values (Figure 6.7).

6.4 Discussion

Our study shows that changes in long range temporal dynamics in the early neonatal EEG can be robustly quantified with DFA paradigm. We show, however, that the neonatal EEG is often not adequately characterized assuming a single underlying process as in the conventional monofractal DFA paradigm. Instead, the recently introduced analytic paradigm for multifractal DFA can readily capture neonatal EEG dynamics in a way that is significantly related to the current clinical EEG grading systems. Our technical assessment of DFA feasibility, as well as the clinical benchmarking, are extending prior literature to include neonatal EEG as a potentially fruitful application for DFA/MF-DFA paradigms. The present findings also corroborate earlier reports from adult EEG that DFA or MF-DFA metrics can quantify brain dynamics associated with neurological conditions ([74], [96], [88]). We also suggest a novel MF-DFA metric for EEG analysis based on observing asymmetric change in MF-DFA spectra between clinically relevant brain states.

The physiological underpinnings of multifractal behaviour in the neonatal brain remain elusive, however our observations provide some tentative ideas to why MF-DFA is suitable in such data. The well-known hallmark of both the early neonatal EEG and the severely abnormal EEG of a term newborn is a salient intermittency ([3], [125]): seemingly erratic ruptures of transient cortical activity alternate with periods of relative quiescence. Considering the structural immaturity of underlying brain networks [69] and/or the pathological mechanisms related to resource constraints [107], it is conceivable that they would readily compromise the extreme long range temporal correlations previously shown in the adult brain [74]. There is ample evidence from the neonatal EEG studies that cortical activity may continue even after extensive structural lesions that lead to physical disconnection of cortical areas. The observed multifractality could hence reflect a spatial and/or temporal fragmentation of large scale brain activity, resulting in multiple partly independent mechanisms in brain activity.

In addition to showing the significant discrimination of background grades with the established MF-DFA metrics, our closer visual inspection of MF-DFA spectra suggested further differences. The highest difference between grades was achieved for the relatively small window size values (<30s or 1.5 in log10(time)s)

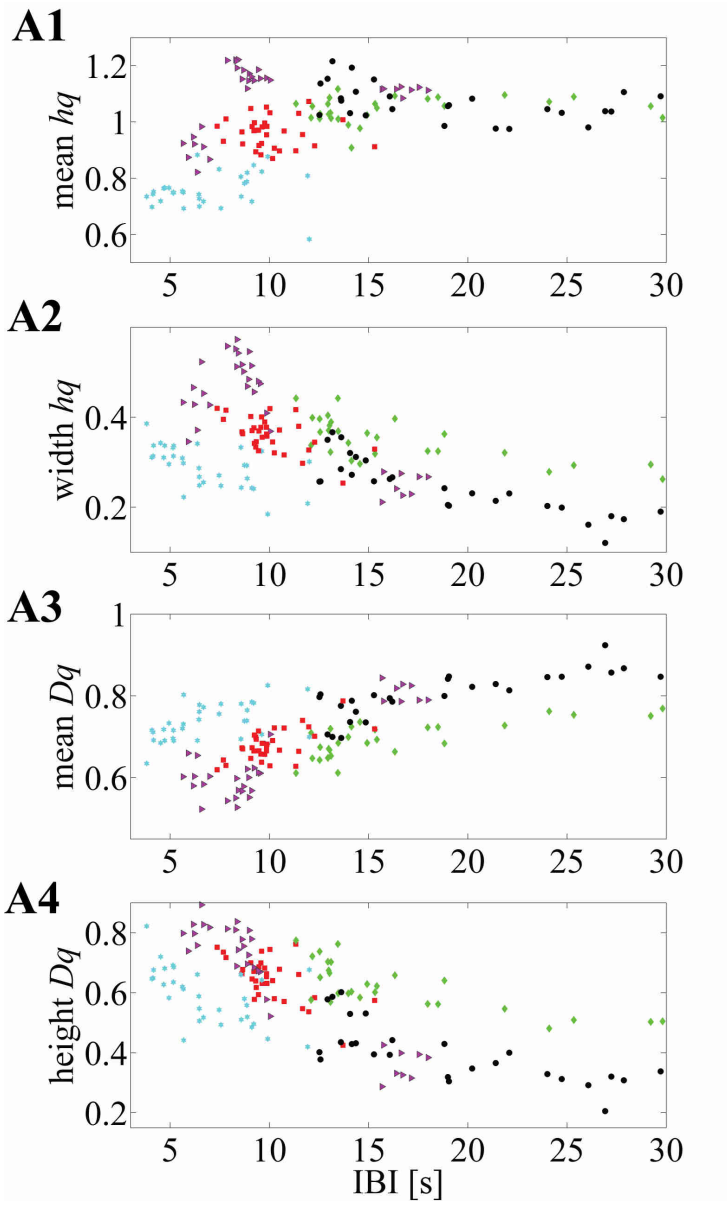

Figure 6.7: Five neonates in which mean IBI values are highly correlated with the MF-DFA metrics (calculated from the right part of the multifractal spectra). Figures (A1)-(A4) respectively, represent the correlation between mean hq, width hq, mean Dq and height Dq values with the mean IBIs. This approach for calculation of MF-DFA based metrics avoids insensitivity to the asymmetry which affects the originally proposed parameters calculated for the complete spectra (see [136]).

(Figure 6.2 B2), which is most sensitive to temporally local variations in signal fluctuations. We also observed that the different background grades yield saliently different shapes, especially the asymmetry, in their corresponding MF-DFA spectra. This is not quantified by the established MF-DFA metrics (cf. [136]), hence we proposed quantification of the right side tail of the spectra for an improved sensitivity. These measures were, indeed, significantly correlating with IBIs in a large proportion of infants. In search of clinical relevance, we benchmarked the MF-DFA metrics with both visual and automated background EEG grading, and show that all our four metrics (mean hq, width hq, mean Dq, height Dq) do significantly co-vary with the visually scored EEG background grades. Three (mean hq, width hq, mean Dq) of our metrics were significantly different between all EEG groups. In addition, the application within patients showed that MF-DFA metrics might even reflect temporal change of background EEG states at individual level as suggested by the significant correlations with IBI levels in 10 out of 25 infants. These correlations suggest that MF-DFA metrics and IBI would at least partly reflect similar pathological brain dynamics, or at least the amplitude fluctuations of burst suppression are reflected in the MF-DFA spectra. However, despite the general correspondence with IBI levels and its evolution, the match between IBI and MF-DFA metrics is neither fully consistent nor complete. Such partial mismatch between suggests that MF-DFA metrics may reflect some as yet latent EEG signal dynamics.

Beyond the physiological interest, our present findings have potential implications in future construction of computational classifiers for neonatal EEG. A number of studies have reported development of various automated EEG background classifiers. Some of them are designed to directly replicate the visual criteria. Using this approach, the recent study by [68], combined a larger set of quantified EEG features and found them indiscriminative with respect to background EEG classes, with special challenges in distinguishing mild vs. moderate grades. A more recent attempt along this line was able to discriminate normal vs abnormal EEG backgrounds as a dichotomous choice [114], which does not yet support its use in EEG monitoring or for more refined needs. Another approach has been to optimize a learning algorithm with a smaller dataset to detect extreme classes of EEG background, such as severe burst-suppression patterns [77], which is further used to output IBI detections. The design of such classifier will ideally allow accurate quantitation of IBIs [40], however, it will not allow constructing methods that can monitor evolution of EEG activity over background grade boundaries, which obviously happens among majority of clinical patients during their brain monitoring.

Prior extensive engineering works have mostly focused on identifying discrete EEG states (e.g. burst suppression), or on discrimination of normal from abnormal backgrounds as benchmarked with visual criteria. One of the

shortcomings in benchmarking with visual EEG grading is its temporal coarseness. Visual grades are commonly assigned hourly to account for slow changes such as sleep-wake cycling ([90], [114], [81]). Other EEG grading systems have been developed to include even longer term evolution, up to over 24h, to characterize recovery from hypoxic insults [22], which as a principle reminds of the conventional approach used in the aEEG assessment [53]. We are not aware of objective computational, graded measures of background EEG activity although the clinical experience shows that the key part of brain monitoring is the follow-up of patients through different stages at hourly time scale. Our findings suggest that measures based on MF-DFA metrics may offer an advantage here: for instance, these metrics may distinguish moderately abnormal EEG from the severe and normal backgrounds, which is clinically very important. Moreover, brain states will change more rapidly in the real life, hence we wanted to compare MF-DFA-based metrics also with the automated algorithm that detects IBI levels in 15 min epochs. This pilot analysis showed that MF-DFA metrics do co-vary with IBI, and they do evolve over time. A systematic characterization and benchmarking with existing trend paradigms, especially aEEG [53] will help to identify the clinical added value of MF-DFA measures.

6.5 Conclusion

In this Chapter we explored the long-range temporal behavior for modeling and quantification of the EEG background abnormalities. For that purpose we explored DFA as well as MF-DFA concepts. Although the results are very promising, we regard our study as initial and exploratory, and various aspects need to be accounted for to determine the clinical robustness and added value obtained from the proposed method. The first practical consideration is the unknown relative sensitivity of our metrics to artefacts that are unavoidably present in real life recordings from intensive care units. This can be assessed formally by simulated addition of real EEG artefacts (cf. [82], [31], [108]). The future artefact avoidance strategies may include rejection by amplitude criteria (cf. [94]), although missing data segments may also introduce as yet unidentified confounders. The second practical consideration is the added clinical value relative to existing measures, especially the aEEG paradigm. It is conceivable that our metrics provide a theoretically and functionally complementary view on neonatal brain dynamics, yet the actual added bedside value needs to be determined in future clinical studies.

Chapter 7

Holistic approach for automated background EEG assessment

The objective of the work in this chapter is to develop an automated algorithm to quantify background EEG abnormalities in full-term neonates with hypoxic ischemic encephalopathy. The algorithm classifies 1h of continuous neonatal EEG (cEEG) into mild, moderate or severe background abnormality grade. The algorithm is based on adaptive EEG segmentation and mapping of the segments into, the so-called, segments' feature space. Three features are suggested and further processing is obtained using a discretized 3D distribution of the segments' features represented as a 3-way data tensor. Further classification has been achieved using recently developed tensor decomposition/classification methods that reduce the size of the model and extract a significant and discriminative set of features. Effective parameterization of cEEG data has been achieved resulting in high classification accuracy (89 %) to grade background EEG abnormalities. For the first time, the algorithm for the background EEG assessment has been validated on an extensive dataset which contained major artifacts and epileptic seizures. The demonstrated high robustness, while processing real-case EEGs, suggests that the algorithm can be used as an assistive tool to monitor the severity of hypoxic insults in newborns.

7.1 Introduction

A visual interpretation of EEG signals is used as the 'gold' standard in clinical practice, whereas automated EEG analysis has been mainly a research tool. For instance, automated EEG segmentation algorithms have been previously developed ([6], [70]). More specifically, in term and premature newborns, research has focused on analysis of certain EEG patterns. For example, effective sleep-wake cycle detection method ([45]), characterization of neonatal sleep EEG patterns ([5], [97]), localisation of ictal activity [35] and automated neonatal seizure detectors ([48], [33], [120], [22]) have been proposed.

Few results are, however, published to automatically assess background EEG abnormality of full-term neonates with HIE. In general, two different approaches are presented in the literature. On the one hand, some approaches focus on the detection of EEG patterns for visual grading of EEG abnormalities. For instance, algorithms for the detection of bursts or interburst intervals (IBIs) are developed ([75], [80], Matic et al dIBI 2015). Several studies, that analyzed premature neonates, also describe algorithms for EEG burst/suppression pattern detection ([95], [60], [86], [67]). On the other hand, researchers have developed methods to detect background EEG states as assessed by an expert EEG reader from selected EEG segments with a duration of 1h. For instance, a method proposed in [76] detects 'burst-suppression' state to distinguish neonates with severe HIE from healthy newborns. Furthermore, methods for automated scoring of background EEG abnormality are proposed in ([68], [114]). These methods consist of a proposed set of discriminative quantitative EEG (qEEG) features, which are used as input into machine learning classifiers. Subsequently, classifiers are optimized to replicate decisions brought by expert EEG readers.

However, in the quest to develop fully automated EEG analysis systems researchers encounter several bottlenecks. First, the number of neonates in datasets is relatively small for the development of inductive (supervised) learning methods. In some studies only six [75] or 13 neonates [97] were used. Larger studies included datasets from only 20-54 neonates ([76], [68]). Hence, low sample size make the use of machine learning techniques challenging. Second, short EEG epochs are analyzed per neonate in order to derive conclusions. For instance, 10 min epochs were selected and analyzed per neonate in [97], whereas 7 min epochs were selected per neonate and used for training of inductive classifiers by [114]. This is rather restrictive for the analysis of the EEG signal that is very nonstationary and can rapidly evolve over time. Third, artifacts represent most likely the major bottleneck for reliable automated EEG analysis. To avoid deterioration of performance, researchers usually preselect segments without artifacts and seizures and derive sets of discriminative qEEG features for background EEG state classification ([97], [68], [114]).

To develop robust and reliable automated EEG analysis systems significant progress has been achieved with EEG artifact-removal tools. For example, methods for removing muscle, electrocardiogram, pulsation and respiration artifacts have been published (e.g. [61], [65], [127], [31]). However, these methods are mostly tuned for one or a few specific artifacts, whereas in fully automated analysis of EEG background, a diverse range of artifacts are encountered that adversely affects system's performance. For example, electrode and wire problems, movement and transient muscle artifacts, to name a few, will hinder the detection accuracy. Unfortunately, a majority of artifacts as well as electrographic seizures are superimposed onto suppressed and discontinuous EEG periods, thereby masking discontinuity and hindering its assessment. Therefore, the presence of artifacts might bias the decisions of automated methods from severe abnormalities (longer EEG discontinuities) towards the group of milder EEG abnormalities.

In this study we present a method for automated assessment of background EEG abnormalities in neonates with HIE, that strives to tackle the major bottlenecks of current approaches. It is our objective to classify cEEG epochs according to one of the three severity grades (mild, moderate or severe) as would have been scored by an experienced clinical neurophysiologist without preselecting clean data segments and including several evolving cEEG epochs per neonate. We propose a tensor-based classification method that can cope with the low sample size and the presence of moderate disturbing EEG segments. The performance and robustness of the proposed method will be assessed as on a dataset of 34 newborns who have suffered perinatal asphyxia.

7.2 Methods

7.2.1 Dataset

EEG data have been recorded at Sophia Children's Hospital, Erasmus MC (Rotterdam, the Netherlands). The 34 neonates included in this study were part of a larger cohort of term asphyxiated neonates who were monitored from March 2003 till August 2007. The inclusion criteria for EEG monitoring were: gestational age of 37-43 weeks with clinical features of encephalopathy, and having at least one of the following features of birth asphyxia: a) arterial pH of umbilical cord blood $\leq$ 7.1, b) Apgar score $\leq$ 5 at 5 minutes, and c) high clinical suspicion (like fetal distress, umbilical cord prolapse, difficult labour, or a history of convulsions). Babies with congenital cardiac abnormalities, multiple congenital anomalies and inborn errors of metabolism were excluded. In addition, the neonates expressing constantly low voltage inactivity (<5 μ

V), that is, isoelectric background EEG activity, were excluded as well. The study had the approval of the Erasmus MC Medical Ethical Review Board. Informed consent was obtained from the parents/guardians prior to the onset of the registration. The EEG recordings started 2-48 (median 19) hours post partum. The median (range) duration of cEEG was 31 (20-96) hours. Seizures were recorded in 18 patients and were treated according to a protocol with anti-epileptic drugs. . The applied EEG sampling frequency was 256Hz and the EEG data were analysed using bipolar montage with 12 channels. The data have been filtered using standard FIR high-pass and low-pass filters at 0.7Hz and 20Hz. In this study, four epochs of 2h continuous EEG recordings have been selected per neonate. The epochs were selected equidistantly across EEG recordings such that the minimal distance between 2h epochs is longer than 4h. Every hour of the 2h segments was independently graded, making in total 272 (=34 x 4 x 2) 1h cEEG epochs. An experienced clinical neurophysiologist (PJC), blinded to the clinical details of the neonates, visually assessed background EEG abnormalities and classified them into: mild (and normal), moderate and severe classes. The applied background EEG grading system was adapted from the one proposed in [90] resulting in:

1. mild (and normal) - approximately interburst intervals (IBIs) < 5s; poorly organized sleep-wake cycle; recovered, continuous background EEG is assigned to this class as well
2. moderate - approximately 5s $\leq$ IBIs $<$ 10s
3. severe abnormality - 10s $\leq$ IBIs $<$ 60s, characterized by prolonged and marked suppressions.

7.2.2 Multi-dimensional structure for capturing EEG dynamics

Tensor methods provide a powerful tool to preserve underlying multidimensional structure and have been shown to be useful to analyze EEG data ([128], [124]). We will exploit the tensor structure of background EEG as illustrated in Figure 7.1. First, EEG channels are independently segmented using an adaptive segmentation algorithm [70]. Next, three features are computed for each segment. These features can be discretized into particular bins and prevalence in the different bins can be quantified as a histogram. The resulting tensor represents the prevalence of segments with a particular segments' feature distribution (Figure 7.1).

In the literature, it has been shown that similar underlying brain functioning generate similar distributions of segments' features ([13], [27]). That is, two

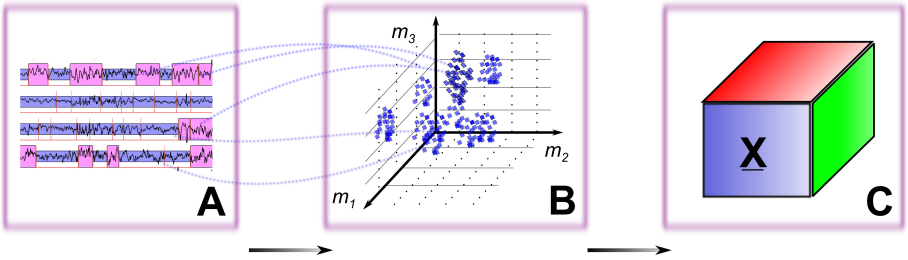

Figure 7.1: Three blocks represent the parameterization of the cEEG data stream. **A**. First, EEG signal is adaptively segmented. **B**. Segment's features are calculated for each segment and depending on the quantized features' index values (m_1, m_2, m_3) they are mapped into the discretized segments' feature space. **C**. 3D distribution is parameterized using the tensor representation to effectively capture the structure of the distribution. That is, tensor elements represent prevalence of segments with a particular discretized feature distribution.

EEG data streams showing similar patterns (e.g. tracé alternant sleep state in newborns) are expected to generate similar distributions in the segments' feature space [54]. Therefore, we assume that similar background EEG abnormalities also produce similar distributions in the segments' feature space.

7.2.3 Design of segments' features

To obtain an automated assessment of the acute severity of neonatal brain injury, features used for the parameterization of EEG segments should be correlated with the expert visual grading of background EEG abnormalities. For example, distribution of EEG amplitude represents a distinctive hallmark used by experts to classify EEG background ([130], [90]). EEG amplitude is expected to have higher values in mild background EEG abnormalities and in continuous EEG periods. In addition, spatial (global) attenuation of amplitude is pronounced in severe HIE, when EEG becomes more simplistic and suppressed. Moreover, the interplay between adjacent segments with different amplitudes within single EEG channel can be used to capture variability of the EEG signal. For instance, higher amplitude variability is expected in more continuous EEG periods. Here, the following features are defined to characterize background EEG abnormalities. For each EEG segment we quantize features' values and calculate three indexes m_1, m_2 and m_3, which would map an EEG segment into the corresponding distribution tensor element $\mathcal{X}$ (m_1, m_2, m_3). In this way, a three-dimensional histogram tensor $\mathcal{X}$ would parameterize overall cEEG epoch. According to the

visual interpretations and guiding rules for the background EEG grading, we suggest the range of features' values and the quantized values of indexes as follows:

m_1 [1-9]: peak-to-peak amplitude is calculated independently for every EEG segment. According to the peak-to-peak amplitude values m_1 obtains the following index values:

amp. (μ V)	0-5	5-10	10-20	20-30	30-40	40-50	50-60	60-120	> 120
m_1	1	2	3	4	5	6	7	8	9

Table 7.1: Index feature m_1 obtains values according to the corresponding amplitudes ranges.

m_2 [1-10]: represents global, spatial amplitude of the EEG data. At the time point, exactly at the segment's center, the amplitude of the spatially aligned segments is estimated across all EEG channels as follows. First, the EEG signal is independently segmented and the segments are classified according to their amplitude values into: Low (L) $<$ 20 μV, 20 $\mu V \leq$ Medium (M) $<$ 40 μV and High (H) $\geq$ 40 μV. Next, we count for each class the occurrences of these segments across EEG channels. To accomplish this we use three Temporal Profile signals one for each amplitude class: Low (LTP), Medium (MTP) and High (HTP). The creation of Temporal Profile signals is depicted in the Figures 7.2 and 7.3. Subsequently, from the Temporal Profile signals we derive the m_2 index:

m_2= floor $(((\text{LTP} + \text{MTP} \cdot 1.5 + HTP \cdot 2) - 12)/12 \cdot 10) + 1$,

floor - rounds towards negative infinity

The segment's index value (m_2) is in the range from 1 to 10 (Figure 7.4). Value 12 corresponds to the number of EEG channels, whereas weighting factors are set to 1.5 and 2. Lower m_2 index values, $m_2 \in [1-2]$, determine the suppressed EEG periods (e.g. from the 7th till the 13th second in the Figures 7.2 and 7.3. On the other hand, continuous EEG patterns commonly have $m_2 \in [5-7]$, whereas burst periods are characterized with values $m_2 \in [8-10]$.

m_3 [1-12]: represents the duration of the consecutive segments having the same amplitude class (L, M or H) within the single EEG montage channel. First, we determine the amplitude class of a segment: Low, Medium or High. Next, we calculate the maximum duration of the adjacent segments having the same amplitude class. Finally, the quantized index value m_3 would have the following values as represented in Table 7.2.

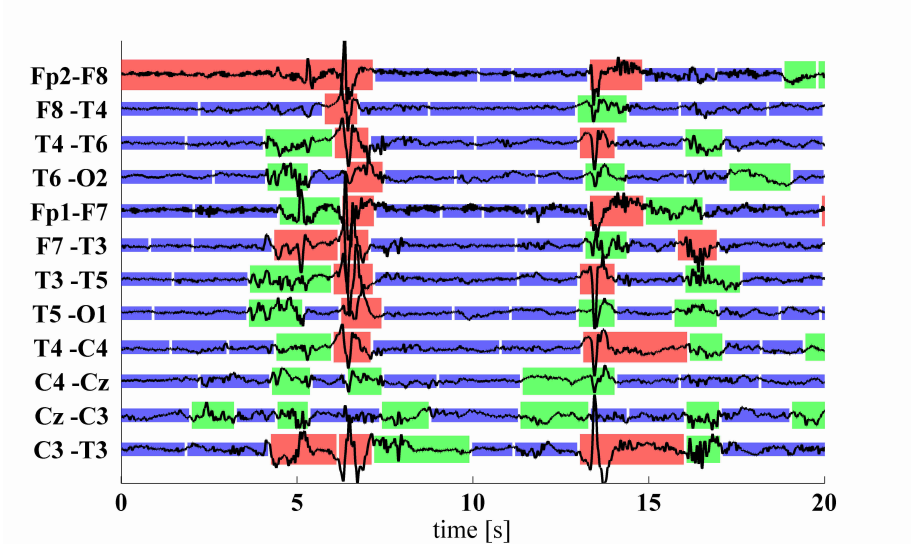

Figure 7.2: An EEG epoch is adaptively segmented and the segments are classified into three peak-to-peak amplitude classes: Low<20 μ V (blue), 20 μ V $\leq$ Medium $<$ 40 μ V (green) and High $\geq$ 40 μV (red).

Table 7.2: A segment is classified into one of the three amplitude classes: Low (L), Medium (M) or High (H). Within the single EEG channel, adjacent segments that express the same amplitude class are merged and duration of this interval is calculated. The interval duration determines the values for m_3 index parameter according to the table. All consecutive segments which are merged in this way would have the same m_3 index values regardless of their position in this segments' stream.

interval [s]	Low	Medium	High
0-5	1	5	9
5 - 10	2	6	10
10 - 20	3	7	11
>20	4	8	12

The following example illustrates the ability of segments' features to capture various interplays of the adjacent EEG segments. Five segments (A, B, C, D, E) are selected and indices m_1, m_2 and m_3 are calculated (Figures 7.5 and 7.6). For example, segments A and E are assigned to frequency bin (2, 4, 1) since their amplitude is attenuated, they are spatially aligned with segments that do not represent the global EEG attenuation (m_2=4) and they are isolated

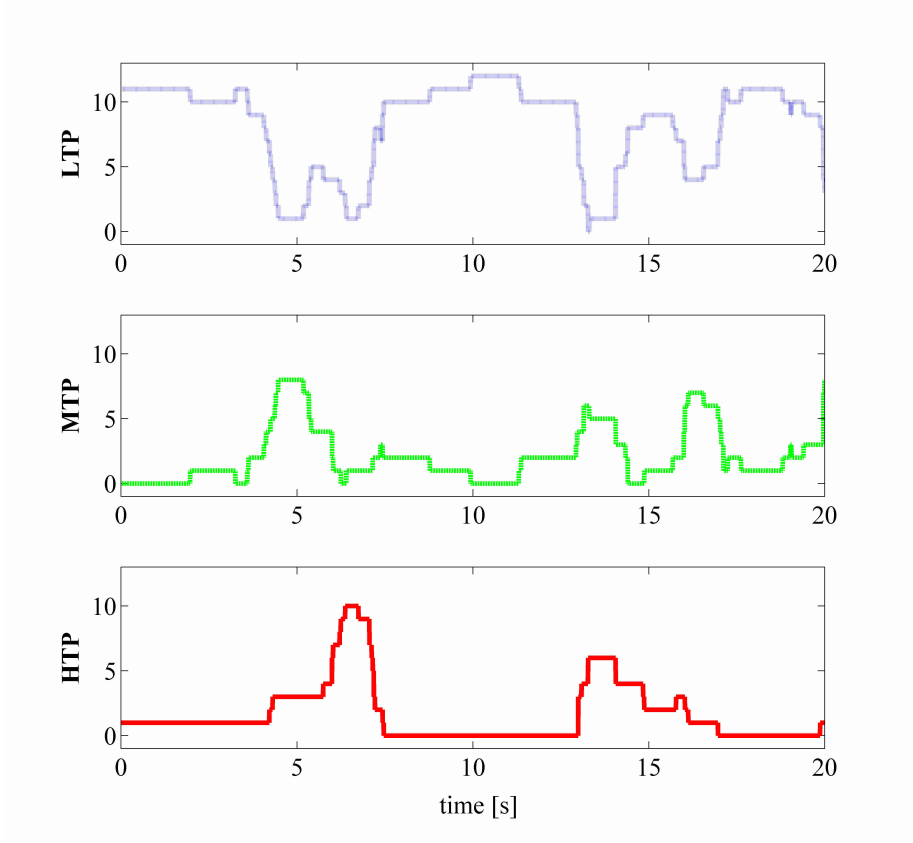

Figure 7.3: Three temporal profile signals (LTP, MTP and HTP) count the occurrences of the amplitude classes across EEG channels.

low amplitude class segments (m_3=1). Segment B is mapped into (7, 5, 9) as it is a high amplitude segment, spatially aligned with segments of 'normal' EEG variability and merged with the consecutive high class segment the entire interval duration is shorter than 5s (m_3=9). Segment C, mapped into (2, 6, 4), is a low amplitude segment quantifying prolonged suppressed activity in this EEG channel (>20s) and therefore m_3=4. On the other hand, the segment D corresponds to the frequency bin (4, 2, 6), since it is a medium class segment that together with the neighboring medium class segments encompasses an interval from 5 till 10 seconds (m_3=6). Further illustration of mapping the segments into a 3D distribution is represented with two 2D plots (Figures 7.7 and 7.8). The elements of the 3D structure are summed along the third mode obtaining a 2D distribution plot. For example, by summing along the mode m_2

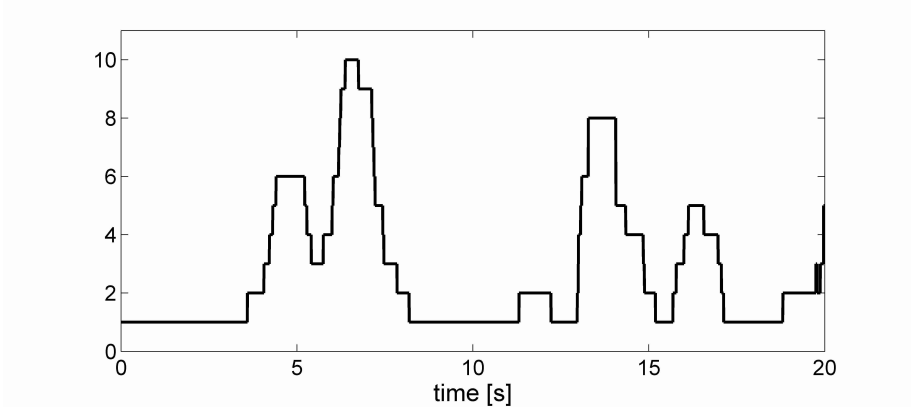

Figure 7.4: Global grade of the spatial EEG amplitude, m_2 value, is derived using the signals (LTP, MTP and HTP).

we generate a 2D distribution:

$$\mathbf{X}2(m_1, m_3) = \sum_{i=1}^{10} \mathcal{X}(m_1, i, m_3)$$

7.2.4 Creating a tensor distribution structure

For every segment within a cEEG epoch we calculate quantized m_1, m_2 and m_3 index values. Next, the corresponding three-dimensional structure is created by counting the prevalence of EEG segments with a particular feature distribution $\mathcal{X}(m_1, m_2, m_3)$. We illustrate in Figures 7.9, 7.10, 7.11, 7.12, 7.13 and 7.14 that the generated 3D distribution structures have clearly distinguishable patterns for different background EEG grades. For each class (mild, medium and severe), 3D distribution structures are averaged across all 1h graded cEEG epochs and depicted in Figures 7.9, 7.10, 7.11, 7.12, 7.13 and 7.14.

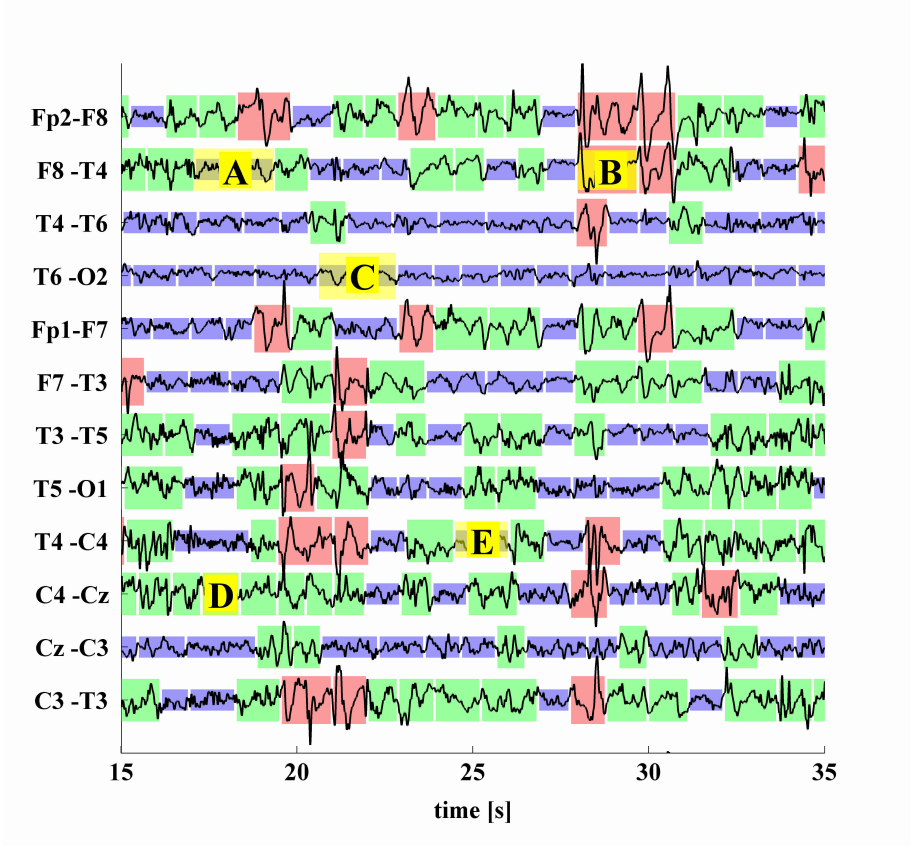

Figure 7.5: Epoch of EEG signal is adaptively segmented. The segments are colored according to their amplitude values into blue (Low), green (Medium) and red (High). Five segments are marked to illustrate the quantification of various interplays with the adjacent segments: A(2, 4, 1) B (7, 5, 9), C(2, 6, 4) D (4 ,2 ,6) , E (2 ,4, 1).

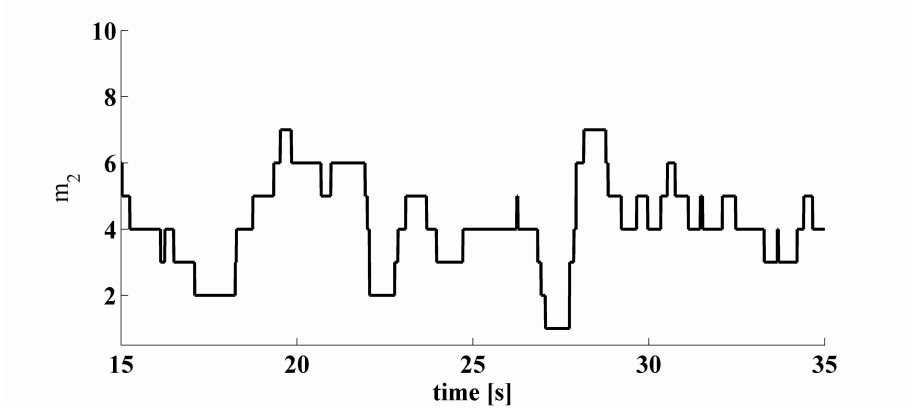

Figure 7.6: Feature index values m_2 representing global amplitude are displayed.

7.2.5 Tensor decomposition techniques: dimensionality reduction step

The main motivation to use multi-dimensional structures is to extract discriminative and interpretable information. The created 3D structure is represented as a 3-way tensor $\mathcal{X}$ of size $R^{9x10x12}$, where each element characterizes corresponding multi-channel EEG activity. Due to a large number of histogram frequency bins (9 x 10 x 12=1080), classical supervised classification techniques cannot be directly applied. The size of the training and testing datasets are too small to obtain a reliable classification due to limited number of encephalopatic neonates (<50). Therefore, to reduce the model dimensions, a recently developed tensor decomposition technique is applied to extract a new, discriminative reduced set of features from a tensor $\mathcal{X}$. The method is based on a Tucker N-way decomposition model. For three-dimensional data, the basic Tucker-3 model of a tensor $\mathcal{X}$ is illustrated in Figure 7.15.

The Tucker-N decomposition model is represented as a product of a core tensor $\mathcal{G}$ and a set of factor (basis) matrices $\mathbf{U}^{(n)}$:

$$\mathcal{X} = \mathcal{G} \times_1 \mathbf{U}^{(1)} \times_2 \mathbf{U}^{(2)} \times_3 \mathbf{U}^{(3)} + \mathcal{E}$$

The core tensor $\mathcal{G}$ is usually of much smaller dimensions than the original tensor $\mathcal{X}$ and tensor $\mathcal{E}$ characterizes the approximation error of a model (or fit). In

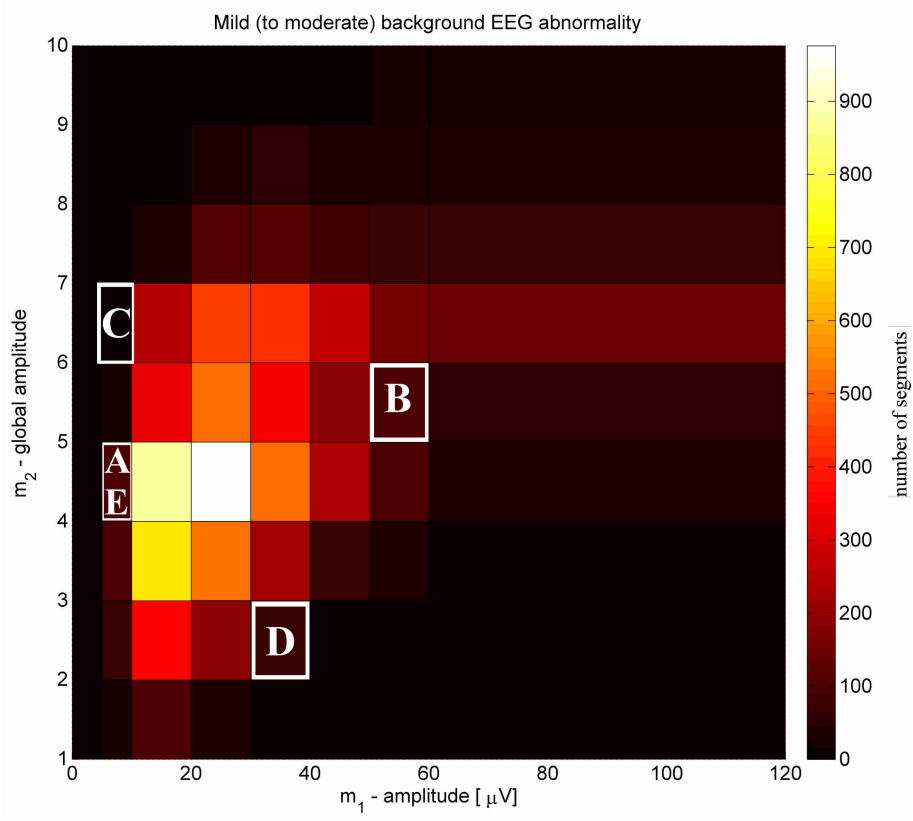

Figure 7.7: Mapping of the EEG segments from Figure 7.5 into the distribution structure. The view is displayed along the axis m_1 and m_2, whereas the color bar represents the number of EEG segments in a particular frequency bin.

case that factor matrices and a core tensor are orthogonal, the Tucker model can be considered as an extension of the Singular Value Decomposition (SVD) model, known as the Higher Order SVD (HO-SVD) [29]. To calculate factor basis $\mathbf{U}^{(n)}$, different algorithms can be applied with respect to the constraints imposed on the factor basis. For instance, orthogonality can be imposed leading to the well-known higher order orthogonal iterations (HOOI) algorithm [30]. In addition, non-negativity, sparseness or statistical mutual independence of the factor basis can be imposed [105]. In this work, we will apply constraints to create a core tensor with discriminative properties that is useful for the multi-class classification tasks [105]. That is, class labels are incorporated into the algorithm to better capture and model the differences of input data tensors

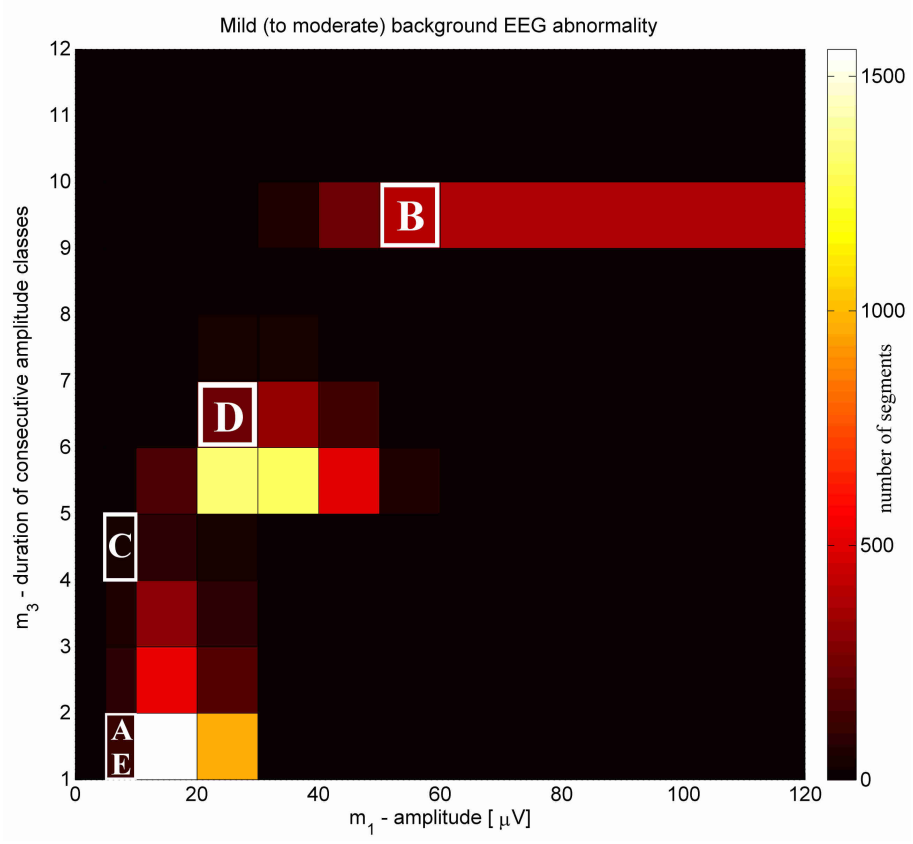

Figure 7.8: Mapping of the EEG segments from Figure 7.5 into the distribution structure. The view is displayed along the axis m_1 and m_3, whereas the color bar represents the number of EEG segments in a particular frequency bin.

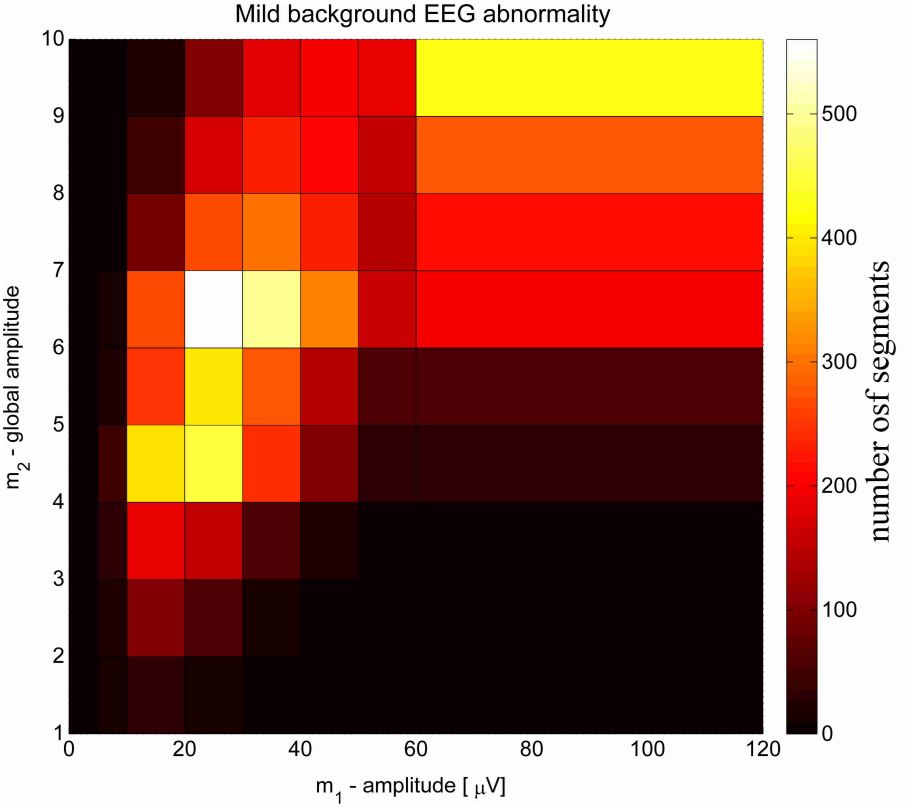

Figure 7.9: 2D distribution of mild background EEG abnormalities displayed along modes m_1 and m_2, whereas the color bar represents the number of EEG segments in a particular frequency bin.

($\mathcal{X}$) between data classes. Mathematical details of the HODA algorithm and how it is applied onto EEG data are described in the sub-chapter 3.5.2. In summary, the HODA algorithm tries to optimize the factor basis in such a way that the core tensors $\mathcal{G}$ from the same classes are as similar as possible. On the other hand, it aims to increase the 'differences' of the core tensors from the different classes. The training part of the algorithm calculates the TUCKER bases using the training data set (Figure 7.16).

As the next step, we use the estimated factor basis $\mathbf{U}^{(n)}$ with a HODA algorithm to build a projection filter (Figure 7.16). To extract the set of features from the test data tensors $\dot{\mathcal{X}}$ (class labels are not known) we create the corresponding core tensors:

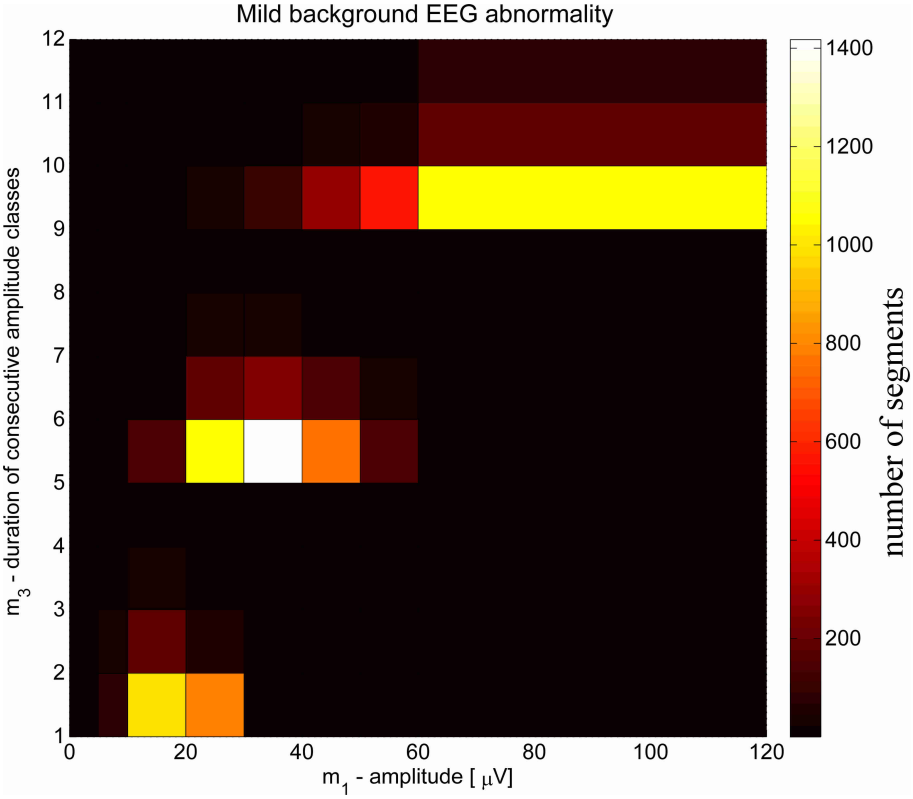

Figure 7.10: 2D distribution of mild background EEG abnormalities displayed along modes m_1 and m_3, whereas the color bar represents the number of EEG segments in a particular frequency bin.

$$\dot{\mathcal{G}}^t = \dot{\mathcal{X}}^t \times_1 \mathbf{U}^{(1)T} \times_2 \mathbf{U}^{(2)T} \times_3 \mathbf{U}^{(3)T}$$

That is, the test data tensors are projected onto a feature subspace spanned by the calculated set of basis factors $\mathbf{U}^{(n)}$. In addition, since the calculated factor basis $\mathbf{U}^{(n)}$ are orthogonal, according to the HODA algorithm implementation, the regular transpose operator of the matrix, T is applied.

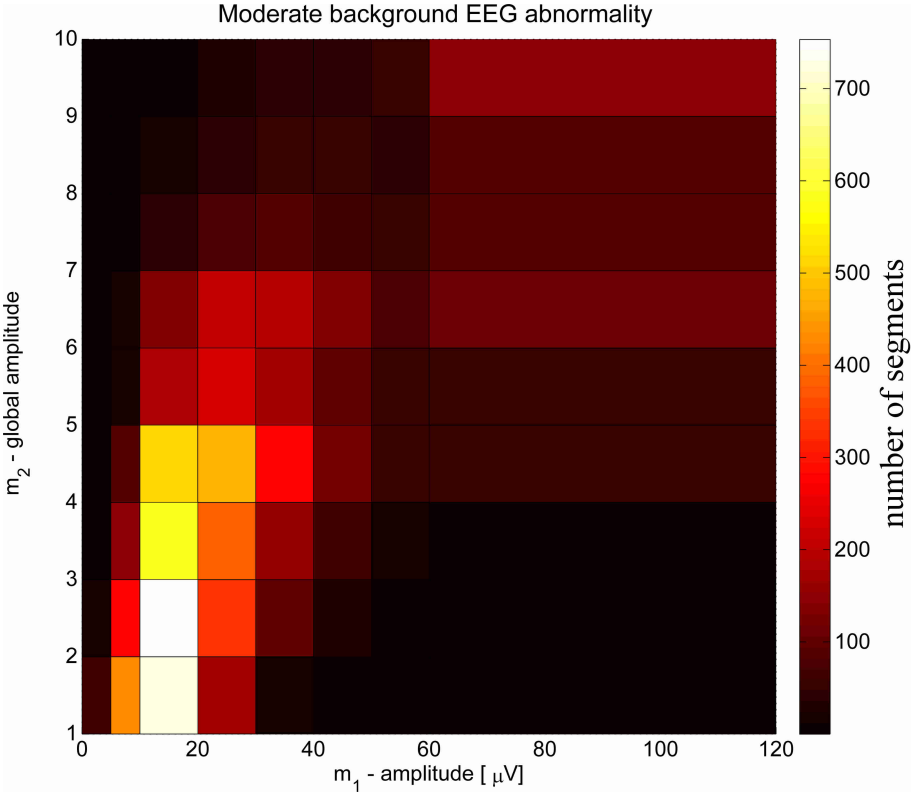

Figure 7.11: 2D distribution of moderate background EEG abnormalities displayed along modes m_1 and m_2, whereas the color bar represents the number of EEG segments in a particular frequency bin.

The extracted features, elements of the core tensor $\dot{\mathcal{G}}^t$, are then compared with the training features using a supervised machine learning classifier (LS-SVM). The training and test phase of the algorithm and the overall classification scheme are depicted in Figure 7.16.

7.2.6 Classification

After the decomposition step, the reduced set of discriminative features $\mathcal{G}$ is calculated both for training and test data samples. To accomplish this, HODA algorithm's parameters were set to model (fit) 95% of the original data tensor. In this way, the original data tensors (9x10x12) are decomposed, resulting in

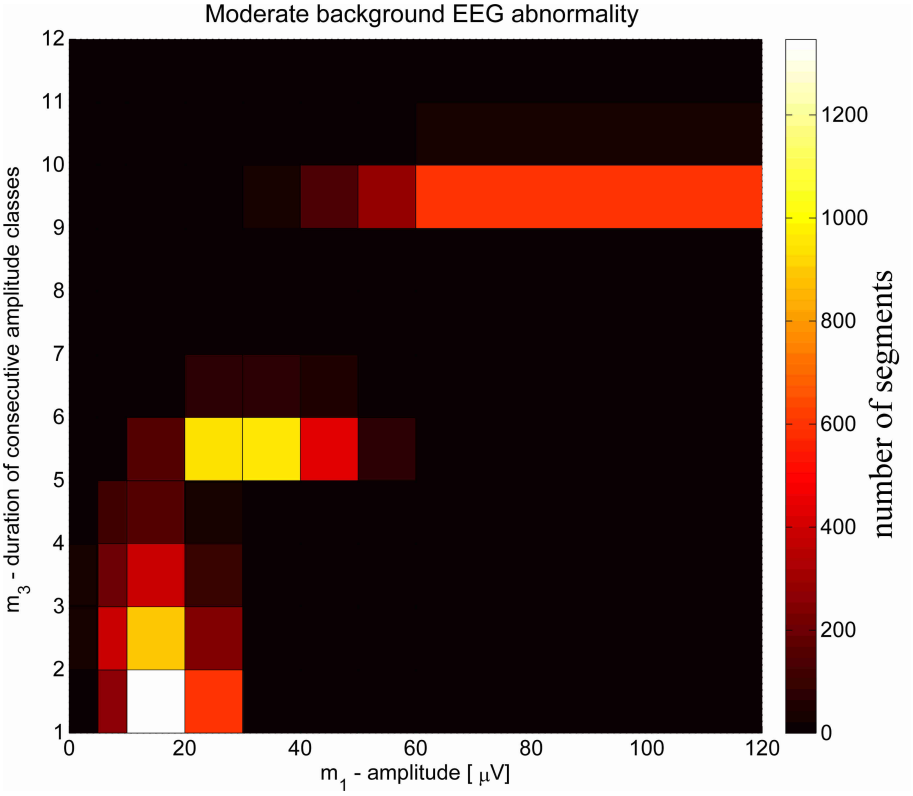

Figure 7.12: 2D distribution of moderate background EEG abnormalities displayed along modes m_1 and m_3, whereas the color bar represents the number of EEG segments in a particular frequency bin.

core tensors ($\mathcal{G}$) of dimensions 4 x 4 x 5 (=80). The number of 80 features is still high and a subset of the most significant and discriminative features (elements) from the core tensors are selected as proposed in [105]. Fisher information ranking score has been applied during the training (and testing) phase and the information indices are calculated for all elements from the core tensors $\mathcal{G}$ and are sorted into descending order. Further classification has been performed using 25 most discriminative elements and used as input feature vectors into LS-SVM classifiers (Figure 7.16). Next, standard inductive supervised classification techniques are applied to classify corresponding background EEG grades. In this study, the Least Squares Support Vector Machine (LS-SVM) classifier has been applied [118]. To perform multi-class classification (3 classes), prior encoding of the classes is applied, resulting in training of two LS-SVM classifiers

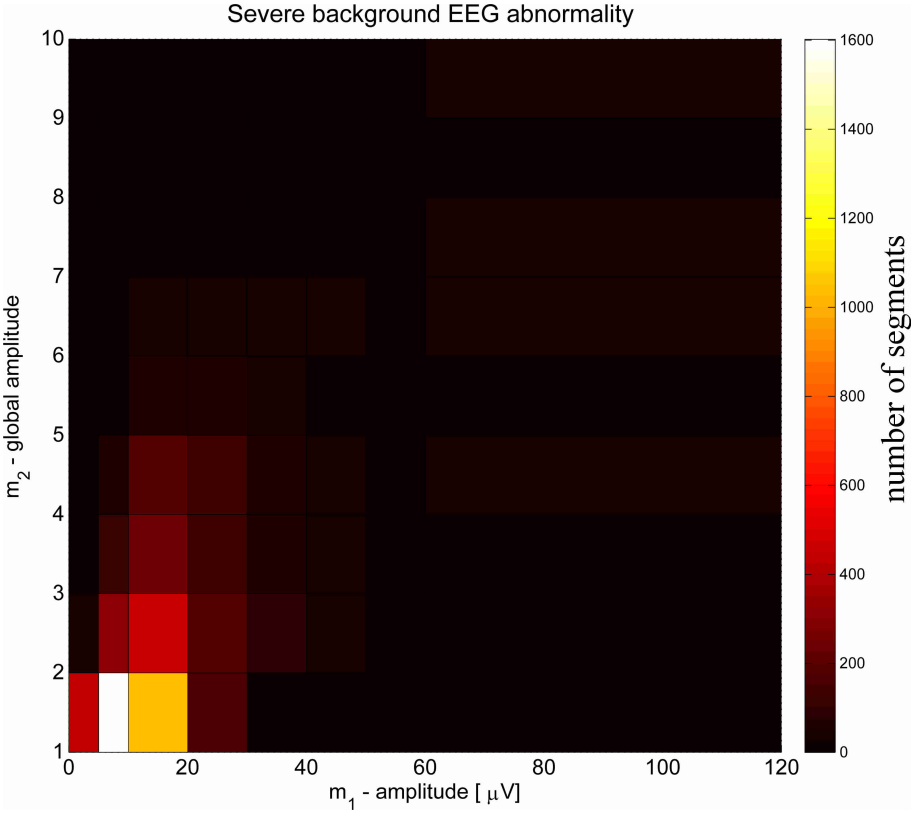

Figure 7.13: 2D distribution of severe background EEG abnormalities displayed along modes m_1 and m_2, whereas the color bar represents the number of EEG segments in a particular frequency bin.

using Gaussian kernel. A 'One vs one' encoding scheme has been applied as proposed in [99]. Next, a 4-fold cross-validation method has been applied and as a criterion function 'misclassification error' has been used. Additionally, the leave-one patient out (LOO) method has been applied during training and testing phase. For a single test patient, 8 epochs of 1h cEEG were used for the automated grading, whereas the 264 1h cEEG epochs were used for the training phase. During each iteration the decomposition of the input data tensors and the training of the LS-SVM classifiers have been repeated.

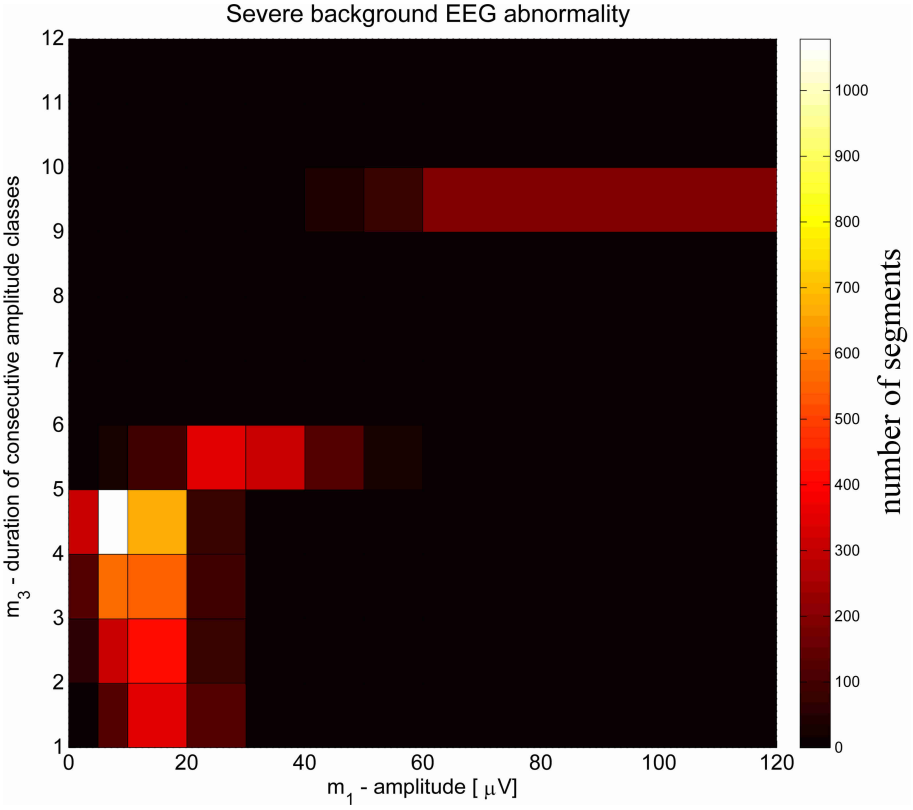

Figure 7.14: 2D distribution of severe background EEG abnormalities displayed along modes m_1 and m_3, whereas the color bar represents the number of EEG segments in a particular frequency bin.

7.3 Results

7.3.1 Automated assessment of background EEG of 1h long epochs

The results of the background EEG classification are presented as a confusion matrix in Table 7.17. The table offers insight into an agreement of automated classification compared to visual background EEG grading by an experienced clinical neurophysiologist (PJC). The achieved classification accuracy is 89%. The algorithm successfully classified the majority of severe and mild cases. Moderate background EEG class resulted in a slightly higher number of

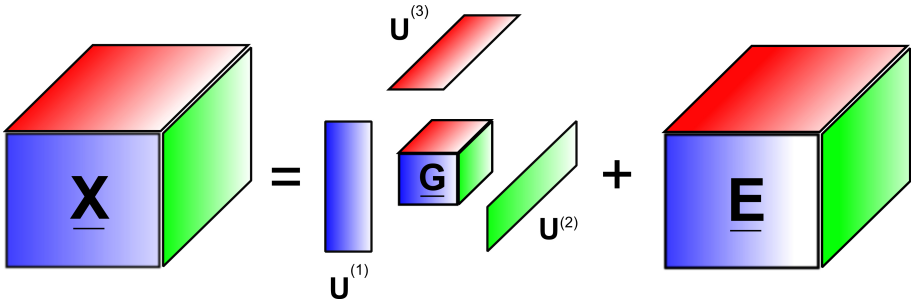

Figure 7.15: Illustration of a tensor decomposition using a Tucker-3 model. The objective is to estimate factor matrices $\mathbf{U}^{(n)}$ and a core tensor $\mathcal{G}$. In general, the constraints are imposed on factor matrices $\mathbf{U}^{(n)}$ such as orthogonality, non-negativity and/or statistical mutual independence. If the orthogonality is imposed, the decomposition can be seen as an extension of the singular value decomposition (SVD) into a higher dimension.

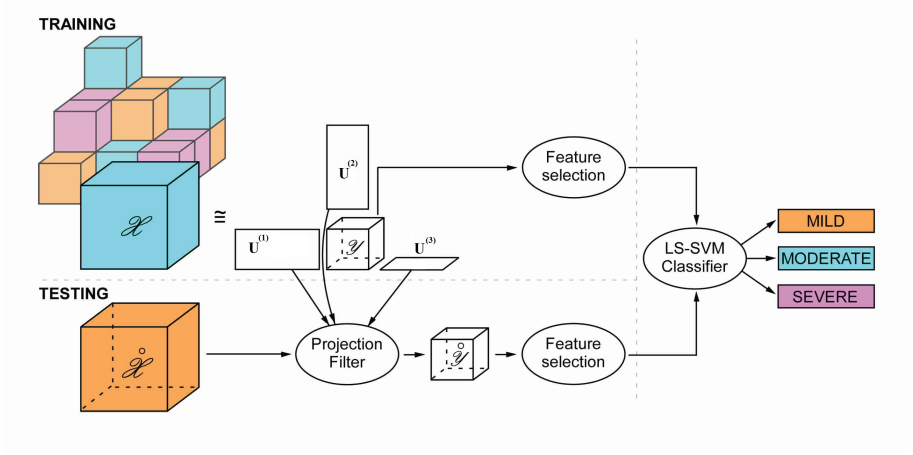

Figure 7.16: Flow chart illustrating a classification procedure based on the Tucker decomposition of the concatenated tensor $\mathcal{X}$ consisting of all sampling training data $\mathcal{X}^{(k)}$. Reduced features are obtained by projecting the testing data tensor $\dot{\mathcal{X}}$ onto the feature subspace spanned by factors (bases) $\mathbf{U}^{(n)}$ (Projection filter). The most discriminative elements are selected from the core tensors, using the Fischer selection score and used for the final classification. Output of the Least-Squares Support Vector Machine (LS-SVM) classifiers provides the assessed background EEG grade.

Automated \ Expert EEG reader	MILD	MODERATE	SEVERE
MILD	73 (91%)	6	1
MODERATE	7	44 (76%)	7
SEVERE	0	8	126 (94%)
Achieved accuracy	91%	76%	(94%)

Figure 7.17: Confusion matrix represents agreement of automated classification method and the expert EEG reader. 1h cEEG epochs were classified into mild, moderate or severe background EEG class. All classified epochs represent non-preselected, real case EEG recordings. The overall classification accuracy of 89% (=(73+44+126)/272) has been achieved.

misclassifications, as it is the 'in-between' class between mild and severe. In 31 patients, correct grading of 1h cEEG epochs ranged from 6 to 8 out of 8 epochs. In two patients, EEG grades were 'in-between' mild and moderate resulting in 4 correct detections out of 8 epochs. Finally, for one neonate, showing severe background EEG with very pronounced artifacts, 4 epochs were misclassified.

7.3.2 Benchmarking

To additionally confirm the results, we examine the scores determined by an expert EEG reader and the automated classifier. We portray those grades with the median interburst interval values detected within the 1h of cEEG using the automated IBI detector [80]. As can be seen from Figure 7.18, the grades are correlated with the median IBI values. Severe background EEG can be determined using IBI detector as it mainly consists of burst-suppression patterns. On the other hand, mild and moderate grades do not always have easily interpretable but rather overlapping ranges of IBIs demonstrating the added value of the new framework. Additionally, 40 out of 80 1h cEEG epochs (50%) scored as grade mild do not contain IBI patterns that can be used for background EEG parameterization. In such cases, our approach still allows to parameterize EEG segments as it does not rely on the strict concept of IBI.

7.4 Discussion

This work was motivated by the need to improve the automated EEG analysis in the NICUs and in particular to assist in real-time monitoring of neonates

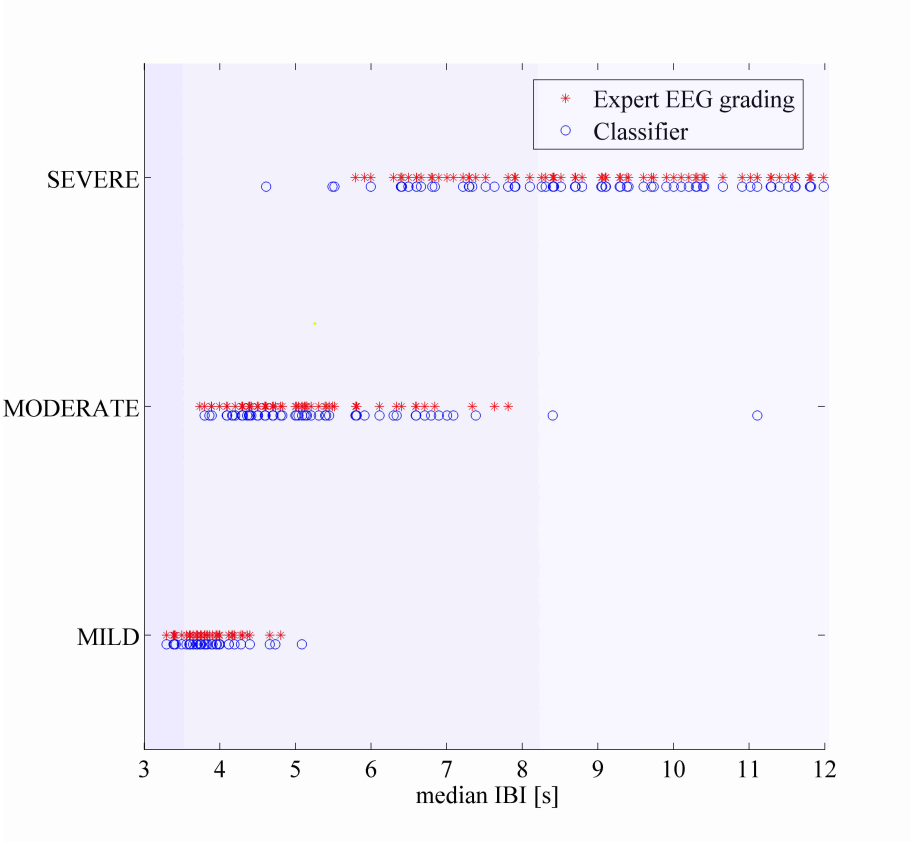

Figure 7.18: Comparison of background EEG grades scored on 1h of cEEG by an experienced clinical neurophysiologist (red) and automated assessment of those grades (blue). These grades show correlation with the median interburst interval (IBI) values. Background EEG activity not containing IBIs are not displayed here (40 out of 80 mild (to normal) background EEG grades).

with HIE. Here, we presented a novel method for the automated assessment of background EEG abnormalities. It is based on a new concept that uses intrinsic structure of 3D prevalence of the designed segments' features. The method classifies cEEG periods of 1h into mild, moderate or severe background EEG classes. First, the method exploits the concept of adaptive EEG segmentation and processing of segments' features in the segments' feature space ([5], [70]). We suggested to quantify the obtained segments with 3 features, which to some degree mimic the visual interpretation of the background EEG abnormalities. Next, we discretized the segments' feature space and represented it as a large 3-way tensor. In this way, continuous EEG data streams have been parameterized. The obtained data tensors have then been efficiently decomposed using a recently developed, higher order discriminative analysis (HODA) algorithm [105]. In this way, a small discriminative set of features has been extracted from the data tensor. Next, using LS-SVM classifiers high accuracy has been achieved to classify background EEG abnormalities. In addition, we did not preselect data based on absence of artifacts and seizures, effectively demonstrating that the proposed method is robust enough to be used in clinical practice.

The main original contribution of this study is the effective and holistic EEG parameterization step. In general, this is a challenging task as features have to be extracted from multiple EEG channels from 1h duration of recordings. Our approach of EEG quantification is an extension of the concepts initially proposed in [5]. In that study, adaptive EEG segments, were mapped into the segments' feature space and certain EEG patterns were explored. In another study, researchers adaptively segmented the EEG signal and used segments' features, expressed as median values, to quantify EEG data in newborns [97]. Here, instead of a single feature's median value, we used a high-dimensional histogram to better capture the overall segments' feature distribution. For instance, we designed nine frequency bins to describe overall amplitude distribution within EEG data. In this way, more discriminative EEG parameterization is obtained, thereby quantifying the differences between distributions' heavy tails. Quantifying these differences, a more effective modeling of background EEG classes has been accomplished. We have extensively tested other segments' features such as power frequency bands (alpha, beta, theta, delta), duration of segments as well as some of the implemented 'hand-chosen' features. All these features were calculated independently for a single EEG segment as done in the previous studies ([5], [97], [98]), but did not give great discrimination between classes. Here, two new features were found more effective to consolidate temporal and spatial relations between adjacent EEG segments (m_2 and m_3). In this way, we succeeded to capture and exploit the multi-channel structure of the EEG signal.

During visual assessment of background EEG abnormalities, researchers

define EEG discontinuity and suppression of amplitude as the main hallmark for the EEG quantification ([130], [90], [123]). More specifically, classical 'burst-suppression' IBIs and/or tracé discontinue IBIs are used for the visual classification of background EEG severity. The guiding rules for background EEG scoring use duration of IBIs as follows: mild (IBI<5s), moderate (IBI<10s) and severe (10s<IBI<60s) ([90], [22]). With respect to this, duration of IBIs is indirectly quantified into the 3D distribution tensor. In particular, low amplitude segments were used to detect interburst intervals in our previous studies ([80]). Therefore, longer duration of consecutive low amplitude classes ($m_3 \in$ [2-4]) which are also globally attenuated across all EEG channels ($m_2 \in$ [1-2]) correspond to IBI patterns. For instance, in moderate background EEG abnormalities duration of IBIs is assumed to be less than 10 seconds. Therefore, EEG segments constituting IBIs<10s would be mapped into a tensor area where EEG is globally attenuated ($m_2 \in$ [1-2]) and where duration of consecutive low amplitude segments is less than 10s ($m_3 \in$ [1-2]). In contrast, in severe background EEG abnormalities (10s<IBIs<60s), the duration of consecutive low amplitude classes would be longer than 10s having $m_3 \in$ [3-4]. Therefore, tensor structure can effectively discriminate various trends of IBI duration encountered in neonatal EEG data. Background EEG of neonates with severe HIE consists of mainly burst-suppression patterns ([40], [129]). These background EEG states can be quantified with an automated IBI detection method ([75], [80]). However, in mild and moderate HIE, EEG background consists of periods of more continuous background activity, expressing higher amplitude variability. Hence, EEG quantification using only IBI values would not be possible [38]. Because of this, researchers defined various EEG states and patterns such as 'transitory discontinuous' [17], 'modified' burst-suppression [111] and 'constantly discontinuous' [38]. In such cases, an expert EEG reader attempts to assess background EEG grades according to the level of amplitude suppression, variability and global amplitude attenuations. Consequently, this motivated us to structure these characteristics into a distribution tensor where we distinguish subtle differences in amplitude values, global level of suppression and alternations of three amplitude classes (L, M and H). It is important to note that, although various background EEG scoring systems (and terminology) have been used, grading using a single system is usually rather consistent with very high inter-rater agreement and consensus ([22], [68]). Last but not least, HIE injury is not static and it evolves over time. When a neonate is recovering from severe asphyxia, EEG is becoming more continuous and burst suppression patterns evolve into tracé discontinue and further to tracé alternant patterns. In such cases, the method developed for IBI detection would stop working accurately. On the other hand, our method will provide accurate background EEG assessment during all phases of monitoring.

In the literature, other approaches for the background EEG quantification

are based on the combination of qEEG features that were fed into supervised classifiers ([76], [68], [114]). In these studies, the EEG features were calculated on fixed-size windows (e.g. 1 min), and were further averaged across EEG channels and across time interval (e.g. 1h). In this way, the researchers assume that HIE is expressed in EEG as a global phenomenon. However, the assumption that HIE is global as observed in EEG does not necessarily always hold. In particular, it is the case in milder EEG asymmetries that the set of features' values averaged across all EEG channels would be difficult to discriminate. On the other hand, our approach investigates segments' amplitude distribution within single EEG channels and can detect subtle EEG abnormalities. For instance, severe attenuation of 40% of the EEG channels implies localized brain injuries (e.g. frontal, occipital areas). This would be reflected in a tensor representation since large number of prolonged consecutive low amplitude classes would occur (e.g. $m_3 \in$ [2-4]), and yet there would be no global EEG attenuation (e.g. $m_2 \in$ [3-5]). Another advantage of the tensorial framework is that it can easily be expanded into a 4D tensor, where mode-4 would correspond to unequivocal brain areas: frontal, parietal, central and occipital. Then, the method would be able to explicitly explain milder EEG abnormalities. This would assist to better study the brain functioning in an automated way. Naturally, other features (modes) can be added into a model, such as a recently developed 'activation synchrony index', which would incorporate interhemispheric synchrony [108].

In addition, our method proved to be very robust to major artifacts. For instance, transient high amplitude EEG patterns (e.g. movement, electrode and eye artifacts and/or paroxysmal like activity-seizures) would be mainly mapped into 'frequency bins' with very high amplitudes (e.g. $>60\mu$V and $m_1 \in$ [8-9]). Hence, they would not interfere with the properties of the remaining EEG segments of prior interest (e.g. $<60\mu$V) and further background EEG classification. Other patterns, such as for instance bursts, would be mapped into globally 'high' amplitude frequency bins and would be analyzed separately from suppressed intervals. On the other hand, approaches that use fixed-length windows would not assess burst and suppression patterns independently, but those would be averaged across proposed qEEG features.

Moreover, an interpretation of the applied features is of paramount importance. Measures related to spectral entropy [76] or white Gaussian processes [114] are not intuitive and easily interpretable. On the other hand, a parameterized distribution model is both discriminative and can be used for visual interpretation. This is a distinctive advantage of our method as we can interpret a cEEG epoch (1h) with two compact 2D distribution plots. Moreover, the distribution plots provide information which are consistent with the visual grading rules as defined in [90]. For instance, the proposed amplitude values of mild background EEG abnormalities (e.g. range 30-50μV) can be observed in

2D distribution plots.

In this study, we have applied tensor methods to structure and process the parameterized EEG data. On the other hand, in previous studies researchers commonly used vectors to quantify and classify continuous EEG data. For instance, the classification method for the detection of 'burst-suppression' background EEG state applied feature vectors and the classification accuracy was high [76]. Yet, this approach performed poorly during the classification of more subtle sleep states in newborns. Compared to this approach, more effective parameterization of EEG sleep states has been achieved in [98] and, as a result, it yielded a large number of parameterization elements structured as a matrix. Subsequently, the comparisons between sleep states (quiet vs. active sleep) have been obtained with factor analysis. In our study we parameterized EEG with a much larger number of elements and employed more advanced methods based on multi-linear algebra that can manage high-dimensional data. The proposed tensor decomposition methods have been successfully applied in many neuroscientific researches and represent a new concept in brain data analysis [23].

The classification accuracy of background EEG classes obtained in our study is 89%. Therefore, it is similar as the results achieved in [114] where a value of 83% is reported. However, these results were obtained on preselected data where parts with major artifacts were excluded and the epochs were inspected so that the background EEG grade is consistent throughout the 1h cEEG epoch. Therefore, in the real case scenarios, it can be concluded that the accuracy of the proposed methods would decrease. On the other hand, our data contained major artifacts as well as epileptic seizures expressing compelling seizure burden in 18 neonates. Moreover, the data have been selected randomly and background EEG grade within 1h was not always consistent.

In this study, the presence of long-lasting severe artifacts mostly affected the EEG data classification. Therefore, the future research studies should be aimed towards the development of even more robust methods and the validation of methods should be performed on large datasets without the pre-selection of the data. In such cases, two directions are feasible, (1) to develop a method which is very robust to artifacts or (2) to develop a method which would pre-select EEG data. For the latter, EEG data periods severely affected with artifacts can be excluded using approaches similar to one proposed in (e.g. [132], [91]). Consequently, the method should provide an automated output for clean EEG periods, assisting in this way clinical staff in the NICUs.

7.5 Conclusion

The idea of exploration of the EEG in the segments' feature space dates back to the 1980s ([6], [5]). In contrast to those initial approaches, we have introduced in this study an interplay of the adjacent segments' and used that as novel features. This contribution to the EEG quantification in our application seemed to be of the greatest added value that enabled very high classification accuracy. Furthermore, the quantification of longer EEG periods (e.g. 15 min or 1h) always yielded a large number of parameters that were difficult to effectively process and analyze. Here, the novelty is that this is the first study that creatively structured EEG within the tensor framework. This idea allows numerous additional improvements and investigations that will improve the current state of the art of the classification algorithms in the neonatal EEG applications.

Chapter 8

Conclusion and Future work

Several algorithms for the neonatal EEG quantification are presented in the previous chapters. Here, we comment and discuss the proposed algorithms and give motivation why the particular choice of the development has been chosen. In addition, we discuss when the algorithms will be the most useful in the NICUs and what are the necessary approaches for their further validation. Finally, we present new directions, challenges and open problems that require focus in future. In this way, the automated solutions may be transferred from research practice into a routine clinical use in the NICUs.

8.1 Overview of the developed algorithms

The work in this thesis was very interdisciplinary. It was driven by the need to provide automated EEG solutions in the busy NICU environment. During the thesis, numerous meetings with clinical EEG experts were held to discuss the relevant EEG patterns. Hence, it was important that the patterns are visually interpretable and acceptable by the medical community. In parallel to this, the emphasis in this thesis was also given to the data-driven findings that are difficult to be assessed visually.

The developed algorithms are designed to detect and quantify the following:

1. dynamic interburst intervals. It has already been mentioned that this parameter is the most established hallmark in visual EEG diagnostics of HIE abnormality. We have developed a robust method that we have

tested on an extensive dataset. In addition to the standard duration of IBIs, we have also introduced the measure of amplitude as an additional bio-marker. In order to get a trustworthy measure, the post-processing step has been introduced to keep only accurate detections whose amplitude levels are not biased by artifacts. Compared to the similar approaches in the literature (e.g. [68], [40]), our solution provides a continuous and gradual monitoring of the HIE evolution. Moreover, such refined monitoring cannot be achieved with the visual, relatively dichotomous background EEG grading using only 4 grades. Here, we illustrate how the algorithm can be used for the bedside clinical use. After the start of the EEG monitoring of an asphyxiated infant, both the duration-decrease and amplitude-increase show the recovery of the HIE in the example infant (Figures 8.1 and 8.2).

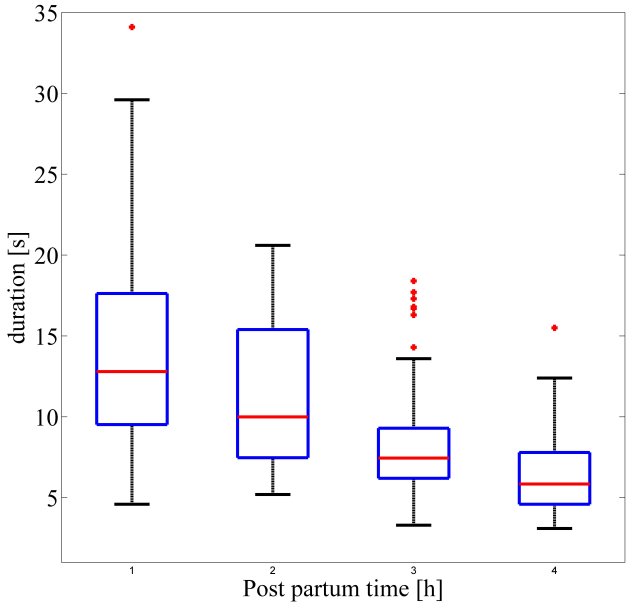

Figure 8.1: Median dIBI durations are plotted for processed four 1h EEG distinctive post partum hours of monitoring: (1) 21-22h, (2) 27-28h, (3) 33-34h and (4) 39-40h. In this example, there is an improvement of the infant's condition. Consequently, this neonate had a normal follow-up at 6 months examination.

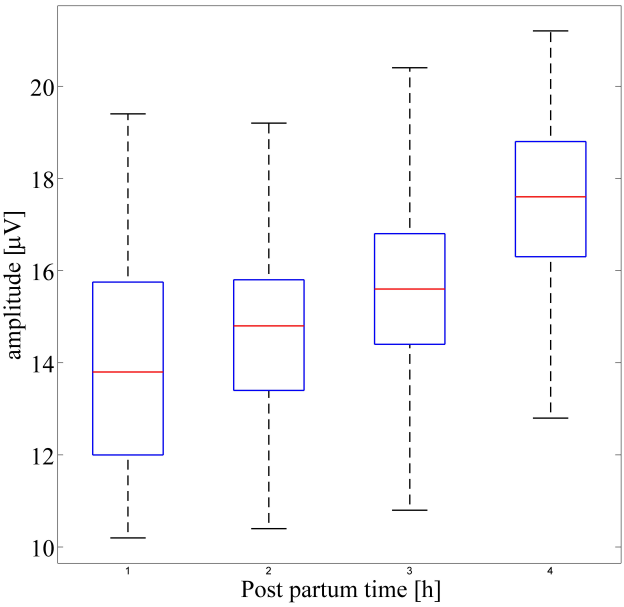

Figure 8.2: Median dIBI amplitudes are plotted for processed four 1h EEG distinctive post partum hours of monitoring: (1) 21-22h, (2) 27-28h, (3) 33-34h and (4) 39-40h. This is the same infant as in the Figure 8.1.

2. Long-range temporal behavior in the neonatal EEG. In this study, we have for the first time explored the LRTC in the neonatal EEG using DFA and MF-DFA paradigms. The importance of this finding is that MF-DFA metric proved to be efficient for the classification of EEG states as well as for the fine real-time tracking of the HIE evolution. The advantage of this method is that the application of the MF-DFA does not require data labeling from clinical EEG experts. With respect to that, this method may be seen as completely objective when compared to other methods.

3. Background EEG grading of 1h long epochs. A holistic approach for the background EEG assessment has been proposed. The algorithm performs segmentation and the segments' features are mapped into higher-order tensor distribution structure. This algorithm showed high accuracy for the classification of the background EEG grades. Its importance is that this algorithm can be used for the differentiation of mild and continuous

EEG epochs when the dIBI parameter is not present. Moreover, it can also detect more severe background EEG grades in which dIBI parameter is not encountered (e.g. low amplitude continuous EEGs). Last but not least, the algorithm proves to be very robust to the presence of artifacts.

Here, we provide a qualitative characterization of the algorithms that we tested and discussed with the clinical experts.

	Intuitive	Visualization	Robust to artifacts	Multichannel structure exploits	EEG states that can be quantified	Mathematical complexity	Objective measure – unbiased
Simple burst-suppression based *thresholding* detector	+++	++	+	+	+	+	++
dIBI concept (amplitude)	+++	+++	++	++	++	++	++
Holistic tensor based approach	+	++	+++	+++	+++	+++	++
Multifractal DFA metric	+	++	+	++	+++	++	+++

Figure 8.3: Qualitative comparison of the algorithms developed in this thesis. The strength is presented with +++, whereas the weaknesses are presented with +.

8.2 Future Work

8.2.1 Monitoring the speed of the HIE recovery

Another important question when evaluating the algorithms is what approach will detect the improvement/deterioration of the infant's condition faster? With respect to this, dIBI and MF-DFA concept will be more informative than the dichotomous automated scoring that uses only 4 distinctive background EEG grades [90]. One way to visualize the condition of the neonate is to plot median dIBI durations and amplitudes for every hour of monitoring (Figure 8.2 and 8.1). Within most of the processed hours of the EEG in asphyxiated infants (e.g. approximately 80% - 90%), the parameter dIBI will be detected (present) in the EEG recordings. However, the dIBI pattern will not be present in all background EEG states of term infants. In particular, normal/continuous background EEG

as well as continuous EEG periods with low amplitudes cannot be quantified with the dIBI parameter. For such states, MF-DFA metrics as well as holistic grading of background EEG would be more suitable. Here, we give an idea how holistic tensor EEG structuring (Chapter 7) can be used for the monitoring of the speed of the HIE recovery. In general, the tensor structure represents a distribution, and if we want to compare two tensor structures we may simply subtract them (e.g. to compare 1h EEGs at 24h and 36h post partum). Then, a new tensor will be obtained, quantifying the differences between the two EEG epochs. For instance, we may illustrate this if we subtract tensors that quantify moderate and severe EEG background abnormalities. For this, we may observe how the distribution of segments' features will change. If we quantify the duration and 'delta 2 power' of the EEG segments, it is possible to notice the changes in the distribution. This is illustrated in Figure 8.4. We may notice the decrease (negative numbers) of longer segments '2-5s long having very low amplitudes (delta 2 power)' and the increase (positive numbers) of shorter segments '1-2s long with higher amplitudes and more variability (more continuous EEG)'. Hence, the difference of the current recording time and the initial hour of the recording will provide a tensor that can be used for further examination of the HIE evolution. Consequently, many other segments' features can be explored (not only correlated with the segments' amplitude) and different EEG structuring can be performed.

8.2.2 Novel data-driven findings

The parameter, (d)IBI, is the most established parameter for the EEG quantification. In particular, the accurate measure of the dIBI amplitude provided a second parameter value, thus allowing better quantification of mildly asphyxiated infants. Furthermore, the goal of the automated method is not only to replicate the visual grading, but also to provide further data mining steps and to derive new insights into the brain functioning. As a simple example, by analyzing all detected dIBIs within 1h, we may also model the distribution of dIBI duration. This distribution can be fitted as a log-normal distribution with two parameters that fully characterize it (μ, σ) (Figure 8.5). Prior to automated analysis, a lot of effort was spent by clinical researchers to find an optimal statistics to characterize EEGs. For instance, maximal duration, most recurring or median IBI duration values were explored and examined.

In our study, we showed that the amplitude of dIBI is different among patient groups with good and poor outcome using automated data-driven processing. In addition, we have also showed the interdependence between duration and amplitude of dIBI. Similarly, a recent work established on data-driven discovery has been published [59]. This study is based on the automated detection of

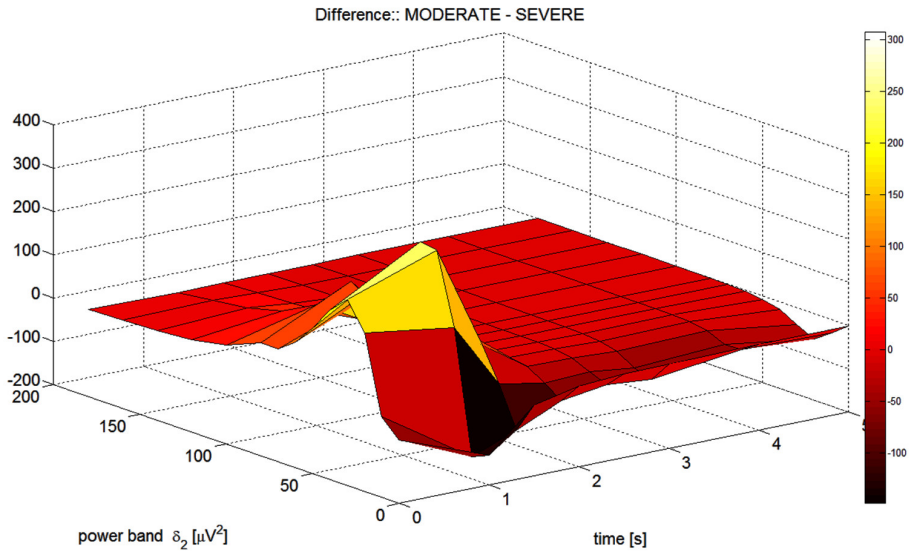

Figure 8.4: The figure illustrates how distribution of 2 simultaneously measured segments' features will behave when the EEG recovers from severe to moderate background EEG. Interpretation is that the recovered EEG will consist of more shorter segments with higher amplitudes and more variability. In addition, low amplitude (lower delta-2 power values), non-responsive segments creating prolonged segments (3-5s long) will be disappearing.

bursts and the analysis of burst metrics 'duration' and 'area' [59]. This study used a novel way to cumulatively characterize the interplay of those parameters, thereby modeling them according to the power-law scaling distribution. Hence, these results show how the detection algorithms may be applied for revealing new insights that can be very challenging to human expert visual EEG analysis.

8.2.3 Improvements in dIBI parameter detections

Several researchers have also published approaches for burst/suppression pattern detection. It is interesting that most of the approaches are the so-called, 'thresholding' algorithms that distinguish suppressed from burst periods. A novel contribution is presented in [67] where the introduction of the adaptive threshold is proposed. This step should be recognized as an important improvement for the detection burst/suppression algorithms. On the other hand, an adaptive threshold will also be biased by the presence of artifacts (e.g.

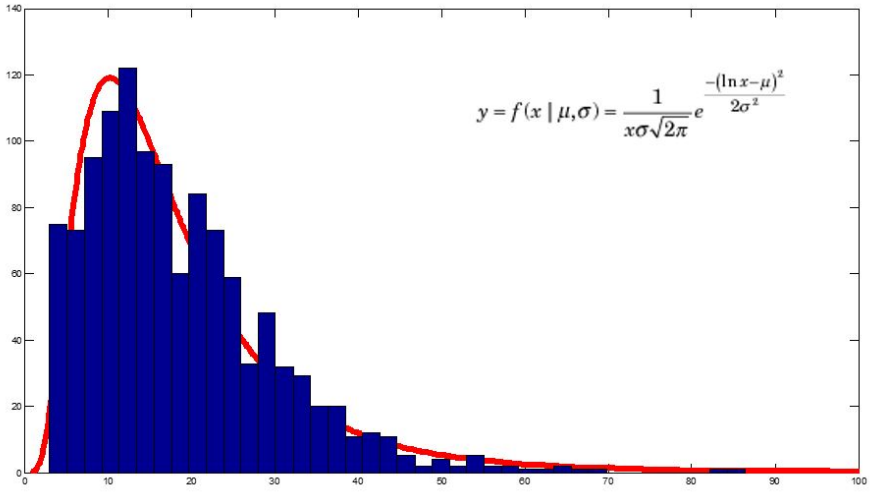

Figure 8.5: Modeling of the duration of detected dIBIs as the log-normal distribution.

major movement/transient as well as continuously persistent ECG/respiratory) and up to now it remained an open question how the data-driven adaptation of the threshold will perform on the large dataset validations.

In this thesis, we have fixed the threshold at the level of 10 μV. In follow-up research, during work on the master thesis, Alex Peiro Lilja in close collaboration with Anneleen Dereymaeker and Jan Vervisch (UZ Leuven, Gasthuisberg), we have improved the current concept by introducing three thresholds of 5, 10 and 20 μV. In this preliminary study, we have included neonates both from Leuven and Rotterdam NICU centers. The results showed that 25% of the bursts were only detected with the use of the 20μV threshold (data are not shown in the thesis). Hence, this approach uses three fixed thresholds, which are insensitive to EEG data adaptation and the presence of artifacts. Moreover, the novelty of this study was also an approach to distinguish bursts from artifacts, which remains an open problem for 'thresholding' based algorithms. This idea is similar to the dIBI refinement step presented in this thesis. In the master thesis work, the emphasis was placed on bursts and artifacts structuring into the tensor that will exploit the overall correlation between EEG channels. We see this as a future way to detect burst/suppression patterns as compared to methods that use simple averaging across all EEG channels (e.g. as done in [76]). In other words, burst patterns should be treated as a multi-channel tensor structure and used for further detection steps.

8.2.4 Clinical validation of the developed algorithms

Development and clinical validation of the EEG processing algorithms requires an essential guidance from clinical experts (neonatologists and EEG experts). One of the most challenging questions in the EEG analysis is the inter-rater disagreement. As the EEG patterns are very complex and can only be described to the certain extent, visual EEG interpretation is regarded as very subjective.

Along with the visual EEG diagnostic support, for the categorization of neonates in this thesis, we have also used the results of the 2-year neurodevelopmental outcome and MRI scores. This data allowed comparison and clinical validation of the EEG-derived findings (Chapter 4; see also [22]). In addition, an alternative benchmarking approach may be tested. For instance, the burst-suppression pattern is occurring in human adults during the anesthesia. The EEG-based bio-marker (bispectral index-BIS) to monitor the depth of the anesthesia is developed and validated in correlation with an administrated dose-related medication ([71], [44]. Therefore, similar experimental benchmarking methods may be used for the objective validation and the confirmation of the EEG-based supportive decisions.

8.3 Using automated approach to recruit infants for the hypothermia treatment

One of the most important applications of the automated neonatal EEG processing is to provide decision support at the early stage of asphyxic injury. This support should advise clinicians whether to start or not with the cooling therapy. However, this represents a very challenging *supervised* classification problem due to numerous logistic factors. For instance, it is very challenging to derive reliable clinical bio-markers, which we can use to initially label the dataset. The labeling should correlate EEGs of infants (e.g. recorded before 6 hours post partum) with the infants that mostly benefited from hypothermia treatment. At present, for the recruitment of infants aEEG/EEG diagnostic as well as clinical scores are used. In the majority of cases, the hypothermia will be initiated if the EEG shows a burst-suppression pattern, with the interburst interval longer than 5 or 10s. This information can be exploited for future EEG quantification as the signal will be significantly simplified. We claim that in such EEGs only a limited number of parameters may be extracted. First, suppression periods will carry information of only the duration and amplitude of the EEG discontinuity. In addition, more informative features can be extracted from that burst period. It has been shown that in adults, the so-called, *identical bursts*

(occurrences of only similar bursts) are clinical bio-markers associated with the poor clinical outcome [55]. Hence, the discriminative features may be searched within the burst spectral properties. It has been also shown that bursts spectra carry significant information that can differentiate neonates with poor and good clinical outcome [121]. For this purpose, the power of EEG frequency bands can be calculated for the burst period (alpha, beta, gama, delta) and used for discriminative purposes. On the other hand, a recent, more sophisticated approach has been proposed as well, using burst descriptors (duration and area) and power-law scaling quantification [59]. Hence, future research may be initiated with those concepts as starting points.

8.4 Benefits of multichannel EEG recordings

Most of the currently developed algorithms do not fully exploit the available information in the neonatal EEG. In this thesis, to some extent this problem was recognized and we have tried to improve the detection accuracy of the algorithms by incorporating multi-channel structure. For instance, within a dIBI parameter, it was necessary to provide a trustworthy estimate of dIBI amplitude. As it can frequently happen that some of the EEG channels are degraded by noise, we have sorted all dIBI amplitude values within single channels and used the median of the third quartile to improve the amplitude assessment. Moreover, within the holistic tensor approach (Chapter 7) we have also developed feature, the so-called, 'global amplitude' in order to quantify the interplay between EEG channels. Limitation of such approaches is that clinical doctors usually want to preserve the topographic information from EEG. Hence, the better solution would be structuring relevant parameters into a tensor framework where one dimension would correspond to brain lobes (e.g. occipital, temporal, parietal, central).

8.5 Future development of the algorithms' accuracy

With more than 4 decades of the research in the neonatal EEG, clinical practice still relies on the visual EEG inspection. Nevertheless, the current algorithms for the neonatal seizure detection [120] and [32], show promising results and very soon they can be used as assistive methods in the clinical practice. Other algorithms, such as those for the detection of IBI patterns also portray high detection accuracy. Nevertheless, the major problem for fully automated EEG

analysis represent the omnipresence of artifacts. Visually, they are easily discarded during analysis, but due to their diversity they still present the bottleneck for the automated solutions. As an example, they may hamper the analysis asymmetry and asynchrony, although relatively robust solutions do exist [108] and [66]. In recent years, several methods for the identification of the artifacts have been proposed ([132], [91], [115]). By isolating and excluding such EEG epochs following those methods, the performance of the algorithms would significantly increase.

8.6 Bringing decision-support systems into the NICUs

Future research work should bring more synergy between engineers and clinical researchers. Now, it is common that engineers develop algorithms for pattern recognition as marked by EEG experts. As the next step, it would be very important that clinicians start using the developed solutions routinely in the NICUs. In the previous years, our experience with seizure detection algorithm, showed that by seeing new patterns (e.g. seizure or artifact), an experienced clinical user will be able to intuitively determine whether the algorithm will detect it or not. This will establish an important feedback for the development of the next generation of the algorithms.

As the next step, within our NeoGuard consortium, the following GUI has been suggested for easy-to-use EEG visualization (Figures 8.6 and 8.7). We hope that such interfaces will allow both use of the algorithms as well as an interactive feedback from the clinical users.

Finally, it is interesting to investigate how the accuracy of the algorithms will increase in future. At the time of writing this thesis, we see that mathematical algorithms significantly outperform and fully replace humans in numerous tasks. Examples are the chess game, recommendation system for purchasing books (e.g. Amazon) or playing the knowledge game Jeopardy (Watson, IBM). We also witness that the novel machine learning methods, such as, deep learning provide the state of the art solutions for object recognition (e.g. traffic signs) and automated translation between different languages. Since most of those signals are similar to EEG (e.g. speech/sound) we may expect that in the following years, automated algorithms will outperform human EEG experts as well. It is though important to note that the development of such methods require relatively large dataset for the training and the optimization of the complex deep learning methods. Hence, it is possible to imagine that in the following years, if significant efforts are involved, the EEG diagnostic may mostly rely on

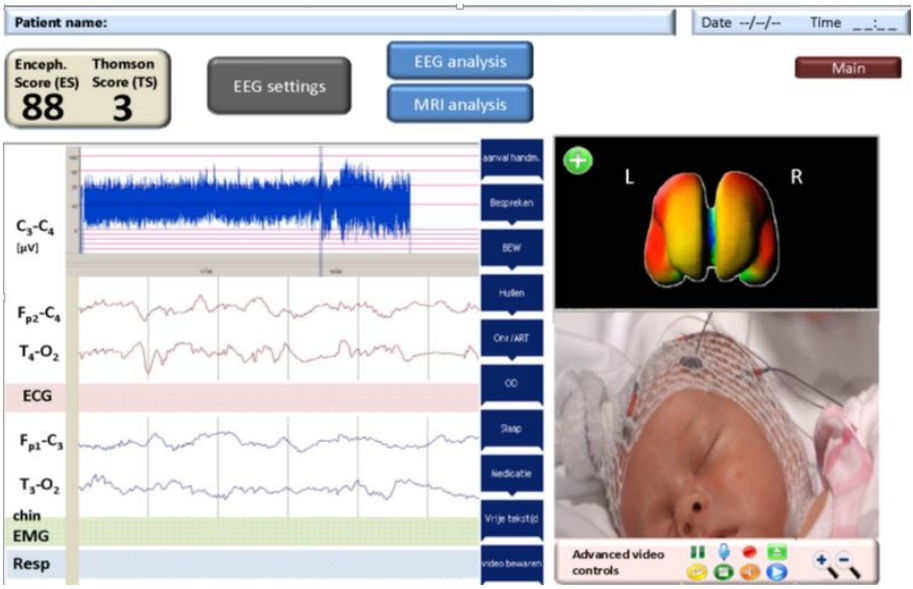

Figure 8.6: The 1st layer of the GUI is shown for the routine clinical use in the NICUs. Developed by IPI Group - University of Ghent and NeoGuard consortium.

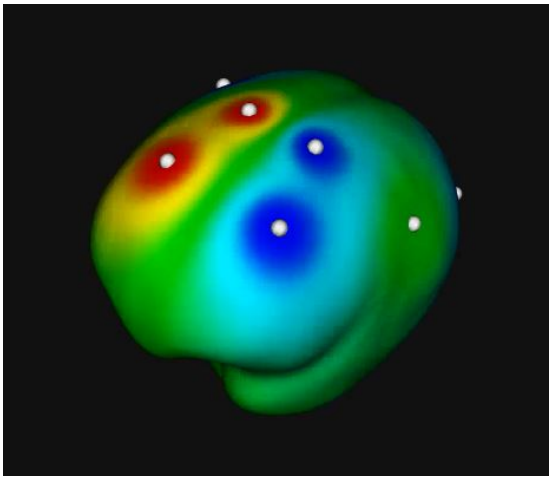

Figure 8.7: Detected parameters will be displayed on the 3D brain model for the expert clinical use. Developed by IPI Group - University of Ghent and NeoGuard consortium

the decisions brought by the algorithms. In this way, this helpful expertise can be brought into NICUs throughout the world and assist newborns who really need it.

Bibliography

[1] Ahtola, E., Stjerna, S., Yrttiaho, S., Nelson, C. A., Leppänen, J. M., and Vanhatalo, S. Dynamic eye tracking based metrics for infant gaze patterns in the face-distractor competition paradigm. *PloS one 9*, 5 (2014), e97299.

[2] Aliefendioğlu, D., Doğru, T., Albayrak, M., DibekMisirlioğlu, E., and Şanli, C. Heart rate variability in neonates with hypoxic ischemic encephalopathy. *The Indian Journal of Pediatrics 79*, 11 (2012), 1468–1472.

[3] André, M., Lamblin, M.-D., d'Allest, A.-M., Curzi-Dascalova, L., Moussalli-Salefranque, F., Nguyen The Tich, S., Vecchierini-Blineau, M.-F., Wallois, F., Walls-Esquivel, E., and Plouin, P. Electroencephalography in premature and full-term infants. developmental features and glossary. *Neurophysiologie Clinique/Clinical Neurophysiology 40*, 2 (2010), 59–124.

[4] Azzopardi, D. V., Strohm, B., Edwards, A. D., Dyet, L., Halliday, H. L., Juszczak, E., Kapellou, O., Levene, M., Marlow, N., Porter, E., et al. Moderate hypothermia to treat perinatal asphyxial encephalopathy. *New England Journal of Medicine 361*, 14 (2009), 1349–1358.

[5] Barlow, J. Computer characterization of tracé alternant and REM sleep patterns in the neonatal EEG by adaptive segmentation—an exploratory study. *Electroencephalography and clinical neurophysiology 60*, 2 (1985), 163–173.

[6] Barlow, J., Creutzfeldt, O., Michael, D., Houchin, J., and Epelbaum, H. Automatic adaptive segmentation of clinical EEGs. *Electroencephalography and Clinical Neurophysiology 51*, 5 (1981), 512–525.

[7] Barnaby, D., Ferrick, K., Kaplan, D. T., Shah, S., Bijur, P., and Gallagher, E. J. Heart rate variability in emergency department patients with sepsis. *Academic emergency medicine 9*, 7 (2002), 661–670.

[8] Beggs, J. M., and Plenz, D. Neuronal avalanches in neocortical circuits. *The Journal of neuroscience 23*, 35 (2003), 11167–11177.

[9] Belouchrani, A., Abed-Meraim, K., Cardoso, J.-F., and Moulines, E. A blind source separation technique using second-order statistics. *Signal Processing, IEEE Transactions on 45*, 2 (1997), 434–444.

[10] Berger, H. Über das elektrenkephalogramm des menschen. *European archives of psychiatry and clinical neuroscience 98*, 1 (1933), 231–254.

[11] Berger, H. Über das elektrenkephalogramm des menschen. *European Archives of Psychiatry and Clinical Neuroscience 103*, 1 (1935), 444–454.

[12] Berthouze, L., and Farmer, S. F. Adaptive time-varying detrended fluctuation analysis. *Journal of neuroscience methods 209*, 1 (2012), 178–188.

[13] Bodenstein, G., Schneider, W., and Malsburg, C. Computerized EEG pattern classification by adaptive segmentation and probability-density-function classification. *Description of the method. Computers in biology and medicine 15*, 5 (1985), 297–313.

[14] Botcharova, M., Farmer, S. F., and Berthouze, L. A maximum likelihood based technique for validating detrended fluctuation analysis (ml-dfa). *arXiv preprint arXiv:1306.5075* (2013).

[15] Boylan, G., Burgoyne, L., Moore, C., O'Flaherty, B., and Rennie, J. An international survey of eeg use in the neonatal intensive care unit. *Acta Paediatrica 99*, 8 (2010), 1150–1155.

[16] Boylan, G. B., Stevenson, N. J., and Vanhatalo, S. Monitoring neonatal seizures. In *Seminars in Fetal and Neonatal Medicine* (2013), vol. 18, Elsevier, pp. 202–208.

[17] C, P., MF, R.-B., JP, R., and N., M. *Neonatal electroencephalography during the first twenty-four hours of life in full-term newborn infants.* Neuropediatrics 1986;17:11–8.

[18] Camm, A., Malik, M., Bigger, J., Breithardt, G., Cerutti, S., Cohen, R., Coumel, P., Fallen, E., Kennedy, H., Kleiger, R., et al. Heart rate variability: standards of measurement, physiological interpretation and clinical use. task force of the european society of

cardiology and the north american society of pacing and electrophysiology. *Circulation 93*, 5 (1996), 1043–1065.

[19] Cammu, H., Martens, E., Martens, G., Van Mol, C., and Defoort, P. Perinatale activiteiten in vlaanderen 2010. *Studie centrum voor perinatale Epidemiologie* (2011).

[20] Cardoso, J.-F., and Souloumiac, A. Blind beamforming for non-gaussian signals. In *IEE Proceedings F (Radar and Signal Processing)* (1993), vol. 140, IET, pp. 362–370.

[21] CC, M., BF, B., and JJ., V. *Prognostic value of neonatal discontinuous EEG*. Pediatr Neurol 2002;27:93–101.

[22] Cherian, P., Deburchgraeve, W., Swarte, R., Vos, D., M., G., P., V. H., S., and Visser, G. Validation of a new automated neonatal seizure detection system: a clinician's perspective. *Clinical Neurophysiology 122*, 8 (2011), 1490–1499.

[23] Cichocki, A. Tensor decompositions: A new concept in brain data analysis? *arXiv preprint arXiv:1305 0395.* (2013).

[24] Cilio, M. R., and Ferriero, D. M. Synergistic neuroprotective therapies with hypothermia. In *Seminars in Fetal and Neonatal Medicine* (2010), vol. 15, Elsevier, pp. 293–298.

[25] Compagnoni, G., Pogliani, L., Lista, G., Castoldi, F., Fontana, P., and Mosca, F. Hypothermia reduces neurological damage in asphyxiated newborn infants. *Neonatology 82*, 4 (2002), 222–227.

[26] Cowan, F., Rutherford, M., Groenendaal, F., Eken, P., Mercuri, E., Bydder, G. M., Meiners, L. C., Dubowitz, L., and de Vries, L. S. Origin and timing of brain lesions in term infants with neonatal encephalopathy. *The Lancet 361*, 9359 (2003), 736–742.

[27] Creutzfeldt, O., Bodenstein, G., and Barlow, J. Computerized EEG pattern classification by adaptive segmentation and probability density function classification. *Clinical evaluation. Electroencephalography and clinical neurophysiology 60*, 5 (1985), 373–393.

[28] De Clercq, W., Vergult, A., Vanrumste, B., Van Paesschen, W., and Van Huffel, S. Canonical correlation analysis applied to remove muscle artifacts from the electroencephalogram. *Biomedical Engineering, IEEE Transactions on 53*, 12 (2006), 2583–2587.

[29] De Lathauwer, L., De Moor, B., and Vandewalle, J. A multilinear singular value decomposition. *SIAM journal on Matrix Analysis and Applications 21*, 4 (2000), 1253–1278.

[30] De Lathauwer, L., De Moor, B., and Vandewalle, J. On the best rank-1 and rank-(r 1, r 2,..., rn) approximation of higher-order tensors. *SIAM Journal on Matrix Analysis and Applications 21*, 4 (2000), 1324–1342.

[31] De Vos, M., Deburchgraeve, W., Cherian, P., Matic, V., Swarte, R., Govaert, P., Visser, G. H., and Van Huffel, S. Automated artifact removal as preprocessing refines neonatal seizure detection. *Clinical Neurophysiology 122*, 12 (2011), 2345–2354.

[32] Deburchgraeve, W., Cherian, P., De Vos, M., Swarte, R., Blok, J., Visser, G. H., Govaert, P., and Van Huffel, S. Automated neonatal seizure detection mimicking a human observer reading eeg. *Clinical Neurophysiology 119*, 11 (2008), 2447–2454.

[33] Deburchgraeve, W., Cherian, P., Vos, D., M., S., R., B., J., V., G., G., P., and Huffel, V. S. *Automated neonatal seizure detection mimicking a human observer reading EEG. Clinical Neurophysiology 119*, 11 (2008), 2447–2454.

[34] Despotovic, I. *Multimodal image analysis of the human brain.* PhD thesis, Ghent University, 2014.

[35] Despotovic, I., Cherian, P., Vos, M., Hallez, H., Deburchgraeve, W., Govaert, P., Lequin, M., Visser, G., Swarte, R., and Vansteenkiste, E. and others. *Relationship of EEG sources of neonatal seizures to acute perinatal brain lesions seen on MRI: A pilot study. Human brain mapping 34*, 10 (2013), 2402–2417.

[36] Doyle, O., Korotchikova, I., Lightbody, G., Marnane, W., Kerins, D., and Boylan, G. Heart rate variability during sleep in healthy term newborns in the early postnatal period. *Physiological measurement 30*, 8 (2009), 847.

[37] Dreyfus-Brisac, C., Samson-Dollfus, D., and Fischgold, H. Activité électrique cérébrale du prématuré et du nouveau-né. *Ann Pediatr 31* (1955), 1–7.

[38] E, B., L, B., A, B., R, P., and G., C. *Constantly discontinuous EEG patterns in full-term neonates with hypoxic-ischaemic encephalopathy.* Clin Neurophysiol 1999;110:1510–5.

[39] FISHER, R. A. The use of multiple measurements in taxonomic problems. *Annals of Eugenics 7*, 2 (1936), 179–188.

[40] Flisberg, A., Kjellmer, I., and L.

[41] Fraley, C., and Raftery, A. E. Model-based clustering, discriminant analysis, and density estimation. *Journal of the American Statistical Association 97*, 458 (2002), 611–631.

[42] Fransson, P., Metsäranta, M., Blennow, M., Åden, U., Lagercrantz, H., and Vanhatalo, S. Early development of spatial patterns of power-law frequency scaling in fmri resting-state and eeg data in the newborn brain. *Cerebral cortex 23*, 3 (2013), 638–646.

[43] Gäddlin, P.-O., Finnström, O., Wang, C., and Leijon, I. A fifteen-year follow-up of neurological conditions in vlbw children without overt disability: relation to gender, neonatal risk factors, and end stage mri findings. *Early human development 84*, 5 (2008), 343–349.

[44] Gajraj, R., Doi, M., Mantzaridis, H., and Kenny, G. Comparison of bispectral eeg analysis and auditory evoked potentials for monitoring depth of anaesthesia during propofol anaesthesia. *British journal of anaesthesia 82*, 5 (1999), 672–678.

[45] Gerla, V., Paul, K., Lhotska, L., and Krajca, V. Multivariate analysis of full-term neonatal polysomnographic data. *Information Technology in Biomedicine, IEEE Transactions on 13*, 1 (2009), 104–110.

[46] Gluckman, P. D., Wyatt, J. S., Azzopardi, D., Ballard, R., Edwards, A. D., Ferriero, D. M., Polin, R. A., Robertson, C. M., Thoresen, M., Whitelaw, A., et al. Selective head cooling with mild systemic hypothermia after neonatal encephalopathy: multicentre randomised trial. *The Lancet 365*, 9460 (2005), 663–670.

[47] Golub, G. H., and Van Loan, C. F. *Matrix computations*, vol. 3. JHU Press, 2012.

[48] Gotman, J., Flanagan, D., Zhang, J., and Rosenblatt, B. Automatic seizure detection in the newborn: methods and initial evaluation. *Electroencephalography and clinical neurophysiology 103*, 3 (1997), 356–362.

[49] Gunn, A., and Thoresen, M. Hypothermic neuroprotection. *NeuroRx 3*, 2 (2006), 154–169.

[50] Gunn, A. J., and Bennet, L. Fetal hypoxia insults and patterns of brain injury: insights from animal models. *Clinics in perinatology 36*, 3 (2009), 579–593.

[51] Hagberg, B., Hagberg, G., Beckung, E., and Uvebrant, P. Changing panorama of cerebral palsy in sweden. viii. prevalence and origin in the birth year period 1991–94. *Acta Paediatrica 90*, 3 (2001), 271–277.

[52] Hardstone, R., Poil, S.-S., Schiavone, G., Jansen, R., Nikulin, V. V., Mansvelder, H. D., and Linkenkaer-Hansen, K. Detrended fluctuation analysis: a scale-free view on neuronal oscillations. *Frontiers in physiology 3* (2012).

[53] Hellström-Westas, L., Rosén, I., De Vries, L., and Greisen, G. Amplitude-integrated eeg classification and interpretation in preterm and term infants. *NeoReviews 7*, 2 (2006), e76–e87.

[54] Hese, V., P., P., W., D. K., J., V. d. W., R., and Lemahieu, I. *Automatic detection of sleep stages using the EEG*. 2, 2001.

[55] Hofmeijer, J., Tjepkema-Cloostermans, M. C., and van Putten, M. J. Burst-suppression with identical bursts: A distinct eeg pattern with poor outcome in postanoxic coma. *Clinical Neurophysiology 125*, 5 (2014), 947–954.

[56] Holmes, G., Rowe, J., Hafford, J., Schmidt, R., Testa, M., and Zimmerman, A. Prognostic value of the electroencephalogram in neonatal asphyxia. *Electroencephalography and clinical neurophysiology 53*, 1 (1982), 60–72.

[57] Hyvärinen, A., Karhunen, J., and Oja, E. *Independent component analysis*, vol. 46. John Wiley & Sons, 2004.

[58] Ihlen, E. A. Introduction to multifractal detrended fluctuation analysis in matlab. *Frontiers in physiology 3* (2012).

[59] Iyer, K. K., Roberts, J. A., Metsäranta, M., Finnigan, S., Breakspear, M., and Vanhatalo, S. Novel features of early burst suppression predict outcome after birth asphyxia. *Annals of Clinical and Translational Neurology 1*, 3 (2014), 209–214.

[60] Jennekens, W., Ruijs, L., Lommen, C., Niemarkt, H., Pasman, J., van Kranen-Mastenbroek, V., Wijn, P., van Pul, C., and Andriessen, P. Automatic burst detection for the EEG of the preterm infant. *Physiological measurement 32*, 10 (2011), 1623.

[61] Joyce, C., Gorodnitsky, I., and Kutas, M. Automatic removal of eye movement and blink artifacts from EEG data using blind component separation. *Psychophysiology 41*, 2 (2004), 313–325.

[62] Kantelhardt, J. W., Zschiegner, S. A., Koscielny-Bunde, E., Havlin, S., Bunde, A., and Stanley, H. E. Multifractal detrended fluctuation analysis of nonstationary time series. *Physica A: Statistical Mechanics and its Applications 316*, 1 (2002), 87–114.

[63] Kim, Y.-D., and Choi, S. Nonnegative tucker decomposition. In *Computer Vision and Pattern Recognition, 2007. CVPR'07. IEEE Conference on* (2007), IEEE, pp. 1–8.

[64] Kinoti, S. Asphyxia of the newborn in east, central and southern africa. *East African medical journal 70*, 7 (1993), 422–433.

[65] Klemm, M., Haueisen, J., and Ivanova, G. Independent component analysis: comparison of algorithms for the investigation of surface electrical brain activity. *Medical biological engineering computing 47*, 4 (2009), 413–423.

[66] Koolen, N., Dereymaeker, A., Räsänen, O., Jansen, K., Vervisch, J., Matic, V., De Vos, M., Van Huffel, S., Naulaers, G., and Vanhatalo, S. Interhemispheric synchrony in the neonatal eeg revisited: activation synchrony index as a promising classifier. *Frontiers in human neuroscience 8* (2014).

[67] Koolen, N., Jansen, K., Vervisch, J., Matic, V., De Vos, M., Naulaers, G., and Van Huffel, S. Line length as a robust method to detect high-activity events: Automated burst detection in premature eeg recordings. *Clinical Neurophysiology* (2014).

[68] Korotchikova, I., Stevenson, N., Walsh, B., Murray, D., and Boylan, G. Quantitative eeg analysis in neonatal hypoxic ischaemic encephalopathy. *Clinical Neurophysiology 122*, 8 (2011), 1671–1678.

[69] Kostović, I., and Judaš, M. The development of the subplate and thalamocortical connections in the human foetal brain. *Acta Paediatrica 99*, 8 (2010), 1119–1127.

[70] Krajca, V., Petránek, S., Patáková, I., and A., V. Automatic identification of significant graphoelements in multichannel EEG recordings by adaptive segmentation and fuzzy clustering. *Int J Biomed Comput 28* (1991), 71–89.

[71] Krishnamurthy, K. B., and Drislane, F. W. Depth of eeg suppression and outcome in barbiturate anesthetic treatment for refractory status epilepticus. *Epilepsia 40*, 6 (1999), 759–762.

[72] Lachenbruch, P. A., and Goldstein, M. Discriminant analysis. *Biometrics 35*, 1 (1979), pp. 69–85.

[73] Lawn, J. E., Cousens, S., and Zupan, J. 4 million neonatal deaths: when? where? why? *The Lancet 365*, 9462 (2005), 891–900.

[74] Linkenkaer-Hansen, K., Nikouline, V. V., Palva, J. M., and Ilmoniemi, R. J. Long-range temporal correlations and scaling behavior in human brain oscillations. *The Journal of neuroscience 21*, 4 (2001), 1370–1377.

[75] Löfhede, J., Löfgren, N., Thordstein, M., Flisberg, A., Kjellmer, I., and Lindecrantz, K. Classification of burst and suppression in the neonatal electroencephalogram. *Journal of neural engineering 5*, 4 (2008), 402.

[76] Löfhede, J., Thordstein, M., Löfgren, N., Flisberg, A., Rosa-Zurera, M., Kjellmer, I., and Lindecrantz, K. Automatic classification of background eeg activity in healthy and sick neonates. *Journal of neural engineering 7*, 1 (2010), 016007.

[77] Löfhede, J., Thordstein, M., Löfgren, N., Flisberg, A., Rosa-Zurera, M., Kjellmer, I., and Lindecrantz, K. Automatic classification of background eeg activity in healthy and sick neonates. *Journal of neural engineering 7*, 1 (2010), 016007.

[78] Lombroso, C. T. Neonatal polygraphy in full-term and premature infants: a review of normal and abnormal findings. *Journal of Clinical Neurophysiology 2*, 2 (1985), 105–156.

[79] Mallat, S. A wavelet tour of signal processing.

[80] Matic, V., Cherian, P. J., Jansen, K., Koolen, N., Naulaers, G., Swarte, R. M., Govaert, P., Visser, G. H., Van Huffel, S., and De Vos, M. Automated eeg inter-burst interval detection in neonates with mild to moderate postasphyxial encephalopathy. In *Engineering in Medicine and Biology Society (EMBC), 2012 Annual International Conference of the IEEE* (2012), IEEE, pp. 17–20.

[81] Matic, V., Cherian, P. J., Koolen, N., Naulaers, G., Swarte, R. M., Govaert, P., Van Huffel, S., and De Vos, M. Holistic approach for automated background eeg assessment in asphyxiated full-term infants. *Journal of neural engineering 11*, 6 (2014), 066007.

[82] Matic, V., Deburchgraeve, W., and Van Huffel, S. Comparison of ica algorithms for ecg artifact removal from eeg signals. In *Proc. of the 4th Annual symposium of the IEEE-EMBS Benelux Chapter.(IEEE-EMBS)* (2009), pp. 137–140.

[83] McBride, M. C., Laroia, N., and Guillet, R. Electrographic seizures in neonates correlate with poor neurodevelopmental outcome. *Neurology 55*, 4 (2000), 506–514.

[84] Menache, C. C., Bourgeois, B. F., and Volpe, J. J. Prognostic value of neonatal discontinuous eeg. *Pediatric neurology 27*, 2 (2002), 93–101.

[85] Minamisawa, H., Smith, M.-L., and Siesjö, B. K. The effect of mild hyperthermia and hypothermia on brain damage following 5, 10, and 15 minutes of forebrain ischemia. *Annals of neurology 28*, 1 (1990), 26–33.

[86] Mitchell, T. J., Neil, J. J., Zempel, J. M., Thio, L. L., Inder, T. E., and Bretthorst, G. L. Automating the analysis of eeg recordings from prematurely-born infants: A bayesian approach. *Clinical Neurophysiology 124*, 3 (2013), 452–461.

[87] Monod, N., Pajot, N., and Guidasci, S. The neonatal eeg: statistical studies and prognostic value in full-term and pre-term babies. *Electroencephalography and clinical neurophysiology 32*, 5 (1972), 529–544.

[88] Monto, S., Vanhatalo, S., Holmes, M. D., and Palva, J. M. Epileptogenic neocortical networks are revealed by abnormal temporal dynamics in seizure-free subdural eeg. *Cerebral Cortex 17*, 6 (2007), 1386–1393.

[89] Mørup, M., Hansen, L. K., and Arnfred, S. M. Algorithms for sparse nonnegative tucker decompositions. *Neural computation 20*, 8 (2008), 2112–2131.

[90] Murray, D. M., Boylan, G. B., Ryan, C. A., and Connolly, S. Early eeg findings in hypoxic-ischemic encephalopathy predict outcomes at 2 years. *Pediatrics 124*, 3 (2009), e459–e467.

[91] Nowotny, T., Rospars, J., Martinez, D., Elbanna, S., and Anton, S. Machine learning for automatic prediction of the quality of electrophysiological recordings. *PloS one 8*, 12 (2013), 80838.

[92] Omidvarnia, A., Fransson, P., Metsäranta, M., and Vanhatalo, S. Functional bimodality in the brain networks of preterm and term human newborns. *Cerebral Cortex* (2013), bht120.

[93] Page, L., Brin, S., Motwani, R., and Winograd, T. The pagerank citation ranking: Bringing order to the web.

[94] Palmu, K., Kirjavainen, T., Stjerna, S., Salokivi, T., and Vanhatalo, S. Sleep wake cycling in early preterm infants: Comparison of polysomnographic recordings with a novel eeg-based index. *Clinical Neurophysiology 124*, 9 (2013), 1807–1814.

[95] Palmu, K., Wikström, S., Hippeläinen, E., Boylan, G., Hellström-Westas, L., and Vanhatalo, S. Detection of 'EEG bursts' in the early preterm EEG: visual vs. *automated detection. Clinical Neurophysiology 121*, 7 (2010), 1015–1022.

[96] Parish, L., Worrell, G., Cranstoun, S., Stead, S., Pennell, P., and Litt, B. Long-range temporal correlations in epileptogenic and non-epileptogenic human hippocampus. *Neuroscience 125*, 4 (2004), 1069–1076.

[97] Paul, K., Krajca, V., Roth, Z., Melichar, J., and Petranek, S. Comparison of quantitative EEG characteristics of quiet and active sleep in newborns. *Sleep Medicine 4*, 6 (2003), 543–552.

[98] Paul, K., Krajca, V., Roth, Z., Melichar, J., and Petranek, S. Quantitative topographic differentiation of the neonatal EEG. *Clinical neurophysiology 117*, 9 (2006), 2050–2058.

[99] Pelckmans, K., Suykens, J., Gestel, V., T., D. B., J., L., L., H., B., D. M., and B., V. *and ewalle.* J, LS-SVMlab, 2002.

[100] Pelckmans, K., Suykens, J. A., Van Gestel, T., De Brabanter, J., Lukas, L., Hamers, B., De Moor, B., and Vandewalle, J. Ls-svmlab toolbox user's guide. *Pattern recognition letters 24* (2003), 659–675.

[101] Peng, C.-K., Buldyrev, S. V., Havlin, S., Simons, M., Stanley, H. E., and Goldberger, A. L. Mosaic organization of dna nucleotides. *Physical Review E 49*, 2 (1994), 1685.

[102] Penzel, T., Kantelhardt, J. W., Grote, L., Peter, J.-H., and Bunde, A. Comparison of detrended fluctuation analysis and spectral analysis for heart rate variability in sleep and sleep apnea. *Biomedical Engineering, IEEE Transactions on 50*, 10 (2003), 1143–1151.

[103] Perumpillichira, J. C. *Improvements in Neonatal Brain Monitoring after Perinatal Asphyxia.* Erasmus MC: University Medical Center Rotterdam, 2010.

[104] Phan, A. *NFEA: Tensor toolbox for feature extraction and applications.* http://www.bsp.brain.riken.jp/~phan/nfea/nfea.html, 2011.

[105] Phan, A., and Cichocki, A. Tensor decompositions for feature extraction and classification of high dimensional datasets. *Nonlinear theory and its applications, IEICE 1*, 1 (2010), 37–68.

[106] Richardus, J. H., Graafmans, W. C., Verloove-Vanhorick, S. P., and Mackenbach, J. P. Differences in perinatal mortality and suboptimal care between 10 european regions: results of an international audit. *BJOG: An International Journal of Obstetrics & Gynaecology 110*, 2 (2003), 97–105.

[107] Roberts, J. A., Iyer, K. K., Finnigan, S., Vanhatalo, S., and Breakspear, M. Scale-free bursting in human cortex following hypoxia at birth. *The Journal of Neuroscience 34*, 19 (2014), 6557–6572.

[108] Räsänen, O., Metsäranta, M., and Vanhatalo, S. Development of a novel robust measure for interhemispheric synchrony in the neonatal EEG: Activation Synchrony Index (ASI). *NeuroImage 69* (2013), 256–266.

[109] Schlögl, A., Vidaurre, C., and Müller, K.-R. Adaptive methods in bci research-an introductory tutorial. In *Brain-Computer Interfaces.* Springer, 2010, pp. 331–355.

[110] Shankaran, S., Laptook, A. R., Ehrenkranz, R. A., Tyson, J. E., McDonald, S. A., Donovan, E. F., Fanaroff, A. A., Poole, W. K., Wright, L. L., Higgins, R. D., et al. Whole-body hypothermia for neonates with hypoxic–ischemic encephalopathy. *New England Journal of Medicine 353*, 15 (2005), 1574–1584.

[111] Sinclair, D., Campbell, M., Byrne, P., Prasertsom, W., and Robertson, C. Eeg and long-term outcome of term infants with neonatal hypoxic-ischemic encephalopathy. *Clinical neurophysiology 110*, 4 (1999), 655–659.

[112] Smith, J. R. The electroencephalogram during normal infancy and childhood: I. rhythmic activities present in the neonate and their subsequent development. *The Pedagogical Seminary and Journal of Genetic Psychology 53*, 2 (1938), 431–453.

[113] Stam, C., Montez, T., Jones, B., Rombouts, S., Van Der Made, Y., Pijnenburg, Y., and Scheltens, P. Disturbed fluctuations of resting state eeg synchronization in alzheimer's disease. *Clinical Neurophysiology 116*, 3 (2005), 708–715.

[114] Stevenson, N., Korotchikova, I., Temko, A., Lightbody, G., Marnane, W., and Boylan, G. An automated system for grading eeg abnormality in term neonates with hypoxic-ischaemic encephalopathy. *Annals of biomedical engineering 41*, 4 (2013), 775–785.

[115] Stevenson, N., O'Toole, J., Korotchikova, I., and Boylan, G. Artefact detection in neonatal eeg. In *Engineering in Medicine and Biology Society (EMBC), 2014 36th Annual International Conference of the IEEE* (2014), IEEE, pp. 926–929.

[116] Stevenson, N. J., Palmu, K., Wikström, S., Hellström-Westas, L., and Vanhatalo, S. Measuring brain activity cycling (bac) in long term eeg monitoring of preterm babies. *Physiological Measurement 35*, 7 (2014), 1493.

[117] Stjerna, S., Voipio, J., Metsäranta, M., Kaila, K., and Vanhatalo, S. Preterm eeg: a multimodal neurophysiological protocol. *Journal of visualized experiments: JoVE*, 60 (2012).

[118] Suykens, J., and V. and ewalle. *J. (1999). Least squares support vector machine classifiers. Neural processing letters 9*, 3 (1999), 293–300.

[119] Suykens, J. A. K., Van Gestel, T., De Brabanter, J., De Moor, B., and Vandewalle, J. *Least Squares Support Vector Machines*. World Scientific, Singapore, 2002.

[120] Temko, A., Thomas, E., Marnane, W., Lightbody, G., and Boylan, G. Eeg-based neonatal seizure detection with support vector machines. *Clinical Neurophysiology 122*, 3 (2011), 464–473.

[121] Thordstein, M., Flisberg, A., Löfgren, N., Bågenholm, R., Lindecrantz, K., Wallin, B., and Kjellmer, I. Spectral analysis of burst periods in eeg from healthy and post-asphyctic full-term neonates. *Clinical neurophysiology 115*, 11 (2004), 2461–2466.

[122] Tokariev, A., Palmu, K., Lano, A., Metsäranta, M., and Vanhatalo, S. Phase synchrony in the early preterm eeg: development of methods for estimating synchrony in both oscillations and events. *Neuroimage 60*, 2 (2012), 1562–1573.

[123] Tsuchida, T. N., Wusthoff, C. J., Shellhaas, R. A., Abend, N. S., Hahn, C. D., Sullivan, J. E., Nguyen, S., Weinstein, S., Scher, M. S., Riviello, J. J., et al. American clinical neurophysiology society standardized eeg terminology and categorization for the description of continuous eeg monitoring in neonates: report of the american clinical neurophysiology society critical care monitoring committee. *Journal of Clinical Neurophysiology 30*, 2 (2013), 161–173.

[124] Vanderperren, K., Mijović, B., Novitskiy, N., Vanrumste, B., and Stiers, P. Van den Bergh. *B., Lagae, L., Sunaert, S., Wagemans, J., Van Huffel, S. and others, (2013). Single trial ERP reading based on parallel factor analysis. Psychophysiology 50*, 1 (2013), 97–110.

[125] Vanhatalo, S., and Kaila, K. Development of neonatal eeg activity: from phenomenology to physiology. In *Seminars in Fetal and Neonatal Medicine* (2006), vol. 11, Elsevier, pp. 471–478.

[126] Vanhatalo, S., Tallgren, P., Andersson, S., Sainio, K., Voipio, J., and Kaila, K. Dc-eeg discloses prominent, very slow activity patterns during sleep in preterm infants. *Clinical neurophysiology 113*, 11 (2002), 1822–1825.

[127] Vos, D., M., R., S., V., K., V., B., A., F., H., V., and Burle, B. Removal of muscle artifacts from EEG recordings of spoken language production. *Neuroinformatics 8*, 2 (2010), 135–150.

[128] Vos, D., M., V., A., D. L., L., D. C., W., V. H., S., D., P., P., A., and Paesschen, V. W. *Canonical decomposition of ictal scalp EEG reliably detects the seizure onset zone. NeuroImage 37*, 3 (2007), 844–854.

[129] Walsh, B., Murray, D., and Boylan, G. The use of conventional eeg for the assessment of hypoxic ischaemic encephalopathy in the newborn: a review. *Clinical neurophysiology 122*, 7 (2011), 1284–1294.

[130] Watanabe, K., Miyazaki, S., Hara, K., and Hakamada, S. Behavioral state cycles, background EEGs and prognosis of newborns with perinatal hypoxia. *Electroencephalography and clinical neurophysiology 49*, 5 (1980), 618–625.

[131] Wikiversity. Blausen gallery 2014 — wikiversity,, 2014. [Online; accessed 16-January-2015].

[132] Wulsin, D., Gupta, J., Mani, R., Blanco, J., and Litt, B. Modeling electroencephalography waveforms with semi-supervised deep belief nets: fast classification and anomaly measurement. *Journal of neural engineering 8*, 3 (2011), 036015.

[133] Xavier-de Souza, S., Suykens, J. A., Vandewalle, J., and Bollé, D. Coupled simulated annealing. *Systems, Man, and Cybernetics, Part B: Cybernetics, IEEE Transactions on 40*, 2 (2010), 320–335.

[134] Zarzoso, V., and Comon, P. Comparative speed analysis of fastica. In *Independent Component Analysis and Signal Separation*. Springer, 2007, pp. 293–300.

[135] Zheng, Y., Gao, J., Sanchez, J. C., Principe, J. C., and Okun, M. S. Multiplicative multifractal modeling and discrimination of human neuronal activity. *Physics Letters A 344*, 2 (2005), 253–264.

[136] Zorick, T., and Mandelkern, M. A. Multifractal detrended fluctuation analysis of human eeg: Preliminary investigation and comparison with the wavelet transform modulus maxima technique. *PloS one 8*, 7 (2013), e68360.

Curriculum

Vladimir Matić was born in Belgrade, Serbia on July 31, 1984.

He received a Diploma and M.Sc. degree at the School of Electrical Engineering, University of Belgrade, Department of Signals and Systems, Serbia in 2007 and in 2010 respectively. His final diploma thesis he completed while working as a research assistant at the Scientific Institute Mihajlo Pupin, Belgrade, Serbia (2007). In March 2010, he joined STADIUS, Department of Electrical Engineering (ESAT), KU Leuven and started his PhD in October 2010. His PhD was supervised by Prof. dr. ir. Sabine Van Huffel and Prof. dr. ir. Maarten De Vos. He worked on the neonatal EEG signal processing within the NeoGuard project (https://neoguard.net). His research was focused on the applications of signal processing and machine learning methods to develop automated algorithms. Their objective is to assist medical doctors at the Neonatal Intensive Care Units (NICUs), while treating the critically ill neonates. During the final year of his PhD, Vladimir was actively involved in the entrepreneurial activities and explored the ways to transfer the developed algorithms from the research practice into the routine use in the NICUs.

Publication list

Papers in international journals

1. Matić, V., Cherian, P. J., Koolen, N., Naulaers, G., Swarte, R. M., Govaert, P., ... De Vos, M. (2014). Holistic approach for automated background EEG assessment in asphyxiated full-term infants. Journal of neural engineering, 11(6), 066007.

2. Matić V., Cherian PJ., Widjaja D., Jansen K., Naulaers G., Van Huffel S., De Vos M., "Heart Rate Variability in Newborns with Hypoxic Brain Injury", Advances in Experimental Medicine and Biology, vol. 789, May 2013, pp. 43-48.

3. Koolen, N., Jansen, K., Vervisch, J., Matić, V., De Vos, M., Naulaers, G., Van Huffel, S. (2014). Line length as a robust method to detect high-activity events: Automated burst detection in premature EEG recordings. Clinical Neurophysiology.

4. Koolen, N., Dereymaeker, A., Rnen, O., Jansen, K., Vervisch, J., Matić, V., ... Vanhatalo, S. (2014). Interhemispheric synchrony in the neonatal EEG revisited: activation synchrony index as a promising classifier. Frontiers in human neuroscience, 8.

5. Liu Y., De Vos M., Gligorijevic I., Matić V., Li Y., Van Huffel S., "Multi-Structural Signal Recovery for Biomedical Compressive Sensing", IEEE Transactions on Biomedical Engineering, vol. 60, no. 10, Oct. 2013, pp. 2794-2805.

6. De Vos M., Deburchgraeve W., Cherian P.J., Matić V., Swarte R.M., Visser G.H., Govaert P., Van Huffel S., "Automated artifact removal as preprocessing refines neonatal seizure detection", Clinical Neurophysiology, Dec. 2011, pp. 2345-2354.

Papers submitted to international journals

1. Matić V, Cherian PJ, Koolen N, Naulaers G, Swarte RM, Govaert P, Van Huffel S, De Vos M, Vanhatalo S. Objective assessment of neonatal EEG background: long range temporal behavior as a quantitative marker of abnormality, *under revision* in Frontiers in human neuroscience.

2. Matić V, Cherian PJ, Jansen K, Koolen N, Naulaers G, Swarte RM, Govaert P, Van Huffel S, De Vos M. Improving reliability of monitoring background EEG dynamics in asphyxiated infants, *submitted*, IEEE Transactions on Biomedical Engineering.

Papers in proceedings of international conferences

1. Koolen N., Dereymaeker A., Jansen K., Vervisch J., Matić V., De Vos M., Naulaers G., Van Huffel S., "Development of an interhemispheric symmetry measurement in the neonatal brain", in Proc. of the International Conference on Pattern Recognition Applications and Methods (ICPRAM 2014), Angers, France, Mar. 2014, pp. 765-770.

2. Matić V., Cherian P.J, Jansen K., Koolen N., Naulaers G., Sware R.M., Govaert P., Visser G.H., Van Huffel S., De Vos M., "Automated EEG inter-burst interval detection in neonates with mild to moderate postasphyxial encephalopathy", in Proc. of the 34th Annual International Conference of the IEEE EMBS (IEEE-EMBS), San Diego, California USA, Aug. 2012, pp. 17-20.

3. Matić V., Cherian PJ., Widjaja D., Jansen K., Naulaers G., Van Huffel S., De Vos M., "Heart Rate Variability in Newborns with Hypoxic Brain Injury". ISOTT conference, Bruges, Belgium, 2012.

4. Koolen N., Jansen K., Vervisch J., Matić V., De Vos M., Naulaers G., Van Huffel S., "Automatic Burst Detection based on Line Length in the Premature EEG", in Proc. of International Conference on bio-inspired systems and signal processing (BIOSIGNALS 2013), Barcelona, Spain, Feb. 2013, pp. 105-111.

5. Liu Y., Gligorijevic I., Matić V., De Vos M., Van Huffel M., "Multi-Sparse Signal Recovery for Compressive Sensing", in Proc. of the 34th Annual International Conference of the IEEE Engineering in Medicine and Biology Society (IEEE EMBC 2012), San Diego, USA, Aug. 2012, pp. 1-4.

6. Cherian, P. J., Deburchgraeve, W., Matić, V., De Vos, M., Swarte, R. M., Blok, J. H., ... Visser, G. H. (2011). Improvement and Validation of an Automated Neonatal Seizure Detector. In BIOSIGNALS (pp. 31-37).

7. Mijovic B., De Vos M., Matić V., Van Huffel S., "Independent Component Analysis as a Preprocessing step for Data Compression of Neonatal EEG", in Proc. of the 33rd Annual International Conference of the IEEE Engineering in Medicine and Biology Society (EMBC 2011). (IEEE-EMBC), Boston, Massachusetts, Aug. 2011.

8. Matić V., Deburchgraeve W., Van Huffel S., "Comparison of ICA algorithms for ECG artifact removal from EEG signals.", in Proc. of the 4th Annual symposium of the IEEE-EMBS Benelux Chapter. (IEEE-EMBS), Twente, The Netherlands, Nov. 2009, pp. 137-140.

Abstracts in proceedings of international conferences

1. Matić V, Mijovic B., De Vos M., Van Huffel, S. Sparse Approximation of the Neonatal EEG. 4th Workshop on Signal Processing with Adaptive Sparse Structured Representations, Edinburgh, UK, June, 2011.

2. Matić V, Cherian PJ, De Vos M, Visser G, Van Huffel S. Distinguishing tremor artifacts from neonatal epileptic seizures. The 6th International Conference Brain Monitoring and Neuroprotection in the Newborn, Amsterdam, the Netherlands, 2011, Poster.

3. Matić V, Cherian PJ, De Vos M, Visser G, Van Huffel S. Distinguishing tremor artifacts from neonatal epileptic seizures. Abstract, 3rd Dutch conference of biomedical engineering. Egmond aan Zee, Feb. 2021, 2011.

Papers in proceedings of national conferences

1. Miljkovic N., Matić V., Van Huffel S., Popovic M. B., "Independent Component Analysis (ICA) Methods for Neonatal EEG Artifact Extraction: Sensitivity to Variation of Artifact Properties", in 10th Symposium on Neural Network Applications in Electrical Engineering (Neurel 2010), Belgrade, Serbia, Sep. 2010.

2. Matić, V. M., Abadzić, S. N. (2007). Acoustic and line echo cancellation using adaptive filters. Telfor. Belgrade. Serbia.

3. Petrović, A., Milosavljević, N., Matić, V. (2006). System for 3D reconstruction and analysis of heart scintigraphic images.Telfor. Belgrade. Serbia.



FACULTY OF ENGINEERING SCIENCE
DEPARTMENT OF ELECTRICAL ENGINEERING
STADIUS CENTER FOR DYNAMICAL SYSTEMS, SIGNAL PROCESSING AND DATA ANALYTICS
Kasteelpark Arenberg 10 box 2446
B-3001 Heverlee
vladimir.matic@esat.kuleuven.be